CHEMICAL AND THERMODYNAMIC PROPERTIES OF ACCEPT2.0 CLUSTERS

By

Dana Lindsey Koeppe

A DISSERTATION

Submitted to
Michigan State University
in partial fulfillment of the requirements
for the degree of

Astrophysics and Astronomy- Doctor of Philosophy

2020

ABSTRACT

CHEMICAL AND THERMODYNAMIC PROPERTIES OF ACCEPT2.0 CLUSTERS

By

Dana Lindsey Koeppe

Clusters of galaxies offer tremendous insight into the formation and evolution of large scale structure in the Universe. While most of the total mass of a cluster is in the form of a dark matter halo, the bulk of the observable matter exists in the form of a hot X-ray emitting gas throughout the intracluster medium (ICM). The presence and ubiquity of this gas make the X-ray observables excellent tools for understanding the thermodynamic and chemical processes that affect cluster formation and evolution. Additionally, measurements of emission lines in the X-ray spectra of clusters revealed that the ICM is polluted with heavy elements that originated in stars in galaxies. The radial distributions of those heavy elements show evidence of interplay between the ICM and the cluster core.

In chapter 2, we describe the data reduction and spectral analysis of an archival sample of X-ray observations of clusters from the second catalog of the Archive of *Chandra* Cluster Entropy Profile Tables (ACCEPT2.0) which are used throughout this thesis to show how cluster X-ray properties can be used to test and constrain our theories of structure growth in the Universe. We also find that our analysis for the $L_X - T$ relation is consistent with previous works.

We continue analysis of the $L_X - T$ in chapter 3 by testing a recent claim that the expansion of the Universe is not uniform in all directions. If the expansion of the universe were isotropic, the luminosity and temperature should scale similarly for clusters in all directions. Using global core-excised luminosities and temperatures for 308 ACCEPT2.0 clusters, we found that our sample supports the assumption of isotropic expansion.

Chapter 4 investigates how the amount of metals in clusters' ICM changes with redshift. Previous works have shown varying results which are more scattered when including core emission. We show that the core-excised abundance for 308 ACCEPT2.0 clusters is not statistically different between cool-core (CC) and non-cool core (NCC) clusters, and that the global metallicity content of the ICM does not change significantly as a function of luminosity or redshift. Furthermore, we explore the degree to which a small systematic bias arising from model uncertainties that affect hot and cool spectra can look like evolution if luminosity bias is not taken into account.

Finally, chapter 5 describes the ongoing work of a data reduction pipeline for the SOAR Adaptive-Module Optical Spectrograph (SAMOS). SAMOS is a multi-object spectrograph which will be commissioned on the

SOuthern Astrophysical Research Telescope (SOAR) in 2021. The current version of the pipeline is able to produce wavelength calibrated spectra from test data using SOAR *Goodman*, and is in active development.

To my sister, mom, and dad–Thank you for always supporting me. I love you forever.

TABLE OF CONTENTS

LIST OF TABLES

LIST OF FIGURES

1 Introduction

As their name suggests, galaxy clusters are made from many individual galaxies living together in a large gravitational potential. These structures are typically $10^{14} - 10^{15} M_{\odot}$[1] and contain anywhere from a few hundred to tens of thousands of galaxies which are visible to us. Zwicky (1933) made one of the first mass estimates of the Coma cluster from observations of galaxy velocity dispersions, and the application of the virial theorem. Zwicky (1933, 1937) showed that if clusters are long-lived structures, there must be 10-100 times more unobserved matter, or "dark matter", which is unaccounted for by the stars in the galaxies. This dark matter comprises 80-85% of the mass of a cluster, with the remainder in the form of observable baryons.

Before X-ray telescopes, clusters were defined by their optical properties. For instance, one could estimate the size of a cluster by the luminosity of its brightest members, or its optical richness. Originally defined by Abell (1958), optical richness is the number of galaxies brighter than some magnitude limit, with the richest clusters containing over 300 such galaxies, and less than 100 in poor clusters. In the 1960s and '70s, extended X-ray emission from the nearby Virgo, Coma, and Perseus clusters (Bradt et al., 1967; Meekins et al., 1971; Gursky et al., 1971; Forman et al., 1972) revealed that most of a cluster's baryonic mass is in the form of hot X-ray emitting plasma that permeates the intracluster medium (ICM). The ubiquity of this hot gas naturally has led us to question the origin of the ICM, and its relation to cluster formation and evolution.

With larger sample sizes, we have been able to study clusters in a broader context, and better understand their general characteristics. However, many samples in the past have been a combination of previously analyzed data from multiple works. Consequently, combining different catalogs necessitates the use of correction factors to account for systematic differences between samples. The second release of the Archive of Chandra Cluster Entropy Profile Tables (Donahue, Baldi, et al, in prep, hereafter, ACCEPT2.0) will be the largest publicly available catalog of uniformly derived X-ray properties from X-ray observations of clusters of galaxies available from the Chandra Data Archive. Its predecessor ACCEPT (Cavagnolo et al., 2009) produced radial profiles of density, gas temperature, and entropy, which are related to the thermal history of a cluster. ACCEPT2.0 is an expansion of ACCEPT, as it includes measurements for more X-ray observables and contains more than twice as many clusters.

This thesis will investigate the differences between the average global X-ray properties of clusters of galaxies at different cosmological epochs, and in different directions on the sky, using X-ray data from

---

[1] $M_{\odot} \equiv 1$ solar mass $\sim 2 \times 10^{30}$ kg.

ACCEPT2.0. Section 1.1 of this introduction will describe the X-ray observables relevant to this dissertation. Section 1.2 defines the terms used throughout this thesis. Section 1.3 will give an overview of recent literature regarding scaling relations. Section 1.4 covers abundance measurements from X-ray spectra. Finally, section 1.5 will present an overview of this thesis.

1.1 Cluster Observables

The obvious observables come from optical properties such as cluster richness (number of galaxies within 2 magnitudes of the third brightest galaxy member) and compactness (number of galaxies within some characteristic radius of the cluster center) (Abell, 1958), but X-ray observables are most important for this thesis, as most of the baryons in a cluster are in the form of hot X-ray emitting gas. For reviews of galaxy clusters and how they relate to cosmology, see the review by Voit (2005). Reviews regarding X-ray emission from clusters are provided by Sarazin (1986) and Böhringer & Werner (2009). We study clusters of galaxies to understand the largest structures in the Universe. One aspect of the theory of gravitational assembly of cosmic structure is the prediction of the cluster mass function. The cluster mass function is the number density of clusters above a certain mass M as a function of redshift, and can be used to answer questions such as how many clusters of mass M do we expect there to be in a range of redshifts? If we could measure the cluster mass function, it would give insights into how large scale structures have evolved with the Universe. Unfortunately, mass is not a directly observable quantity, which is where X-ray observations come in handy. Temperature T and luminosity L_X are easily derived from X-ray spectra. The temperature is tightly correlated with the mass, while the luminosity is more affected by processes such as recent mergers or AGN activity. Due to the dynamics affecting cluster luminosity, the scaling of luminosity with temperature $L_X - T$ and mass $L_X - M$ are more scattered than $M - T$. Therefore, we can use temperature and (less directly) luminosity in lieu of direct mass measurements.

Another spectral probe of the ICM comes in the form of emission lines. The ubiquitous presence of heavy elements such as iron in the spectra of clusters is evidence that the ICM is comprised of gas processed in stars and subsequently distributed throughout the cluster. The global metallicity content of the clusters acts as a tracer for when metals became part of the ICM, and spatially resolved measurements give clues for how this enrichment occurs.

1.2 Terminology

Before proceeding, it is important to define some terminology that will be used throughout this thesis.

1.2.1 Cosmology vernacular

An object's redshift z is a dimensionless distance estimate based on the Doppler effect which arises from the finite speed of light and the expanding Universe. Consequently, the rest-frame wavelength of light from an object is lengthened–or "redshifted"–as the it recedes. The wavelength of emitted light increases by a factor of $1 + z$–i.e. $\lambda_{\rm obs} = \lambda_{\rm rest}(1 + z)$. Nearly a century ago, Edwin Hubble noticed that the recession velocity of galaxies increased in proportion to their distance, so more distant objects are moving away from us more quickly than nearby objects. We now characterize this expansion of the Universe through the Hubble parameter $H(z)$, where the present day Hubble constant H_0 is related to an object's recessional velocity v and Hubble distance[2] d,

$$v = H_0 \times d. \tag{1.1}$$

Here, H_0 = 70 km s^{-1} Mpc^{-1}, where 1 Mpc (mega-parsec) = 3.26×10^6 light-years = 3.086×10^{24} cm. The "constant" here refers to expansion that is isotropic in all directions. We can trace this expansion backwards to obtain an estimate for the current age of the Universe, or Hubble time, $t_H \equiv 1/H_0 \simeq 13.97$ Gyr $\simeq 4.4 \times 10^{17}$ s. However, H_0 does have a dependence on the time since expansion began, due to the changing contents of the Universe. For instance, an empty Universe has a constant expansion, but that expansion slows down in the presence of any matter. Dark energy, however, accelerates the expansion.

We relate Hubble constant as a function of redshift to the present day value via,

$$H(z) = H_0 E(z), \tag{1.2}$$

where $E(z) = \sqrt{\Omega_M(1+z)^3 + \Omega_\Lambda}$, and the cosmological parameters $\Omega_m \simeq 0.3$ and $\Omega_\Lambda \simeq 0.7$ refer to the matter and dark energy content of the Universe, and redshift z serves as a distance measure. Objects that are moving outward along the line of sight experience a redshift due to the Doppler Effect, so z is able to give a general idea of the distance to a source based on its recession velocity. For local systems, redshift is $z \sim 0$. The redshift of a cluster is important for estimating its properties because it tells us about the environment in which it formed. For a given redshift, there is some critical density $\rho_c(z)$ at which the gravitational potential of material within some radius overcomes and slows the expansion of space. The critical density is the maximum average density a Universe without dark energy can have before it would continue to expand forever. For reference, the present day critical density is,

---

[2] This equation is applicable for small redshifts, where the Hubble distance d is equal to the co-moving radial distance. At larger redshifts, we use $d(z) = c\int_0^z dz/H(z)$

$$\rho_{c,0} = \frac{3H_0^2}{8\pi G} \approx 10^{-29}\text{g cm}^{-3}, \tag{1.3}$$

where $G = 6.67 \times 10^{-8}$ cm^{3}g^{-1}s^{-2} is the gravitational constant. We relate the critical density at different cosmological epochs to the present day critical density $\rho_{c,0}$ via,

$$\rho_c(z) = E(z)^2 \rho_{c,0}. \tag{1.4}$$

Ideally, clusters are spherical virialized structures in which a sphere of gas is supported against further collapse by outward pressure provided by the kinetic energy of the particles.

1.2.2 Anatomy of galaxy clusters

For a model ICM, the virial radius R_v is often used as a reference point for the "edge" of a cluster, and, based on simulations, turns out to be the radius at which the density of material is ∼180-200 times the critical density of the Universe at the epoch of interest (Voit, 2005). Because the R_v is out of the typical X-ray instrument field of view for most nearby systems, we often use scaled radii R_Δ to define our regions of interest for a cluster. R_Δ refers to the radius at which the density is Δ times the critical density of the Universe at the redshift of the cluster. Similarly, we define characteristic mass M_Δ and temperatures T_Δ as the mass and temperature within the scaled radius. Two commonly used values of Δ are 2500 and 500, with the virial radius being $\sim R_{200}$.

An interesting distinction between clusters is their status as either cool-core (CC) or non-cool core (NCC). The term "cool-core" arises from the drop in temperature towards the center. Increased density towards the centers of CCs result in sharper peaks in surface brightness aligning with the drop in the temperature profile. NCCs, however, show less dramatic central luminosity peaks and flatter temperature profiles in their cores. Outside the core radius however, their temperatures and X-ray surface brightness profiles are nearly indistinguishable when scaled by size. The stacked profiles of CC ABELL_2390 and NCC ABELL_2219 give good examples of differences in surface brightness (figure 1.2.2) and radial temperature (figure 1.2.2) between CCs and NCCs. Choice of aperture is therefore crucial when characterizing clusters by global X-ray properties.

With adequate spatial resolution, global X-ray properties can be estimated for clusters within a full aperture, or for a core-excised (CE) aperture. We use core-excised global properties because they minimize dependence on a cluster's core status. The "core" is used to describe the region inside which the density is such that thermodynamics unrelated to gravity can affect the gas in times comparable to the Hubble time, and shorter timescales increase the scatter in observable properties (Vikhlinin et al., 2005; Pratt et al., 2006). We define the core in terms of scale radius: $r_c = 0.3R_{2500}$.

1.3 X-ray scaling relations

Early X-ray observations showed a strong correlation between luminosity and temperature (Mitchell et al., 1976; Fabian et al., 1994; Cavaliere et al., 1997; Arnaud & Evrard, 1999), which are used for comparison to expectations from theoretical models. It is easiest to model the ICM as a hydrostatic sphere which has collapsed under gravitational pressure and is supported against further collapse via thermal pressure. The gravitational potential of the system, and therefore the temperature, is set by the size of the initial overdensity from which it came. Because gravity is scale-invariant, the simplified hydrostatic model of the ICM results in clusters which are identical when scaled by mass. This leads to predictable, self-similar scaling relations between the observables and the mass (Kaiser, 1986; Reichert et al., 2011). For this model, the mass enclosed within some scaled radius is,

$$M_\Delta = \frac{4}{3}\pi R_\Delta^3 \Delta \rho_c(z) \propto E(z)^2 R_\Delta^3. \tag{1.5}$$

We remind the reader that the Δ in equation 1.5 is a scalar number (i.e 200, 500, 2500, etc.).

The virial theorem states that a sphere in hydrostatic equilibrium will have average kinetic energy equal to half the total gravitational potential energy. According to the theorem, potential is related to kinetic energy of the particles by,

$$\frac{M_\Delta}{R_\Delta} \propto \sigma_v^2 \propto T. \tag{1.6}$$

Temperature should therefore scale with mass as

$$T \propto [E(z)M]^{2/3}. \tag{1.7}$$

For typical ICM temperatures of 10^7-10^8 keV, the ICM radiates primarily via thermal bremsstrahlung due to collisions between ions and electrons. Assuming the gas is isothermal, the bolometric luminosity is $L_X \propto n_e^2 \Lambda(T)$, where the cooling function $\Lambda(T) \propto T^{1/2} \mathrm{e}^{-E/kT}$ for thermal bremsstrahlung. Observations of the Perseus cluster by Branduardi-Raymont et al. (1981) showed a strongly peaked surface brightness profile which deviated from the isothermal model inside of ~10 kpc. The profile of the Coma cluster, which is recovering from a recent merger, was shown to be consistent with the expected model (Branduardi-Raymont

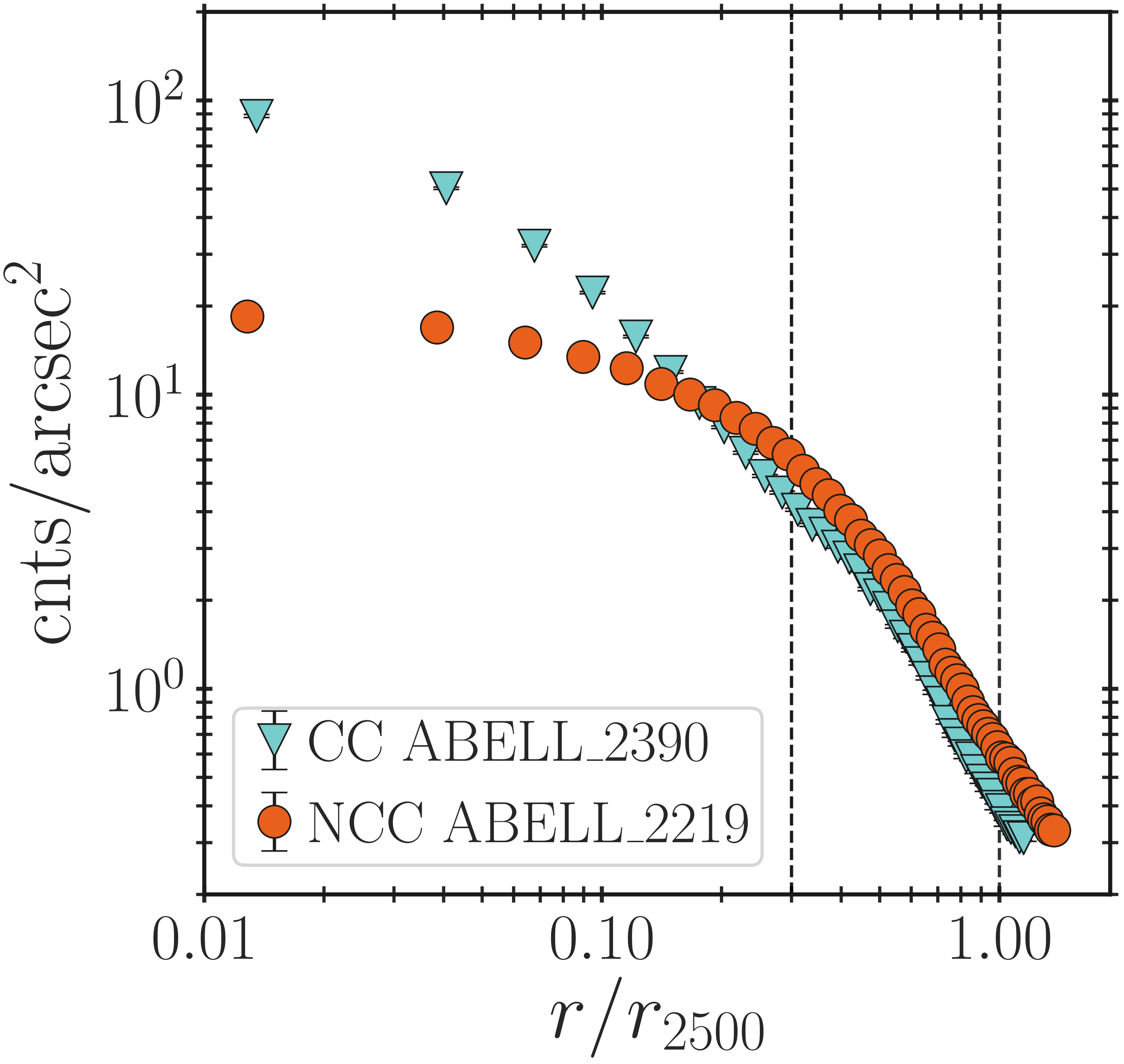

Figure 1.1 ACCEPT2.0 surface brightness profile and the 1σ errors for cool-core cluster ABELL_2390 (*blue triangles*) and non-cool core cluster ABELL_2219 (*red circles*). The dotted lines represent the core-excised region $0.3R_{2500} < r < 1R_{2500}$, where R_{2500} is the distance at which the mean density is 2500 times the background density.

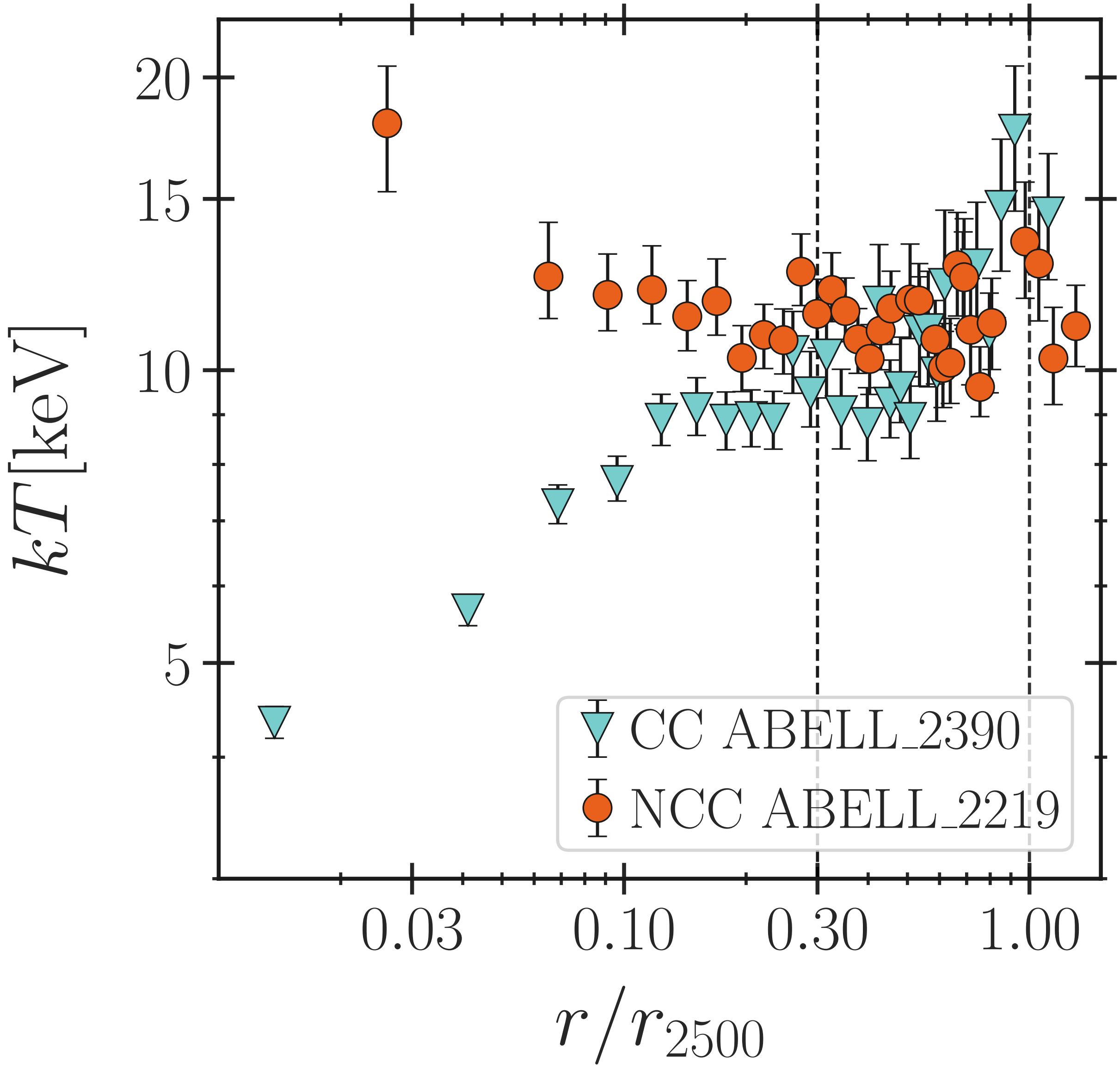

Figure 1.2 Projected radial temperature profiles and their 1σ errors using the same labels as figure 1.2.2.

et al., 1985; Briel et al., 1992; Jones & Forman, 1999). Other works which considered larger cluster samples Jones & Forman (1984); Neumann & Arnaud (1999) showed that clusters could generally be separated into two categories: those with a discernible peak in the surface brightness and those with a flatter profile inside the core. CC clusters have been observed to have a steep decline in temperature and increased luminosity towards the center, as opposed to NCC clusters (Fabian, 1994; Arnaud et al., 2002; Maughan et al., 2012). Outside of the denser regions, clusters are more well-behaved because the cooling time for the gas there is longer than the Hubble time, and therefore a tracks the results of cosmological processes with longer timescales. Scaling relations of luminosity and temperature, with cluster mass, are therefore often evaluated using both core-excised and core-included measurements, where excising the core has been found to significantly reduce the scatter in the $L_X - T$ relation (Markevitch, 1998; Pratt et al., 2009; Maughan et al., 2012). These results suggests that clusters evolve self-similarly outside of the core region.

Still, the outer regions of clusters have been shown to deviate from the self-similar model. In the absence of extra heating and cooling of the gas, numerical simulations predict,

$$\frac{L_X}{E(z)} \propto [M_\Delta E(z)]^{4/3} \propto T^2. \tag{1.8}$$

However, observations have shown a steeper slope of ∼3 instead of 2 (Arnaud & Evrard, 1999; Ettori et al., 2004; Pratt et al., 2009; Mittal et al., 2011). Additionally, the observed $L_X - T$ relation may steepen even further for lower temperature systems (Maughan et al., 2012; Sun, 2012), although the increased scatter in the lower luminosity systems and the effects of selection bias makes this steepening challenging to verify. The break from self-similarity in the $L_X - T$ relation for all clusters and groups may be indicative of some source of non-gravitational processes such as AGN feedback, supernovae feedback, and radiative cooling, which likely become more important compared to the energy per particle incurred from gravitational accretion for systems with shallower potential wells. Heating/cooling of gas does not necessarily raise/lower the temperature of the gas so much as it decreases/increases the density, or, more specifically, increases/lowers the gas entropy. When heat is injected into the ICM, the gas puffs up and decreases the luminosity. Gas entropy, here scaled as $K \propto T n_e^{-2/3}$ is therefore a useful tracer of this heating and cooling (Ponman et al., 1999; Voit, 2005). Relaxed CC clusters with high central densities (and therefore strongly peaked surface brightness profiles, as discussed previously in section 1.2.2) have low central entropy K_0. Conversely, NCC clusters have higher central entropies as a result of recent mergers or AGN outbursts. The Bullet cluster is a famous example of a merging system.

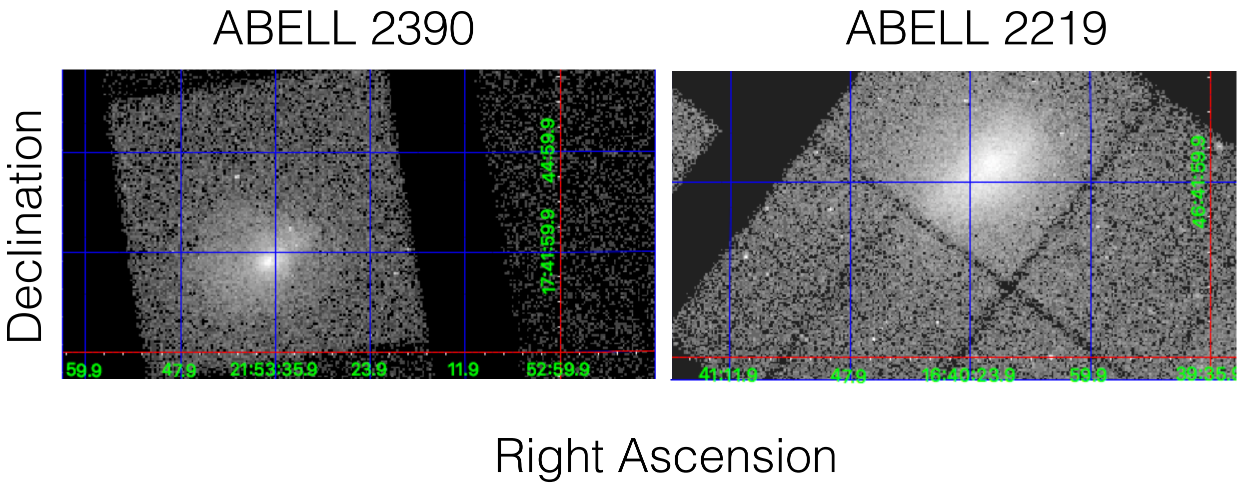

Figure 1.3 The core is much brighter and more concentrated in CC ABELL_2390 (*left*) than that of NCC cluster ABELL_2219 has more diffuse X-ray emission (*right*)

1.4 Metals in the ICM

In addition to gas temperature, the X-ray spectrum is influenced by chemical abundance. Heavy elements can be detected and measured in a spectrum through the analysis of an X-ray spectrum that includes emission lines produced by interactions between electrons and various ion species in the ICM. Detection of iron in the X-ray spectra of the Perseus, Virgo, Coma, and Centaurus clusters gave the first evidence that gas is not primordial[3] in nature, but had been polluted with heavy elements from stars in galaxies and subsequently ejected and distributed throughout the ICM (Mitchell et al., 1976; Mitchell & Culhane, 1977; Serlemitsos et al., 1977). The sheer quantity of hot gas in clusters of galaxies far exceeds the mass in stars by at least a factor of 5, which means that most of this gas *is* primordial, but stars and their end-states (particularly merging white dwarfs and merging neutron stars) are very good at making heavy elements and then distributing them to their environments. Energy ranges available to the *ROSAT* and *Einstein* missions were limited to below $\sim 2-3$ keV, where the brightest lines are part of a region called the iron-L complex, near 1 keV. With *ASCA* (Tanaka et al., 1994), we were able to sample a much broader energy range to include more line features, including the Fe-K complex at ~7 keV. For reviews of observations of ICM metallicity, see Werner et al. (2008) and Mernier et al. (2018). Metals are formed from stars and supernovae (mostly SNIa but also a little SNII, a little contribution from asymptotic giant branch stars, and very heavy

---

[3] Primordial means that the gas has never been in any star.

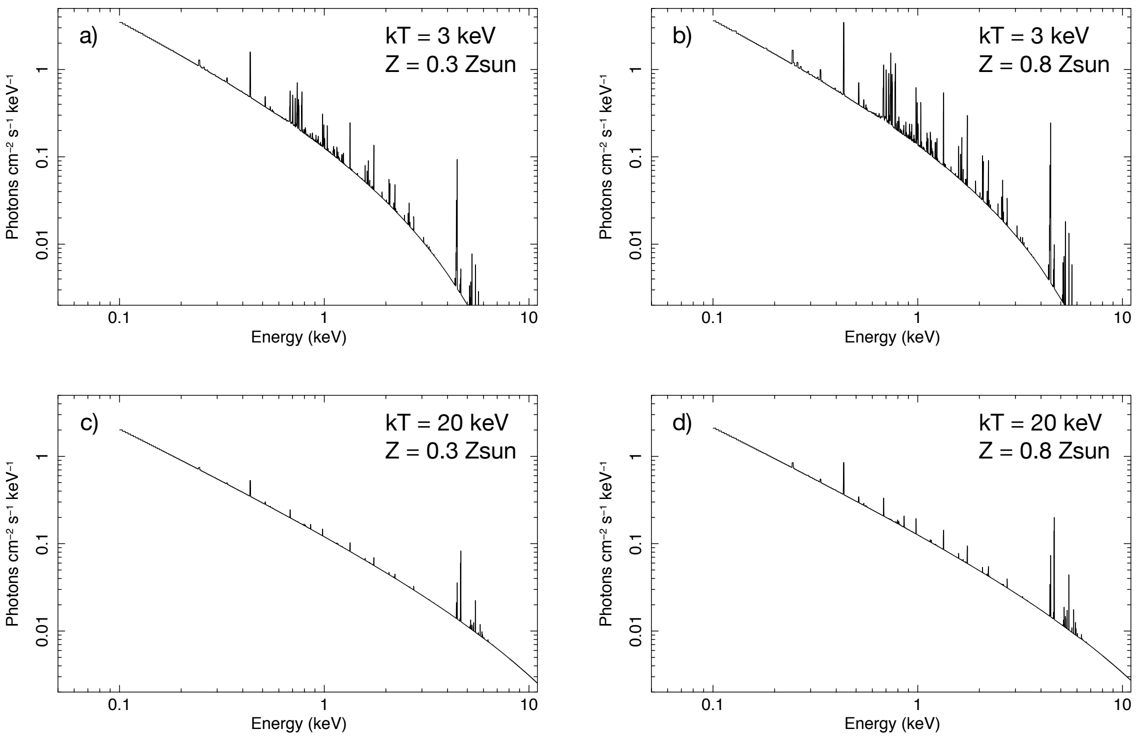

Figure 1.4 Simulated X-ray spectra for gases with varying temperatures and metallicities. a) Relatively cool (kT=3 keV) gas with solar abundance (Z=0.3 $Z_{\odot}$). b) Cool gas with higher metallicity shows stronger emission lines. The spectra were generated using $XSPECv12.11$ (Arnaud, 1996).

elements like gold are formed in neutron star mergers). Excellent spectral resolution is needed to measure individual elements, but the most important emission feature for a relatively hot ICM is the Fe-K complex. Figure 1.4 shows an example of how the spectrum changes with respect to temperature and metallicity. The abundance is estimated from the strength of the emission line in comparison to the continuum. At higher gas temperatures, the strength of the Fe-K lines are easier to discern than the Fe-L features at lower energies, while at lower temperatures the spectra become more dominated by emission lines and the hydrogen-helium bremsstrahlung continuum cuts off at lower energies ($E \sim kT$, because of the exponential cutoff). The difference in the spectra has to do with the ionization state of the gas at a given temperature and the atomic structure of the iron ions. Gas with hydrogen-like iron is hot enough to be stripped of it's outer L-shell electrons, leaving mostly K-shell transitions. At cooler temperatures, the iron ions with bound electrons in the L-shell dominate.

Naturally, the ubiquity of line emission from heavy elements leads us to questions of when and how the gas made it out of individual galaxies (where most of the stars are) and into the ICM. Spatially resolved observations showed characteristic differences in the radial distribution of metals which coincided with the differences in surface brightness and temperature profiles between CC and NCC clusters. CCs typically have stronger metallictiy gradients which increase towards the core, whereas NCCs have flatter, although still peaked[4], profiles (De Grandi & Molendi, 2001). Simulations have been able to replicate the metallicity profiles with AGN feedback models. At larger radii and outside of the reach of the AGN, the ICM of massive clusters appear to be independent of core status, which agrees with the notion that the characteristics of the gas evolve on cosmological timescales, and can therefore be used to track the metal distribution history of a cluster. Recently, larger cluster samples with wider redshift ranges seem to support a model for early enrichment ($z \gtrsim 1$), which is supported by the core-excised global abundances in ACCEPT2.0 (described in chapter 4).

1.5 This work

This thesis will use measurements from ACCEPT2.0 show how X-ray observations of galaxy clusters can be used to constrain our understanding of their thermodynamic and chemical properties, and how they relate to the formation and evolution of large-scale structure in the Universe. Chapter 2 describes the ACCEPT2.0 data used throughout this thesis. We will show that the global properties are able to reproduce previous observations of the $L_X - T$ relation described in section 1.3. In chapter 3, we continue our work with this scaling relation and use global core-excised temperatures and luminosities to test the standard assumption of the isotropic expansion of the Universe. Chapter 4, looks at the relationship between the heavy metal content of the ICM and other properties such as core status, luminosity, and cluster redshift. We also compare our results with those obtained from another sample which used different data reduction methods. Finally, chapter 5 describes the active development of a data reduction pipeline for the *SOAR* Adaptive-optics Multi-Object Spectrograph (*SAMOS*).

---

[4] Because metallicity is emission-weighted, metallicities of very low density environments are more difficult to approximate as they subject to low S/N.

2 ACCEPT2.0

2.1 Archive of Chandra Cluster Entropy Profile Tables (ACCEPT)

The Archive of Chandra Cluster Entropy Profile Tables (ACCEPT) began as an analysis of entropy profiles for 239 clusters (Cavagnolo et al., 2009). The goal was to understand what X-ray observations of the intracluster medium (ICM) can teach us about how the core interacts with the rest of a cluster. Entropy, $K \propto kTn^{-2/3}$, is associated with changes in gas density and temperature and a well-known tracer for the thermal history of the ICM (Bower, 1997; Ponman et al., 1999; Pearce et al., 2000). Left alone, the ICM will convect until $dK/dr \geq 0$ everywhere, or all the high density/low temperature gas is below the low density/high temperature gas. A relaxed cluster (no recent merger event) would likely have a dominant central galaxy at the center, called the brightest cluster galaxy (BCG). Entropy profiles are, for the most part, compatible with hierarchical formation models outside of the core, but have been shown to flatten inside of $r_c \sim 100$ kpc[1] (Ponman et al., 2003; Donahue et al., 2006). With 239 entropy profiles in ACCEPT, Cavagnolo et al. (2009) showed that clusters generally follow model predictions and decrease in entropy from the outskirts, but flatten to a nearly constant central entropy K_0 in the core. Later assessments of cluster entropy profiles showed that CC systems could also be modeled with the broken power law (equation 2.1), with a steeper outer component ($\propto r^{1.1}$) and a shallower inner slope ($\propto 2/3$), where NCCs have even flatter core entropy profiles, approaching r^0 (Panagoulia et al., 2013; Hogan et al., 2017). The entropy profile is modeled as,

$$K(r) = K_0 + K_{100} \left(\frac{r}{100\text{kpc}} \right)^{\alpha}, \tag{2.1}$$

where K_0 is the central entropy, K_{100} is the normalization constant, and α is the slope of the entropy profile. The flattened profiles indicate that something prevents gas from cooling and condensing past some limit by displacing large amounts of gas around the core. We now know this phenomenon is caused by a feedback relationship between a cluster's active galactic nucleus (AGN) (Bower et al., 2006; McNamara & Nulsen, 2007). When turned on, the AGN puffs up the surrounding gas and raises the entropy. Consequently, the effects of feedback from AGN in addition to other thermodynamic processes such as radiative cooling and feedback from supernovae (SNe) are observed in other X-ray observables.

Until now, ACCEPT was the largest publicly available collection of uniformly derived radial profiles of

---

[1] 1 kpc = 3.26 $\times 10^3$ ly = 3.086×10^{21}

Table 2.1 Main differences between ACCEPT and ACCEPT2.0. Major updates for ACCEPT2.0 include spatially resolved temprature and metallicity profiles, global estimates for temperature, luminosity and metallicity, and morphological classifications.

	ACCEPT	ACCEPT2.0
# of clusters	239	606
# of entropy profiles	239	348
# of kT, Z profiles	⋯	398
Global T, L_X, Z	⋯	✓
Morphology	⋯	✓

density, temperature, and entropy. ACCEPT2.0 (Donahue, Baldi, et al, in prep) adds more clusters and expands the suite of derived X-ray properties. In addition to more than doubling the number of targets in its predecessor, ACCEPT2.0 includes estimates for morphological properties, global X-ray observables for temperature, luminosity, and metallicity, as well as ∼400 radial temperature and metallicity profiles. The major differences between ACCEPT and ACCEPT2.0 are highlighted in table 2.1.

2.2 ACCEPT2.0

The entropy profiles and core entropy K_0 values in ACCEPT2.0 were calculated by Rachel Frisbie (Frisbie, MSU dissertation, anticipated October 2020) and the main ACCEPT2.0 data analysis was performed by Alessandro Baldi using CIAO v4.7 (Fruscione et al., 2006) and SHERPA (Freeman et al., 2001) with the *Chandra* calibration database CALDBv24.5. An first quick estimate of the temperature by the pipeline was used to set a count threshold for further analysis. Simulations determined that, for the 0.5-7 keV band, a minimum number of counts of $n_{min,res} = 1377 \cdot kT - 537$ (where kT is the temperature of the cluster in keV) were necessary to obtain a 20% error on the measure of the cluster temperature in at least three spatial bins, whereas $n_{min,glb} = (1377 \cdot kT - 537)/3$ was necessary to have the same error on the temperature in a single spatial bin. The pipeline set $n_{min,glb}$ and $n_{min,res}$ as the minimum counts necessary to include a cluster in the total sample and in the spatially resolved sample, respectively.

ACCEPT2.0 global properties were estimated for three spatial regions: the cluster with the core included (CI, $r < R_\Delta$), core of the cluster (C, $r < r_{\rm core}$), and the cluster with the core excised (CE, $r_{\rm core} < r < R_\Delta$), where Δ=2500 or 500. The core radius is usually taken to be some fraction of the scale radius. The quantities of interest to this thesis are approximated for radius R_{2500} because the aperture extent is consistent across 535 ACCEPT2.0 objects and we define the core radius as $r_{\rm core} = 0.3\ R_{2500}$. The fits to R_{2500}, and the relative average temperature, T_{2500}, were performed using the formula derived by Vikhlinin et al. (2006),

$$R_{2500} h E(z) = 0.501 \left(\frac{T_{2500}}{5\ \mathrm{keV}} \right)^{0.55} \mathrm{Mpc}, \tag{2.2}$$

where $E(z) = \sqrt{\Omega_m(1+z)^3 + \Omega_\Lambda}$ and $h = H_0/(100)$ km s^{-1} Mpc^{-1}. The pipeline used an input value of $T_{2500} = 5$ keV to estimate the first-guess for R_{2500} and extracting the core-excised ($0.3R_{2500} < r < R_{2500}$) region from the spectrum. The pipeline then iterated over values for T_{2500} and R_{2500} until the model achieves convergence to a stable temperature ($\Delta T_{2500} \leq 0.01$keV between two successive iterations). The three different global regions were used because gas inside the core region evolve on time scales shorter than the age of the Universe, which results in high variability between the X-ray observables. Outside of this region, clusters appear mostly self-similar (Maughan et al., 2012).

The source spectra and background were fitted simultaneously using spectral models in *Sherpa*. There are several different models useful for observations of the ICM because it involves numerous calculations for various atomic interactions. ACCEPT2.0 source emission was fit to a model for a hot diffuse gas called a *mekal* model (Kaastra et al., 1996; Liedahl et al., 1995) with the following parameters: The ratio between the elements were fixed to the solar value as in Anders & Grevesse (1989). The pipeline considered line of sight absorption fixed at the Galactic value n_H (Stark et al., 1992), and an additional internal absorption component left free to vary (consistent with zero in the large majority of clusters). The free parameters in the *mekal* model were the temperature kT, the metal abundance Z, and the normalization. The redshift z has been fixed at the literature value for the cluster. The background model used was made by two power-law models, several gaussian emission lines and an *apec* thermal model at low temperature ($kT = 0.17$ keV, to take into account the soft diffuse X-ray background). The slopes of the power-laws and the quantity, position and strength of the emission lines depend on the specific ACIS chips and they are adjusted accordingly. The shape of this spectrum is held fixed.

2.3 K-correction and bolometric correction

Spectra were fit by the pipeline over the observed 0.5-8 keV band. The pipeline did not compute the bolometric and K-corrections[2] of the observed fluxes and luminosities, so those calculations were done by this author to support further scientific use. We used bolometric corrections to convert the bandpass spectral energy distribution (SED) to a spectrum that covers the full range of energies, and the K-correction to account for cosmology. Because of expansion, photons from distant objects become redshifted as they travel towards us. Thus, their observed energies are lower than those of the photons emitted in the rest-frame and require correction.

We perform the bolometric and K-corrections by modeling spectra in *XSPEC v12.11.0*(Arnaud, 1996). First, we convert the observed fluxes and luminosities to rest-frame energies by shifting the energy range

---

[2] The "K" here is an arbitrary variable that Hubble used in Hubble (1936). However, Kinney et al. (1996) mentions that an earlier usage of the term from Wirtz (1918), but it is written in German so we many never know.

via $E_{\rm rest} = (1+z)E_{\rm observed}$. We then extrapolate the best-fit spectrum to a very broad energy range for "bolometric"[3] values. We use to compute the correction factors by simulating observations of each cluster based on the temperature, metallicty, and redshift.

Each simulated cluster returned values for the observed flux and luminosity with their corresponding rest-frame and bolometric quantities. The ratios of rest-frame and bolometric values to those of the observer frame were used as the correction factors for the real data. The specific process and the code for the K-correction procedure is provided in appendix A.

2.4 Vetting of the Data

For nearby clusters and groups with strong temperature gradients, global temperature and (emission-weighted) abundance estimations have been shown as biased towards those of the core region when fit to an isothermal model, and may be better characterized by a multitemperature model (Buote, 2000) because the line of sight passes through gas of different temperatures, even with a simple radial temperature gradient. However, mentioned in section 1.3, previous observations have shown that after excising the core region, the ICM fits well to a single temperature.

One of the goals of ACCEPT2.0 was to assign uniformly measured global properties to each cluster. These measurements come from spectroscopic fits to a single temperature *mekal* model for spectra obtained by a single large aperture. We obtained global properties in three main types of aperture: core-excised (CE), core-included (CI), and core only (C).

To verify that the CE spectra for clusters in ACCEPT2.0 are adequately characterized by a single-temperature model, we compared ACCEPT2.0 spatially resolved temperature profiles of 154 objects to their global spectral temperatures. In summary, we found that 91% of the spectrum-approximated CE temperatures are within 1 standard deviation of the radially averaged value. The CE global properties here refer to measurements obtained within the region [0.3-1]R_{2500}. We do the same thing with the core-included (CI) region defined as [0-1]R_{2500}.

2.4.1 Initial Cuts

Originally 535 ACCEPT2 objects have global spectra for the [0.3-1]R_{2500} aperture, 67 of which were removed from any further analysis for any of the following reasons (number of affected clusters written in parentheses):

- Clusters with updated redshift measurements, $\Delta z > 10\%$. (12)

---

[3] These are not true bolometric values, as that would imply integration over all energies and *XSPEC* does not have calculations for infinity.

Table 2.2 There are 15 ACCEPT2.0 clusters that have had updated redshifts since their spectra were analyzed. These clusters were left out of any further analysis, except for clusters marked with a † which had their CE global temperatures and abundances refit (but were left out of the $L_X - T$ analysis). The references are as follows: Ah2012-Ahn et al. (2012), Al2015-Alam et al. (2015), AS2017-Andrade-Santos et al. (2017), B2015-Bleem et al. (2015), C2017-Caminha et al. (2017), D2002-Donahue et al. (2002), M2016-McDonald et al. (2016), P2011-Piffaretti et al. (2011), S2013-Sifón et al. (2013), R2016-Rykoff et al. (2016), Wb2013-Webb et al. (2013), Wn2012-Wen et al. (2012), Wn2015-Wen & Han (2015).

ACCEPT2.0 Name	z_{old}	z_{new}	*Chandra* Obs. ID	Reference
ABELL_3084	0.098	0.219	9413	P2011
ABELL_3140	0.062	0.173	9416	P2011
ACT-CL_J0235-5121	0.430	0.278	12262	S2013
ACT-CL_J0237-4939	0.400	0.334	12266	S2013
ACT-CL_J0304-4921	0.470	0.392	12265	S2013
†ACT-CL_J0616-5227	0.710	0.684	12261,1312	S2013
ACT-CL_J0707-5522	0.430	0.296	12271	S2013
G115.71+17.52	0.400	0.300	13383	AS2017
†MACS_J0416.1-2403	0.420	0.396	16237,1044	C2017
NSCS_J144726+082824	0.195	0.376	10481	Ah2012, Wb2013
OC06_J1119+2127	0.400	0.061	5790	D2002, P2011
RCS_J2327-0204	0.200	0.700	14361,7355	Wn2015
SPT-CL_J0102-4915	0.750	0.870	14022,1402	S2013, B2015, M2016
†SPT-CL_J2344-4243	0.620	0.596	13401	S2013
ZwCl_1309.1+2216	0.266	0.170	7898,14014	R2016

- Spectral fits did not achieve a reliable temperature convergence[4]. (20)
- Too much of the core-excised aperture was outside the field of view to produce reliable global estimates. (35)

There are 15 clusters (table 2.2) that were found to have updated redshifts, but three of them had percent changes below 10%. For these clusters with small redshift updates, we refit the global temperatures and abundances for the core-excised R_{2500} spectra and they have been flagged. Formally, the apertures used to compute the luminosities for these clusters has changed somewhat, and therefore the luminosities from the pipeline are not quite right, even if they are calculated using the correct luminosity distance. The luminosities for these clusters were therefore left out of the $L_X - T$ analysis in this work.

There are therefore 468 objects with spectral analysis in the global, core-excised aperture ($0.3 \lesssim r/R_{2500} \lesssim 1$). From the procedure described below, we cut out 36 objects with reduced chi-square $\chi^2 \lesssim 1.4$. Below this value, we found general agreement between the global measurements and those calculated from the weighted means.

---

[4] some of these clusters overlap with those that are too large to fit in the aperture.

2.4.2 Radially weighted temperature and abundance

This section's goal is to define a reasonable reduced χ^2 beyond which to cut global temperature and abundance approximations in the region (0.3-1)R_{2500} for the non-spatially resolved objects in the sample.

Objects lacking radial profiles that host multiphase gas in their ICM can lead to misleading results from the spectral fit. Measurements for high S/N systems with multi-temperature plasma can have misleading goodness-of-fits when applied to an isothermal model, despite having reliable parameter estimates. Here, we use a subsample of spatially resolved ACCEPT2.0 clusters and compared their spectrum-derived temperature estimates to those computed via their radial profiles to test the reliability of ACCEPT2.0 global properties.

There are ∼400 clusters in ACCEPT2.0 with spatially resolved data, 154 of which have at least 3 data points in the region of interest, $0.3 < r/R_{2500} < 1$. We used projected radial temperature profiles to calculate each cluster‘s weighted mean ($\bar{X}$), mean error (σ_w), and standard deviation ($\sigma_{\rm std}$), defined as follows,

$$\bar{X}_w = \frac{\Sigma w_i X_i}{\Sigma w_i} \tag{2.3}$$

$$\sigma_w = \sqrt{\frac{1}{\Sigma w_i}} \tag{2.4}$$

$$\sigma_{\rm std} = \sqrt{\frac{\Sigma w_i (X_i - \bar{X}_w)^2}{\Sigma w_i}}, \tag{2.5}$$

where the weight on each radial data point is $w_i = 1/\sigma_i^2$. If a cluster hosts a relatively flat temperature profile outside the core, then $\sigma_{\rm std}/\sigma_w$ should be of order unity. We compute radially weighted abundances in the same manner as above, but use the temperatures in the vetting process.

We found that ∼91% of the weighted means were well within their stated uncertainties, and global properties with suspicious chi-square (and therefore underestimated uncertainties) were limited to clusters with unresolved temperature structure in the ICM.

In general, the values obtained from the global spectral fits are good estimates for the global average, despite the occasional underestimation of the error bars due to poor chi-square. In general, we found good agreement between global properties and the weighted average. When possible we replaced global temperatures, metallicities, and their respective errors with values from the radially weighted profiles. For good fits (χ^2/d.o.f>1.2), we found no difference between using the global and radially averaged values. Beyond that, the data uncertainties were more representative of the quality of spectral fit for χ^2/d.o.f$\lesssim$1.4. Of the clusters without radial profiles, we removed only 36 global measurements for having poor (reduced) chi-square. The radial metallicity profiles are in appendix B, and the radial temperature profiles are shown in appendix C. The global CE properties for the final 432 ACCEPT2.0 clusters and groups is provided in table 4.7. We followed the same procedure for the CI global properties. This replacement procedure ensured that objects with resolved multi-temperature gas are represented by data points with error bars based on good fits.

2.4.3 $L_X - T$ relation

Here, we use the global CE and CI L_X and T values for 305 clusters (with CE bolometric luminosities $L_X \gtrsim 4 \times 10^{43}$ erg s^{-1}) to illustrate that the global CE quantities do a good job of removing scatter in the relation caused by core emission. There is a noticeable separation between CC (blue triangles) and NCC (red circles) clusters in the upper panel of figure 2.1. In the lower panel, this scatter is significantly reduced. As mentioned previously in section 1.3, CCs typically have higher core densities (lower central entropy K_0[5]) than NCCs, which makes them brighter. For our sample, CCs are defined as having central entropies of $K_0 < 30$ keV cm^2, and those with higher K_0 are NCCs. Clusters with no core status are plotted as crosses.

We fit[6] both the CE and the CI values to the $L_X - T$ relation of the form,

$$\ln\frac{L_X E(z)^{-1}}{10^{44}\ \mathrm{erg\ s^{-1}}} = \ln L_{X,0} + \beta \ln\frac{kT}{6\ \mathrm{keV}}. \tag{2.6}$$

We used an MCMC algorithm to obtain normalization $L_{X,0}$, slope β, and intrinsic scatter $\sigma_{\rm int}$, assuming Gaussian data and errors. We used uniform priors on the variables (-5<$\ln L_{X,0} > 5$, $0 < \beta < 5$, $-10 < \ln\sigma_{\rm int} < 1.5$) and linear step sizes (0.01 for $L_{X,0}$, and 0.05 for β and $\sigma_{\rm int}$). The results of the fit are shown in figure 2.1. The upper panel of this figure shows the best fit model for the CI values, which have higher luminosities, so the relation has higher normalization of $L_{X,0}^{\rm CI} \simeq 6.849^{+0.221}_{-0.214} \times 10^{44}$ erg s^{-1} compared to the CE normalization $L_{X,0}^{\rm CE} \simeq 3.713^{+0.085}_{-0.082} \times 10^{44}$ erg s^{-1}, but the slopes are similar for both ($\beta^{\rm CI} \simeq 2.793^{+0.095}_{-0.092}$ and $\beta^{\rm CE} \simeq 2.859^{+0.067}_{-0.065}$).

As expected from the separation between CCs and NCCs in the top half of figure 2.1 (and the lack thereof in the lower half), the scatter in the relation is reduced when using CE measurements, with $\sigma_{\rm int}^{\rm CI} \simeq 0.246^{+0.027}_{-0.023}$ and $\sigma_{\rm int}^{\rm CE} \simeq 0.093^{+0.013}_{-0.011}$. These $L_T - T$ results that agree with previous works (Pratt et al., 2009; Mittal et al., 2011; Maughan et al., 2012) reassures of the quality of the data in ACCEPT2.0.

---

[5] Central entropies were calculated by Rachel Frisbie (Frisbie, MSU dissertation, anticipated October 2020).

[6] Details of the fitting procedure for the $L_X - T$ relation are in chapter 3.

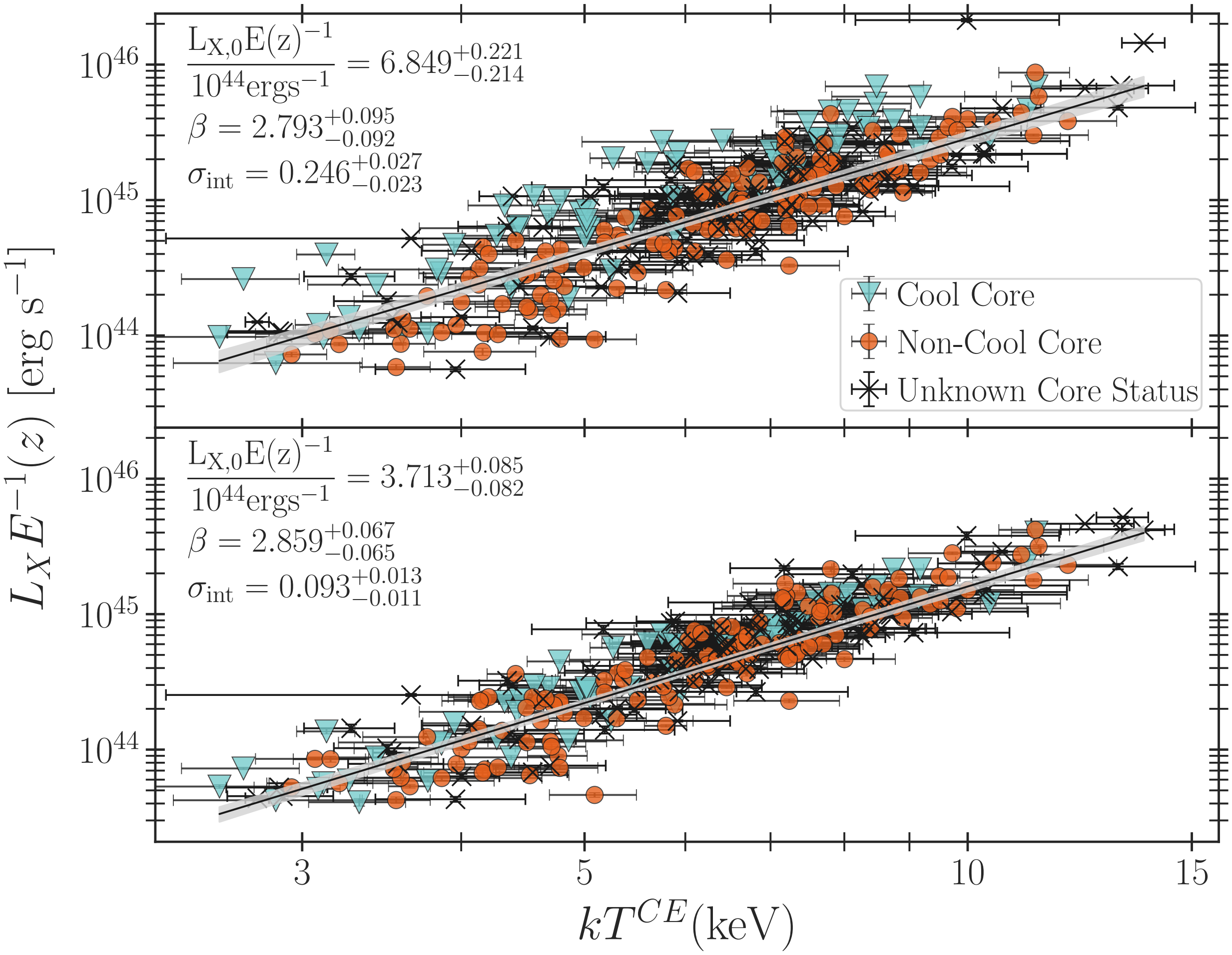

Figure 2.1 Best fit $L_X - T$ relation for 305 clusters with global CI ([0-1]R_{2500}) and CE [0.3-1]R_{2500} quantities. The upper panel shows the relation with luminosities measured in the CI aperture, and the lower panel shows the CE luminosities (both use CE temperatures.). The errors on the data points and best fit parameters are 1σ.

Table 2.3: Full list of 432 ACCEPT2.0 clusters presented in this thesis. This table includes the clusters that had their global temperatures and abundances refit.

2MASSi_J0913454+405628	0.442	457	6.416	0.590	0.406	0.092	4.631	0.189	6.963	0.284	1.152	
2MASX_J13312961+1107566	0.079	155	0.640	0.042	0.206	0.173	0.008	0.004	0.012	0.006	1.022	
2MFGC_06756	0.241	445	5.082	0.508	0.287	0.098	2.694	0.055	3.823	0.078	1.057	✓
3C_089	0.139	439	4.528	0.333	0.166	0.096	0.464	0.020	0.647	0.028	1.164	
400d_J0237-5224	0.136	355	3.171	0.430	0.385	0.201	0.303	0.048	0.403	0.065	1.319	
400d_J0245+0936	0.147	323	2.629	0.538	0.700	0.541	0.169	0.041	0.220	0.054	1.270	
400d_J0302-0423	0.350	410	4.755	0.748	0.617	0.241	3.657	0.341	5.080	0.473	1.096	
400d_J0318-0302	0.370	447	5.621	1.316	0.027	0.108	2.455	0.252	3.587	0.368	1.168	
400d_J0328-2140	0.590	404	6.033	0.995	0.262	0.168	3.038	0.308	4.494	0.456	1.137	
400d_J0405-4100	0.686	362	5.318	1.079	0.012	0.076	2.769	0.287	4.000	0.415	1.088	
400d_J0720+7108	0.231	320	2.801	0.309	0.408	0.161	0.245	0.029	0.325	0.038	1.181	
400d_J0838+1948	0.123	334	2.815	0.673	0.534	0.424	0.166	0.043	0.219	0.056	1.314	
400d_J0926+1242	0.489	405	5.471	1.018	0.239	0.209	1.533	0.140	2.217	0.202	1.067	
400d_J0956+4107	0.587	357	4.894	0.859	0.424	0.196	2.522	0.289	3.542	0.406	1.114	
400d_J1120+2326	0.562	355	4.457	0.577	0.279	0.159	2.181	0.169	3.024	0.234	1.152	
400d_J1202+5751	0.677	275	3.184	0.758	0.949	0.609	1.944	0.352	2.532	0.458	1.112	
400d_J1221+4918	0.700	428	7.160	1.083	0.299	0.138	4.586	0.318	7.143	0.495	1.080	
400d_J1312+3900	0.404	390	4.481	1.148	0.138	0.235	1.239	0.146	1.725	0.204	1.106	
400d_J1340+4017	0.171	244	1.583	0.167	0.360	0.155	0.074	0.015	0.101	0.021	1.021	
400d_J1354-0221	0.546	351	4.417	1.070	0.275	0.231	1.525	0.239	2.111	0.331	1.025	
400d_J1641+4001	0.464	346	3.941	0.826	0.423	0.285	1.098	0.149	1.488	0.203	1.103	
A1882a	0.141	385	3.317	0.158	0.302	0.080	0.316	0.017	0.424	0.022	1.129	✓
A98ss	0.129	331	2.639	0.402	0.465	0.272	0.209	0.028	0.277	0.037	1.163	
ABELL_0013	0.094	461	5.032	0.635	0.209	0.124	0.641	0.016	0.899	0.023	1.048	✓
ABELL_0068	0.255	618	9.717	1.436	0.662	0.210	5.993	0.281	10.429	0.489	1.270	
ABELL_0085	0.055	543	6.170	0.588	0.358	0.150	2.609	0.019	3.925	0.028	2.290	✓
ABELL_0098N	0.104	405	3.782	0.387	0.540	0.166	0.332	0.026	0.445	0.034	1.278	
ABELL_0119	0.044	541	5.916	0.591	0.290	0.131	1.115	0.013	1.628	0.019	3.338	✓
ABELL_0141	0.230	525	6.576	0.772	0.184	0.120	3.050	0.122	4.635	0.186	1.383	
ABELL_0160	0.045	275	1.807	0.375	0.094	0.069	0.084	0.006	0.117	0.009	2.120	✓
ABELL_0193	0.049	407	3.725	0.483	0.307	0.115	0.398	0.011	0.536	0.015	1.191	✓

ACCEPT2.0 Name	redshift	R_{2500}	kT	err_kT	Z	err_Z	L_X	err_L_X	L_X	err_L_X	χ^2/d.o.f	WTD
									[0.5-7 keV]			
		kpc	keV		$Z_\odot$		10^{44}erg s^{-1}		10^{44}erg s^{-1}			
ABELL_0209	0.206	607	8.547	0.665	0.250	0.082	6.310	0.161	10.466	0.266	1.313	
ABELL_0267	0.231	563	7.570	0.630	0.393	0.106	4.166	0.105	6.600	0.166	1.224	
ABELL_0368	0.220	497	6.080	0.768	0.305	0.138	3.443	0.181	5.101	0.268	1.276	
ABELL_0370	0.375	558	8.753	0.459	0.285	0.074	6.827	0.110	11.422	0.183	1.206	
ABELL_0376	0.048	468	4.174	0.670	0.346	0.208	0.515	0.011	0.713	0.016	1.875	✓
ABELL_0383	0.187	470	5.438	0.297	0.338	0.110	2.012	0.064	2.881	0.092	1.239	✓
ABELL_0399	0.072	574	6.857	0.581	0.243	0.136	2.554	0.021	3.926	0.032	3.135	✓
ABELL_0401	0.074	609	7.881	0.877	0.282	0.099	4.434	0.016	7.035	0.025	1.488	✓
ABELL_0402	0.322	552	8.228	1.236	0.045	0.085	4.452	0.190	7.293	0.311	1.175	
ABELL_0478	0.088	598	7.546	0.554	0.270	0.121	5.866	0.038	9.322	0.060	1.116	✓
ABELL_0514	0.071	402	3.959	0.534	0.257	0.035	0.317	0.014	0.430	0.018	1.588	✓
ABELL_0539	0.028	362	2.909	0.272	0.251	0.095	0.269	0.007	0.359	0.010	4.717	✓
ABELL_0545	0.154	582	7.372	0.311	0.124	0.052	3.448	0.047	5.431	0.073	1.265	
ABELL_0548A	0.040	371	3.221	0.352	0.335	0.188	0.261	0.012	0.348	0.016	1.560	✓
ABELL_0550	0.099	507	5.669	0.298	0.141	0.067	2.168	0.062	3.165	0.090	1.202	
ABELL_0562	0.110	353	2.946	0.451	0.237	0.083	0.392	0.019	0.526	0.025	1.122	✓
ABELL_0578	0.087	331	2.641	0.148	0.417	0.067	0.149	0.012	0.197	0.016	1.408	✓
ABELL_0586	0.171	516	6.241	0.395	0.374	0.075	3.337	0.093	4.977	0.139	1.157	
ABELL_0598	0.189	457	5.052	0.538	0.068	0.091	1.695	0.085	2.417	0.121	1.291	
ABELL_0611	0.288	571	7.993	0.430	0.408	0.118	4.697	0.124	7.783	0.205	1.017	✓
ABELL_0644	0.070	567	6.580	0.821	0.317	0.089	2.890	0.031	4.410	0.047	2.778	✓
ABELL_0665	0.182	614	8.136	0.857	0.260	0.075	4.817	0.059	7.910	0.096	1.314	✓
ABELL_0697	0.282	713	11.987	1.107	0.333	0.106	12.109	0.291	23.094	0.555	1.311	
ABELL_0773	0.217	581	7.630	0.833	0.272	0.081	5.866	0.132	9.528	0.214	1.237	✓
ABELL_0795	0.136	466	5.002	0.300	0.164	0.062	1.863	0.048	2.645	0.068	1.275	
ABELL_0853	0.166	430	4.441	0.481	0.236	0.129	0.861	0.054	1.194	0.075	1.146	
ABELL_0868	0.153	432	4.414	0.222	0.252	0.070	2.610	0.086	3.615	0.119	1.137	
ABELL_0907	0.153	504	5.772	0.537	0.335	0.142	2.833	0.056	4.152	0.083	1.381	✓
ABELL_0963	0.206	527	6.364	0.782	0.226	0.113	4.534	0.076	6.861	0.115	1.259	✓
ABELL_0970	0.059	454	4.504	0.402	0.276	0.014	0.817	0.027	1.134	0.038	1.387	✓
ABELL_0980	0.158	529	5.902	1.038	0.220	0.086	3.039	0.090	4.606	0.136	1.204	✓
ABELL_1033	0.126	501	5.886	0.583	0.266	0.038	1.475	0.025	2.143	0.037	1.207	✓

ACCEPT2.0 Name	redshift	R_{2500}	kT	err_kT	Z	err_Z	L_X	err_L_X	L_X	err_L_X	χ^2/d.o.f	WTD
									[0.5-7 keV]			
		kpc	keV		$Z_\odot$		10^{44}erg s^{-1}		10^{44}erg s^{-1}			
ABELL_1068	0.138	463	5.225	0.552	0.370	0.092	1.884	0.042	2.664	0.060	1.078	✓
ABELL_1142	0.035	311	2.147	0.169	0.145	0.051	0.032	0.002	0.044	0.003	1.246	
ABELL_1190	0.075	397	3.597	0.190	0.271	0.083	0.599	0.028	0.808	0.038	1.247	
ABELL_1201	0.169	492	5.309	0.543	0.359	0.060	2.527	0.054	3.681	0.079	1.254	✓
ABELL_1204	0.171	423	4.327	0.277	0.218	0.084	1.629	0.066	2.253	0.092	1.310	
ABELL_1285	0.106	496	5.361	0.617	0.314	0.026	2.267	0.042	3.281	0.060	1.219	✓
ABELL_1300	0.307	786	11.265	1.174	0.262	0.099	9.614	0.240	17.836	0.446	1.285	
ABELL_1413	0.143	578	7.350	0.558	0.231	0.089	4.175	0.044	6.581	0.070	1.459	✓
ABELL_1423	0.213	441	5.932	0.945	0.245	0.115	0.323	0.010	0.447	0.014	1.393	✓
ABELL_1446	0.103	390	3.606	0.513	0.332	0.163	0.707	0.019	0.950	0.025	1.123	✓
ABELL_1553	0.165	568	7.238	0.587	0.518	0.105	3.879	0.113	6.048	0.176	1.136	
ABELL_1569	0.073	315	2.223	0.326	0.239	0.089	0.261	0.020	0.348	0.027	1.575	✓
ABELL_1576	0.279	566	8.001	0.772	0.057	0.063	2.870	0.107	4.654	0.174	1.187	
ABELL_1644	0.047	481	4.858	0.506	0.344	0.141	0.818	0.007	1.171	0.009	3.047	✓
ABELL_1650	0.084	514	5.726	0.524	0.286	0.106	2.247	0.018	3.278	0.026	1.737	✓
ABELL_1664	0.128	468	4.732	0.484	0.239	0.047	1.930	0.041	2.747	0.059	1.178	✓
ABELL_1682	0.234	550	7.205	0.618	0.116	0.092	3.710	0.105	5.803	0.164	1.131	
ABELL_1689	0.183	676	10.000	0.874	0.279	0.110	8.559	0.103	15.062	0.181	1.410	✓
ABELL_1722	0.328	631	8.969	2.186	0.553	0.267	3.531	0.237	5.955	0.399	1.251	
ABELL_1736	0.046	387	3.070	0.313	0.322	0.158	0.638	0.013	0.854	0.017	3.124	✓
ABELL_1750C	0.068	450	3.861	0.768	0.263	0.095	0.445	0.017	0.617	0.024	1.310	✓
ABELL_1750N	0.084	397	3.586	0.230	0.165	0.070	0.458	0.022	0.621	0.029	1.350	
ABELL_1763	0.223	555	7.669	0.593	0.388	0.084	6.919	0.180	11.013	0.286	1.252	
ABELL_1775	0.072	408	3.760	0.413	0.503	0.110	0.923	0.011	1.238	0.015	1.616	✓
ABELL_1831	0.061	399	3.541	0.159	0.447	0.077	0.538	0.017	0.720	0.023	1.347	
ABELL_1835	0.253	646	9.175	1.354	0.348	0.157	12.004	0.170	21.457	0.303	1.213	✓
ABELL_1914	0.171	633	8.422	1.044	0.213	0.053	9.446	0.147	15.799	0.246	1.398	✓
ABELL_1930	0.131	440	4.366	0.629	0.587	0.028	0.951	0.038	1.311	0.053	1.235	✓
ABELL_1942_AND_CLUMP	0.224	465	5.305	0.486	0.373	0.031	1.401	0.046	2.016	0.066	1.219	✓
ABELL_1991	0.059	346	2.695	0.319	0.299	0.114	0.329	0.010	0.438	0.013	1.106	✓
ABELL_2009	0.153	543	6.695	0.309	0.443	0.071	3.537	0.097	5.386	0.148	1.392	✓
ABELL_2034	0.113	595	7.555	0.875	0.303	0.108	2.975	0.031	4.685	0.049	1.568	✓

ACCEPT2.0 Name	redshift	R_{2500}	kT	err_kT	Z	err_Z	L_X	err_L_X	L_X	err_L_X	χ^2/d.o.f	WTD
									[0.5-7 keV]			
		kpc	keV		$Z_\odot$		10^{44}erg s^{-1}		10^{44}erg s^{-1}			
ABELL_2061	0.078	457	4.310	0.527	0.278	0.118	1.171	0.022	1.631	0.031	1.083	✓
ABELL_2069	0.116	525	5.936	0.646	0.301	0.128	1.793	0.032	2.675	0.048	1.712	✓
ABELL_2104	0.153	565	7.200	1.018	0.245	0.153	3.731	0.049	5.815	0.077	1.354	✓
ABELL_2107	0.041	434	3.766	0.480	0.265	0.114	0.433	0.009	0.588	0.012	3.251	✓
ABELL_2111	0.229	567	7.700	0.575	0.186	0.085	3.754	0.081	5.996	0.129	1.146	
ABELL_2124	0.066	485	4.839	0.219	0.354	0.091	0.326	0.012	0.463	0.017	1.104	✓
ABELL_2125	0.246	343	3.158	0.206	0.197	0.089	0.632	0.031	0.850	0.042	1.133	
ABELL_2142	0.091	626	7.675	0.570	0.276	0.080	4.832	0.043	7.887	0.069	3.074	✓
ABELL_2147	0.035	449	4.275	0.343	0.321	0.101	0.537	0.007	0.737	0.010	4.436	✓
ABELL_2151	0.037	358	2.794	0.342	0.268	0.174	0.183	0.023	0.243	0.031	3.062	✓
ABELL_2163	0.203	795	13.183	1.347	0.240	0.045	20.636	0.140	42.292	0.288	1.603	✓
ABELL_2187	0.184	554	6.709	0.765	0.183	0.122	2.384	0.100	3.644	0.152	1.389	
ABELL_2204	0.152	654	8.269	1.172	0.319	0.143	6.250	0.044	10.792	0.077	1.623	✓
ABELL_2218	0.176	520	6.318	0.550	0.201	0.076	4.315	0.084	6.482	0.127	1.287	✓
ABELL_2219	0.226	699	11.017	0.888	0.280	0.093	14.778	0.091	27.420	0.169	1.223	✓
ABELL_2244	0.097	515	5.919	0.484	0.327	0.096	2.680	0.024	3.927	0.036	1.106	✓
ABELL_2249	0.082	486	5.153	0.342	0.168	0.086	1.267	0.035	1.811	0.051	1.204	
ABELL_2255	0.081	530	6.086	0.559	0.325	0.113	2.107	0.026	3.133	0.038	1.828	✓
ABELL_2256	0.058	586	6.782	0.465	0.381	0.135	3.438	0.033	5.363	0.052	1.886	✓
ABELL_2259	0.164	508	6.089	0.502	0.427	0.128	3.248	0.119	4.806	0.176	1.254	
ABELL_2261	0.224	593	7.714	1.178	0.349	0.077	7.182	0.156	11.669	0.253	1.276	✓
ABELL_2302	0.179	447	4.821	0.382	0.203	0.096	1.324	0.055	1.862	0.077	1.157	
ABELL_2319	0.056	670	8.664	1.413	0.319	0.131	5.846	0.046	10.028	0.078	3.532	✓
ABELL_2355	0.124	586	7.240	0.690	0.289	0.118	1.465	0.045	2.290	0.071	1.276	
ABELL_2384	0.094	516	5.246	0.839	0.390	0.162	1.119	0.018	1.628	0.026	2.330	✓
ABELL_2390	0.228	668	10.095	1.521	0.290	0.096	13.625	0.092	25.178	0.169	1.068	✓
ABELL_2409	0.148	510	5.955	0.382	0.462	0.093	4.281	0.134	6.289	0.197	1.292	
ABELL_2415	0.058	344	2.583	0.284	0.347	0.094	0.401	0.012	0.534	0.016	1.236	✓
ABELL_2426	0.098	522	5.825	0.389	0.251	0.100	1.671	0.053	2.451	0.077	1.305	
ABELL_2445	0.166	414	4.162	0.215	0.545	0.086	1.718	0.057	2.340	0.077	1.190	
ABELL_2457	0.059	414	3.595	0.099	0.326	0.059	0.550	0.015	0.744	0.021	1.352	✓
ABELL_2465	0.245	294	2.378	0.209	0.354	0.143	0.343	0.030	0.457	0.040	1.165	

ACCEPT2.0 Name	redshift	R_{2500}	kT	err_kT	Z	err_Z	L_X	err_L_X	L_X	err_L_X	χ^2/d.o.f	WTD
									[0.5-7 keV]			
		kpc	keV		$Z_\odot$		10^{44}erg s^{-1}		10^{44}erg s^{-1}			
ABELL_2485	0.247	511	6.250	0.714	0.231	0.129	2.703	0.119	4.043	0.178	1.247	
ABELL_2507	0.196	414	4.309	0.433	0.426	0.154	1.003	0.065	1.377	0.089	1.069	
ABELL_2537	0.295	506	6.629	0.625	0.224	0.038	4.650	0.104	7.083	0.158	1.157	✓
ABELL_2550	0.123	276	2.009	0.165	0.211	0.125	0.216	0.015	0.297	0.020	1.077	✓
ABELL_2556	0.087	413	3.756	0.398	0.356	0.086	0.814	0.018	1.105	0.024	1.157	✓
ABELL_2597	0.085	442	4.266	0.259	0.279	0.080	0.878	0.010	1.214	0.015	1.310	✓
ABELL_2626	0.055	382	3.263	0.379	0.378	0.131	0.443	0.012	0.593	0.016	1.119	✓
ABELL_2627	0.126	601	10.850	4.147	0.736	0.770	0.319	0.036	0.581	0.065	1.287	
ABELL_2631	0.273	580	8.024	0.961	0.169	0.100	7.191	0.246	11.658	0.398	1.254	
ABELL_2645	0.251	512	6.470	0.782	0.297	0.119	3.698	0.171	5.582	0.258	1.118	
ABELL_2657	0.040	403	3.567	0.307	0.302	0.165	0.583	0.016	0.785	0.021	3.162	✓
ABELL_2667	0.230	556	7.604	0.677	0.163	0.084	7.819	0.208	12.434	0.331	1.046	
ABELL_2670	0.076	435	4.001	0.706	0.310	0.114	0.743	0.021	1.019	0.028	2.206	✓
ABELL_2744	0.308	640	10.245	0.770	0.299	0.102	13.170	0.165	23.686	0.296	1.234	✓
ABELL_2813	0.292	559	7.950	0.739	0.287	0.086	7.287	0.223	11.762	0.361	1.303	
ABELL_3017	0.220	538	7.115	0.939	0.111	0.106	3.931	0.175	6.124	0.272	1.080	
ABELL_3088	0.253	576	7.316	0.762	0.236	0.099	5.317	0.193	8.344	0.302	1.279	
ABELL_3094	0.068	371	3.029	0.092	0.272	0.103	0.242	0.013	0.323	0.017	1.421	✓
ABELL_3126	0.086	476	4.994	0.309	0.470	0.083	1.212	0.037	1.707	0.052	1.203	
ABELL_3128	0.060	373	2.860	0.484	0.269	0.111	0.316	0.015	0.423	0.020	1.502	✓
ABELL_3158	0.060	480	5.435	0.313	0.387	0.082	2.057	0.018	2.899	0.026	2.722	✓
ABELL_3322	0.200	544	6.649	0.599	0.146	0.092	3.793	0.142	5.786	0.216	1.104	
ABELL_3343	0.191	513	6.429	0.528	0.269	0.099	3.027	0.089	4.563	0.135	1.175	
ABELL_3376	0.046	496	4.696	0.499	0.386	0.121	0.541	0.006	0.762	0.008	3.323	✓
ABELL_3378	0.141	453	4.780	0.273	0.360	0.088	3.198	0.099	4.474	0.139	1.160	
ABELL_3391	0.051	549	5.794	0.222	0.232	0.068	1.028	0.021	1.498	0.031	3.227	✓
ABELL_3399	0.203	542	6.759	0.453	0.276	0.084	3.297	0.073	5.045	0.111	1.084	
ABELL_3402	0.146	311	2.399	0.420	0.372	0.284	0.189	0.049	0.251	0.065	1.087	
ABELL_3404	0.167	640	7.851	0.642	0.049	0.062	6.357	0.151	10.236	0.244	1.148	
ABELL_3411	0.169	519	6.161	0.454	0.348	0.095	2.842	0.053	4.247	0.079	1.119	✓
ABELL_3444	0.253	552	7.915	0.451	0.338	0.060	7.473	0.123	12.037	0.197	0.974	
ABELL_3562	0.049	470	4.701	0.503	0.340	0.125	0.826	0.018	1.149	0.026	3.211	✓

ACCEPT2.0 Name	redshift	R_{2500}	kT	err_kT	Z	err_Z	L_X	err_L_X	L_X	err_L_X	χ^2/d.o.f	WTD
								[0.5-7 keV]				
		kpc	keV		$Z_\odot$		10^{44}erg s^{-1}		10^{44}erg s^{-1}			
ABELL_3653	0.109	450	4.781	0.341	0.345	0.071	0.524	0.015	0.733	0.021	1.222	
ABELL_3695	0.089	550	6.465	0.427	0.161	0.084	1.909	0.042	2.887	0.064	1.352	
ABELL_3739	0.165	516	6.084	0.527	0.413	0.111	2.874	0.120	4.251	0.177	1.096	
ABELL_3809	0.062	354	3.117	0.292	0.413	0.138	0.426	0.014	0.565	0.019	1.303	✓
ABELL_3827	0.098	585	7.338	0.789	0.339	0.144	3.243	0.032	5.080	0.050	1.302	✓
ABELL_3854	0.149	472	5.181	0.394	0.258	0.092	2.281	0.081	3.256	0.116	1.197	
ABELL_3880	0.058	356	2.897	0.277	0.305	0.143	0.341	0.018	0.453	0.023	2.280	✓
ABELL_3911	0.097	544	6.106	0.393	0.285	0.081	2.198	0.061	3.262	0.090	1.183	
ABELL_3921	0.093	522	5.766	0.762	0.360	0.085	1.981	0.037	2.916	0.054	1.879	✓
ABELL_4023	0.193	507	6.256	0.635	0.268	0.117	1.996	0.082	2.984	0.123	1.216	
ABELL_4038	0.028	369	2.878	0.263	0.286	0.118	0.394	0.007	0.525	0.009	3.540	✓
ABELL_S0295	0.300	529	7.072	0.896	0.257	0.059	9.202	0.310	14.464	0.487	1.200	✓
ABELL_S0463	0.039	353	2.503	0.532	0.214	0.139	0.094	0.004	0.125	0.005	2.257	✓
ABELL_S0520	0.295	573	8.269	0.732	0.140	0.076	6.561	0.201	10.757	0.330	1.167	
ABELL_S0579	0.152	449	4.789	0.352	0.213	0.092	1.508	0.056	2.119	0.078	1.146	
ABELL_S0592	0.222	598	8.581	0.651	0.312	0.080	7.970	0.188	13.233	0.313	1.363	
ABELL_S0780	0.236	551	7.021	0.628	0.310	0.122	5.352	0.074	8.395	0.117	1.065	✓
ABELL_S0821	0.237	511	6.386	0.506	0.302	0.072	5.443	0.174	8.184	0.261	1.108	
ABELL_S1063	0.347	663	11.302	0.722	0.359	0.070	22.560	0.412	41.905	0.765	1.219	
ABELL_S1101	0.058	345	2.698	0.286	0.199	0.089	0.541	0.010	0.726	0.013	2.076	✓
ABELL_S1150	0.261	453	5.221	1.320	0.230	0.291	0.851	0.103	1.217	0.148	1.079	
ACT-CL_J0346-5438	0.550	359	4.573	0.813	0.253	0.158	3.950	0.440	5.499	0.613	0.989	
ACT-CL_J0616-5227	0.710	441	0.360	0.200	7.150		6.591	0.809	10.537	1.293	1.043	
Abell_222	0.211	404	4.137	0.274	0.216	0.070	1.664	0.067	2.287	0.092	1.032	
Abell_223	0.207	473	5.470	0.500	0.247	0.100	1.370	0.062	1.981	0.089	1.152	
Abell_2276	0.141	338	2.831	0.277	0.202	0.104	0.501	0.046	0.672	0.061	1.249	
BLOX_J1023.6+0411.1	0.291	589	8.052	0.966	0.285	0.096	8.464	0.127	14.162	0.213	1.289	✓
Bullet_Cluster	0.296	708	12.364	1.145	0.208	0.066	24.166	0.131	46.462	0.252	1.326	✓
CGCG_514-050	0.017	241	1.231	0.043	0.225	0.029	0.003	0.000	0.005	0.000	1.337	
CIZA_J0107.7+5408	0.107	634	6.642	1.385	0.184	0.136	3.881	0.057	6.191	0.092	1.257	✓
CIZA_J0616.3-2156	0.171	557	7.236	0.511	0.313	0.086	2.994	0.067	4.678	0.105	1.178	
CIZA_J1804.4+1002	0.152	545	7.097	0.592	0.092	0.075	5.159	0.144	8.034	0.225	1.225	

ACCEPT2.0 Name	redshift	R_{2500}	kT	err_kT	Z	err_Z	L_X	err_L_X	L_X	err_L_X	χ^2/d.o.f	WTD
								[0.5-7 keV]				
		kpc	keV		$Z_\odot$		10^{44}erg s^{-1}		10^{44}erg s^{-1}			
CIZA_J1938.3+5409	0.260	539	7.202	0.728	0.356	0.091	8.739	0.350	13.629	0.546	1.124	
CIZA_J2242.8+5301	0.192	595	7.813	1.165	0.183	0.120	4.117	0.053	6.747	0.088	1.048	✓
CXOU_J052215-481816	0.296	458	5.616	1.217	0.319	0.274	1.036	0.106	1.504	0.154	1.249	
ClG_1137.5+6625	0.782	334	5.174	0.629	0.228	0.122	5.411	0.347	7.728	0.495	1.088	
ClG_2153.8+3746	0.292	608	8.940	1.321	0.240	0.103	11.047	0.148	19.077	0.256	1.148	✓
Cl_0016+16	0.541	557	9.727	0.745	0.198	0.063	16.147	0.355	28.163	0.619	0.964	
ESO3060170-A	0.036	352	2.569	0.426	0.304	0.175	0.180	0.007	0.238	0.010	2.696	✓
ESO_351-_G_021	0.057	228	1.297	0.092	0.269	0.103	0.027	0.004	0.037	0.006	1.169	✓
ESO_552-_G_020	0.031	316	2.455	0.267	0.536	0.173	0.074	0.004	0.099	0.006	4.796	✓
G113.82+44.35	0.226	495	6.017	0.680	0.004	0.053	2.620	0.128	3.891	0.189	1.037	
G139.59+24.18	0.270	539	7.189	0.635	0.378	0.086	7.876	0.283	12.273	0.440	1.169	
GALEX_J094712.4+762313	0.354	550	8.581	0.841	0.286	0.196	7.738	0.176	12.772	0.291	1.088	✓
GMBCG_J179.81192+49.79669	0.383	569	10.276	1.691	0.267	0.141	7.801	0.394	13.915	0.702	1.111	
GMBCG_J215.94948+24.07846	0.543	462	6.887	0.360	0.327	0.029	6.151	0.118	9.624	0.185	1.000	✓
HCG_037	0.022	203	0.963	0.238	0.205	0.174	0.003	0.004	0.004	0.006	1.120	
HCG_051	0.026	235	1.319	0.031	0.294	0.038	0.014	0.001	0.020	0.002	1.156	
HCG_097	0.022	197	0.812	0.035	0.135	0.030	0.007	0.001	0.012	0.002	1.166	
Hercules_A	0.155	419	3.653	1.309	0.181	0.097	1.836	0.034	2.531	0.047	1.224	✓
Hydra_A	0.055	431	3.951	0.219	0.289	0.046	1.145	0.005	1.566	0.006	1.219	✓
IC_1365	0.049	429	3.966	0.438	0.509	0.083	0.574	0.025	0.781	0.034	2.480	✓
III_Zw_054	0.029	335	2.255	0.217	0.196	0.110	0.169	0.007	0.229	0.009	3.292	✓
LCDCS_0829	0.451	718	13.426	2.267	0.213	0.073	20.538	0.248	41.656	0.503	1.160	✓
LCDCS_0954	0.670	213	2.017	0.679	0.295	0.377	1.323	0.599	1.794	0.812	0.932	
MACS0140.0-0555	0.454	476	7.139	0.822	0.256	0.103	7.056	0.392	10.985	0.610	1.149	
MACS_J0011.7-1523	0.378	451	5.892	0.399	0.271	0.066	6.014	0.194	8.839	0.285	1.132	
MACS_J0025.4-1222	0.584	470	7.817	0.597	0.256	0.060	8.852	0.347	14.205	0.557	1.134	
MACS_J0242.6-2132	0.314	459	5.751	0.774	0.151	0.115	4.837	0.298	7.085	0.436	1.156	
MACS_J0308.9+2645	0.324	603	9.656	1.047	0.159	0.085	10.682	0.298	18.580	0.518	1.285	
MACS_J0358.8-2955	0.425	548	8.747	0.487	0.143	0.052	12.749	0.337	21.346	0.564	1.130	
MACS_J0416.1-2403	0.420	550	0.210	0.080	8.690		9.072	0.326	15.127	0.544	1.130	
MACS_J0417.5-1154	0.440	624	10.945	0.936	0.211	0.093	21.550	0.366	40.079	0.680	1.108	✓
MACS_J0429.6-0253	0.399	491	7.000	0.900	0.302	0.132	5.376	0.254	8.315	0.393	1.159	

ACCEPT2.0 Name	redshift	R_{2500}	kT	err_kT	Z	err_Z	L_X	err_L_X	L_X	err_L_X	χ^2/d.o.f	WTD
									[0.5-7 keV]			
		kpc	keV		$Z_\odot$		10^{44}erg s^{-1}		10^{44}erg s^{-1}			
MACS_J0451.9+0006	0.430	443	5.844	0.829	0.411	0.206	5.882	0.364	8.608	0.533	1.101	
MACS_J0455.2+0657	0.425	478	6.845	0.998	0.571	0.226	6.452	0.414	9.878	0.634	1.135	
MACS_J0553.4-3342	0.407	649	10.463	0.680	0.192	0.055	13.416	0.212	24.118	0.382	1.119	
MACS_J0712.3+5931	0.328	409	4.676	0.539	0.289	0.126	2.554	0.218	3.563	0.304	1.176	
MACS_J0717+3745	0.546	647	12.868	1.576	0.181	0.048	25.993	0.368	51.818	0.734	1.136	✓
MACS_J0744.9+3927	0.698	442	7.805	0.634	0.179	0.067	13.375	0.576	21.465	0.924	1.114	
MACS_J0911.2+1746	0.505	460	6.808	0.894	0.133	0.102	5.371	0.324	8.253	0.497	1.124	
MACS_J0949.8+1708	0.383	576	10.311	1.712	0.184	0.151	9.104	0.381	16.267	0.681	1.258	
MACS_J1006.9+3200	0.359	638	6.890	1.667	0.045	0.114	4.249	0.342	6.562	0.528	1.209	
MACS_J1105.7-1014	0.466	589	9.115	2.406	0.383	0.258	7.646	0.598	12.986	1.015	1.249	
MACS_J1108.9+0906	0.449	472	6.863	0.744	0.193	0.106	5.708	0.269	8.786	0.414	1.128	
MACS_J1115.8+0129	0.352	589	9.180	0.730	0.189	0.068	8.020	0.227	13.674	0.388	1.253	
MACS_J1206.2-0847	0.440	606	11.369	1.423	0.225	0.109	16.980	0.490	31.633	0.913	1.235	
MACS_J1311.0-0311	0.494	428	6.031	0.482	0.228	0.071	4.349	0.189	6.435	0.280	1.128	
MACS_J1354.6+7715	0.397	467	6.384	0.815	0.314	0.119	4.673	0.251	7.024	0.378	1.103	
MACS_J1359.2-1929	0.447	456	6.565	1.197	0.103	0.124	2.590	0.194	3.938	0.296	1.198	
MACS_J1427.6-2521	0.318	410	4.689	0.340	0.443	0.114	2.061	0.095	2.865	0.132	1.186	
MACS_J1532.8+3021	0.345	522	7.129	0.720	0.239	0.065	6.570	0.112	10.388	0.177	1.141	✓
MACS_J1621.3+3810	0.465	482	7.226	0.580	0.199	0.066	4.964	0.186	7.763	0.291	1.167	
MACS_J1720.2+3536	0.391	530	7.870	0.653	0.367	0.080	6.766	0.206	10.872	0.331	1.279	
MACS_J1824.3+4309	0.487	476	7.102	2.235	0.060	0.211	1.922	0.182	2.995	0.283	1.099	
MACS_J1829.0+6913	0.203	402	4.057	0.305	0.335	0.109	0.843	0.044	1.151	0.060	1.234	
MACS_J1931.8-2635	0.352	540	7.793	0.786	0.374	0.147	8.805	0.104	14.152	0.168	1.326	✓
MACS_J2046.0-3430	0.423	428	5.606	0.447	0.212	0.086	4.194	0.216	6.100	0.314	1.136	
MACS_J2129-0741	0.589	479	8.117	0.943	0.454	0.126	12.133	0.669	19.708	1.086	1.130	
MACS_J2135-0102	0.325	557	8.365	1.066	0.580	0.154	4.768	0.219	7.826	0.360	1.246	
MACS_J2140.2-2339	0.313	468	5.638	0.740	0.306	0.144	3.985	0.110	5.860	0.162	1.070	✓
MACS_J2214-1359	0.483	530	8.833	0.989	0.194	0.093	10.888	0.419	18.292	0.705	1.120	
MACS_J2229.8-2756	0.324	464	5.882	0.562	0.397	0.108	4.070	0.190	5.967	0.279	1.233	
MACS_J2245.0+2637	0.304	499	6.710	0.933	0.330	0.146	4.480	0.241	6.835	0.368	1.224	
MCXC_J0027.8+2616	0.367	477	6.438	0.978	0.039	0.082	3.049	0.194	4.615	0.294	1.086	
MCXC_J0035.4-2015	0.364	509	7.187	0.645	0.338	0.090	10.772	0.355	16.792	0.554	1.146	

ACCEPT2.0 Name	redshift	R_{2500}	kT	err_kT	Z	err_Z	L_X	err_L_X	L_X	err_L_X	χ^2/d.o.f	WTD
									[0.5-7 keV]			
		kpc	keV		$Z_\odot$		10^{44}erg s^{-1}		10^{44}erg s^{-1}			
MCXC_J0142.0+2131	0.280	526	7.218	0.649	0.118	0.090	5.460	0.165	8.543	0.258	1.265	
MCXC_J0152.5-2853	0.341	457	5.815	0.584	0.058	0.081	4.091	0.126	6.018	0.186	1.125	
MCXC_J0220.9-3829	0.229	414	4.346	0.368	0.546	0.140	2.352	0.136	3.225	0.187	1.230	
MCXC_J0301.6+0155	0.170	432	4.450	0.333	0.233	0.090	1.687	0.079	2.341	0.110	1.190	
MCXC_J0303.7-7752	0.274	630	9.344	0.891	0.318	0.085	6.901	0.197	11.840	0.338	1.143	
MCXC_J0331.1-2100	0.188	495	5.859	0.528	0.204	0.092	2.604	0.104	3.827	0.153	1.380	
MCXC_J0340.8-4542	0.070	338	2.419	0.420	0.298	0.184	0.189	0.020	0.251	0.027	1.756	✓
MCXC_J0352.9+1941	0.109	364	3.085	0.533	0.263	0.124	1.013	0.041	1.362	0.055	1.111	✓
MCXC_J0425.8-0833	0.040	379	3.088	0.125	0.256	0.073	0.384	0.016	0.514	0.022	3.255	✓
MCXC_J0437.1+0043	0.285	518	6.101	0.632	0.265	0.041	4.937	0.134	7.580	0.205	1.251	✓
MCXC_J0439.0+0520	0.208	451	5.024	0.480	0.251	0.107	1.883	0.103	2.670	0.145	1.220	
MCXC_J0439.0+0715	0.230	513	6.528	0.534	0.293	0.083	5.310	0.166	8.038	0.252	1.160	
MCXC_J0443.1+0210	0.190	406	4.147	0.474	0.348	0.149	1.189	0.087	1.628	0.120	0.998	
MCXC_J0454.1-0300	0.550	576	10.644	0.768	0.206	0.082	15.974	0.296	28.925	0.536	1.309	
MCXC_J0510.7-0801	0.220	552	7.152	0.434	0.280	0.060	8.412	0.212	13.101	0.330	1.082	
MCXC_J0520.7-1328	0.340	515	7.335	0.692	0.345	0.111	5.821	0.181	9.131	0.284	1.265	
MCXC_J0528.2-2942	0.158	434	4.607	0.499	0.564	0.197	1.634	0.086	2.245	0.119	1.327	✓
MCXC_J0532.9-3701	0.275	594	8.644	0.843	0.136	0.080	6.799	0.197	11.333	0.329	1.134	
MCXC_J0547.0-3904	0.210	457	5.186	0.699	0.046	0.106	0.974	0.060	1.398	0.086	1.352	
MCXC_J0819.6+6336	0.119	384	3.498	0.321	0.170	0.088	0.758	0.044	1.025	0.060	1.238	
MCXC_J1000.5+4409	0.154	367	3.278	0.268	0.183	0.095	1.065	0.070	1.437	0.095	1.243	
MCXC_J1010.5-1239	0.301	494	6.484	0.395	0.222	0.062	4.060	0.084	6.139	0.127	1.108	
MCXC_J1022.0+3830	0.049	343	2.664	0.237	0.361	0.098	0.047	0.003	0.062	0.004	1.229	
MCXC_J1053.7+5452	0.070	281	2.029	0.371	0.164	0.075	0.196	0.021	0.276	0.029	1.103	✓
MCXC_J1130.0+3637	0.060	269	1.649	0.249	0.084	0.064	0.070	0.004	0.100	0.006	1.188	✓
MCXC_J1215.4-3900	0.119	494	5.505	0.361	0.429	0.110	1.605	0.038	2.315	0.055	1.167	
MCXC_J1234.2+0947	0.229	421	4.552	0.485	0.134	0.112	1.747	0.111	2.439	0.154	1.255	
MCXC_J1252.5-3116	0.053	352	2.869	0.165	0.515	0.102	0.229	0.013	0.301	0.017	1.344	
MCXC_J1514.9-1523	0.223	616	8.899	0.481	0.141	0.048	5.561	0.090	9.372	0.151	1.105	
MCXC_J1524.2-3154	0.103	444	4.426	0.719	0.362	0.129	1.365	0.019	1.900	0.026	1.326	✓
MCXC_J1558.3-1410	0.097	483	5.018	0.356	0.371	0.106	2.001	0.021	2.850	0.029	1.330	✓
MCXC_J1623.5+2634	0.426	449	6.365	0.908	0.201	0.124	3.854	0.228	5.798	0.342	1.005	

ACCEPT2.0 Name	redshift	R_{2500}	kT	err_kT	Z	err_Z	L_X	err_L_X	L_X	err_L_X	χ^2/d.o.f	WTD
									[0.5-7 keV]			
		kpc	keV		$Z_\odot$		10^{44}erg s^{-1}		10^{44}erg s^{-1}			
MCXC_J1731.6+2251	0.366	551	8.608	0.849	0.299	0.123	6.784	0.211	11.278	0.351	1.320	
MCXC_J1750.2+3504	0.171	442	4.639	0.356	0.126	0.083	1.689	0.078	2.364	0.109	1.187	
MCXC_J1852.1+5711	0.109	418	4.003	0.283	0.259	0.096	0.465	0.019	0.635	0.026	1.345	
MCXC_J1853.9+6822	0.093	423	4.129	0.221	0.190	0.074	1.031	0.025	1.419	0.034	1.199	
MCXC_J1947.3-7623	0.217	574	7.337	0.632	0.338	0.086	5.483	0.179	8.604	0.280	1.214	
MCXC_J1958.2-3011	0.117	399	3.283	0.982	0.182	0.452	0.088	0.012	0.119	0.016	1.212	
MCXC_J2003.5-2323	0.317	599	9.178	0.804	0.131	0.072	7.858	0.190	13.401	0.324	1.222	
MCXC_J2011.3-5725	0.279	363	3.629	0.373	0.231	0.110	2.134	0.151	2.886	0.205	1.156	
MCXC_J2014.8-2430	0.161	560	6.629	0.996	0.447	0.125	4.182	0.099	6.499	0.154	1.190	✓
MCXC_J2031.8-4037	0.342	494	6.735	0.918	0.128	0.117	7.965	0.430	12.201	0.659	1.116	
MCXC_J2049.9-3216	0.325	528	7.423	0.952	0.262	0.109	5.290	0.221	8.338	0.348	1.259	
MCXC_J2211.7-0349	0.270	655	9.815	1.315	0.221	0.121	6.301	0.219	11.029	0.383	1.394	
MCXC_J2218.6-3853	0.138	499	5.604	0.330	0.200	0.075	3.292	0.092	4.789	0.134	1.240	
MCXC_J2228.6+2036	0.412	550	8.249	0.824	0.352	0.116	10.081	0.348	16.485	0.569	1.176	
MCXC_J2311.5+0338	0.300	598	9.518	1.005	0.334	0.103	7.260	0.281	12.544	0.486	1.333	
MCXC_J2344.2-0422	0.079	450	4.501	0.143	0.406	0.261	1.473	0.038	2.031	0.052	1.422	✓
MKW_03s	0.045	394	3.434	0.404	0.261	0.113	0.650	0.006	0.875	0.008	2.072	✓
MZ_10451	0.061	179	0.733	0.041	0.158	0.167	0.010	0.002	0.016	0.004	1.073	
MaxBCG_J016.70077+01.05926	0.254	419	4.059	0.412	0.267	0.111	2.126	0.070	2.961	0.098	1.028	✓
NGC_1132	0.023	211	1.045	0.023	0.245	0.032	0.012	0.001	0.018	0.002	1.211	
NGC_3402_GROUP	0.015	179	0.833	0.052	0.387	0.085	0.006	0.001	0.008	0.001	1.052	✓
NGC_3551	0.032	271	1.623	0.062	0.320	0.051	0.023	0.002	0.032	0.002	1.229	
NGC_4104_GROUP	0.028	279	1.696	0.236	0.118	0.055	0.020	0.001	0.029	0.002	1.249	✓
NGC_4325_GROUP	0.025	202	1.019	0.015	0.311	0.092	0.018	0.001	0.027	0.002	1.141	✓
NGC_5044	0.009	187	1.320	0.026	0.404	0.049	0.001	0.000	0.001	0.000	0.996	
NGC_5098_GROUP	0.037	213	1.134	0.060	0.188	0.066	0.024	0.001	0.037	0.002	1.257	✓
NGC_6269	0.035	308	1.813	0.314	0.107	0.111	0.078	0.004	0.108	0.006	3.295	✓
NGC_6338	0.027	336	2.233	0.328	0.186	0.091	0.106	0.003	0.144	0.004	4.791	✓
NSCS_J000619+105206	0.167	466	5.184	0.399	0.350	0.092	1.850	0.072	2.636	0.102	1.073	
NSCS_J011502+002441	0.045	353	2.482	0.382	0.306	0.132	0.197	0.006	0.261	0.008	3.115	✓
NSCS_J121831+401236	0.320	475	6.090	0.651	0.210	0.116	4.257	0.182	6.320	0.271	1.216	
NSCS_J122648+215157	0.370	407	4.785	0.474	0.191	0.095	1.608	0.082	2.259	0.115	1.082	

ACCEPT2.0 Name	redshift	R_{2500}	kT	err_kT	Z	err_Z	L_X	err_L_X	L_X	err_L_X	χ^2/d.o.f	WTD
								[0.5-7 keV]				
		kpc	keV		$Z_\odot$		10^{44}erg s^{-1}		10^{44}erg s^{-1}			
NSCS_J145715+222009	0.258	452	5.120	0.434	0.296	0.101	3.947	0.081	5.650	0.115	1.135	✓
NSCS_J150117+422152	0.292	483	6.182	1.276	0.111	0.149	2.468	0.193	3.686	0.289	1.260	
NSC_J084254+292723	0.194	505	5.023	0.901	0.519	0.181	1.485	0.048	2.174	0.070	1.052	✓
NSC_J092017+303027	0.258	506	6.352	0.661	0.352	0.105	3.036	0.123	4.554	0.184	1.115	
NSC_J121733+033929	0.077	576	6.694	0.647	0.292	0.170	2.565	0.050	3.947	0.077	2.787	✓
NSC_J125947+312215	0.059	190	0.910	0.104	0.142	0.075	0.026	0.008	0.040	0.012	1.349	
NSC_J174715+451155	0.157	447	4.729	0.378	0.182	0.084	1.518	0.066	2.128	0.093	1.142	
OC02_J1701+6412	0.453	453	6.371	0.771	0.379	0.154	2.479	0.125	3.720	0.188	1.122	
PKS_0745-19	0.103	628	8.360	0.483	0.304	0.083	5.794	0.034	9.484	0.055	1.593	✓
PLCKESZ_G167.65+17.64	0.174	517	6.176	0.412	0.229	0.080	4.844	0.111	7.219	0.165	1.140	
PLCKESZ_G264.41+19.48	0.240	567	7.503	0.702	0.090	0.077	3.615	0.128	5.726	0.203	1.126	
PLCKESZ_G286.58-31.25	0.210	536	6.484	0.540	0.301	0.091	3.759	0.128	5.678	0.194	1.060	
PLCKESZ_G292.51+21.98	0.300	606	8.702	0.784	0.233	0.076	5.929	0.172	9.902	0.287	1.104	
PLCKESZ_G304.84-41.42	0.410	559	9.797	1.232	0.150	0.096	7.488	0.269	13.102	0.470	1.170	
PLCKESZ_G337.09-25.97	0.264	563	7.658	0.539	0.118	0.070	6.544	0.138	10.438	0.221	1.181	
RBS_0653	0.284	594	8.558	0.836	0.258	0.066	7.669	0.109	13.057	0.185	1.153	✓
RCS_J2318.5+0034	0.780	382	6.597	1.195	0.152	0.138	2.373	0.178	3.611	0.271	1.091	
RDCS_J0542-4100	0.640	410	6.455	0.885	0.108	0.125	3.762	0.216	5.691	0.327	1.168	
RX_J0848.8+4455	0.543	248	2.498	0.491	0.355	0.249	0.393	0.081	0.524	0.108	1.104	
SC_1329-313	0.048	406	3.182	0.222	0.184	0.092	0.269	0.014	0.362	0.019	2.819	✓
SDSS-C4-DR3_3018	0.051	341	2.516	0.440	0.328	0.144	0.089	0.005	0.119	0.007	1.265	✓
SDSS-C4-DR3_3144	0.081	269	1.806	0.280	0.251	0.117	0.077	0.005	0.106	0.007	1.001	✓
SDSS-C4_3072	0.164	560	7.066	0.427	0.413	0.059	4.348	0.075	6.753	0.116	1.371	✓
SDSSCGB_08842	0.426	323	3.294	1.238	0.233	0.284	0.317	0.082	0.427	0.110	1.109	
SDSS_+137.3+11.0+0.18	0.180	475	5.605	0.799	0.248	0.072	2.688	0.078	3.869	0.112	1.140	✓
SDSS_J015021.27-100530.5_GROUP	0.365	378	4.233	0.485	0.229	0.112	3.501	0.257	4.825	0.354	1.190	
SDSS_J1029+2623	0.584	397	5.809	0.958	0.074	0.099	3.401	0.230	5.000	0.338	1.136	
SDSS_J1115+5319_CLUSTER	0.466	604	10.328	1.639	0.141	0.157	8.139	0.364	14.554	0.651	1.084	
SPT-CLJ0014-4952	0.752	388	6.880	0.966	0.406	0.162	5.112	0.336	7.853	0.517	1.096	
SPT-CLJ0058-6145	0.830	322	4.416	1.052	0.341	0.229	3.844	0.629	5.312	0.869	1.053	
SPT-CLJ0106-5943	0.348	426	5.114	0.725	0.326	0.158	3.107	0.249	4.416	0.354	1.192	
SPT-CLJ0123-4821	0.620	340	4.551	0.743	0.464	0.195	2.711	0.300	3.751	0.415	1.070	

ACCEPT2.0 Name	redshift	R_{2500}	kT	err_kT	Z	err_Z	L_X	err_L_X	L_X	err_L_X	χ^2/d.o.f	WTD
									[0.5-7 keV]			
		kpc	keV		$Z_\odot$		10^{44}erg s^{-1}		10^{44}erg s^{-1}			
SPT-CLJ0151-5954	1.030	246	3.561	0.956	0.386	0.316	2.655	0.702	3.561	0.941	1.039	
SPT-CLJ0156-5541	1.220	266	5.334	1.101	0.017	0.081	8.173	1.394	11.753	2.004	1.075	
SPT-CLJ0243-5930	0.635	410	6.502	1.066	0.347	0.140	5.702	0.535	8.615	0.808	1.042	
SPT-CLJ0252-4824	0.421	453	6.352	1.450	0.313	0.191	2.527	0.249	3.793	0.373	1.072	
SPT-CLJ0256-5617	0.580	410	5.820	1.006	0.241	0.136	4.804	0.410	7.044	0.602	1.096	
SPT-CLJ0307-5042	0.550	400	5.538	0.936	0.173	0.127	4.468	0.408	6.486	0.592	1.100	
SPT-CLJ0307-6225	0.579	341	4.325	1.059	0.616	0.361	1.857	0.297	2.540	0.406	1.036	
SPT-CLJ0310-4647	0.709	360	5.370	0.927	0.206	0.189	3.699	0.296	5.329	0.427	1.154	
SPT-CLJ0324-6236	0.730	361	5.380	1.158	0.032	0.092	4.985	0.724	7.213	1.047	1.003	
SPT-CLJ0334-4659	0.485	427	5.822	1.133	0.182	0.147	3.884	0.379	5.702	0.556	1.145	
SPT-CLJ0352-5647	0.670	427	6.834	1.370	0.006	0.095	3.616	0.269	5.573	0.415	1.135	
SPT-CLJ0426-5455	0.630	358	5.347	1.715	0.066	0.141	2.940	0.473	4.245	0.683	1.051	
SPT-CLJ0456-5116	0.562	419	6.352	1.188	0.376	0.176	3.322	0.290	4.981	0.435	1.079	
SPT-CLJ2034-5936	0.920	298	4.721	0.886	0.298	0.170	6.077	0.871	8.490	1.216	1.101	
SPT-CLJ2043-5035	0.723	356	5.436	0.683	0.190	0.099	6.360	0.474	9.192	0.685	1.073	
SPT-CLJ2106-5844	1.132	329	7.158	0.782	0.193	0.096	22.470	1.818	34.961	2.829	1.044	
SPT-CLJ2135-5726	0.427	477	6.922	1.301	0.108	0.157	3.586	0.199	5.541	0.307	1.099	
SPT-CLJ2145-5644	0.480	462	6.866	1.278	0.006	0.078	4.965	0.361	7.663	0.557	1.053	
SPT-CLJ2146-4633	0.933	339	6.267	1.339	0.010	0.092	3.815	0.471	5.731	0.707	1.102	
SPT-CLJ2148-6116	0.571	436	6.735	1.175	0.272	0.195	3.484	0.229	5.327	0.351	1.039	
SPT-CLJ2218-4519	0.650	398	5.831	1.117	0.619	0.292	3.405	0.277	4.965	0.405	1.132	
SPT-CLJ2232-5959	0.594	394	4.530	1.074	0.330	0.218	4.175	0.545	5.792	0.756	1.104	
SPT-CLJ2233-5339	0.480	466	6.791	1.168	0.075	0.121	4.392	0.264	6.750	0.406	1.089	
SPT-CLJ2245-6206	0.580	416	6.221	1.324	0.077	0.121	4.606	0.550	6.897	0.823	1.051	
SPT-CLJ2259-6057	0.750	411	7.265	1.064	0.694	0.215	4.949	0.246	7.715	0.384	1.200	
SPT-CLJ2345-6405	0.940	379	7.900	1.510	0.072	0.128	5.516	0.406	8.901	0.656	1.095	
SPT-CL_J0232-4421	0.284	541	7.636	0.811	0.218	0.095	8.792	0.304	13.995	0.485	1.259	
SPT-CL_J0234-5831	0.415	556	10.958	3.630	0.244	0.314	4.706	0.410	8.628	0.752	1.120	
SPT-CL_J0417-4748	0.620	396	5.910	0.897	0.205	0.123	9.277	0.832	13.660	1.225	1.077	
SPT-CL_J0509-5342	0.463	565	9.069	1.716	0.145	0.164	4.295	0.208	7.291	0.353	1.176	
SPT-CL_J0551-5709	0.423	363	4.060	0.603	0.296	0.176	1.975	0.204	2.700	0.279	1.074	
SPT-CL_J0559-5249	0.611	357	4.818	0.622	0.170	0.095	3.915	0.379	5.512	0.534	1.073	

ACCEPT2.0 Name	redshift	R_{2500}	kT	err_kT	Z	err_Z	L_X	err_L_X	L_X	err_L_X	χ^2/d.o.f	WTD
									[0.5-7 keV]			
		kpc	keV		$Z_\odot$		10^{44}erg s^{-1}		10^{44}erg s^{-1}			
SPT-CL_J2023-5535	0.232	609	8.387	0.761	0.291	0.085	5.848	0.172	9.627	0.283	1.121	
SPT-CL_J2331-5051	0.571	419	6.486	1.747	0.096	0.143	3.893	0.380	5.899	0.575	1.078	
SPT-CL_J2337-5942	0.781	435	8.326	1.621	0.186	0.161	15.389	1.279	25.287	2.101	1.065	
SPT-CL_J2341-5119	0.998	384	8.270	1.573	0.336	0.195	7.073	0.735	11.579	1.203	1.085	
SPT-CL_J2344-4243	0.620	529	0.093	0.150	9.940		21.473	1.351	37.864	2.383	1.096	
SPT-CL_J2355-5056	0.350	395	4.536	0.913	0.273	0.202	2.270	0.258	3.154	0.358	1.119	
SPT-CL_J2359-5009	0.760	294	4.011	0.806	0.423	0.215	1.729	0.295	2.350	0.401	1.006	
SSGC_081	0.050	398	3.207	0.393	0.282	0.087	0.418	0.015	0.565	0.020	2.178	✓
SpARCS_J161314+564930	0.871	392	7.485	1.895	0.161	0.205	6.243	0.566	9.876	0.895	1.090	
UGC_00842	0.045	265	1.745	0.173	0.197	0.151	0.038	0.003	0.054	0.004	1.095	✓
WARP_J0030.5+2618	0.500	286	2.853	0.494	0.669	0.358	1.158	0.254	1.513	0.332	1.074	
WARP_J1113.0-2615	0.725	310	4.239	0.552	0.498	0.262	1.505	0.150	2.058	0.205	1.149	
WARP_J1120.1+4318	0.600	348	4.710	0.906	0.088	0.128	5.466	0.670	7.677	0.941	1.022	
WARP_J1226.9+3332	0.890	539	13.126	1.968	0.193	0.189	11.315	0.521	22.466	1.035	1.117	
WARP_J1524.6+0957	0.516	338	4.020	0.378	0.610	0.200	2.210	0.156	2.988	0.210	1.079	
WARP_J2302.8+0843	0.722	407	6.818	1.234	0.169	0.180	1.736	0.111	2.667	0.170	1.139	
WBL_154	0.022	179	1.199	0.178	0.150	0.116	0.024	0.001	0.035	0.001	1.485	✓
WBL_518	0.027	368	2.895	0.370	0.269	0.134	0.140	0.005	0.186	0.006	3.427	✓
WBL_671	0.051	208	1.004	0.119	0.111	0.061	0.012	0.004	0.019	0.006	1.187	
WHL_J022825.9+003202	0.414	373	2.425	1.333	0.018	0.373	0.286	0.174	0.394	0.239	1.006	
WHL_J091834.3+295318	0.289	235	1.703	0.589	0.639	1.389	0.424	0.349	0.558	0.460	0.906	
WHL_J092207.6+034558	0.280	596	8.434	3.353	0.165	0.354	1.787	0.209	2.951	0.345	1.204	
WHL_J093820.9+520243	0.360	477	6.417	0.504	0.165	0.073	5.414	0.181	8.169	0.274	1.081	
WHL_J102339.9+490838	0.144	533	6.513	0.589	0.156	0.083	3.321	0.111	5.034	0.168	1.099	
WHL_J114224.8+583205	0.311	609	8.855	0.679	0.127	0.073	7.812	0.182	13.142	0.306	1.166	
WHL_J125933.4+600409	0.330	501	6.894	0.515	0.112	0.068	3.904	0.145	6.024	0.223	1.062	
WHL_J130558.9+263048	0.305	537	7.269	0.948	0.151	0.097	4.356	0.192	6.829	0.300	1.082	
WHL_J131505.2+514902	0.291	583	8.765	0.771	0.025	0.048	6.692	0.136	11.224	0.229	1.149	
WHL_J134850.2+491801	0.162	421	4.274	0.675	0.163	0.170	0.451	0.034	0.624	0.048	1.392	
WHL_J135716.8+623249	0.563	382	5.225	1.059	0.127	0.155	2.449	0.255	3.513	0.366	1.052	
WHL_J141623.8+444528	0.386	345	3.649	0.283	0.750	0.269	1.653	0.149	2.195	0.197	1.100	
WHL_J142716.1+440730	0.498	601	10.403	1.424	0.236	0.142	6.679	0.271	11.975	0.486	1.328	

ACCEPT2.0 Name	redshift	R_{2500}	kT	err_kT	Z	err_Z	L_X	err_L_X	L_X	err_L_X	χ^2/d.o.f	WTD
								[0.5-7 keV]				
		kpc	keV		$Z_\odot$		10^{44}erg s^{-1}		10^{44}erg s^{-1}			
WHL_J150407.5-024816	0.215	620	8.482	0.751	0.238	0.070	9.519	0.130	16.069	0.219	1.463	✓
WHL_J224319.8-093530	0.432	488	7.179	0.672	0.267	0.085	14.006	0.520	21.842	0.811	1.214	
XMMU_J0954+1738	0.828	271	3.574	0.901	0.587	0.357	1.806	0.359	2.407	0.478	1.087	
XMMU_J1230.3+1339	0.975	325	6.000	1.033	0.244	0.154	4.400	0.455	6.500	0.671	1.126	
ZwCl_0008.8+5215	0.104	456	4.711	0.300	0.164	0.087	0.751	0.030	1.052	0.043	1.264	
ZwCl_0040.8+2404	0.083	437	3.826	0.623	0.291	0.102	0.823	0.028	1.129	0.038	1.280	✓
ZwCl_0735.7+7421	0.216	516	6.447	0.632	0.331	0.103	3.873	0.033	5.843	0.050	1.236	✓
ZwCl_0806.5+2822	0.300	552	6.806	1.897	0.071	0.210	1.869	0.191	2.874	0.293	1.211	
ZwCl_0823.2+0425	0.225	427	4.660	0.514	0.510	0.168	1.718	0.107	2.383	0.148	1.271	
ZwCl_0848.5+3341	0.371	504	7.258	1.760	0.380	0.288	2.719	0.210	4.250	0.328	1.054	
ZwCl_0857.9+2107	0.230	414	4.517	0.176	0.356	0.160	2.167	0.079	2.994	0.110	0.993	✓
ZwCl_0949.6+5207	0.214	479	5.346	0.581	0.291	0.096	2.228	0.048	3.243	0.069	1.088	✓
ZwCl_1006.1+1201	0.221	488	5.860	0.459	0.305	0.027	2.803	0.071	4.111	0.105	1.133	✓
ZwCl_1742.1+3306	0.076	437	4.076	0.352	0.374	0.179	1.099	0.017	1.507	0.024	1.653	✓
_EAD2007__188	0.072	351	2.840	0.221	0.275	0.095	0.269	0.020	0.359	0.027	1.157	
_SBV2004__RS_28	0.275	420	4.643	0.809	0.115	0.133	2.509	0.217	3.514	0.304	1.254	
a1750ss	0.091	330	2.405	0.202	0.238	0.096	0.138	0.016	0.185	0.021	1.175	

3 Luminosity-temperature relation of ACCEPT2.0 clusters

We characterize galaxy clusters through observations of the X-ray spectra of the intracluster medium (ICM). Observed correlations between X-ray observables like temperature T and luminosity L_X (Mitchell et al., 1976; Cavaliere et al., 1997; Pratt et al., 2009; Maughan et al., 2012; Migkas et al., 2020) make scaling relations for clusters of galaxies effective tools for understanding large scale structure and its evolution. Simple models of the ICM lead to predictions for how cluster mass M relates to T and L_X and therefore, how T and L_X should relate to each other. Observations connecting the cluster observable properties (such as L_X and T_X) to properties of clusters well-constrained by theory (such as cluster mass M) to allow us to constrain our cosmological models and improve our understanding of how overdensities in the early Universe have grown and evolved over time (full review by Voit (2005)).

We make predictions for cluster temperatures and luminosities by assuming the ICM is a self-gravitating sphere. The virial theorem states that the kinetic energy is related to gravitational potential energy by $KE = PE/2$. The virial radius R_v for a cluster at redshift z is the radius inside which the virial theorem for bound galaxies or particles is satisfied. In a simulation, the virial radius can be estimated based on this condition, because the simulator can know the exact positions and velocities of all the galaxies in their simulation. In the real Universe, the virial radius is based on calibration by simulations which indicate that the virial radius is the radius at which the average interior density is approximately 200 times the critical density at that redshift. Recall from from section 1.2.1 that the critical density $\rho_c(z)$ is the maximum average density and is defined as,

$$\rho_c(z) = E(z)^2 \rho_{c,0}, \tag{3.1}$$

where $\rho_{c,0} = \rho_c(z = 0) = 3H_0^2/8\pi G$ is the present day critical density, $H(z) = H_0 E(z)$, and $E(z) = \sqrt{\Omega_M(1+z)^3 + \Omega_\Lambda}$ where $\Omega_M = 0.3$ and Ω_Λ=0.7 account for the matter and dark energy content of the Universe. The virial radius r_v is large and outside of the typical X-ray telescope's instrumental field of view for most nearby systems, so we often characterize cluster properties for some radius r_Δ within which the density is Δ times the critical density $\rho_c(z)$. For a cluster with mass M_Δ at scaled radius r_Δ,

$$M_\Delta \propto E(z)^2 r_\Delta^3. \tag{3.2}$$

The virial theorem assumes that the ICM temperature is due to heating from the gas as it falls into the gravitational potential and leads to the expected relation,

$$T \propto [E(z) M_{\Delta}^{2/3}], \tag{3.3}$$

where T is the isothermal throughout the cluster.

The scaling of temperature and mass of a cluster through its luminosity is less straightforward, as it requires an assumption of the density structure and knowledge of radiative processes of the gas including bremsstrahlung (or free-free) emission, and collisionally-excited emission lines from iron K- and L- shell transitions, and transitions from other elements. At typical cluster temperatures, radiation of the gas is dominated by bremsstrahlung emission wherein electrons are deflected by the Coulomb field of an ion. We are able to express the radiation from all processes in terms of a cooling function $\Lambda(T, Z)$. The cooling function is integrated over all emission processes and then weighted by the energy of emitted photons (Peterson & Fabian, 2006). For bremsstrahlung emission, $\Lambda(T) \propto T^{1/2}$, which leads to the expected relation $L_X \propto T^2$. However, observations have shown steeper slopes and increased scatter among the lower temperature clusters and groups (Cavaliere et al., 1997; Arnaud & Evrard, 1999; Pratt et al., 2009; Maughan et al., 2012).

The existence of a reliable $L_X - T$ relation for clusters of galaxies could in principle allow for their use as standard candles, although they are not generally considered as such because the extended emission is by nature difficult to measure and their luminosities–particularly in the core–are affected by local astrophysics in addition to having large scatter in the $L_X - T$ relation. While clusters are not great standard candles in practice, large sample sizes might lead to interesting results. For example, we often approach cosmology under the generally accepted assumption of homogeneous isotropic expansion, but this assumption can be tested. This test was conducted recently by Migkas et al. (2020) (hereafter, M20), who used a sample of 313 clusters to investigate the $L_X - T$ relation towards different directions on the sky and found a significant difference in normalization factor when observing the $L_X - T$ relation from different regions of the sky. Specifically, they found that clusters within a 60° radius of galactic coordinates $(l, b) \sim (281^\circ, -16^\circ)$ are fainter than those towards $(l, b) \sim (34^\circ, +4^\circ)$ by up to 36%. They suggest that their results are due to inconsistencies in the Hubble constant H_0, and thus caused by anisotropic expansion. We performed a similar analysis for 308 clusters from the second catalog of the Archive of Chandra Cluster Entropy Profile Tables (Donahue, Baldi, et al, in prep, hereafter, ACCEPT2.0) and do not find the same difference in normalizations. We surmise that the discrepancies between ours and the results of M20 can be attributed to systematic differences in the data analysis procedure and systematics related to Galactic absorption, since the direction of the discrepancies are relatively close to the Galactic plane.

The outline of this chapter is as follows: Section 3.1 describes the cluster sample from ACCEPT2.0. Section 3.2 gives the $L_X - T$ model and fitting procedure, followed by the results in section 3.3. We compare our results to M20 in section 3.4 and discuss reasons for the discrepancy between results, and summarize our analysis in section 3.5. We assume a ΛCDM cosmology throughout the paper with H_0=70 km s^{-1}Mpc^{-1},Ω_m=0.3, and Ω_Λ=0.7.

3.1 The Sample

The $L_X - T$ relation becomes more scattered with decreasing temperature (or equivalently, mass) (Maughan et al., 2012). For a sample with selection based on luminosity, an $L_X - T$ relation with higher scatter will be more affected by luminosity selection bias than a sample with low scatter in $L_X - T$. We aim to limit the effects of this selection bias by restricting the luminosities to a range similar to M20. We selected a subsample of 308 clusters with global bolometric L>4×10^{43} erg s^{-1} (although, we used luminosities measured in the bandpass [0.5-8] keV. M20 used *ROSAT* luminosities in the energy range [0.1-2.5] keV).

Scatter in the relation also arises from the differences between cool core (CC) and non-cool core (NCC) clusters. CCs have profiles with steep drops in temperature towards the center, whereas NCCs have comparatively flat temperature profiles and a less centrally concentrated density structure. The CC clusters can be classified most straight forwardly by using the central entropy $K_0 = kTn^{-2/3}$ keV cm^2. Here, we follow the classification of Cavagnolo et al. (2009) and ACCEPT2.0[1], which defines $K_0 \simeq 30$ keV cm^2 as the threshold below which a cluster is considered a CC. There are 67 CCs (∼22%) and 135 (∼44%) NCCs in our sample, where the remaining 106 (∼34%) clusters are undetermined.

The difference in temperature and density profiles for CC and NCC clusters can increase the scatter in the $L_X - T$ relation, the angular resolution of *Chandra* allows us to obtain global temperature and luminosity estimates for a core-excised aperture of [0.3-1]r_{2500}. M20 however, used luminosities for the full aperture inside of r_{500}, because the angular resolution of *ROSAT* does not allow core-excised measurements.

There are 47 and 41 ACCEPT2.0 clusters in the 60° radius surrounding the regions $(l, b) \sim (281^\circ, -16^\circ)$ and $(l, b) \sim (34^\circ, +4^\circ)$, respectively. Migkas et al. (2020) found that clusters towards $(281^\circ, -16^\circ)$ were fainter, while those of the comparison region tended to be brighter. Therefore, these two regions will be designated as RF and RB, and clusters lying in neither sky region will be called NR. The full sample covers a redshift range of $z \sim [0.02 - 0.9]$. The RF clusters cover a redshift range of $z \sim [0.05 - 0.75]$, and RB clusters cover the range $z \sim [0.04 - 0.47]$. M20 uses a sample of local clusters with redshifts $z \lesssim 0.4$[2].

---

[1] K0's from ACCEPT2 (Frisbie, MSU dissertation, anticipated October 2020)

[2] We find no difference in our results when restricting our redshift range to the same $z \lesssim 0.4$, so for this work, we use an unrestricted redshift sample.

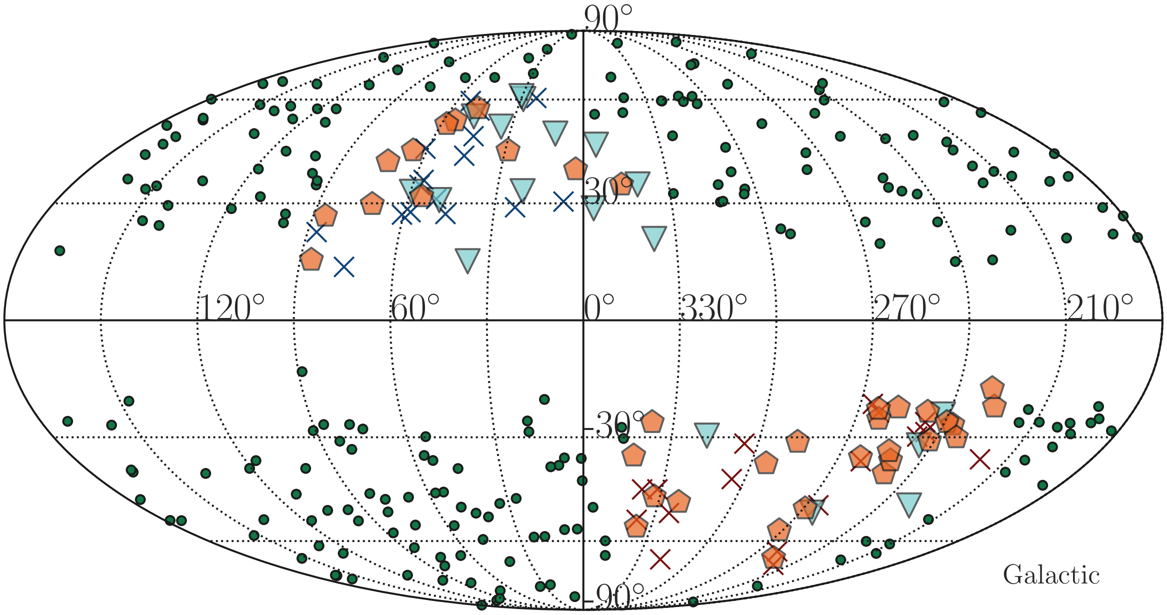

Figure 3.1 Distribution of ACCEPT2.0 clusters colored according to region or core status. Red pentagons are NCC clusters and blue triangles are CC clusters, while clusters with no core status are red or blue crosses. Clusters that do not belong to a region subset are plotted in green. Red crosses are part of the region centered on galactic coordinates $(l, b) \sim (281°, -16°)$ (RF), blue crosses are inside the region centered on $(l, b) \sim (34°, +4°)$(RB). Clusters within 10° of the galactic latitude $b = 0°$ were excluded from all subsamples.

3.2 Methods

We used the following linear model with intrinsic scatter as an estimate for the underlying $L_X - T$ relation,

$$l = \beta_0 + \beta_1 t + \ln\sigma_{\rm int}, \tag{3.4}$$

where $l \equiv \ln\frac{L_X E(z)^{-1}}{10^{44}{\rm ergs}^{-1}}, t \equiv \ln\frac{kT}{6{\rm keV}}$, and $E(z) = \sqrt{\Omega_m(1+z)^3 + \Omega_\Lambda}$ accounts for redshift evolution of the relation. We implemented an MCMC algorithm to obtain independent normalization, slope, and intrinsic scatter estimates for each sample using a likelihood function that assumes the data and errors are Gaussian.

$$\ln\mathscr{L} = -\frac{1}{2}\Sigma_i\left[\frac{(y_i - \bar{y})^2}{\sigma_{\rm int}^2 + \sigma_{y,i}^2} + \ln(2\pi(\sigma_{\rm int}^2 + \sigma_{y,i}^2))\right] \tag{3.5}$$

We used uniform priors on all parameters and linear steps and assumed the data follow a Gaussian distribution. M20 found that the normalization is the biggest contributor to the difference of the $L_X - T$ relation towards different regions of the sky. They used a model similar to equation 3.2 and fixed the slope to the value obtained from the full sample. We therefore performed a second fit of our data assuming that the slope (β_1) and intrinsic scatter ($\sigma_{\rm int}$) for all three samples are the same. However, instead of fixing these parameters in two of the analyses, we performed the regression over the three subsamples simultaneously and allowed only the normalization to vary between them. We chose a log-likelihood (equation 3.5) which tied the three subsamples because while M20 was able to show that fixing the slope did not significantly affect their results, this method does not take into account the uncertainty of the slope for the full sample.

We fit the five parameters, ${}^{\rm NR}\beta_0$, ${}^{\rm RB}\beta_0$, ${}^{\rm RF}\beta_0$, β_1, and $\sigma_{\rm int}$ using the following log-likelihood:

$$\begin{aligned}\ln\mathcal{L} = -\frac{1}{2}\Bigg[&\sum_i\left(\ln({}^{\rm NR}\sigma_i^2 + \sigma_{\rm int}^2) + \frac{({}^{\rm NR}l_i - ({}^{\rm NR}\beta_0 +{}^{\rm NR} t_i\beta_1))^2}{{}^{\rm NR}\sigma_i^2 + \sigma_{\rm int}^2}\right)\\ &+ \sum_i\left(\ln({}^{\rm RF}\sigma_i^2 + \sigma_{\rm int}^2) + \frac{({}^{\rm RF}t_i - ({}^{\rm RF}\beta_0 +{}^{\rm RB} t_i\beta_1))^2}{{}^{\rm RF}\sigma_i^2 + \sigma_{\rm int}^2}\right)\\ &+ \sum_i\left(\ln({}^{\rm RB}\sigma_i^2 + \sigma_{\rm int}^2) + \frac{({}^{\rm RB}t_i - ({}^{\rm RB}\beta_0 +{}^{\rm RB} t_i\beta_1))^2}{{}^{\rm RB}\sigma_i^2 + \sigma_{\rm int}^2}\right)\Bigg]\end{aligned} \tag{3.6}$$

3.3 Results

Results for the model parameters according to region are shown in table 3.1, with the errors reported as the 16th and 84th percentiles of the output parameter chain. The upper panel shows parameter output using tied log-likelihood (equation 3.6) for simultaneous fitting and the lower panel shows parameters for the separate fits (equation 3.5. The left panel of figure 3.3 contains the overplotted simultaneous fits, and the right panel shows the individual model fits, with the shaded regions representing the 1σ uncertainty for the model. The normalizations $L_{X,0}$ show no significant difference between using the tied or separate fitting models for any one subsample. While not significant, the simultaneous fit produced slightly larger values for slope ($\beta = 2.516^{+0.075}_{0.072}$) and intrinsic scatter ($\sigma_{\mathrm{int}} = 0.122^{+0.016}_{-0.012}$) than all of the individual fits, with the faint region RF showing the greatest difference with $\beta = 2.332^{+0.229}_{-0.221}$ and $\sigma_{\mathrm{int}} = 0.095^{0.044}_{-0.032}$. When fit individually, we find no statistical difference in β or σ_{int} between subsamples, which is consistent with Migkas et al. (2020).

There was no statistical difference in $L_{X,0}$ between RB and RF, with ${}^{RB}_{RF}\Delta L_{X,0}$ = -0.004± 0.212 for the tied model, and ${}^{RB}_{RF}\Delta L_{X,0} = -0.014 \pm 0.236$ for the separate model. For both the tied and separate fitting mechanisms, $\Delta L_{X,0}$ was smaller between RB and RF than between NR and either RB or RF. For the simultaneous fits, ${}^{NR}_{RB}\Delta L_{X,0} = 0.191 \pm 0.168$ and ${}^{NR}_{RF}\Delta L_{X,0} = 0.187 \pm 0.164$. For the individual fits, ${}^{NR}_{RB}\Delta L_{X,0} = 0.197 \pm 0.191$, and , ${}^{NR}_{RF}\Delta L_{X,0} = 0.183 \pm 0.175$.

3.4 Discussion

None of the differences in $L_{X,0}$ between for the different regions are statistically significant, which is contrary to the result of M20. In fact, ACCEPT2.0 clusters towards the extreme bright region RB described by M20 appear marginally *fainter* than those towards the extreme faint region RF. The low significance in $\Delta L_{X,0}$ across all three samples can be attributed to systematic differences in the data between *ROSAT* and *Chandra*. Possible reasons for the discrepancy between ours and M20's results are described below.

3.4.1 Core-excised vs. core included L_X

Both samples use core-excised temperatures from *Chandra*, but M20 uses luminosities from *ROSAT* because its large field of view allows for global parameters for apertures within R_{500}. Unfortunately, *ROSAT*'s low spatial resolution means their luminosity measurements are not core-excised. Core excision is important because cores of "cool-core" (CC) clusters have higher gas densities than the cores of non-cool core clusters (NCC), and therefore radiate more efficiently which results in higher SNR data. Unfortunately, this can

Table 3.1 Output parameters for the fit to equation 3.2. The upper half refers to parameters fit using the tied log-likelihood model 3.6. Parameters in the bottom half were computed for each subsample using separate log-likelihoods (3.5)

Model	Subsample	$L_{X,0}$	β	σ_{int}
Tied model	NR	$2.381^{+0.073}_{-0.068}$	$2.516^{+0.075}_{-0.072}$	$0.122^{+0.016}_{-0.012}$
	RB	$2.190^{+0.160}_{-0.145}$		
	RF	$2.194^{+0.150}_{-0.146}$		
Separate models	NR	$2.376^{+0.078}_{-0.073}$	$2.496^{+0.092}_{-0.090}$	$0.118^{+0.019}_{-0.016}$
	RB	$2.179^{+0.185}_{-0.167}$	$2.427^{+0.233}_{-0.225}$	$0.114^{+0.052}_{-0.037}$
	RF	$2.193^{+0.163}_{-0.154}$	$2.332^{+0.229}_{-0.221}$	$0.095^{+0.044}_{-0.032}$

Table 3.2 Differences in normalization $L_{X,0}$ between clusters towards different parts of the sky. Top half shows differences between normalization subsamples evaluated independently and the lower half shows the differences from the tied model with an extra column containing the results reported by Migkas et al. (2020) (M20) for comparison. M20 fit for each sample separately using the same fixed slope ($\beta = 2.102 \pm 0.064$) obtained from the full sample and allowing only the normalization to vary.

Model	Subsample	$\Delta L_{X,0}$ $[10^{44}\mathrm{ergs}^{-1}]$	Migkas et al. (2020)$\Delta L_{X,0}$ $[10^{44}\mathrm{ergs}^{-1}]$
Tied	(RB-RF)	0.004 ± 0.212	
	(NR-RB)	0.191 ± 0.168	
	(NR-RF)	0.187 ± 0.164	
Separate	(RB-RF)	0.014 ± 0.236	0.406±0.086
	(NR-RB)	0.197 ± 0.191	0.198±0.070
	(NR-RF)	0.183 ± 0.175	0.208±0.084

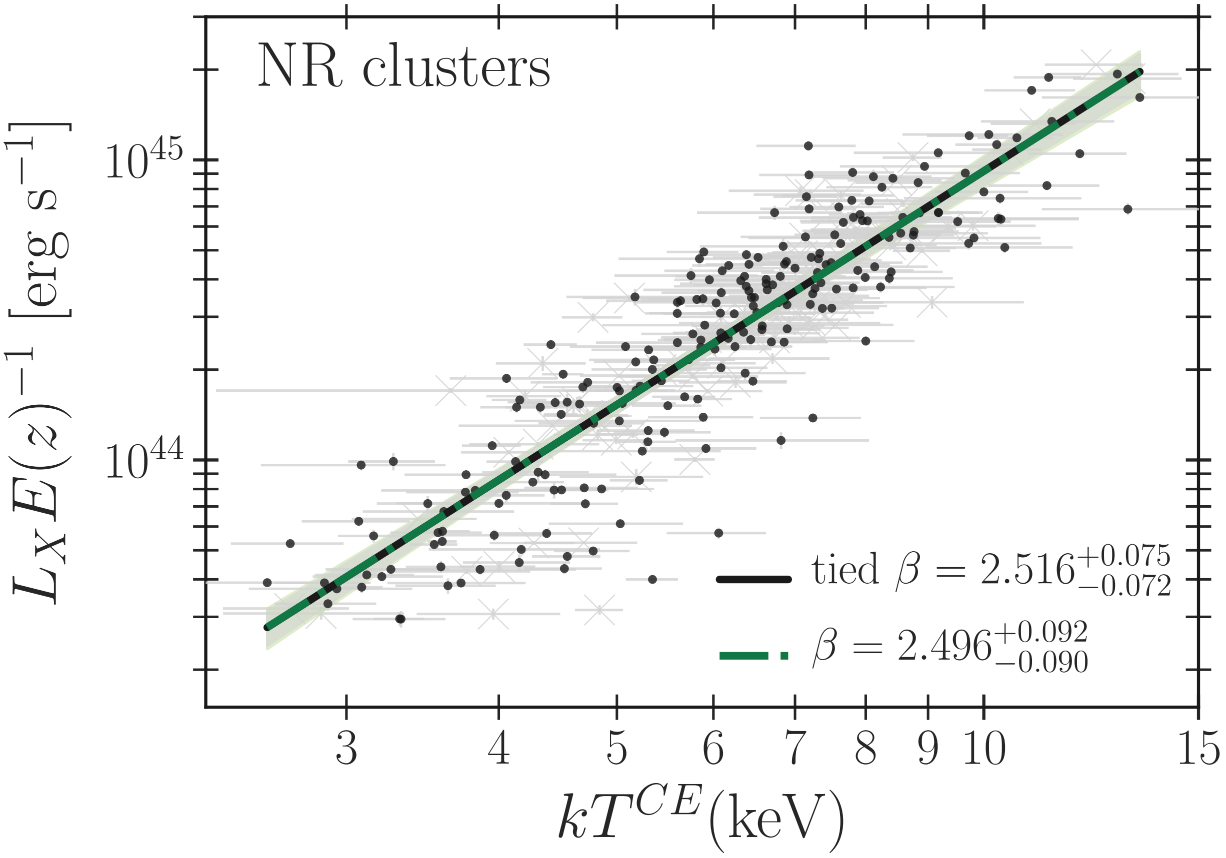

Figure 3.2 Best fit models for the luminosity-temperature for 221 NR clusters. Filled circles represent clusters used for the fit. Gray crosses are the clusters which were left out of the fit to NR because they belong to either RB or RF.

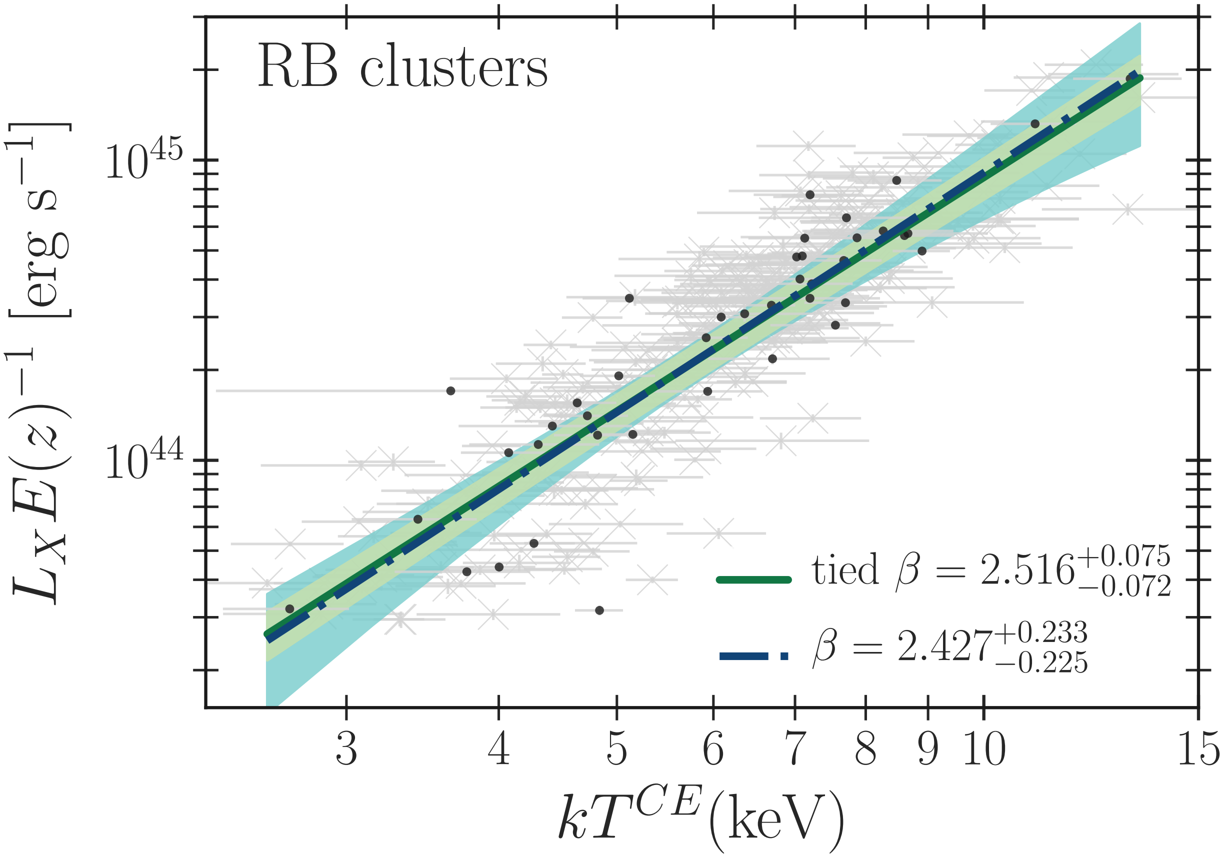

Figure 3.3 Same plot as 3.3 but for 41 RB clusters in the region surrounding RB = $(l, b) \sim (34°, +4°)$.

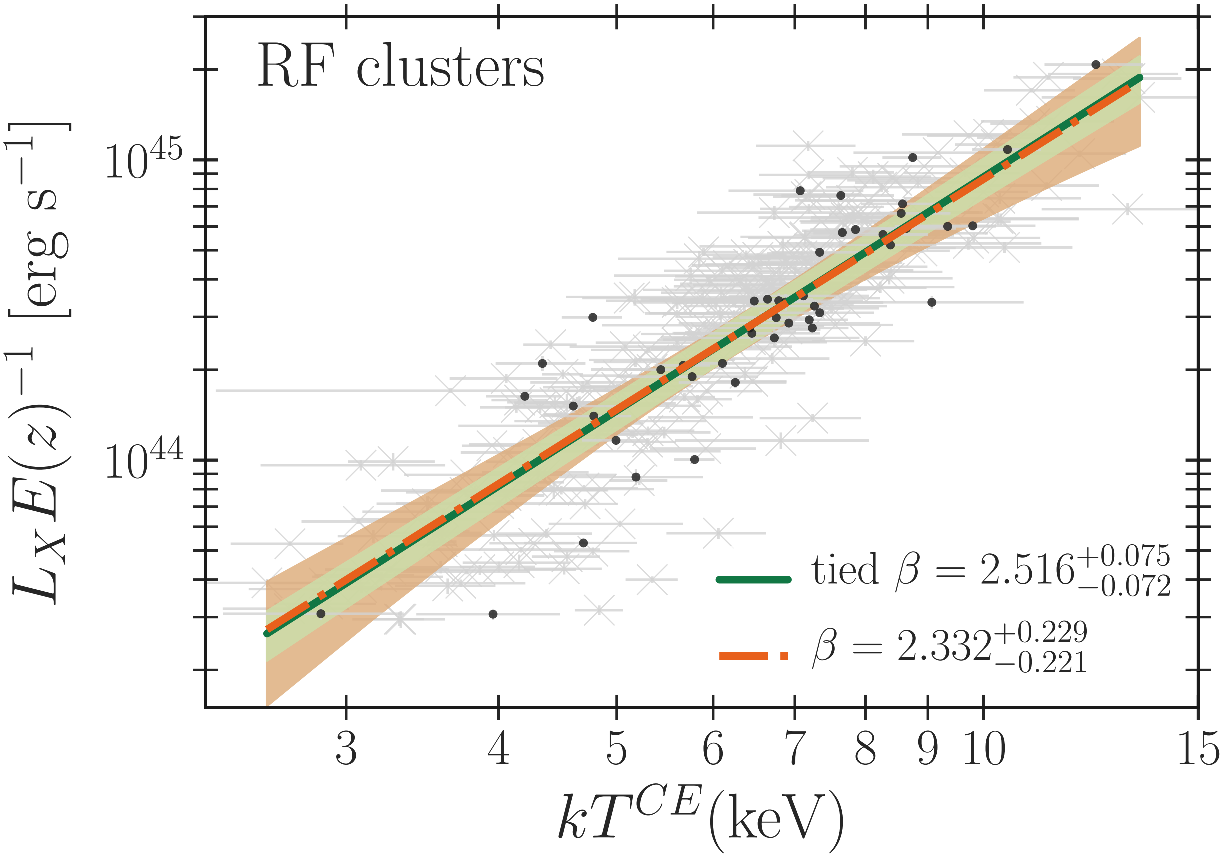

Figure 3.4 Same plot as 3.3 and 3.3 but for 46 RF clusters in the region surrounding RF = $(l, b) \sim (281°, -16°)$.

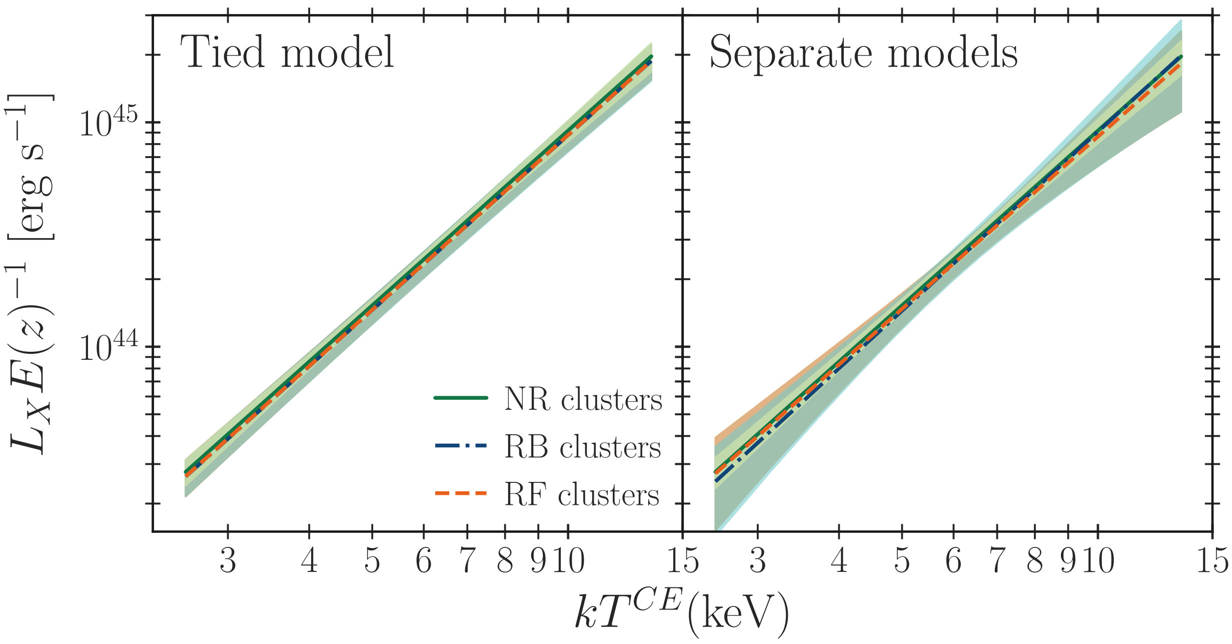

Figure 3.5 Best fit models for the luminosity-temperature for the tied parameter model (*left*) and independent models (*right*).

introduce a bias in the luminosity because of the brighter central regions of CCs compared to those of NCCs. Presumably, this excess luminosity in CCs would not affect the results as much if both regions had equal distributions of CC and NCC clusters. This perfect mixing of CCs and NCCs is not the case for our samples, which can be seen in figure 3.1. In RF, there are 29 out of 46 clusters have K_0 estimates, with 5 CCs and 24 NCCs. In RB, 25 out of 41 clusters with K_0 are about evenly split with 13 CCs and 12 NCCs. RF has a lower fraction of clusters with bright cores, which could bias the normalization of the $L_X - T$ relation low for that region. Because the luminosities used in M20 are for the full $r \lesssim r_{500}$ aperture, an excess or paucity of CCs in one region of the sky could affect $L_{X,0}$.

3.4.2 Different spectral energy bandpasses

Contributions from different radiation processes affect X-ray emissivity over different bandpasses. Therefore, the spectral energy range over which luminosity is measured can affect the observed $L_X - T$ relation. For instance, *ROSAT* is sensitive to soft X-rays in the bandpass [0.1-2.5] keV, which is where the cooling function is less sensitive to the exponential cutoff at $E \sim kT$, characteristic of radiation from thermal bremsstrahlung, and the soft X-ray luminosity is less dependent on temperature. The $L_X - T$ relation will therefore be shallower for a bandpass-limited L_X, particularly when confined to the lower energy range [0.1-2] keV. This effect can be seen in figure 3.4.2 which shows the best fit tied model for NR clusters

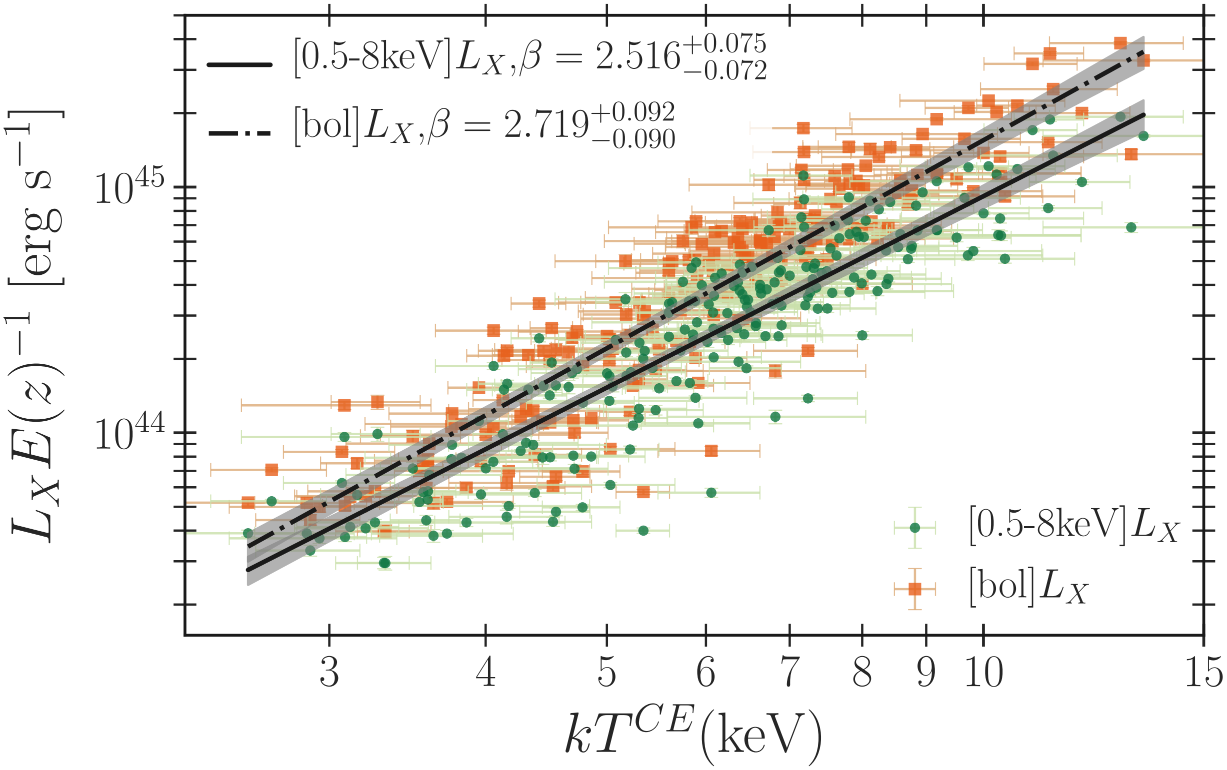

Figure 3.6 Best fit models for NR clusters using bolometric and bandpass luminosities. Luminosity is less dependent on temperature for low energy ranges, which results in a weaker relation when using [0.5-8] keV luminosities.

using bolometric versus bandpass limited luminosities. The slope of the $L_X - T$ relation using bandpass luminosities is $\beta = 2.516^{+0.075}_{-0.072}$ and $\beta = 2.719^{+0.092}_{-0.090}$ with bolometric luminosities. For comparison, the slope of the relation for the full sample in M20 is $\beta = 2.102 \pm 0.064$ using bandpass luminosities in the energy range [0.1-2.5] keV.

More importantly, below energies of kT ~2 keV, X-ray observables are more subject to systematics from Galactic absorption N_H. Each cluster in ACCEPT2.0 was assigned a single line-of-sight absorption value N_H given by Stark et al. (1992), whereas M20 combined column densities from both Stark et al. (1992) and Dickey & Lockman (1990). M20 accounted for differences between catalogs by assigning a correction factor for each cluster based on discrepancies between the treatments for Galactic absorption. That correction is not the likely source of the differences, but the correction for Galactic absorption is important for estimating intrinsic X-ray luminosity, and higher gas column densities require larger corrections. However, X-ray column densities arise from absorption along the line of sight of metals which are related to hydrogen, rather than the hydrogen itself. Therefore, the absorption correction based on neutral hydrogen column might not account for all the material along the line of sigh with a scaling between neutral and X-ray absorbing materials, especially for objects near the Galactic plane. If the difference reported by M20 is real, the result should not change with a different bandpass or N_H treatment.

The result in M20 was surprising because a statistical difference in the normalization of the $L_X - T$ relation would suggest that, when correcting for redshift, different regions of the sky are subject to different cosmologies. If clusters in RF are truly fainter, it would suggest that their redshift-corrected, or comoving distance D_C is larger towards that region, which would be a consequence of greater H_0. Luminosity L_X of an object with flux S_X at redshift z is,

$$L_X = S_X[(1+z)D_C]^2. \tag{3.7}$$

D_C is the comoving distance and relates to the Hubble constant H_0 via,

$$D_C = \frac{c}{H_0}\int \frac{dz}{E(z)}, \tag{3.8}$$

where $E(z) = \sqrt{(1+z)^3\Omega_M + \Omega_\Lambda}$. A true difference in luminosity would suggest that H_0 differs depending on where one looks on the sky and that the Universe is not expanding uniformly in all directions.

M20's conclusion is also surprising because the $L_X - T$ relation would be our only standard candle to show anisotropic expansion. For instance, distance estimates can be extrapolated from observations of objects with known absolute magnitude. For instance, if the value of H_0 were truly anisotropic, we would expect to see differences in type Ia supernovae (SNe Ia), which have well-defined peak magnitudes and predictable light curves (Colgate, 1979). At the highest redshifts, the Cosmic Microwave Background (CMB) should show large-scale temperature anisotropy that correlates with observed small fluctuations, but various tests have not yielded statistically significant results (Bennett et al., 2011). Instead, it is more likely that the result in M20 can be attributed to differences in systematics rather than differences in cosmology.

3.5 Conclusion

We used global core-excised temperatures and luminosities for 308 ACCEPT2.0 clusters to investigate differences in the $L_X - T$ relation towards different regions of the sky based on the results reported by M20. M20 found that clusters within a 60 degree cone towards galactic coordinates $(34°, +4°)$ (RB) were up to 36% brighter than those towards $(281°, -16°)$ (RF), where the difference is ${}^{\mathrm{RB}}_{\mathrm{RF}}\Delta L_0 = 0.406 \pm 0.086$. This is contrary to our differences of ${}^{RB}_{RF}\Delta L_{X,0} = -0.014 \pm 0.236$ and ${}^{RB}_{RF}\Delta L_{X,0} =$ -0.004± 0.212 for individual and simultaneous fitting models. The implication of an $L_X - T$ relation that changes depending on sky location is that expansion of the Universe is not the same in all directions, and it would require us to learn a new cosmological model and give different treatments of cluster samples depending on where they reside on the sky. We performed a similar analysis for 308 ACCEPT2.0 clusters divided into 46 clusters towards the RF direction, 41 towards the RB direction, and 221 remaining clusters covering the rest of the sky. We performed the fit for two different model assumptions: a separate model for which all the parameters are independent of sky location, and a tied model where each subset is fit simultaneously and only the normalizations are allowed to vary between the subsamples. We found no statistical difference in the $L_X - T$ relation in different directions on the sky for either model, suggesting that the more likely explanation for results found by M20 are due to systematic effects.

Table 3.3: Full list of 308 ACCEPT2.0 global core-excised X-ray properties and their region on the sky. RB refers to the region $(l, b) \sim (34°, +4°)$, RF refers to the region $(l, b) \sim (281°, -16°)$, and NR clusters belong to neither region.

Name	ID	z	L_X [0.5-8 keV] 10^{44} erg s^{-1}	eL_X [0.5-8 keV]	L_X [bol] 10^{44} erg s^{-1}	e_LX [bol]	kT keV	e_kT	$Z/Z_\odot$ $Z_\odot$	e_Z	χ^2_{red}
2MASSi_J0913454+405628	NR	0.4422	4.631	0.189	6.963	0.284	6.416	0.590	0.406	0.092	1.152
*2MFGC_06756	NR	0.2411	2.694	0.055	3.823	0.078	5.082	0.508	0.287	0.098	1.057
3C_089	NR	0.1386	0.464	0.020	0.647	0.028	4.528	0.333	0.166	0.096	1.164
*3C_444	NR	0.153	0.613	0.021	0.876	0.030	4.379	0.393	0.332	0.098	1.334
*A1882a	NR	0.1405	0.316	0.017	0.424	0.022	3.317	0.158	0.302	0.080	1.129
*ABELL_0013	NR	0.0943	0.641	0.016	0.899	0.023	5.032	0.635	0.209	0.124	1.048
ABELL_0068	NR	0.255	5.993	0.281	10.429	0.489	9.717	1.436	0.662	0.210	1.270
*ABELL_0085	NR	0.0551	2.609	0.019	3.925	0.028	6.170	0.588	0.358	0.150	2.290
*ABELL_0119	NR	0.0442	1.115	0.013	1.628	0.019	5.916	0.591	0.290	0.131	3.338
ABELL_0141	NR	0.23	3.050	0.122	4.635	0.186	6.576	0.772	0.184	0.120	1.383
*ABELL_0193	NR	0.0486	0.398	0.011	0.536	0.015	3.725	0.483	0.307	0.115	1.191
ABELL_0209	NR	0.206	6.310	0.161	10.466	0.266	8.547	0.665	0.250	0.082	1.313
ABELL_0267	NR	0.231	4.166	0.105	6.600	0.166	7.570	0.630	0.393	0.106	1.224
ABELL_0368	NR	0.22	3.443	0.181	5.101	0.268	6.080	0.768	0.305	0.138	1.276
ABELL_0370	NR	0.375	6.827	0.110	11.422	0.183	8.753	0.459	0.285	0.074	1.206
*ABELL_0376	NR	0.0484	0.515	0.011	0.713	0.016	4.174	0.670	0.346	0.208	1.875
*ABELL_0383	NR	0.1871	2.012	0.064	2.881	0.092	5.438	0.297	0.338	0.110	1.239
*ABELL_0399	NR	0.0718	2.554	0.021	3.926	0.032	6.857	0.581	0.243	0.136	3.135
*ABELL_0401	NR	0.0737	4.434	0.016	7.035	0.025	7.881	0.877	0.282	0.099	1.488
ABELL_0402	NR	0.3224	4.452	0.190	7.293	0.311	8.228	1.236	0.045	0.085	1.175
*ABELL_0478	NR	0.0881	5.866	0.038	9.322	0.060	7.546	0.554	0.270	0.121	1.116
*ABELL_0514	RF	0.0713	0.317	0.014	0.430	0.018	3.959	0.534	0.257	0.035	1.588

Name	ID	z	LX	e_LX	LX	e_LX	kT	e_kT	Z	e_Z	χ^2_{red}
			[0.5-8 keV]	[0.5-8 keV]	[bol]	[bol]					
			10^{44} erg s^{-1}		10^{44} erg s^{-1}		keV		$Z_{\odot}$		
ABELL_0545	NR	0.154	3.448	0.047	5.431	0.073	7.372	0.311	0.124	0.052	1.265
ABELL_0550	RF	0.099	2.168	0.062	3.165	0.090	5.669	0.298	0.141	0.067	1.202
*ABELL_0562	NR	0.11	0.392	0.019	0.526	0.025	2.946	0.451	0.237	0.083	1.122
ABELL_0586	NR	0.171	3.337	0.093	4.977	0.139	6.241	0.395	0.374	0.075	1.157
ABELL_0598	NR	0.1894	1.695	0.085	2.417	0.121	5.052	0.538	0.068	0.091	1.291
*ABELL_0611	NR	0.288	4.697	0.124	7.783	0.205	7.993	0.430	0.408	0.118	1.017
*ABELL_0644	NR	0.0704	2.890	0.031	4.410	0.047	6.580	0.821	0.317	0.089	2.778
*ABELL_0665	NR	0.1819	4.817	0.059	7.910	0.096	8.136	0.857	0.260	0.075	1.314
ABELL_0697	NR	0.282	12.109	0.291	23.094	0.555	11.987	1.107	0.333	0.106	1.311
*ABELL_0773	NR	0.217	5.866	0.132	9.528	0.214	7.630	0.833	0.272	0.081	1.237
ABELL_0795	NR	0.1359	1.863	0.048	2.645	0.068	5.002	0.300	0.164	0.062	1.275
ABELL_0853	NR	0.1664	0.861	0.054	1.194	0.075	4.441	0.481	0.236	0.129	1.146
ABELL_0868	NR	0.153	2.610	0.086	3.615	0.119	4.414	0.222	0.252	0.070	1.137
*ABELL_0907	NR	0.1527	2.833	0.056	4.152	0.083	5.772	0.537	0.335	0.142	1.381
*ABELL_0963	NR	0.206	4.534	0.076	6.861	0.115	6.364	0.782	0.226	0.113	1.259
*ABELL_0970	NR	0.0587	0.817	0.027	1.134	0.038	4.504	0.402	0.276	0.014	1.387
*ABELL_0980	NR	0.1582	3.039	0.090	4.606	0.136	5.902	1.038	0.220	0.086	1.204
*ABELL_1033	NR	0.1259	1.475	0.025	2.143	0.037	5.886	0.583	0.266	0.038	1.207
*ABELL_1068	NR	0.1375	1.884	0.042	2.664	0.060	5.225	0.552	0.370	0.092	1.078
ABELL_1190	NR	0.0751	0.599	0.028	0.808	0.038	3.597	0.190	0.271	0.083	1.247
*ABELL_1201	NR	0.1688	2.527	0.054	3.681	0.079	5.309	0.543	0.359	0.060	1.254
ABELL_1204	NR	0.1706	1.629	0.066	2.253	0.092	4.327	0.277	0.218	0.084	1.310
ABELL_1240	NR	0.159	0.492	0.032	0.675	0.044	4.158	0.420	0.279	0.137	1.411
*ABELL_1285	NR	0.1061	2.267	0.042	3.281	0.060	5.361	0.617	0.314	0.026	1.219
ABELL_1300	NR	0.3072	9.614	0.240	17.836	0.446	11.265	1.174	0.262	0.099	1.285
*ABELL_1413	NR	0.1427	4.175	0.044	6.581	0.070	7.350	0.558	0.231	0.089	1.459
*ABELL_1446	NR	0.1035	0.707	0.019	0.950	0.025	3.606	0.513	0.332	0.163	1.123
ABELL_1553	NR	0.1652	3.879	0.113	6.048	0.176	7.238	0.587	0.518	0.105	1.136
ABELL_1576	NR	0.279	2.870	0.107	4.654	0.174	8.001	0.772	0.057	0.063	1.187
*ABELL_1644	NR	0.0473	0.818	0.007	1.171	0.009	4.858	0.506	0.344	0.141	3.047
*ABELL_1650	NR	0.0838	2.247	0.018	3.278	0.026	5.726	0.524	0.286	0.106	1.737
ABELL_1651	NR	0.0849	2.848	0.058	4.381	0.089	6.897	0.336	0.348	0.081	2.492
*ABELL_1664	NR	0.1283	1.930	0.041	2.747	0.059	4.732	0.484	0.239	0.047	1.178
ABELL_1668	NR	0.0634	0.304	0.019	0.409	0.026	3.326	0.291	0.245	0.094	1.442
ABELL_1682	NR	0.2339	3.710	0.105	5.803	0.164	7.205	0.618	0.116	0.092	1.131
*ABELL_1689	NR	0.1832	8.559	0.103	15.062	0.181	10.000	0.874	0.279	0.110	1.410
*ABELL_1736	NR	0.0458	0.638	0.013	0.854	0.017	3.070	0.313	0.322	0.158	3.124
*ABELL_1750C	NR	0.0678	0.445	0.017	0.617	0.024	3.861	0.768	0.263	0.095	1.310

Name	ID	z	LX	e_LX	LX	e_LX	kT	e_kT	Z	e_Z	χ^2_{red}
			[0.5-8 keV]	[0.5-8 keV]	[bol]	[bol]					
			10^{44} erg s^{-1}		10^{44} erg s^{-1}		keV		$Z_\odot$		
ABELL_1750N	NR	0.0837	0.458	0.022	0.621	0.029	3.586	0.230	0.165	0.070	1.350
ABELL_1763	NR	0.223	6.919	0.180	11.013	0.286	7.669	0.593	0.388	0.084	1.252
ABELL_1767	NR	0.0703	1.188	0.037	1.703	0.053	5.301	0.290	0.293	0.081	1.412
*ABELL_1775	NR	0.0717	0.923	0.011	1.238	0.015	3.760	0.413	0.503	0.110	1.616
ABELL_1831	NR	0.0615	0.538	0.017	0.720	0.023	3.541	0.159	0.447	0.077	1.347
*ABELL_1835	NR	0.2532	12.004	0.170	21.457	0.303	9.175	1.354	0.348	0.157	1.213
*ABELL_1914	NR	0.1712	9.446	0.147	15.799	0.246	8.422	1.044	0.213	0.053	1.398
*ABELL_1930	NR	0.1313	0.951	0.038	1.311	0.053	4.366	0.629	0.587	0.028	1.235
*ABELL_1942_AND_CLUMP	NR	0.224	1.401	0.046	2.016	0.066	5.305	0.486	0.373	0.031	1.219
*ABELL_1991	RB	0.0587	0.329	0.010	0.438	0.013	2.695	0.319	0.299	0.114	1.106
*ABELL_2009	RB	0.1532	3.537	0.097	5.386	0.148	6.695	0.309	0.443	0.071	1.392
*ABELL_2034	RB	0.113	2.975	0.031	4.685	0.049	7.555	0.875	0.303	0.108	1.568
*ABELL_2061	RB	0.0784	1.171	0.022	1.631	0.031	4.310	0.527	0.278	0.118	1.083
*ABELL_2069	RB	0.116	1.793	0.032	2.675	0.048	5.936	0.646	0.301	0.128	1.712
*ABELL_2104	RB	0.1533	3.731	0.049	5.815	0.077	7.200	1.018	0.245	0.153	1.354
*ABELL_2107	RB	0.0411	0.433	0.009	0.588	0.012	3.766	0.480	0.265	0.114	3.251
ABELL_2111	RB	0.229	3.754	0.081	5.996	0.129	7.700	0.575	0.186	0.085	1.146
*ABELL_2124	RB	0.0656	0.326	0.012	0.463	0.017	4.839	0.219	0.354	0.091	1.104
ABELL_2125	NR	0.2465	0.632	0.031	0.850	0.042	3.158	0.206	0.197	0.089	1.133
*ABELL_2142	RB	0.0909	4.832	0.043	7.887	0.069	7.675	0.570	0.276	0.080	3.074
*ABELL_2147	RB	0.035	0.537	0.007	0.737	0.010	4.275	0.343	0.321	0.101	4.436
*ABELL_2163	RB	0.203	20.636	0.140	42.292	0.288	13.183	1.347	0.240	0.045	1.603
ABELL_2187	RB	0.1836	2.384	0.100	3.644	0.152	6.709	0.765	0.183	0.122	1.389
*ABELL_2204	RB	0.1522	6.250	0.044	10.792	0.077	8.269	1.172	0.319	0.143	1.623
*ABELL_2218	NR	0.1756	4.315	0.084	6.482	0.127	6.318	0.550	0.201	0.076	1.287
*ABELL_2219	RB	0.2256	14.778	0.091	27.420	0.169	11.017	0.888	0.280	0.093	1.223
*ABELL_2244	RB	0.0968	2.680	0.024	3.927	0.036	5.919	0.484	0.327	0.096	1.106
ABELL_2249	RB	0.0816	1.267	0.035	1.811	0.051	5.153	0.342	0.168	0.086	1.204
*ABELL_2255	NR	0.0806	2.107	0.026	3.133	0.038	6.086	0.559	0.325	0.113	1.828
*ABELL_2256	NR	0.0581	3.438	0.033	5.363	0.052	6.782	0.465	0.381	0.135	1.886
ABELL_2259	RB	0.164	3.248	0.119	4.806	0.176	6.089	0.502	0.427	0.128	1.254
*ABELL_2261	RB	0.224	7.182	0.156	11.669	0.253	7.714	1.178	0.349	0.077	1.276
ABELL_2294	NR	0.1694	4.578	0.170	7.178	0.266	7.303	0.736	0.260	0.106	1.415
ABELL_2302	RB	0.179	1.324	0.055	1.862	0.077	4.821	0.382	0.203	0.096	1.157
*ABELL_2319	RB	0.0557	5.846	0.046	10.028	0.078	8.664	1.413	0.319	0.131	3.532
ABELL_2355	NR	0.1244	1.465	0.045	2.290	0.071	7.240	0.690	0.289	0.118	1.276
*ABELL_2384	NR	0.0943	1.119	0.018	1.628	0.026	5.246	0.839	0.390	0.162	2.330
*ABELL_2390	NR	0.228	13.625	0.092	25.178	0.169	10.095	1.521	0.290	0.096	1.068

Name	ID	z	LX	e_LX	LX	e_LX	kT	e_kT	Z	e_Z	χ^2_{red}
			[0.5-8 keV]	[0.5-8 keV]	[bol]	[bol]					
			10^{44} erg s^{-1}		10^{44} erg s^{-1}		keV		$Z_\odot$		
ABELL_2409	NR	0.1479	4.281	0.134	6.289	0.197	5.955	0.382	0.462	0.093	1.292
*ABELL_2415	NR	0.0581	0.401	0.012	0.534	0.016	2.583	0.284	0.347	0.094	1.236
ABELL_2426	NR	0.0978	1.671	0.053	2.451	0.077	5.825	0.389	0.251	0.100	1.305
ABELL_2443	NR	0.108	1.709	0.050	2.495	0.072	5.683	0.338	0.170	0.082	1.574
ABELL_2445	NR	0.166	1.718	0.057	2.340	0.077	4.162	0.215	0.545	0.086	1.190
*ABELL_2457	NR	0.0594	0.550	0.015	0.744	0.021	3.595	0.099	0.326	0.059	1.352
ABELL_2485	NR	0.2472	2.703	0.119	4.043	0.178	6.250	0.714	0.231	0.129	1.247
ABELL_2507	NR	0.196	1.003	0.065	1.377	0.089	4.309	0.433	0.426	0.154	1.069
*ABELL_2537	NR	0.295	4.650	0.104	7.083	0.158	6.629	0.625	0.224	0.038	1.157
*ABELL_2556	NR	0.0871	0.814	0.018	1.105	0.024	3.756	0.398	0.356	0.086	1.157
*ABELL_2597	NR	0.0852	0.878	0.010	1.214	0.015	4.266	0.259	0.279	0.080	1.310
*ABELL_2626	NR	0.0553	0.443	0.012	0.593	0.016	3.263	0.379	0.378	0.131	1.119
ABELL_2631	NR	0.273	7.191	0.246	11.658	0.398	8.024	0.961	0.169	0.100	1.254
ABELL_2645	NR	0.251	3.698	0.171	5.582	0.258	6.470	0.782	0.297	0.119	1.118
*ABELL_2657	NR	0.0402	0.583	0.016	0.785	0.021	3.567	0.307	0.302	0.165	3.162
ABELL_2665	NR	0.0556	0.489	0.018	0.680	0.025	4.553	0.294	0.310	0.095	1.412
ABELL_2667	NR	0.23	7.819	0.208	12.434	0.331	7.604	0.677	0.163	0.084	1.046
*ABELL_2670	NR	0.0762	0.743	0.021	1.019	0.028	4.001	0.706	0.310	0.114	2.206
*ABELL_2744	NR	0.308	13.170	0.165	23.686	0.296	10.245	0.770	0.299	0.102	1.234
ABELL_2813	NR	0.2924	7.287	0.223	11.762	0.361	7.950	0.739	0.287	0.086	1.303
ABELL_2895	NR	0.227	4.742	0.143	7.809	0.236	8.394	0.858	0.301	0.107	1.471
ABELL_3017	RF	0.2195	3.931	0.175	6.124	0.272	7.115	0.939	0.111	0.106	1.080
ABELL_3088	NR	0.2534	5.317	0.193	8.344	0.302	7.316	0.762	0.236	0.099	1.279
ABELL_3126	RF	0.0856	1.212	0.037	1.707	0.052	4.994	0.309	0.470	0.083	1.203
*ABELL_3128	RF	0.0599	0.316	0.015	0.423	0.020	2.860	0.484	0.269	0.111	1.502
*ABELL_3158	RF	0.0597	2.057	0.018	2.899	0.026	5.435	0.313	0.387	0.082	2.722
ABELL_3292	RF	0.1723	1.775	0.082	2.441	0.112	4.204	0.297	0.271	0.098	1.410
ABELL_3322	RF	0.2	3.793	0.142	5.786	0.216	6.649	0.599	0.146	0.092	1.104
ABELL_3343	RF	0.1913	3.027	0.089	4.563	0.135	6.429	0.528	0.269	0.099	1.175
ABELL_3364	RF	0.1483	3.151	0.079	4.925	0.124	7.194	0.546	0.126	0.081	1.411
*ABELL_3376	RF	0.0456	0.541	0.006	0.762	0.008	4.696	0.499	0.386	0.121	3.323
ABELL_3378	RF	0.141	3.198	0.099	4.474	0.139	4.780	0.273	0.360	0.088	1.160
*ABELL_3391	RF	0.0514	1.028	0.021	1.498	0.031	5.794	0.222	0.232	0.068	3.227
ABELL_3399	RF	0.2026	3.297	0.073	5.045	0.111	6.759	0.453	0.276	0.084	1.084
ABELL_3404	RF	0.167	6.357	0.151	10.236	0.244	7.851	0.642	0.049	0.062	1.148
*ABELL_3411	NR	0.1687	2.842	0.053	4.247	0.079	6.161	0.454	0.348	0.095	1.119
ABELL_3444	NR	0.2533	7.473	0.123	12.037	0.197	7.915	0.451	0.338	0.060	0.974
ABELL_3528B	NR	0.053	0.585	0.025	0.865	0.037	6.060	0.567	0.375	0.145	2.930

Name	ID	z	LX	e_LX	LX	e_LX	kT	e_kT	Z	e_Z	χ^2_{red}
			[0.5-8 keV]	[0.5-8 keV]	[bol]	[bol]					
			10^{44} erg s^{-1}		10^{44} erg s^{-1}		keV		$Z_\odot$		
ABELL_3532	NR	0.0554	0.878	0.028	1.249	0.040	5.218	0.285	0.493	0.094	4.296
*ABELL_3562	NR	0.049	0.826	0.018	1.149	0.026	4.701	0.503	0.340	0.125	3.211
ABELL_3653	NR	0.1089	0.524	0.015	0.733	0.021	4.781	0.341	0.345	0.071	1.222
ABELL_3695	NR	0.0894	1.909	0.042	2.887	0.064	6.465	0.427	0.161	0.084	1.352
ABELL_3739	NR	0.1651	2.874	0.120	4.251	0.177	6.084	0.527	0.413	0.111	1.096
*ABELL_3809	NR	0.0623	0.426	0.014	0.565	0.019	3.117	0.292	0.413	0.138	1.303
*ABELL_3827	RF	0.0984	3.243	0.032	5.080	0.050	7.338	0.789	0.339	0.144	1.302
ABELL_3854	NR	0.1492	2.281	0.081	3.256	0.116	5.181	0.394	0.258	0.092	1.197
*ABELL_3880	NR	0.0584	0.341	0.018	0.453	0.023	2.897	0.277	0.305	0.143	2.280
ABELL_3911	RF	0.0965	2.198	0.061	3.262	0.090	6.106	0.393	0.285	0.081	1.183
*ABELL_3921	RF	0.0928	1.981	0.037	2.916	0.054	5.766	0.762	0.360	0.085	1.879
ABELL_4023	RF	0.1934	1.996	0.082	2.984	0.123	6.256	0.635	0.268	0.117	1.216
*ABELL_4038	NR	0.0282	0.394	0.007	0.525	0.009	2.878	0.263	0.286	0.118	3.540
*ABELL_S0295	RF	0.3	9.202	0.310	14.464	0.487	7.072	0.896	0.257	0.059	1.200
ABELL_S0520	RF	0.2952	6.561	0.201	10.757	0.330	8.269	0.732	0.140	0.076	1.167
ABELL_S0579	RF	0.152	1.508	0.056	2.119	0.078	4.789	0.352	0.213	0.092	1.146
ABELL_S0592	RF	0.2216	7.970	0.188	13.233	0.313	8.581	0.651	0.312	0.080	1.363
*ABELL_S0780	RB	0.2357	5.352	0.074	8.395	0.117	7.021	0.628	0.310	0.122	1.065
ABELL_S0821	NR	0.2371	5.443	0.174	8.184	0.261	6.386	0.506	0.302	0.072	1.108
ABELL_S1063	NR	0.3475	22.560	0.412	41.905	0.765	11.302	0.722	0.359	0.070	1.219
*ABELL_S1101	NR	0.058	0.541	0.010	0.726	0.013	2.698	0.286	0.199	0.089	2.076
Abell_222	NR	0.211	1.664	0.067	2.287	0.092	4.137	0.274	0.216	0.070	1.032
Abell_223	NR	0.207	1.370	0.062	1.981	0.089	5.470	0.500	0.247	0.100	1.152
*BLOX_J1023.6+0411.1	NR	0.2906	8.464	0.127	14.162	0.213	8.052	0.966	0.285	0.096	1.289
BLOX_J1056.9-0337.3	NR	0.8231	7.212	0.383	11.420	0.607	7.494	1.083	0.096	0.107	1.444
*Bullet_Cluster	RF	0.296	24.166	0.131	46.462	0.252	12.364	1.145	0.208	0.066	1.326
*CIZA_J0107.7+5408	NR	0.1066	3.881	0.057	6.191	0.092	6.642	1.385	0.184	0.136	1.257
CIZA_J0616.3-2156	RF	0.171	2.994	0.067	4.678	0.105	7.236	0.511	0.313	0.086	1.178
CIZA_J1804.4+1002	RB	0.1525	5.159	0.144	8.034	0.225	7.097	0.592	0.092	0.075	1.225
CIZA_J1938.3+5409	RB	0.26	8.739	0.350	13.629	0.546	7.202	0.728	0.356	0.091	1.124
*CIZA_J2242.8+5301	NR	0.1921	4.117	0.053	6.747	0.088	7.813	1.165	0.183	0.120	1.048
ClG_1137.5+6625	NR	0.782	5.411	0.347	7.728	0.495	5.174	0.629	0.228	0.122	1.088
*ClG_2153.8+3746	NR	0.292	11.047	0.148	19.077	0.256	8.940	1.321	0.240	0.103	1.148
Cl_0016+16	NR	0.541	16.147	0.355	28.163	0.619	9.727	0.745	0.198	0.063	0.964
G113.82+44.35	NR	0.2257	2.620	0.128	3.891	0.189	6.017	0.680	0.004	0.053	1.037
G139.59+24.18	NR	0.27	7.876	0.283	12.273	0.440	7.189	0.635	0.378	0.086	1.169
*GALEX_J094712.4+762313	NR	0.3541	7.738	0.176	12.772	0.291	8.581	0.841	0.286	0.196	1.088
GMBCG_J179.81192+49.79669	NR	0.383	7.801	0.394	13.915	0.702	10.276	1.691	0.267	0.141	1.111

Name	ID	z	LX	e_LX	LX	e_LX	kT	e_kT	Z	e_Z	χ^2_{red}
			[0.5-8 keV]	[0.5-8 keV]	[bol]	[bol]					
			10^{44} erg s^{-1}		10^{44} erg s^{-1}		keV		$Z_{\odot}$		
*GMBCG_J215.94948+24.07846	NR	0.5431	6.151	0.118	9.624	0.185	6.887	0.360	0.327	0.029	1.000
*Hercules_A	RB	0.155	1.836	0.034	2.531	0.047	3.653	1.309	0.181	0.097	1.224
*Hydra_A	NR	0.0549	1.145	0.005	1.566	0.006	3.951	0.219	0.289	0.046	1.219
*IC_1365	NR	0.0493	0.574	0.025	0.781	0.034	3.966	0.438	0.509	0.083	2.480
*LCDCS_0829	NR	0.451	20.538	0.248	41.656	0.503	13.426	2.267	0.213	0.073	1.160
MACS0140.0-0555	NR	0.4541	7.056	0.392	10.985	0.610	7.139	0.822	0.256	0.103	1.149
MACS_J0011.7-1523	NR	0.378	6.014	0.194	8.839	0.285	5.892	0.399	0.271	0.066	1.132
MACS_J0025.4-1222	NR	0.5843	8.852	0.347	14.205	0.557	7.817	0.597	0.256	0.060	1.134
MACS_J0242.6-2132	NR	0.314	4.837	0.298	7.085	0.436	5.751	0.774	0.151	0.115	1.156
MACS_J0308.9+2645	NR	0.324	10.682	0.298	18.580	0.518	9.656	1.047	0.159	0.085	1.285
MACS_J0358.8-2955	RF	0.425	12.749	0.337	21.346	0.564	8.747	0.487	0.143	0.052	1.130
*MACS_J0417.5-1154	NR	0.44	21.550	0.366	40.079	0.680	10.945	0.936	0.211	0.093	1.108
MACS_J0429.6-0253	NR	0.399	5.376	0.254	8.315	0.393	7.000	0.900	0.302	0.132	1.159
MACS_J0451.9+0006	NR	0.43	5.882	0.364	8.608	0.533	5.844	0.829	0.411	0.206	1.101
MACS_J0455.2+0657	NR	0.425	6.452	0.414	9.878	0.634	6.845	0.998	0.571	0.226	1.135
MACS_J0553.4-3342	RF	0.407	13.416	0.212	24.118	0.382	10.463	0.680	0.192	0.055	1.119
*MACS_J0717+3745	NR	0.5458	25.993	0.368	51.818	0.734	12.868	1.576	0.181	0.048	1.136
MACS_J0744.9+3927	NR	0.6976	13.375	0.576	21.465	0.924	7.805	0.634	0.179	0.067	1.114
MACS_J0911.2+1746	NR	0.5049	5.371	0.324	8.253	0.497	6.808	0.894	0.133	0.102	1.124
MACS_J0949.8+1708	NR	0.3826	9.104	0.381	16.267	0.681	10.311	1.712	0.184	0.151	1.258
MACS_J1108.9+0906	NR	0.449	5.708	0.269	8.786	0.414	6.863	0.744	0.193	0.106	1.128
MACS_J1115.8+0129	NR	0.352	8.020	0.227	13.674	0.388	9.180	0.730	0.189	0.068	1.253
MACS_J1206.2-0847	NR	0.44	16.980	0.490	31.633	0.913	11.369	1.423	0.225	0.109	1.235
MACS_J1311.0-0311	NR	0.494	4.349	0.189	6.435	0.280	6.031	0.482	0.228	0.071	1.128
MACS_J1354.6+7715	NR	0.3967	4.673	0.251	7.024	0.378	6.384	0.815	0.314	0.119	1.103
MACS_J1427.6-2521	NR	0.318	2.061	0.095	2.865	0.132	4.689	0.340	0.443	0.114	1.186
*MACS_J1532.8+3021	RB	0.345	6.570	0.112	10.388	0.177	7.129	0.720	0.239	0.065	1.141
MACS_J1621.3+3810	RB	0.465	4.964	0.186	7.763	0.291	7.226	0.580	0.199	0.066	1.167
MACS_J1720.2+3536	RB	0.3913	6.766	0.206	10.872	0.331	7.870	0.653	0.367	0.080	1.279
MACS_J1829.0+6913	NR	0.203	0.843	0.044	1.151	0.060	4.057	0.305	0.335	0.109	1.234
*MACS_J1931.8-2635	NR	0.352	8.805	0.104	14.152	0.168	7.793	0.786	0.374	0.147	1.326
MACS_J2046.0-3430	NR	0.423	4.194	0.216	6.100	0.314	5.606	0.447	0.212	0.086	1.136
MACS_J2129-0741	NR	0.5889	12.133	0.669	19.708	1.086	8.117	0.943	0.454	0.126	1.130
MACS_J2135-0102	NR	0.325	4.768	0.219	7.826	0.360	8.365	1.066	0.580	0.154	1.246
*MACS_J2140.2-2339	NR	0.313	3.985	0.110	5.860	0.162	5.638	0.740	0.306	0.144	1.070
MACS_J2214-1359	NR	0.483	10.888	0.419	18.292	0.705	8.833	0.989	0.194	0.093	1.120
MACS_J2229.8-2756	NR	0.324	4.070	0.190	5.967	0.279	5.882	0.562	0.397	0.108	1.233
MACS_J2245.0+2637	NR	0.304	4.480	0.241	6.835	0.368	6.710	0.933	0.330	0.146	1.224

Name	ID	z	LX	e_LX	LX	e_LX	kT	e_kT	Z	e_Z	χ^2_{red}
			[0.5-8 keV]	[0.5-8 keV]	[bol]	[bol]					
			10^{44} erg s^{-1}		10^{44} erg s^{-1}		keV		$Z_{\odot}$		
MCXC_J0027.8+2616	NR	0.3668	3.049	0.194	4.615	0.294	6.438	0.978	0.039	0.082	1.086
MCXC_J0035.4-2015	NR	0.364	10.772	0.355	16.792	0.554	7.187	0.645	0.338	0.090	1.146
MCXC_J0142.0+2131	NR	0.2803	5.460	0.165	8.543	0.258	7.218	0.649	0.118	0.090	1.265
MCXC_J0152.5-2853	NR	0.341	4.091	0.126	6.018	0.186	5.815	0.584	0.058	0.081	1.125
MCXC_J0220.9-3829	RF	0.2287	2.352	0.136	3.225	0.187	4.346	0.368	0.546	0.140	1.230
MCXC_J0301.6+0155	NR	0.1695	1.687	0.079	2.341	0.110	4.450	0.333	0.233	0.090	1.190
MCXC_J0303.7-7752	RF	0.2742	6.901	0.197	11.840	0.338	9.344	0.891	0.318	0.085	1.143
MCXC_J0331.1-2100	NR	0.188	2.604	0.104	3.827	0.153	5.859	0.528	0.204	0.092	1.380
*MCXC_J0352.9+1941	NR	0.109	1.013	0.041	1.362	0.055	3.085	0.533	0.263	0.124	1.111
*MCXC_J0425.8-0833	NR	0.0397	0.384	0.016	0.514	0.022	3.088	0.125	0.256	0.073	3.255
*MCXC_J0437.1+0043	NR	0.285	4.937	0.134	7.580	0.205	6.101	0.632	0.265	0.041	1.251
MCXC_J0439.0+0520	NR	0.208	1.883	0.103	2.670	0.145	5.024	0.480	0.251	0.107	1.220
MCXC_J0439.0+0715	NR	0.23	5.310	0.166	8.038	0.252	6.528	0.534	0.293	0.083	1.160
MCXC_J0454.1-0300	NR	0.55	15.974	0.296	28.925	0.536	10.644	0.768	0.206	0.082	1.309
MCXC_J0510.7-0801	NR	0.2195	8.412	0.212	13.101	0.330	7.152	0.434	0.280	0.060	1.082
MCXC_J0520.7-1328	NR	0.34	5.821	0.181	9.131	0.284	7.335	0.692	0.345	0.111	1.265
*MCXC_J0528.2-2942	RF	0.1582	1.634	0.086	2.245	0.119	4.607	0.499	0.564	0.197	1.327
MCXC_J0532.9-3701	RF	0.2747	6.799	0.197	11.333	0.329	8.644	0.843	0.136	0.080	1.134
MCXC_J0547.0-3904	RF	0.21	0.974	0.060	1.398	0.086	5.186	0.699	0.046	0.106	1.352
MCXC_J0819.6+6336	NR	0.119	0.758	0.044	1.025	0.060	3.498	0.321	0.170	0.088	1.238
MCXC_J1000.5+4409	NR	0.154	1.065	0.070	1.437	0.095	3.278	0.268	0.183	0.095	1.243
MCXC_J1010.5-1239	NR	0.301	4.060	0.084	6.139	0.127	6.484	0.395	0.222	0.062	1.108
MCXC_J1215.4-3900	NR	0.119	1.605	0.038	2.315	0.055	5.505	0.361	0.429	0.110	1.167
MCXC_J1234.2+0947	NR	0.229	1.747	0.111	2.439	0.154	4.552	0.485	0.134	0.112	1.255
MCXC_J1514.9-1523	RB	0.2226	5.561	0.090	9.372	0.151	8.899	0.481	0.141	0.048	1.105
*MCXC_J1524.2-3154	RB	0.1028	1.365	0.019	1.900	0.026	4.426	0.719	0.362	0.129	1.326
*MCXC_J1558.3-1410	RB	0.097	2.001	0.021	2.850	0.029	5.018	0.356	0.371	0.106	1.330
MCXC_J1623.5+2634	RB	0.426	3.854	0.228	5.798	0.342	6.365	0.908	0.201	0.124	1.005
MCXC_J1731.6+2251	RB	0.366	6.784	0.211	11.278	0.351	8.608	0.849	0.299	0.123	1.320
MCXC_J1750.2+3504	RB	0.171	1.689	0.078	2.364	0.109	4.639	0.356	0.126	0.083	1.187
MCXC_J1852.1+5711	RB	0.1094	0.465	0.019	0.635	0.026	4.003	0.283	0.259	0.096	1.345
MCXC_J1853.9+6822	NR	0.0928	1.031	0.025	1.419	0.034	4.129	0.221	0.190	0.074	1.199
MCXC_J1947.3-7623	RF	0.217	5.483	0.179	8.604	0.280	7.337	0.632	0.338	0.086	1.214
MCXC_J2003.5-2323	NR	0.3171	7.858	0.190	13.401	0.324	9.178	0.804	0.131	0.072	1.222
*MCXC_J2014.8-2430	NR	0.1612	4.182	0.099	6.499	0.154	6.629	0.996	0.447	0.125	1.190
MCXC_J2031.8-4037	NR	0.3416	7.965	0.430	12.201	0.659	6.735	0.918	0.128	0.117	1.116
MCXC_J2049.9-3216	NR	0.325	5.290	0.221	8.338	0.348	7.423	0.952	0.262	0.109	1.259
MCXC_J2211.7-0349	NR	0.27	6.301	0.219	11.029	0.383	9.815	1.315	0.221	0.121	1.394

Name	ID	z	LX	e_LX	LX	e_LX	kT	e_kT	Z	e_Z	χ^2_{red}
			[0.5-8 keV]	[0.5-8 keV]	[bol]	[bol]					
			10^{44} erg s^{-1}		10^{44} erg s^{-1}		keV		$Z_\odot$		
MCXC_J2218.6-3853	NR	0.1379	3.292	0.092	4.789	0.134	5.604	0.330	0.200	0.075	1.240
MCXC_J2228.6+2036	NR	0.412	10.081	0.348	16.485	0.569	8.249	0.824	0.352	0.116	1.176
MCXC_J2311.5+0338	NR	0.2998	7.260	0.281	12.544	0.486	9.518	1.005	0.334	0.103	1.333
*MCXC_J2344.2-0422	NR	0.0786	1.473	0.038	2.031	0.052	4.501	0.143	0.406	0.261	1.422
*MKW_03s	RB	0.045	0.650	0.006	0.875	0.008	3.434	0.404	0.261	0.113	2.072
*MaxBCG_J016.70077+01.05926	NR	0.2539	2.126	0.070	2.961	0.098	4.059	0.412	0.267	0.111	1.028
NSCS_J000619+105206	NR	0.167	1.850	0.072	2.636	0.102	5.184	0.399	0.350	0.092	1.073
NSCS_J121831+401236	NR	0.32	4.257	0.182	6.320	0.271	6.090	0.651	0.210	0.116	1.216
NSCS_J122648+215157	NR	0.37	1.608	0.082	2.259	0.115	4.785	0.474	0.191	0.095	1.082
NSCS_J135021+094042	NR	0.09	0.397	0.023	0.540	0.032	3.634	0.343	0.128	0.088	1.538
*NSCS_J145715+222009	RB	0.2578	3.947	0.081	5.650	0.115	5.120	0.434	0.296	0.101	1.135
*NSC_J084254+292723	NR	0.194	1.485	0.048	2.174	0.070	5.023	0.901	0.519	0.181	1.052
NSC_J092017+303027	NR	0.2578	3.036	0.123	4.554	0.184	6.352	0.661	0.352	0.105	1.115
*NSC_J121733+033929	NR	0.0767	2.565	0.050	3.947	0.077	6.694	0.647	0.292	0.170	2.787
NSC_J174715+451155	RB	0.1565	1.518	0.066	2.128	0.093	4.729	0.378	0.182	0.084	1.142
OC02_J1701+6412	NR	0.453	2.479	0.125	3.720	0.188	6.371	0.771	0.379	0.154	1.122
*PKS_0745-19	NR	0.1028	5.794	0.034	9.484	0.055	8.360	0.483	0.304	0.083	1.593
PLCKESZ_G167.65+17.64	NR	0.174	4.844	0.111	7.219	0.165	6.176	0.412	0.229	0.080	1.140
PLCKESZ_G264.41+19.48	NR	0.24	3.615	0.128	5.726	0.203	7.503	0.702	0.090	0.077	1.126
PLCKESZ_G286.58-31.25	RF	0.21	3.759	0.128	5.678	0.194	6.484	0.540	0.301	0.091	1.060
PLCKESZ_G292.51+21.98	NR	0.3	5.929	0.172	9.902	0.287	8.702	0.784	0.233	0.076	1.104
PLCKESZ_G304.84-41.42	RF	0.41	7.488	0.269	13.102	0.470	9.797	1.232	0.150	0.096	1.170
PLCKESZ_G337.09-25.97	RF	0.2636	6.544	0.138	10.438	0.221	7.658	0.539	0.118	0.070	1.181
*RBS_0653	RF	0.2839	7.669	0.109	13.057	0.185	8.558	0.836	0.258	0.066	1.153
RDCS_J0542-4100	RF	0.64	3.762	0.216	5.691	0.327	6.455	0.885	0.108	0.125	1.168
*SDSS-C4_3072	RB	0.164	4.348	0.075	6.753	0.116	7.066	0.427	0.413	0.059	1.371
*SDSS_+137.3+11.0+0.18	NR	0.18	2.688	0.078	3.869	0.112	5.605	0.799	0.248	0.072	1.140
SDSS_J1115+5319_CLUSTER	NR	0.466	8.139	0.364	14.554	0.651	10.328	1.639	0.141	0.157	1.084
SPT-CLJ0014-4952	RF	0.752	5.112	0.336	7.853	0.517	6.880	0.966	0.406	0.162	1.096
SPT-CLJ2135-5726	RF	0.427	3.586	0.199	5.541	0.307	6.922	1.301	0.108	0.157	1.099
SPT-CLJ2148-6116	RF	0.571	3.484	0.229	5.327	0.351	6.735	1.175	0.272	0.195	1.039
SPT-CLJ2233-5339	RF	0.48	4.392	0.264	6.750	0.406	6.791	1.168	0.075	0.121	1.089
SPT-CLJ2259-6057	RF	0.75	4.949	0.246	7.715	0.384	7.265	1.064	0.694	0.215	1.200
SPT-CL_J0232-4421	RF	0.2836	8.792	0.304	13.995	0.485	7.636	0.811	0.218	0.095	1.259
SPT-CL_J0509-5342	RF	0.4626	4.295	0.208	7.291	0.353	9.069	1.716	0.145	0.164	1.176
SPT-CL_J2023-5535	RF	0.232	5.848	0.172	9.627	0.283	8.387	0.761	0.291	0.085	1.121
*SSGC_081	NR	0.0495	0.418	0.015	0.565	0.020	3.207	0.393	0.282	0.087	2.178
WARP_J1226.9+3332	NR	0.89	11.315	0.521	22.466	1.035	13.126	1.968	0.193	0.189	1.117

Name	ID	z	LX	e_LX	LX	e_LX	kT	e_kT	Z	e_Z	χ^2_{red}
			[0.5-8 keV]	[0.5-8 keV]	[bol]	[bol]					
			10^{44} erg s^{-1}		10^{44} erg s^{-1}		keV		$Z_\odot$		
WARP_J2302.8+0843	NR	0.722	1.736	0.111	2.667	0.170	6.818	1.234	0.169	0.180	1.139
WEIN_051	NR	0.0222	0.404	0.010	0.580	0.015	5.348	0.263	0.282	0.055	2.898
WHL_J093820.9+520243	NR	0.3605	5.414	0.181	8.169	0.274	6.417	0.504	0.165	0.073	1.081
WHL_J102339.9+490838	NR	0.144	3.321	0.111	5.034	0.168	6.513	0.589	0.156	0.083	1.099
WHL_J114224.8+583205	NR	0.3109	7.812	0.182	13.142	0.306	8.855	0.679	0.127	0.073	1.166
WHL_J125933.4+600409	NR	0.33	3.904	0.145	6.024	0.223	6.894	0.515	0.112	0.068	1.062
WHL_J130558.9+263048	NR	0.3047	4.356	0.192	6.829	0.300	7.269	0.948	0.151	0.097	1.082
WHL_J131505.2+514902	NR	0.2911	6.692	0.136	11.224	0.229	8.765	0.771	0.025	0.048	1.149
WHL_J135949.5+623047	NR	0.3216	4.018	0.121	6.184	0.186	6.859	0.590	0.199	0.084	1.468
WHL_J142716.1+440730	NR	0.4981	6.679	0.271	11.975	0.486	10.403	1.424	0.236	0.142	1.328
*WHL_J150407.5-024816	RB	0.2153	9.519	0.130	16.069	0.219	8.482	0.751	0.238	0.070	1.463
WHL_J224319.8-093530	NR	0.4319	14.006	0.520	21.842	0.811	7.179	0.672	0.267	0.085	1.214
ZwCl_0008.8+5215	NR	0.104	0.751	0.030	1.052	0.043	4.711	0.300	0.164	0.087	1.264
*ZwCl_0040.8+2404	NR	0.083	0.823	0.028	1.129	0.038	3.826	0.623	0.291	0.102	1.280
*ZwCl_0735.7+7421	NR	0.216	3.873	0.033	5.843	0.050	6.447	0.632	0.331	0.103	1.236
ZwCl_0823.2+0425	NR	0.2248	1.718	0.107	2.383	0.148	4.660	0.514	0.510	0.168	1.271
*ZwCl_0857.9+2107	NR	0.23	2.167	0.079	2.994	0.110	4.517	0.176	0.356	0.160	0.993
*ZwCl_0949.6+5207	NR	0.214	2.228	0.048	3.243	0.069	5.346	0.581	0.291	0.096	1.088
*ZwCl_1006.1+1201	NR	0.221	2.803	0.071	4.111	0.105	5.860	0.459	0.305	0.027	1.133
*ZwCl_1742.1+3306	RB	0.0757	1.099	0.017	1.507	0.024	4.076	0.352	0.374	0.179	1.653

4 Global metallicity evolution of ACCEPT2.0 clusters

The first detection of iron in the X-ray spectra of galaxy clusters was evidence that the intracluster medium (ICM) is enriched with heavy elements that have been made by stars in galaxies (Mitchell et al., 1976; Mushotzky et al., 1996; Renzini, 1997). Therefore, we can study the metallicity of the ICM over a wide range of redshifts to understand when enrichment occurs, and if the enrichment process is ubiquitous for most clusters. Consequently, simulations of galaxy clusters began to implement feedback from stellar and AGN sources to reproduce the observed chemical properties of the ICM.

Early spatially-resolved observations of the ICM by *ASCA* and *BeppoSAX* showed that certain clusters, now referred to as cool core (CC), exhibit a significant increase in metallicity towards their centers, and a comparatively flat radial distribution in non-cool core (NCC) clusters (Fabian et al., 1994; Fukazawa et al., 1994; De Grandi & Molendi, 2001). CCs are characterized by a dramatic decrease in gas temperature towards the center in comparison to flatter temperature profiles of NCC clusters. Outside of their core radii, the intra-cluster medium (ICM) is similar for both CC and NCC clusters, suggesting that differences in the global abundance is localized to the region surrounding a brightest cluster galaxy (BCG) (De Grandi & Molendi, 2001; De Grandi et al., 2004; Baldi et al., 2012; Ettori et al., 2015; McDonald et al., 2016). We often use measurements excluding the core regions of clusters when studying their global metallicity. Ettori et al. (2015) used 83 clusters with measurements in the region $[0.15\text{-}0.4]R_{500}$ and fit to a functional form that included a dependency on radius r. McDonald et al. (2016) redid the Ettori et al. (2015) analysis and fit to a model without the extra radial dependence and found $Z_0^{Fe} = 0.4 \pm 0.19$. McDonald et al. (2016) analyzed X-ray data from 153 clusters and found no evidence for metallicity evolution outside the core. Mantz et al. (2017) had the largest data set to date with 245 cluster observations compiled from four separate catalogues. For apertures $[0.1\text{-}0.5]R_{500}$, they report a normalization of $Z_{[z=0.19]}^{Fe} = 0.413 \pm 0.007$ and slope $\beta = -0.71 \pm 0.15$.

The analysis reported in this chapter uses a sample of global core excised (CE) metallicities for 308 clusters from ACCEPT2.0 (chapter 2) to assess the abundance evolution of the ICM. In section 4.1, we give an overview of the clusters used in this analysis. Section 4.2 goes over the methods. Section 4.3 details the dependence of our sample of global CE abundance on a cluster's CC status (section 4.3.1), on luminosity (section 4.3.2, and redshift (section 4.3.3). Section 4.3.5 fits the data to a linear model with dependence on luminosity and redshift. Then we apply the methods to more targeted samples in sections 4.3.4 and 4.3.6.

4.1 The Sample

For this analysis, we selected 308 clusters from ACCEPT2.0 with SNR>15 and $L_X \gtrsim 4 \times 10^{43} \mathrm{ergs}^{-1}$. We did not include low luminosity systems because their X-ray observables differ from those of clusters due to their shallower gravitational potential wells. As a result, non-gravitational processes can influence the gas differently than those of more massive clusters.

Because the difference in observations of the global metallicity content of the ICM can be biased depending on the choice of aperture (Mushotzky & Loewenstein, 1997; Balestra et al., 2006; Maughan et al., 2008; Leccardi & Molendi, 2008; Anderson et al., 2009), we use the core-excised global X-ray properties from ACCEPT2.0 so we may treat CCs and NCCs in the same manner. Additionally, core-excised flux can be underestimated for nearby objects that are larger than the *Chandra* field of view. We found that systems above this threshold were massive and distant enough where most of their core-excised apertures fit within the ACIS CCDs. There are 16 clusters with global core-excised abundance approximations consistent with zero at 1σ.[1] These are plotted as their 3σ upper limits. Table 4.7 of clusters is at the end of this chapter.

4.2 Methods

The methods described here were used test the global abundance dependencies on various parameters. To summarize, we separated the data according to core-excised luminosity, L_X, or cluster redshift, z. We then compared the medians of these subsamples, all of which are provided in table 4.1. We chose to use the median global abundance so as to minimize contribution from outliers. The errors on the medians are $\sigma = \sigma_{\mathrm{std}}/\sqrt{N}$, where σ_{std} is the weighted standard deviation defined as,

$$\sigma_{\mathrm{std}} = \sqrt{\frac{\Sigma w_i (X_i - \bar{X}_w)^2}{\Sigma w_i}}, \tag{4.1}$$

where the weight on each radial data point is $w_i = 1/\sigma_i^2$. We found that, when the sample is divided according to luminosity and redshift the differences warrant further investigation at $\sim 3\sigma$.

We tested the significance by simulating clusters based on a null-hypothesis model assuming constant metallicity with intrinsic scatter. The simulated points have the same uncertainties as the observed data, but each simulated value was drawn from two Gaussian distributions. The first draw was centered on the sample mean with an intrinsic dispersion. The first draw is used as a mean for the second Gaussian which has width determined by the uncertainty of the simulated observation.

---

[1] We find no significant difference in our results when these clusters are excluded.

Each simulated sample was divided at the median redshift or luminosity and compared statistically in the same manner as the real data. We compared the halves of every new simulated sample to the preceding samples to generate a probability distribution of observed differences between the simulated samples. The simulated clusters are modeled under the null assumption that the global core-excised metallicities have no dependence on luminosity or redshift. The only source of variation in the measured global abundance is therefore assumed to be due to systematic errors and intrinsic scatter $\sigma_{\rm int}$, provided that $\sigma_{\rm int}$ is non-negligible. We therefore approximate the values of Z_0 and $\sigma_{\rm int}$ via likelihood maximization. The log-likelihood function for data with intrinsic scatter is,

$$\ln\mathscr{L} = -\frac{1}{2}\Sigma_i \left[\frac{(y_i - \bar{y})^2}{\sigma_{\rm int}^2 + \sigma_{y,i}^2} + \ln(2\pi(\sigma_{\rm int}^2 + \sigma_{y,i}^2)) \right], \tag{4.2}$$

where $\sigma_{y,i}$ is the log error on Z_i and $y_i \equiv \ln Z_i$. We fit this with MCMC over 10^5 linearly spaced steps with uniform priors, and the step sizes 0.005 for the abundance y, and 0.009 for the intrinsic scatter $\sigma_{\rm int}$. The bounds for these parameters were -5$\leq y \leq$5 and $-10 \leq \ln\sigma_{\rm int} \leq$10. This resulted in a best-fit parameters Z_0=0.260$\pm$0.006 and $\sigma_{\rm int}$=$0.067^{+0.006}_{-0.005}$. This mean and scatter is used to define a consistent null hypothesis model where no trend in either luminonsity or redshift exists. That model model then is used to simulate data with an underlying constant metallicity Z_0 and variation from adding randomly selected points from normal distributions with mean zero and widths corresponding to $\sigma_{\rm int}$ and the original data error. The result is a simulated sample with constant metallicity and variation solely due to underlying intrinsic scatter and errors on our data.

4.3 Results

4.3.1 Dependence on core status

We aim to determine whether the global abundances of clusters have changed significantly since redshift $z \sim$1. As alluded to in section 1.4, this requires a general view of each cluster without bias from the inner regions of cool cores. We therefore use the temperature and abundance measurements excluding the region r<0.3R$_{2500}$. The difference between cool core clusters versus non-cool core clusters is evidenced by their radial abundance profiles in figures 4.2 and 4.3. These figures show the median spatial distribution of metals for 11 (9) CC (NCC) bins at 100 data points per bin, with the exception of the final bins, which contain 56 and 65 points for CC and NCC clusters, respectively. It should be noted, however, that the extent of data points inside $0.3R_{2500}$ is different between CCs and NCCs because Z is an emission-weighted measurement, and the less dense environment of NCCs, does not allow for as many radial bins to meet the count threshold required for spectral extraction. The error bars are centered on the median metallicity, $\widetilde{Z}$, with sizes corresponding to the mean error, $\sigma = (\Sigma w_i)^{-1/2}$. The shaded region of 4.2 represents the standard deviations, σ_{int}, of each bin. The sizes of these shaded regions in comparison to the error bars is an indication that $\sigma_{\text{int}} \gg \sigma_w$. This profile shows that while radial abundances can vary from cluster to cluster, the profiles as a whole follow a general trend, depending on their central entropy. The binned radial profiles are stacked in figure 4.3 to better show the contrast in spatial distribution of metals between CC and NCCs.

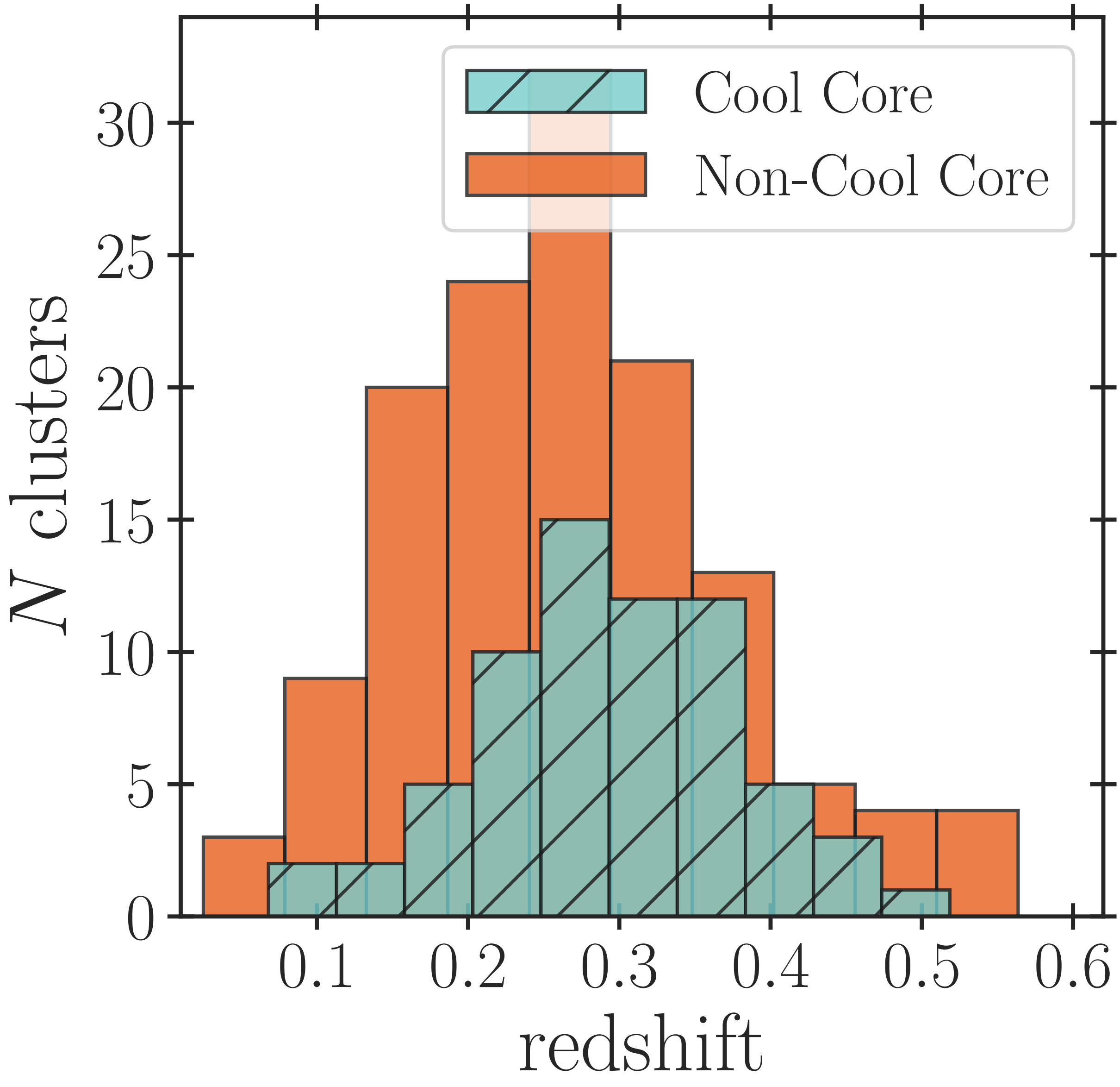

Figure 4.1 Redshift distribution for 67 CC clusters (*hatch blue*) and 134 NCC clusters (*red*).

The median global core-excised metallicities for 67 CC and 135 NCC clusters are $\widetilde{Z}$=0.290±0.012$Z_\odot$ and

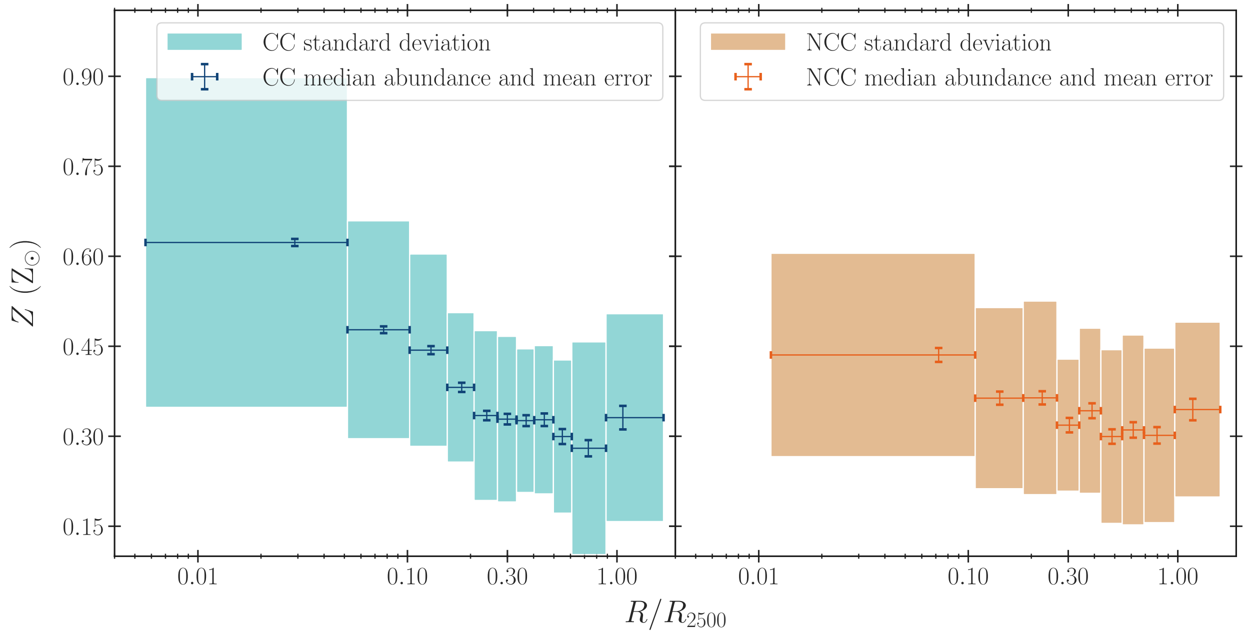

Figure 4.2 Binned weighted means for projected metallicity profiles for CC (*left*) and NCC (*right*) clusters. There is a lack of data points for the innermost regions of NCC clusters because abundance is an emission weighted measurement and the diffuse gas in the cores of these clusters means we can't see it.

$\widetilde{Z}$=0.265±0.009$Z_\odot$, respectively. The low significance of their difference, $\Delta Z_\odot = 0.025 \pm 0.015$, is consistent with recent works, which found that the state of the ICM at outer radii is virtually independent of core status (Neumann, 2005; Leccardi & Molendi, 2008; Eckert et al., 2011) and provides reassurance that the $0.3 < r < 1r_{2500}$ aperture adequately excised the core. These results are summarized in table 4.1.

4.3.2 Luminosity dependence

ACCEPT2.0 contains clusters for which there were enough data to obtain a temperature estimate and radial profiles of the X-ray properties. We therefore need to make sure the global abundances are independent of luminosity (4.4).

After dividing the full sample at the median bolometric luminosity $L_X \simeq 5.2 \times 10^{44}$ erg s^{-1}, the difference in median abundance between low- and high-luminosity clusters is $\Delta Z = 0.033 \pm 0.011 Z_\odot$. We found that this difference is significant at slightly less than 3σ (Figure 4.5, left) using only the standard deviation as an estimator of 1σ. After simulating the null model, we found 68% of the simulations had differences between (0.017,0.018) slightly larger than the weighted estimate and a 3σ upper limit of 0.052, which exceeds the observed difference. With a significance less than 3σ, we conclude that any dependence of global abundance on luminosity here is weak at best.

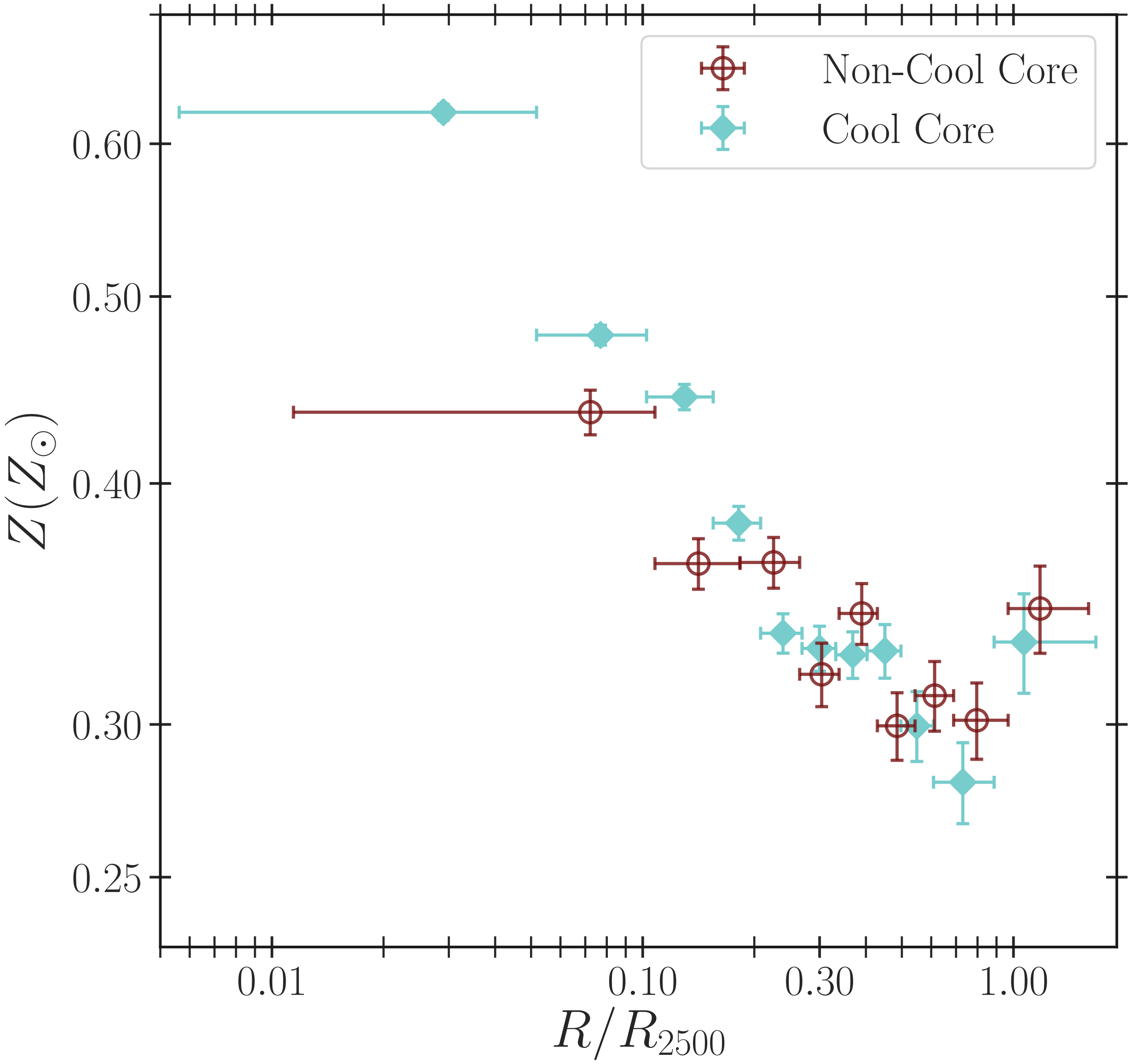

Figure 4.3 Binned weighted mean for projected metallicity profiles for CC (*closed circles)* and NCC (*open diamonds)* clusters.

4.3.3 Redshift Dependence

The global core-excised iron abundance and redshift distributions are shown on the right side of figure 4.4. The difference between the low redshift and high redshift subsamples is $\Delta\widetilde{Z} = 0.035 \pm 0.012 Z_\odot$ (table 4.1). After comparing the medians of subsamples from 100 simulated sets of data, we found that 68% of the simulated null models were in the range (-0.018,+0.019) (figure 4.5), with a 3σ upper limit of 0.047. Because the observed difference is below 3σ, we conclude that any dependence on redshift is weak, although it does not appear to be as weak as the dependence on luminosity.

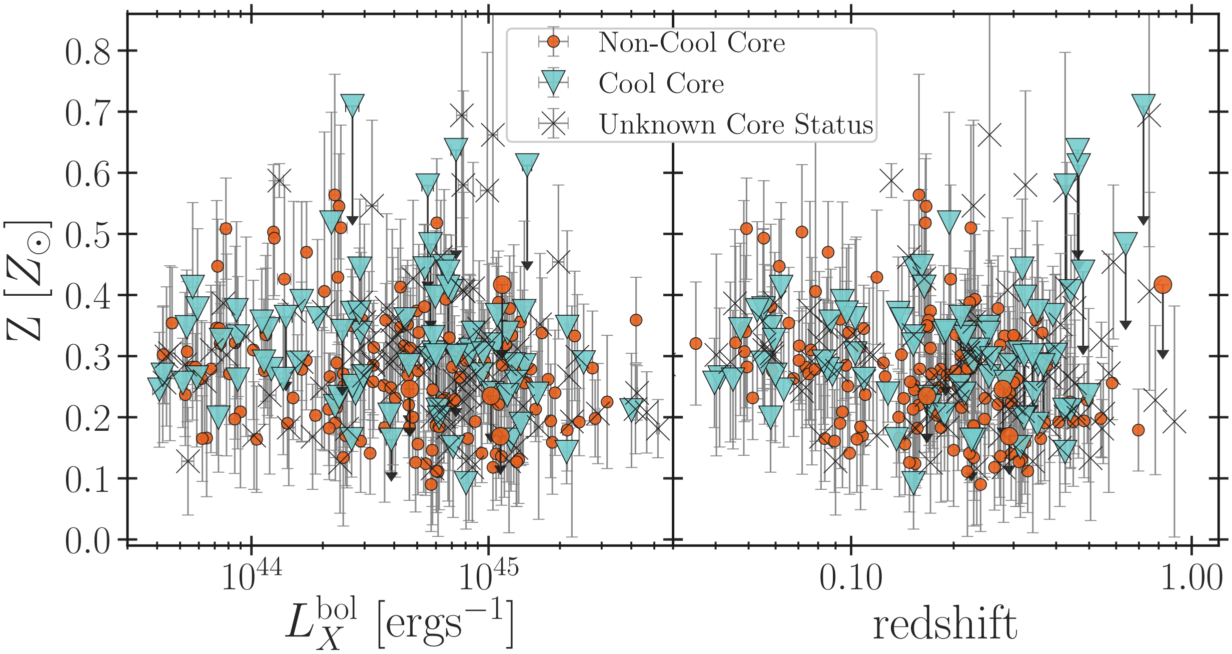

Figure 4.4 Core excised global abundance as a function of bolometric luminosity (*left*) and redshift (*right*) for 308 ACCEPT2.0 clusters. Clusters are classified as either cool core (CC,*blue triangles)* or non-cool core (NCC *orange circles)*. Unclassified clusters are shown as crosses.

Table 4.1 Median core-excised global abundances for sub populations of ACCEPT2.0 clusters. Col(1) is the name of the sub sample, col(2) is the sub sample size, cols(3,4) is the median and mean error of the sub sample, and cols(5,6) is the difference between the median abundances and error. Cols(7,8) show the 1σ lower and upper bounds for the simulated differences.

Subsample	Split Value	N clusters	$\widetilde{Z}[Z_\odot]$	$\sigma_{\rm std}/\sqrt{N}$	$\Delta\widetilde{Z}[Z_\odot]$	$\sigma_{\Delta\widetilde{Z}}$	68% $\Delta\widetilde{Z}^{\rm sim}$	99.7 percentile
Cool Core	30 keV cm^2	67	0.291	0.011	0.024	0.013	···	···
Non-Cool Core		135	0.266	0.008				
Lo L_X	5.2×10^{44}	154	0.289	0.105	0.033	0.011	(-0.017,+0.018)	0.052
Hi L_X		154	0.256	0.096				
Lo z	0.21	154	0.286	0.104	0.035	0.012	(-0.018,+0.019)	0.047
Hi z		154	0.251	0.098				

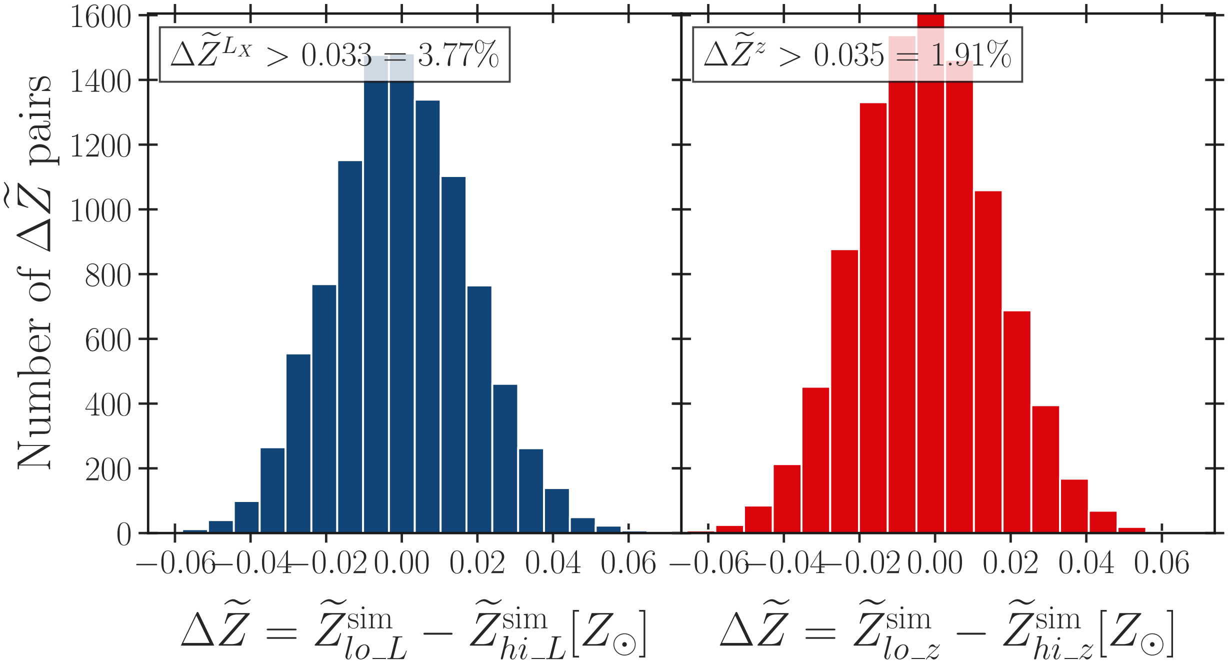

Figure 4.5 Distribution of differences between pairs of simulated data based on the null model. Subsample pairs were separated by either luminosity (*left*) or redshift (*right*).

4.3.4 Procedure with tighter sample constraints

While the above procedure shows no statistical difference in median metallicity for clusters when separated by luminosity or redshift, it did find a weaker dependence on luminosity than redshift. We want to see how much the luminosity affects the redshift dependence by repeating the procedure for a subset of clusters that uniformly cover a luminosity-redshift range.

We chose two sub sets of clusters with uniform coverage in luminosity-redshift, outlined in figure 4.6. The green solid box contains 140 clusters with luminosity and redshift ranges of $2 < \frac{L_X}{10^{44}\mathrm{ergs}^{-1}} < 10$ and $0.05 < z < 0.4$, respectively. The red dashed box contains 69 clusters with $0.35 < \frac{L_X}{10^{44}\mathrm{ergs}^{-1}} < 2$ and $0.03 < z < 0.25$. They have median luminosities and redshifts of $L_X \simeq 4.8\times10^{44}\mathrm{ergs}^{-1}$ and $z \simeq 0.185$, and $L_X \simeq 0.86 \times 10^{44}\mathrm{ergs}^{-1}$ and $z \simeq 0.076$. With the higher luminosity sample, change in ICM metallicity with respect to both luminosity and redshift was negligible and did not warrant further inspection. Similarly, the change in metallicity with respect to L_X is consistent with zero for the low luminosity sample. This is less true when these clusters are separated by redshift, but still not statistically significant at $\Delta\widetilde{Z} = 0.041 \pm 0.025 Z_\odot$. These results are summarized in table 4.2.

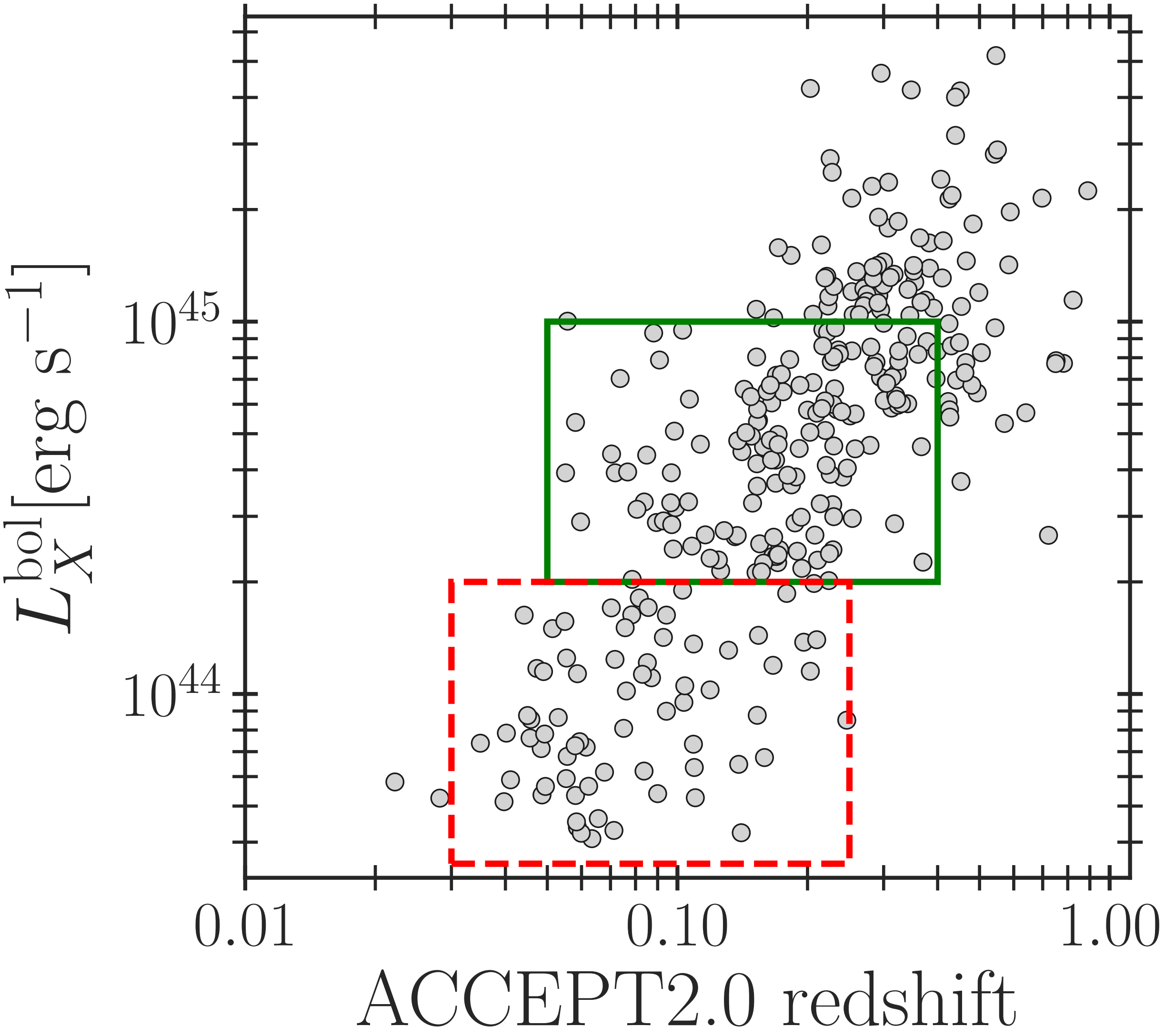

Figure 4.6 Global core-excised luminosity as a function of redshift for 308 ACCEPT2.0 clusters. We redid the analysis using subsamples outlined in solid green or dashed red.

4.3.5 Multiple Linear Regression Analysis

We investigated this further by fitting the data to the functional form,

$$\ln Z(L_X, z) = \ln Z_0 + \alpha \ln \frac{L_X}{L_{\rm piv}} + \beta \ln z. \tag{4.3}$$

By allowing the function to vary with luminosity and redshift simultaneously, we are able to gauge which dependence is stronger. For the full sample, the model dependence on L_X is $\alpha = -0.047 \pm 0.029$, and on redshift is $\beta = -0.014 \pm 0.046$. The results are shown in table 4.3.

Table 4.2 Comparison of median CE global abundances for subsets of ACCEPT2.0 clusters. Clusters with in the solid green box of figure 4.3.4 are in the upper half, and clusters within the red dotted box are in the lower half.

Sample	Split Value	$\mathrm{N}_{clusters}$	$\widetilde{Z}[Z_\odot]$	$\sigma_{\mathrm{std}}/\sqrt{N}$	$\Delta\widetilde{Z}[Z_\odot]$	$\sigma_{\Delta\widetilde{Z}}$	68% $\Delta\widetilde{Z}^{\mathrm{sim}}$	$N^{\mathrm{sim}} \geq \Delta\widetilde{Z}$
				Solid Green Box				
Lo L_X	4.8×10^{44} erg s^{-1}	70	0.270	0.011	0.002	0.02	$\cdots$	$\cdots$
Hi L_X		70	0.268	0.011				
Lo z	0.185	70	0.276	0.011	0.012	0.016	$\cdots$	$\cdots$
Hi z		70	0.264	0.012				
				Dotted Red Box				
Lo L_X	0.860×10^{44} erg s^{-1}	35	0.305	0.012	0.015	0.022	$\cdots$	$\cdots$
Hi L_X		34	0.290	0.019				
Lo z	0.076	35	0.310	0.008	0.041	0.025	(-0.037,+0.036)	964
Hi z		34	0.269	0.024				

Table 4.3 Output parameters for the linear fit of the full sample to equation 4.3. When metallicity is fit to both luminosity and redshift simultaneously, there is a greater dependence on L_X than z, but neither are statsically significant.

Sample	Median L_X	Z_0	α	β	σ_{int}
	[10^{44}erg s^{-1}]	[$Z_\odot$]			
full	5.214	$0.290^{+0.025}_{-0.023}$	$-0.047^{+0.029}_{-0.029}$	$-0.014^{+0.046}_{-0.046}$	$0.163^{+0.021}_{-0.019}$

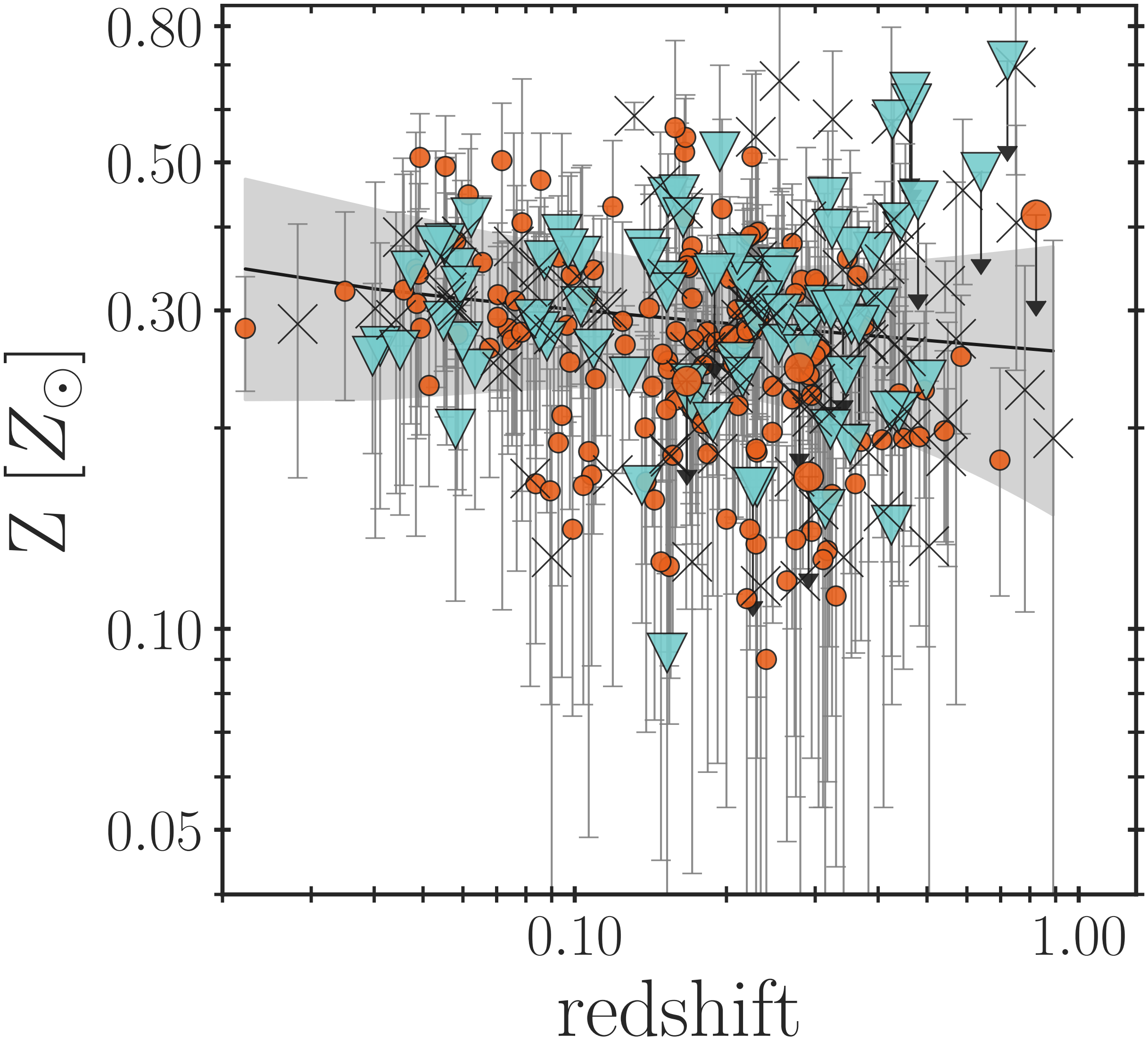

Figure 4.7 Results of the fit to the model. When ICM metallicity is allowed to vary as a function of luminosity and redshift, dependence on luminosity is stronger than the dependence on metallicity, but neither dependence is statistically significant.

4.3.6 Comparison to Maughan et al. (2008)

We compared the results of our above analysis to those by M08, which used 115 clusters observed with *Chandra* and uniformly reduced for two apertures ([0-1]r_{500} and [0.15-1]r_{500}). Their model for constant metallicity was rejected at 99.9% for the core-included aperture, but this significance was not present when the core-excised values were used, in agreement with the results of section 4.3.1. We found 64 clusters in our sample that we share with M08, so we were able to redo the M08 analysis using their metallicities and compare them to what we get using our own. We found that temperatures from M08 are on average lower than ours in ACCEPT2.0, with increasing disparity at higher ACCEPT2.0 temperatures. The higher temperatures in ACCEPT2.0 result in slightly lower abundances than M08 (figure 4.3.6). Private communication from Maughan revealed that he finds his temperatures from Maughan et al. (2012) and presumably M08 may be overestimated by a factor of about 15% owing to difference in the statistical treatments and the energy binning scheme used. This 15% correction appears as the dashed line in figure 4.3.6.

Table 4.6 shows the ACCEPT2.0 cluster temperatures in comparison to M08, and table 4.5 shows the comparison between our luminosities and metallicities. We divided the overlapping M08 and ACCEPT2.0 clusters by luminosity and redshift, and found the difference in median metallicities for both subsets to be higher for the M08 clusters. When split by luminosity, the ACCEPT2.0 clusters have $\Delta\widetilde{Z} = 0.015 \pm 0.021 Z_{\odot}$, and the M08 clusters show $\Delta\widetilde{Z} = 0.075 \pm 0.026 Z_{\odot}$. When split by redshift, ACCEPT2.0 clusters have $\Delta\widetilde{Z} = 0.045 \pm 0.020 Z_{\odot}$ and M08 clusters have $\Delta\widetilde{Z} = 0.065 \pm 0.027 Z_{\odot}$. When we simulate the clusters with no dependence on luminosity or redshift, The samples do still show the same lack of discernible dependence on luminosity and redshift.

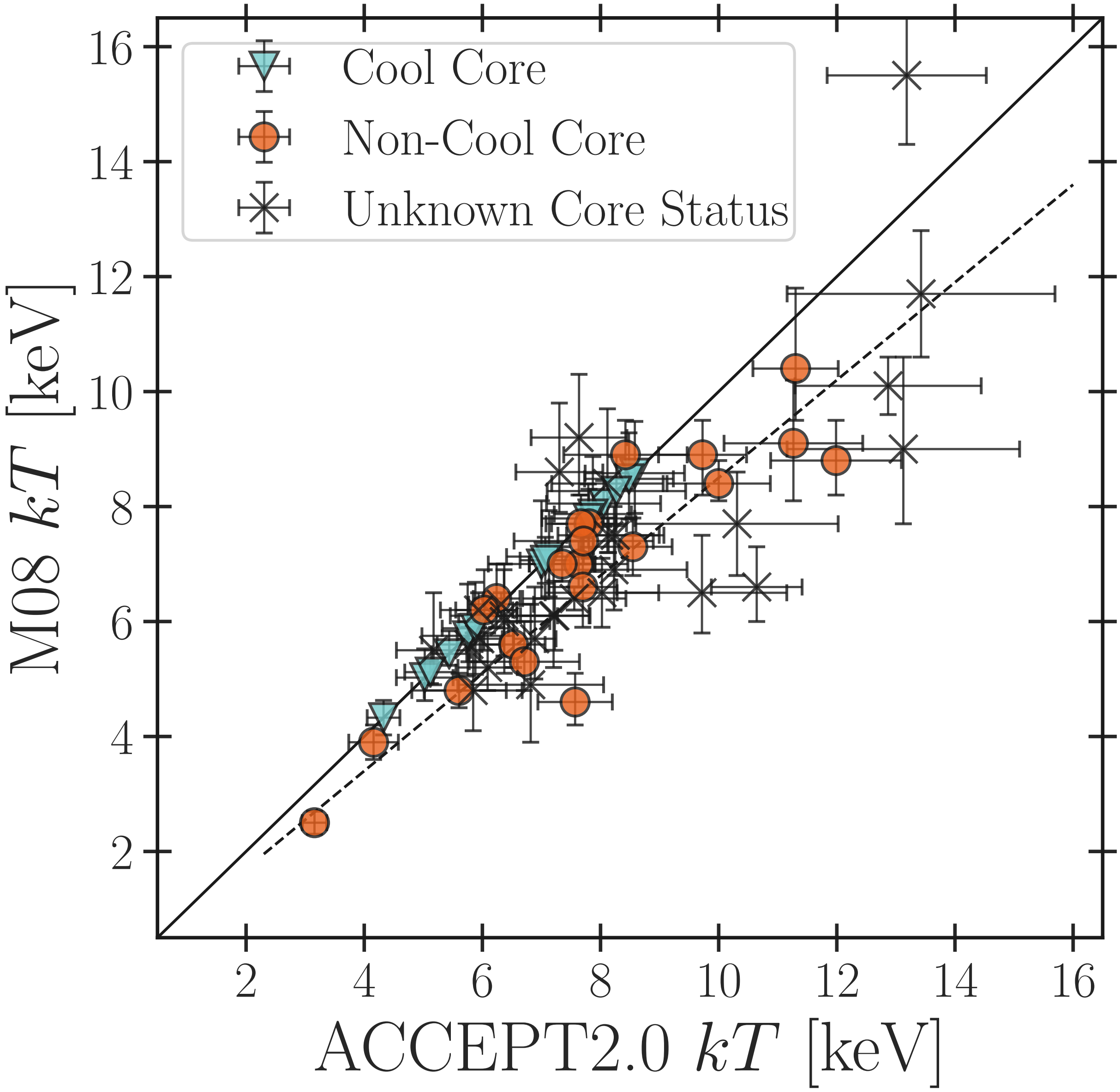

Figure 4.8 Comparison of ACCEPT2.0 global CE temperatures to those of M08. The solid line represents the 1:1 ratio and the dashed line shows the approximate relation between ACCEPT2.0 clusters and M08 clusters that have been reduced by 15%.

Table 4.4 Median CE global abundance for the subsets of ACCEPT2.0 (*top half*) and M08 (*bottom half*) clusters that overlap with M08. Columns are the same as in table 4.1.

Sample	Split Value	$N_{clusters}$	$\widetilde{Z}[Z_\odot]$	$\sigma_{\rm std}/\sqrt{N}$	$\Delta\widetilde{Z}[Z_\odot]$	$\sigma_{\Delta\widetilde{Z}}$	68% $\Delta\widetilde{Z}^{\rm sim}$	$N^{\rm sim} \geq \Delta\widetilde{Z}$
			ACCEPT2.0 Clusters					
Lo L_X	8.176×10^{44}erg s^{-1}	32	0.260	0.097	0.015	0.021	(-0.032,0.031)	6325
Hi L_X		32	0.275	0.071				
Lo z	0.265	32	0.279	0.081	0.045	0.020	(-0.030,0.031)	1522
Hi z		32	0.234	0.082				
			M08 Clusters					
Lo L_X	9.250×10^{44}erg s^{-1}	32	0.325	0.104	0.075	0.026	(-0.038,0.036)	333
Hi L_X		32	0.400	0.102				
Lo z	0.267	32	0.335	0.094	0.065	0.027	(-0.038,0.036)	716
Hi z		32	0.400	0.121				

Table 4.5: Luminosity and metallicities for clusters in ACCEPT2.0 clusters that overlap with M08. ACCEPT2.0 observables are from the [0.3-1]r_{2500} aperture. Column(1) is the ACCEPT2.0 name, column(2) is the ACCEPT2.0 redshift, columns(3,4) are bolometric luminosities and error, columns(5,6) are abundances in solar units. Column(7) is the cluster name from M08. Column(8) is the redshift used by M08. Columns(9,10) are M08 bolometric luminosities, and columns(11-13) are the metallicities measured by M08, where the last two columns are the positive and negative uncertainties on the abundance.)

ACCEPT2.0 Name	redshift	L_X	e_L_X	Z	e_Z	M08 Name	redshift	L_X	e_L_X	Z	E_Z	e_Z
		10^{44} erg s^{-1}		$Z_\odot$				10^{44} erg s^{-1}			$Z_\odot$	
ABELL_0068	0.255	10.429	0.489	0.662	0.210	A68	0.255	9.300	0.500	0.460	0.220	0.210
ABELL_0209	0.206	10.466	0.266	0.250	0.082	A209	0.206	12.200	0.300	0.290	0.100	0.090
ABELL_0267	0.231	6.600	0.166	0.393	0.106	A267	0.230	7.000	0.500	0.640	0.270	0.240
ABELL_0383	0.187	2.881	0.092	0.338	0.110	A383	0.187	3.600	0.100	0.350	0.120	0.110
ABELL_0402	0.322	7.293	0.311	0.045	0.085	MACS J0257.6-2209	0.322	8.100	0.300	0.170	0.170	0.170
ABELL_0586	0.171	4.977	0.139	0.374	0.075	A586	0.171	6.500	0.300	0.840	0.230	0.210
ABELL_0665	0.182	7.910	0.096	0.260	0.075	A665	0.182	15.200	0.200	0.340	0.060	0.050

ABELL_0697	0.282	23.094	0.555	0.333	0.106	A697	0.282	24.400	0.500	0.470	0.100	0.100
ABELL_0773	0.217	9.528	0.214	0.272	0.081	A773	0.217	10.900	0.300	0.570	0.090	0.080
ABELL_0907	0.153	4.152	0.083	0.335	0.142	A907	0.153	4.800	0.100	0.360	0.050	0.050
ABELL_1204	0.171	2.253	0.092	0.218	0.084	A1204	0.171	2.700	0.100	0.130	0.100	0.100
ABELL_1240	0.159	0.675	0.044	0.279	0.137	A1240	0.159	1.600	0.100	0.180	0.110	0.100
ABELL_1300	0.307	17.836	0.446	0.262	0.099	MACS J1131.8-1955	0.307	20.900	0.600	0.410	0.150	0.150
ABELL_1413	0.143	6.581	0.070	0.231	0.089	A1413	0.143	7.400	0.100	0.340	0.050	0.050
ABELL_1682	0.234	5.803	0.164	0.116	0.092	A1682	0.234	7.500	0.500	0.330	0.340	0.300
ABELL_1689	0.183	15.062	0.181	0.279	0.110	A1689	0.183	14.300	0.200	0.400	0.070	0.070
ABELL_1763	0.223	11.013	0.286	0.388	0.084	A1763	0.223	13.700	0.300	0.260	0.090	0.090
ABELL_1914	0.171	15.799	0.246	0.213	0.053	A1914	0.171	12.400	0.200	0.280	0.090	0.090
ABELL_2034	0.113	4.685	0.049	0.303	0.108	A2034	0.113	6.200	0.100	0.360	0.050	0.050
ABELL_2069	0.116	2.675	0.048	0.301	0.128	A2069	0.116	5.100	0.100	0.260	0.060	0.050
ABELL_2111	0.229	5.996	0.129	0.186	0.085	A2111	0.229	7.700	0.300	0.200	0.190	0.180
ABELL_2125	0.246	0.850	0.042	0.197	0.089	A2125	0.246	1.500	0.100	0.200	0.080	0.070
ABELL_2163	0.203	42.292	0.288	0.240	0.045	A2163	0.203	54.100	1.200	0.480	0.130	0.130
ABELL_2204	0.152	10.792	0.077	0.319	0.143	A2204	0.152	12.300	0.300	0.320	0.120	0.110
ABELL_2218	0.176	6.482	0.127	0.201	0.076	A2218	0.176	8.300	0.100	0.350	0.060	0.060
ABELL_2259	0.164	4.806	0.176	0.427	0.128	A2259	0.164	5.200	0.200	0.410	0.170	0.160
ABELL_2261	0.224	11.669	0.253	0.349	0.077	A2261	0.224	13.500	0.200	0.330	0.080	0.080
ABELL_2294	0.169	7.178	0.266	0.260	0.106	A2294	0.178	8.700	0.300	0.230	0.190	0.180
ABELL_2409	0.148	6.289	0.197	0.462	0.093	A2409	0.148	6.300	0.200	0.320	0.120	0.110
ABELL_2631	0.273	11.658	0.398	0.169	0.100	A2631	0.273	13.500	0.500	0.430	0.160	0.150
ABELL_S1063	0.347	41.905	0.765	0.359	0.070	AS 1063	0.252	16.400	0.400	0.130	0.130	0.130
BLOX_J1023.6+0411.1	0.291	14.162	0.213	0.285	0.096	Zw 3146	0.291	15.600	0.300	0.220	0.080	0.080
ClG_1137.5+6625	0.782	7.728	0.495	0.228	0.122	MS 1137.5+6625	0.782	7.100	0.400	0.200	0.220	0.200
Cl_0016+16	0.541	28.163	0.619	0.198	0.063	MS 0015.9+1609	0.541	34.500	0.600	0.240	0.070	0.070
GALEX_J094712.4+762313	0.354	12.772	0.291	0.286	0.196	RBS797	0.354	11.700	0.600	0.540	0.230	0.210
GMBCG_J215.94948+24.07846	0.543	9.624	0.185	0.327	0.029	MACS J1423.8+2404	0.543	11.300	0.700	0.430	0.230	0.210
LCDCS_0829	0.451	41.656	0.503	0.213	0.073	RX J1347.5-1145	0.451	38.300	0.800	0.480	0.100	0.100
MACS_J0242.6-2132	0.314	7.085	0.436	0.151	0.115	MACS J0242.5-2132	0.314	7.900	0.400	0.080	0.180	0.080
MACS_J0429.6-0253	0.399	8.315	0.393	0.302	0.132	MACS J0429.6-0253	0.399	9.200	0.400	0.390	0.180	0.180
MACS_J0451.9+0006	0.430	8.608	0.533	0.411	0.206	MACS J0451.9+0006	0.430	10.900	0.800	0.440	0.320	0.280
MACS_J0717+3745	0.546	51.818	0.734	0.181	0.048	MACS J0717.5+3745	0.546	57.100	0.800	0.320	0.060	0.060
MACS_J0744.9+3927	0.698	21.465	0.924	0.179	0.067	MACS J0744.9+3927	0.697	26.300	1.000	0.310	0.090	0.090
MACS_J0949.8+1708	0.383	16.267	0.681	0.184	0.151	MACS J0949.8+1708	0.384	17.200	0.600	0.270	0.150	0.150
MACS_J1311.0-0311	0.494	6.435	0.280	0.228	0.071	MACS J1311.0-0310	0.494	6.700	0.200	0.270	0.140	0.140
MACS_J1532.8+3021	0.345	10.388	0.177	0.239	0.065	RX J1532.9+3021	0.345	12.300	0.600	0.420	0.190	0.180
MACS_J1621.3+3810	0.465	7.763	0.291	0.199	0.066	MACS J1621.3+3810	0.463	8.700	0.500	0.260	0.120	0.120
MACS_J1720.2+3536	0.391	10.872	0.331	0.367	0.080	MACS J1720.2+3536	0.387	11.200	0.500	0.440	0.200	0.180
MACS_J1931.8-2635	0.352	14.152	0.168	0.374	0.147	MACS J1931.8-2634	0.352	15.300	0.500	0.110	0.100	0.100

MACS_J2129-0741	0.589	19.708	1.086	0.454	0.126	MACS J2129.4-0741	0.594	21.000	1.000	0.400	0.220	0.210
MACS_J2229.8-2756	0.324	5.967	0.279	0.397	0.108	MACS J2229.7-2755	0.324	6.900	0.300	0.250	0.180	0.170
MACS_J2245.0+2637	0.304	6.835	0.368	0.330	0.146	MACS J2245.0+2637	0.301	6.900	0.400	0.620	0.230	0.210
MCXC_J0439.0+0520	0.208	2.670	0.145	0.251	0.107	RX J0439+0520	0.208	3.000	0.300	0.350	0.260	0.220
MCXC_J0439.0+0715	0.230	8.038	0.252	0.293	0.083	RX J0439.0+0715	0.230	8.700	0.200	0.280	0.110	0.100
MCXC_J0454.1-0300	0.550	28.925	0.536	0.206	0.082	MS 0451.6-0305	0.550	28.800	1.200	0.330	0.160	0.150
MCXC_J1623.5+2634	0.426	5.798	0.342	0.201	0.124	MS 1621.5+2640	0.426	7.800	0.400	0.540	0.200	0.190
MCXC_J2228.6+2036	0.412	16.485	0.569	0.352	0.116	MACS J2228.5+2036	0.412	20.800	0.600	0.410	0.130	0.130
NSCS_J145715+222009	0.258	5.650	0.115	0.296	0.101	MS 1455.0+2232	0.258	6.300	0.100	0.400	0.060	0.060
OC02_J1701+6412	0.453	3.720	0.188	0.379	0.154	RX J1701+6414	0.453	5.300	0.300	0.540	0.260	0.230
SDSS-C4_3072	0.164	6.753	0.116	0.413	0.059	RX J1720.1+2638	0.164	7.800	0.200	0.450	0.070	0.070
SDSS_+137.3+11.0+0.18	0.180	3.869	0.112	0.248	0.072	MS 0906.5+1110	0.180	4.700	0.100	0.220	0.090	0.090
SPT-CL_J0232-4421	0.284	13.995	0.485	0.218	0.095	RX J0232.2-4420	0.284	17.600	0.500	0.410	0.160	0.160
WARP_J1226.9+3332	0.890	22.466	1.035	0.193	0.189	CL J1226.9+3332	0.890	21.700	1.100	0.520	0.220	0.220
WARP_J2302.8+0843	0.722	2.667	0.170	0.169	0.180	CL J2302.8+0844	0.722	3.300	0.300	0.040	0.230	0.040
WHL_J150407.5-024816	0.215	16.069	0.219	0.238	0.070	RX J1504-0248	0.215	14.300	0.400	0.350	0.140	0.130

Table 4.6: Temperatures for clusters in ACCEPT2.0 clusters that overlap with M08. ACCEPT2.0 observables are from the [0.3-1]r_{2500} aperture. Column(1) is the ACCEPT2.0 name, columns(2,3) are the core excised temperatures. Column(4) is the cluster name from M08, and columns(5-7) are the temperatures from M08, where column(6) is the positive uncertainty and column(7) is the negative uncertainty.)

A2 Name	kT	e_kT	M08 Name	kT	E_kT	e_kT
		keV			keV	
ABELL_0068	9.717	1.436	A68	6.500	1.000	0.700
ABELL_0209	8.547	0.665	A209	7.300	0.500	0.500
ABELL_0267	7.570	0.630	A267	4.600	0.500	0.400
ABELL_0383	5.438	0.297	A383	4.200	0.400	0.200
ABELL_0402	8.228	1.236	MACS J0257.6-2209	6.900	1.100	0.700
ABELL_0586	6.241	0.395	A586	6.400	0.600	0.500
ABELL_0665	8.136	0.857	A665	7.500	0.300	0.300
ABELL_0697	11.987	1.107	A697	8.800	0.700	0.600
ABELL_0773	7.630	0.833	A773	7.000	0.400	0.400
ABELL_0907	5.772	0.537	A907	5.600	0.300	0.300
ABELL_1204	4.327	0.277	A1204	3.800	0.300	0.300

ABELL_1240	4.158	0.420	A1240	3.900	0.300	0.300
ABELL_1300	11.265	1.174	MACS J1131.8-1955	9.100	1.100	1.000
ABELL_1413	7.350	0.558	A1413	7.000	0.300	0.300
ABELL_1682	7.205	0.618	A1682	6.100	1.100	0.900
ABELL_1689	10.000	0.874	A1689	8.400	0.400	0.300
ABELL_1763	7.669	0.593	A1763	7.700	0.500	0.500
ABELL_1914	8.422	1.044	A1914	8.900	0.600	0.600
ABELL_2034	7.555	0.875	A2034	6.400	0.200	0.200
ABELL_2069	5.936	0.646	A2069	6.200	0.300	0.300
ABELL_2111	7.700	0.575	A2111	6.600	0.900	0.700
ABELL_2125	3.158	0.206	A2125	2.500	0.200	0.200
ABELL_2163	13.183	1.347	A2163	15.500	1.200	1.200
ABELL_2204	8.269	1.172	A2204	7.400	0.600	0.600
ABELL_2218	6.318	0.550	A2218	6.300	0.200	0.200
ABELL_2259	6.089	0.502	A2259	5.200	0.600	0.400
ABELL_2261	7.714	1.178	A2261	7.400	0.400	0.400
ABELL_2294	7.303	0.736	A2294	8.600	1.200	0.700
ABELL_2409	5.955	0.382	A2409	5.700	0.400	0.400
ABELL_2631	8.024	0.961	A2631	6.500	0.600	0.600
ABELL_S1063	11.302	0.722	AS 1063	10.400	1.400	0.900
BLOX_J1023.6+0411.1	8.052	0.966	Zw 3146	8.200	0.400	0.400
ClG_1137.5+6625	5.174	0.629	MS 1137.5+6625	5.500	1.000	0.600
Cl_0016+16	9.727	0.745	MS 0015.9+1609	8.900	0.600	0.700
GALEX_J094712.4+762313	8.581	0.841	RBS797	6.300	0.900	0.700
GMBCG_J215.94948+24.07846	6.887	0.360	MACS J1423.8+2404	5.700	0.900	0.700
LCDCS_0829	13.426	2.267	RX J1347.5-1145	11.700	1.100	1.100
MACS_J0242.6-2132	5.751	0.774	MACS J0242.5-2132	5.900	0.900	0.700
MACS_J0429.6-0253	7.000	0.900	MACS J0429.6-0253	6.800	1.100	0.600
MACS_J0451.9+0006	5.844	0.829	MACS J0451.9+0006	4.800	1.000	0.700
MACS_J0717+3745	12.868	1.576	MACS J0717.5+3745	10.100	0.500	0.500
MACS_J0744.9+3927	7.805	0.634	MACS J0744.9+3927	7.700	0.600	0.600
MACS_J0949.8+1708	10.311	1.712	MACS J0949.8+1708	7.700	0.900	0.900
MACS_J1311.0-0311	6.031	0.482	MACS J1311.0-0310	6.200	0.700	0.700
MACS_J1532.8+3021	7.129	0.720	RX J1532.9+3021	6.100	0.800	0.700
MACS_J1621.3+3810	7.226	0.580	MACS J1621.3+3810	6.100	0.600	0.600
MACS_J1720.2+3536	7.870	0.653	MACS J1720.2+3536	7.800	1.000	1.000
MACS_J1931.8-2635	7.793	0.786	MACS J1931.8-2634	5.800	0.600	0.500
MACS_J2129-0741	8.117	0.943	MACS J2129.4-0741	8.400	1.300	1.200
MACS_J2229.8-2756	5.882	0.562	MACS J2229.7-2755	5.900	0.800	0.800
MACS_J2245.0+2637	6.710	0.933	MACS J2245.0+2637	5.300	0.700	0.500
MCXC_J0439.0+0520	5.024	0.480	RX J0439+0520	3.800	0.500	0.400

MCXC_J0439.0+0715	6.528	0.534	RX J0439.0+0715	5.600	0.400	0.400
MCXC_J0454.1-0300	10.644	0.768	MS 0451.6-0305	6.600	0.700	0.600
MCXC_J1623.5+2634	6.365	0.908	MS 1621.5+2640	6.100	0.800	0.700
MCXC_J2228.6+2036	8.249	0.824	MACS J2228.5+2036	7.500	0.800	0.700
NSCS_J145715+222009	5.120	0.434	MS 1455.0+2232	4.700	0.200	0.200
OC02_J1701+6412	6.371	0.771	RX J1701+6414	6.000	1.000	0.900
SDSS-C4_3072	7.066	0.427	RX J1720.1+2638	7.200	0.400	0.400
SDSS_+137.3+11.0+0.18	5.605	0.799	MS 0906.5+1110	4.800	0.300	0.300
SPT-CL_J0232-4421	7.636	0.811	RX J0232.2-4420	9.200	1.100	1.000
WARP_J1226.9+3332	13.126	1.968	CL J1226.9+3332	9.000	1.600	1.300
WARP_J2302.8+0843	6.818	1.234	CL J2302.8+0844	4.900	1.400	1.000
WHL_J150407.5-024816	8.482	0.751	RX J1504-0248	8.300	0.800	0.700

4.4 Discussion

Our results show no statistical dependence of core-excised metallicity with either redshift or luminosity. At first glance, there appears to be a marginal difference in median metallicity of $\Delta\widetilde{Z} = 0.033 \pm 0.011 Z_\odot$ and $\Delta\widetilde{Z} = 0.035 \pm 0.012 Z_\odot$ between cluster samples when they are divided by redshift and luminosity, respectively. However, 10,000 simulated populations of clusters gave 3σ upper limits of ∼0.052 for luminosity, and ∼ 0.047 for redshift. When we fit the full set of data to a linear model with dependence on L_X and z (4.3), we found marginally stronger dependence on luminosity. We checked this by further dividing our clusters into groups that uniformly cover a redshift and luminosity range. The higher luminosity group is outlined by the solid green box in figure 4.3.4, and the lower luminosity group is outlined in a dotted red box. The higher luminosity clusters show virtually no difference in metallicity with L_X or z. The lower luminosity red clusters exhibited a slight difference Z between the low redshift half and the high redshift half with $\Delta\widetilde{Z} = 0.041 \pm 0.025 Z_\odot$, but after simulating the samples we found the observed difference is not significant as the data has a 3σ upper limit of ∼0.098.

4.4.1 Comparison to observations

The difference in radial abundance profiles between CC and NCC clusters in section 4.3.1 has been observed previously observed, and we found that using core excised abundance and luminosity removes most of the core bias from the global abundance approximations, which is consistent with previous works (Buote, 2000; De Grandi et al., 2004; Maughan et al., 2008; Leccardi et al., 2010; McDonald et al., 2016; Mernier et al., 2017). We also find a lack of statistical dependence of global abundance on both luminosity and redshift. We tested this with a subset of clusters that overlap with those of M08 and found that, while neither sample shows statistical differences in median metallicity according to L_X or z, the differences observed with M08 data were greater than for ACCEPT2.0 clusters. Although both sets used the same clusters, the difference in results can be attributed to systematic differences regarding data reduction, which is evidenced by figure 4.3.6 where ACCEPT2.0 shows slightly higher temperature estimates than M08, with the discrepancy becoming larger for higher temperatures.

The difference in temperatures can stem from a number of reasons including how background emission is accounted for and the model used to fit the X-ray spectrum. M08 extracted spectra from source-free regions of each observations, and from the same regions in the corresponding blank-sky background. This method uses the assumption that some of the field of view does not include cluster emission, which can lead to overestimation of the soft background emission. Additionally, M08 source emission was modeled as an absorbed APEC model in the 0.6-9 keV band, while ACCEPT2.0 emission was modeled as an absorbed MEKAL model and includes a robust fit to the background emission. Another difference is that M08 used chi-square and minimum counts per bin to estimate the temperatures, which can result in poor estimates in the low-S/N regime. Rather than subtraction, ACEPT2.0 statistical analysis used cstat background modeling, which does not require minimum count spectral binning (but in practice workers usually require a minimum of 1 count per energy bin). The way different spectral codes treat sources of X-ray emission introduces an extra level of systematic uncertainty, which can make global abundance approximations a little noisier, especially when combining cluster observables from different catalogs.

4.4.2 Comparison to simulations

Incorporating heavy elements in simulations is a difficult task because it involves stellar evolution models to create the metals and then various methods to distribute those metals throughout the ICM. In the past few decades, simulations have been able to reproduce the metallicity content and distribution of the ICM by including contributions from stellar ejecta and AGN (Valdarnini, 2003; Ettori, 2005; Rasia et al., 2015; Biffi et al., 2017).

The radial distributions of CC and NCC clusters shown in section 4.3.1 are in agreement with simulations which include AGN feedback (Borgani et al., 2008; Rasia et al., 2015; Biffi et al., 2017). Both CC and NCC clusters show higher metallicity inside $r \sim 0.3 r_{2500}$, with a steeper gradient in CC than in NCC clusters. Because AGN activity is more dominant in the core regions of massive clusters, enrichment outside the core looks the same for both CC and NCC clusters. However, present day AGNs are not powerful enough to displace the amount of metals required to explain the nearly solar ICM abundance of local clusters in our sample. Given that we see no statistical evidence for evolution since redshift $z \sim 0.89$, it suggests the ICM must have been enriched at earlier times. Vogelsberger et al. (2017) observed clusters at different redshifts from $IllustrisTNG$ simulations and found the abundances of the outer ICM to be relatively constant since redshift $z \sim 2$. To obtain more constraints on evolution since $z \sim 2$, we would need more observations of high redshift clusters.

4.5 Summary and Conclusions

Improvements in the spatial resolution of X-ray telescopes have allowed for more robust investigations of global abundance trends in the ICM. Previous observations such as those of Balestra et al. (2007), which did not excise core emission, were able to detect some evolution in Z, but we later learned that peaks in central metallicity of CC clusters in comparison to NCCs could affect the results. However, at larger radii, the ICM appears to be oblivious to the mechanics of the core, and are thought to evolve on cosmological time scales, which makes the outer ICM a useful place for tracking the stellar evolution history of clusters with respect to redshift. We have used a sample of 308 global core excised metallicity estimates from ACCEPT2.0 to test their dependence on luminosity and redshift. First, we confirmed that the presence of CC and NCC clusters in our sample did not affect the global core excised metallicity, which supports the idea that AGN activity is confined to the regions surrounding cluster cores. Outside the core, characteristics of the ICM are governed by processes that shape clusters over cosmological time scales. Recent attempts to quantify this evolution have found little evidence for change in recent times. Because ACCEPT2.0 is an archival sample, it is subject to selection biases which can introduce a metallicity dependence on luminosity. Additionally, we show that systematic uncertainties can affect the quantities obtained from the X-ray spectrum because of different methods of data reduction. The statistical and systematic limitations of this sample and analysis indicate that outside of the cores, the global cluster abundance has changed by less than $\sim 15\%$ between $0.02 \lesssim z \lesssim 0.9$.

Table 4.7: Full sample of 308 clusters. Column(1) is the cluster name, column(2) is the redshift, column(3) is the cluster scaled radius r_{2500}, columns(4,5) are bolometric luminosity and error, columns(6,7) are global temperature and error, columns(8,9) are global abundance and error, and column(10) is the goodness of fit for the global properties. Names marked by a '*' are clusters for which the global spectral kT and Z estimates were replaced by radially averaged values (see chapter 2 for details).

ACCEPT2.0 Name	redshift	r_{2500}	L_X	e_L_X	Z	Z_err	kT	kT_err	χ^2/d.o.f
		(kpc)	(10^{44} erg s^{-1})		($Z_\odot$)		(keV)		
2MASSi_J0913454+405628	0.442	457	6.963	0.284	0.406	0.092	6.416	0.590	1.152
*2MFGC_06756	0.241	445	3.823	0.078	0.287	0.098	5.082	0.508	1.057
3C_089	0.139	439	0.647	0.028	0.166	0.096	4.528	0.333	1.164
*3C_444	0.153	473	0.876	0.030	0.332	0.098	4.379	0.393	1.334
*A1882a	0.141	385	0.424	0.022	0.302	0.080	3.317	0.158	1.129
*ABELL_0013	0.094	461	0.899	0.023	0.209	0.124	5.032	0.635	1.048
ABELL_0068	0.255	618	10.429	0.489	0.662	0.210	9.717	1.436	1.270
*ABELL_0085	0.055	543	3.925	0.028	0.358	0.150	6.170	0.588	2.290
*ABELL_0119	0.044	541	1.628	0.019	0.290	0.131	5.916	0.591	3.338
ABELL_0141	0.230	525	4.635	0.186	0.184	0.120	6.576	0.772	1.383
*ABELL_0193	0.049	407	0.536	0.015	0.307	0.115	3.725	0.483	1.191
ABELL_0209	0.206	607	10.466	0.266	0.250	0.082	8.547	0.665	1.313
ABELL_0267	0.231	563	6.600	0.166	0.393	0.106	7.570	0.630	1.224
ABELL_0368	0.220	497	5.101	0.268	0.305	0.138	6.080	0.768	1.276
ABELL_0370	0.375	558	11.422	0.183	0.285	0.074	8.753	0.459	1.206
*ABELL_0376	0.048	468	0.713	0.016	0.346	0.208	4.174	0.670	1.875
*ABELL_0383	0.187	470	2.881	0.092	0.338	0.110	5.438	0.297	1.239
*ABELL_0399	0.072	574	3.926	0.032	0.243	0.136	6.857	0.581	3.135
*ABELL_0401	0.074	609	7.035	0.025	0.282	0.099	7.881	0.877	1.488
ABELL_0402	0.322	552	7.293	0.311	0.045	0.085	8.228	1.236	1.175
*ABELL_0478	0.088	598	9.322	0.060	0.270	0.121	7.546	0.554	1.116
*ABELL_0514	0.071	402	0.430	0.018	0.257	0.035	3.959	0.534	1.588
ABELL_0545	0.154	582	5.431	0.073	0.124	0.052	7.372	0.311	1.265
ABELL_0550	0.099	507	3.165	0.090	0.141	0.067	5.669	0.298	1.202
*ABELL_0562	0.110	353	0.526	0.025	0.237	0.083	2.946	0.451	1.122
ABELL_0586	0.171	516	4.977	0.139	0.374	0.075	6.241	0.395	1.157
ABELL_0598	0.189	457	2.417	0.121	0.068	0.091	5.052	0.538	1.291
*ABELL_0611	0.288	571	7.783	0.205	0.408	0.118	7.993	0.430	1.017
*ABELL_0644	0.070	567	4.410	0.047	0.317	0.089	6.580	0.821	2.778
*ABELL_0665	0.182	614	7.910	0.096	0.260	0.075	8.136	0.857	1.314

ACCEPT2.0 Name	redshift	r_{2500}	L_X	e_L_X	Z	Z_err	kT	kT_err	χ^2/d.o.f
		(kpc)	(10^{44} erg s^{-1})		($Z_\odot$)		(keV)		
ABELL_0697	0.282	713	23.094	0.555	0.333	0.106	11.987	1.107	1.311
*ABELL_0773	0.217	581	9.528	0.214	0.272	0.081	7.630	0.833	1.237
ABELL_0795	0.136	466	2.645	0.068	0.164	0.062	5.002	0.300	1.275
ABELL_0853	0.166	430	1.194	0.075	0.236	0.129	4.441	0.481	1.146
ABELL_0868	0.153	432	3.615	0.119	0.252	0.070	4.414	0.222	1.137
*ABELL_0907	0.153	504	4.152	0.083	0.335	0.142	5.772	0.537	1.381
*ABELL_0963	0.206	527	6.861	0.115	0.226	0.113	6.364	0.782	1.259
*ABELL_0970	0.059	454	1.134	0.038	0.276	0.014	4.504	0.402	1.387
*ABELL_0980	0.158	529	4.606	0.136	0.220	0.086	5.902	1.038	1.204
*ABELL_1033	0.126	501	2.143	0.037	0.266	0.038	5.886	0.583	1.207
*ABELL_1068	0.138	463	2.664	0.060	0.370	0.092	5.225	0.552	1.078
ABELL_1190	0.075	397	0.808	0.038	0.271	0.083	3.597	0.190	1.247
*ABELL_1201	0.169	492	3.681	0.079	0.359	0.060	5.309	0.543	1.254
ABELL_1204	0.171	423	2.253	0.092	0.218	0.084	4.327	0.277	1.310
ABELL_1240	0.159	415	0.675	0.044	0.279	0.137	4.158	0.420	1.411
*ABELL_1285	0.106	496	3.281	0.060	0.314	0.026	5.361	0.617	1.219
ABELL_1300	0.307	786	17.836	0.446	0.262	0.099	11.265	1.174	1.285
*ABELL_1413	0.143	578	6.581	0.070	0.231	0.089	7.350	0.558	1.459
*ABELL_1446	0.103	390	0.950	0.025	0.332	0.163	3.606	0.513	1.123
ABELL_1553	0.165	568	6.048	0.176	0.518	0.105	7.238	0.587	1.136
ABELL_1576	0.279	566	4.654	0.174	0.057	0.063	8.001	0.772	1.187
*ABELL_1644	0.047	481	1.171	0.009	0.344	0.141	4.858	0.506	3.047
*ABELL_1650	0.084	514	3.278	0.026	0.286	0.106	5.726	0.524	1.737
ABELL_1651	0.085	568	4.381	0.089	0.348	0.081	6.897	0.336	2.492
*ABELL_1664	0.128	468	2.747	0.059	0.239	0.047	4.732	0.484	1.178
ABELL_1668	0.063	383	0.409	0.026	0.245	0.094	3.326	0.291	1.442
ABELL_1682	0.234	550	5.803	0.164	0.116	0.092	7.205	0.618	1.131
*ABELL_1689	0.183	676	15.062	0.181	0.279	0.110	10.000	0.874	1.410
*ABELL_1736	0.046	387	0.854	0.017	0.322	0.158	3.070	0.313	3.124
*ABELL_1750C	0.068	450	0.617	0.024	0.263	0.095	3.861	0.768	1.310
ABELL_1750N	0.084	397	0.621	0.029	0.165	0.070	3.586	0.230	1.350
ABELL_1763	0.223	555	11.013	0.286	0.388	0.084	7.669	0.593	1.252
ABELL_1767	0.070	495	1.703	0.053	0.293	0.081	5.301	0.290	1.412
*ABELL_1775	0.072	408	1.238	0.015	0.503	0.110	3.760	0.413	1.616
ABELL_1831	0.061	399	0.720	0.023	0.447	0.077	3.541	0.159	1.347
*ABELL_1835	0.253	646	21.457	0.303	0.348	0.157	9.175	1.354	1.213
*ABELL_1914	0.171	633	15.799	0.246	0.213	0.053	8.422	1.044	1.398
*ABELL_1930	0.131	440	1.311	0.053	0.587	0.028	4.366	0.629	1.235

ACCEPT2.0 Name	redshift	r_{2500}	L_X	e_L_X	Z	Z_err	kT	kT_err	χ^2/d.o.f
		(kpc)	(10^{44} erg s^{-1})		($Z_\odot$)		(keV)		
*ABELL_1942_AND_CLUMP	0.224	465	2.016	0.066	0.373	0.031	5.305	0.486	1.219
*ABELL_1991	0.059	346	0.438	0.013	0.299	0.114	2.695	0.319	1.106
*ABELL_2009	0.153	543	5.386	0.148	0.443	0.071	6.695	0.309	1.392
*ABELL_2034	0.113	595	4.685	0.049	0.303	0.108	7.555	0.875	1.568
*ABELL_2061	0.078	457	1.631	0.031	0.278	0.118	4.310	0.527	1.083
*ABELL_2069	0.116	525	2.675	0.048	0.301	0.128	5.936	0.646	1.712
*ABELL_2104	0.153	565	5.815	0.077	0.245	0.153	7.200	1.018	1.354
*ABELL_2107	0.041	434	0.588	0.012	0.265	0.114	3.766	0.480	3.251
ABELL_2111	0.229	567	5.996	0.129	0.186	0.085	7.700	0.575	1.146
*ABELL_2124	0.066	485	0.463	0.017	0.354	0.091	4.839	0.219	1.104
ABELL_2125	0.246	343	0.850	0.042	0.197	0.089	3.158	0.206	1.133
*ABELL_2142	0.091	626	7.887	0.069	0.276	0.080	7.675	0.570	3.074
*ABELL_2147	0.035	449	0.737	0.010	0.321	0.101	4.275	0.343	4.436
*ABELL_2163	0.203	795	42.292	0.288	0.240	0.045	13.183	1.347	1.603
ABELL_2187	0.184	554	3.644	0.152	0.183	0.122	6.709	0.765	1.389
*ABELL_2204	0.152	654	10.792	0.077	0.319	0.143	8.269	1.172	1.623
*ABELL_2218	0.176	520	6.482	0.127	0.201	0.076	6.318	0.550	1.287
*ABELL_2219	0.226	699	27.420	0.169	0.280	0.093	11.017	0.888	1.223
*ABELL_2244	0.097	515	3.927	0.036	0.327	0.096	5.919	0.484	1.106
ABELL_2249	0.082	486	1.811	0.051	0.168	0.086	5.153	0.342	1.204
*ABELL_2255	0.081	530	3.133	0.038	0.325	0.113	6.086	0.559	1.828
*ABELL_2256	0.058	586	5.363	0.052	0.381	0.135	6.782	0.465	1.886
ABELL_2259	0.164	508	4.806	0.176	0.427	0.128	6.089	0.502	1.254
*ABELL_2261	0.224	593	11.669	0.253	0.349	0.077	7.714	1.178	1.276
ABELL_2294	0.169	570	7.178	0.266	0.260	0.106	7.303	0.736	1.415
ABELL_2302	0.179	447	1.862	0.077	0.203	0.096	4.821	0.382	1.157
*ABELL_2319	0.056	670	10.028	0.078	0.319	0.131	8.664	1.413	3.532
ABELL_2355	0.124	586	2.290	0.071	0.289	0.118	7.240	0.690	1.276
*ABELL_2384	0.094	516	1.628	0.026	0.390	0.162	5.246	0.839	2.330
*ABELL_2390	0.228	668	25.178	0.169	0.290	0.096	10.095	1.521	1.068
ABELL_2409	0.148	510	6.289	0.197	0.462	0.093	5.955	0.382	1.292
*ABELL_2415	0.058	344	0.534	0.016	0.347	0.094	2.583	0.284	1.236
ABELL_2426	0.098	522	2.451	0.077	0.251	0.100	5.825	0.389	1.305
ABELL_2443	0.108	510	2.495	0.072	0.170	0.082	5.683	0.338	1.574
ABELL_2445	0.166	414	2.340	0.077	0.545	0.086	4.162	0.215	1.190
*ABELL_2457	0.059	414	0.744	0.021	0.326	0.059	3.595	0.099	1.352
ABELL_2485	0.247	511	4.043	0.178	0.231	0.129	6.250	0.714	1.247
ABELL_2507	0.196	414	1.377	0.089	0.426	0.154	4.309	0.433	1.069

ACCEPT2.0 Name	redshift	r_{2500}	L_X	e_L_X	Z	Z_err	kT	kT_err	χ^2/d.o.f
		(kpc)	(10^{44} erg s^{-1})		($Z_\odot$)		(keV)		
*ABELL_2537	0.295	506	7.083	0.158	0.224	0.038	6.629	0.625	1.157
*ABELL_2556	0.087	413	1.105	0.024	0.356	0.086	3.756	0.398	1.157
*ABELL_2597	0.085	442	1.214	0.015	0.279	0.080	4.266	0.259	1.310
*ABELL_2626	0.055	382	0.593	0.016	0.378	0.131	3.263	0.379	1.119
ABELL_2631	0.273	580	11.658	0.398	0.169	0.100	8.024	0.961	1.254
ABELL_2645	0.251	512	5.582	0.258	0.297	0.119	6.470	0.782	1.118
*ABELL_2657	0.040	403	0.785	0.021	0.302	0.165	3.567	0.307	3.162
ABELL_2665	0.056	458	0.680	0.025	0.310	0.095	4.553	0.294	1.412
ABELL_2667	0.230	556	12.434	0.331	0.163	0.084	7.604	0.677	1.046
*ABELL_2670	0.076	435	1.019	0.028	0.310	0.114	4.001	0.706	2.206
*ABELL_2744	0.308	640	23.686	0.296	0.299	0.102	10.245	0.770	1.234
ABELL_2813	0.292	559	11.762	0.361	0.287	0.086	7.950	0.739	1.303
ABELL_2895	0.227	594	7.809	0.236	0.301	0.107	8.394	0.858	1.471
ABELL_3017	0.220	538	6.124	0.272	0.111	0.106	7.115	0.939	1.080
ABELL_3088	0.253	576	8.344	0.302	0.236	0.099	7.316	0.762	1.279
ABELL_3126	0.086	476	1.707	0.052	0.470	0.083	4.994	0.309	1.203
*ABELL_3128	0.060	373	0.423	0.020	0.269	0.111	2.860	0.484	1.502
*ABELL_3158	0.060	480	2.899	0.026	0.387	0.082	5.435	0.313	2.722
ABELL_3292	0.172	416	2.441	0.112	0.271	0.098	4.204	0.297	1.410
ABELL_3322	0.200	544	5.786	0.216	0.146	0.092	6.649	0.599	1.104
ABELL_3343	0.191	513	4.563	0.135	0.269	0.099	6.429	0.528	1.175
ABELL_3364	0.148	571	4.925	0.124	0.126	0.081	7.194	0.546	1.411
*ABELL_3376	0.046	496	0.762	0.008	0.386	0.121	4.696	0.499	3.323
ABELL_3378	0.141	453	4.474	0.139	0.360	0.088	4.780	0.273	1.160
*ABELL_3391	0.051	549	1.498	0.031	0.232	0.068	5.794	0.222	3.227
ABELL_3399	0.203	542	5.045	0.111	0.276	0.084	6.759	0.453	1.084
ABELL_3404	0.167	640	10.236	0.244	0.049	0.062	7.851	0.642	1.148
*ABELL_3411	0.169	519	4.247	0.079	0.348	0.095	6.161	0.454	1.119
ABELL_3444	0.253	552	12.037	0.197	0.338	0.060	7.915	0.451	0.974
ABELL_3528B	0.053	497	0.865	0.037	0.375	0.145	6.060	0.567	2.930
ABELL_3532	0.055	495	1.249	0.040	0.493	0.094	5.218	0.285	4.296
*ABELL_3562	0.049	470	1.149	0.026	0.340	0.125	4.701	0.503	3.211
ABELL_3653	0.109	450	0.733	0.021	0.345	0.071	4.781	0.341	1.222
ABELL_3695	0.089	550	2.887	0.064	0.161	0.084	6.465	0.427	1.352
ABELL_3739	0.165	516	4.251	0.177	0.413	0.111	6.084	0.527	1.096
*ABELL_3809	0.062	354	0.565	0.019	0.413	0.138	3.117	0.292	1.303
*ABELL_3827	0.098	585	5.080	0.050	0.339	0.144	7.338	0.789	1.302
ABELL_3854	0.149	472	3.256	0.116	0.258	0.092	5.181	0.394	1.197

ACCEPT2.0 Name	redshift	r_{2500}	L_X	e_L_X	Z	Z_err	kT	kT_err	χ^2/d.o.f
		(kpc)	(10^{44} erg s^{-1})		($Z_\odot$)		(keV)		
*ABELL_3880	0.058	356	0.453	0.023	0.305	0.143	2.897	0.277	2.280
ABELL_3911	0.097	544	3.262	0.090	0.285	0.081	6.106	0.393	1.183
*ABELL_3921	0.093	522	2.916	0.054	0.360	0.085	5.766	0.762	1.879
ABELL_4023	0.193	507	2.984	0.123	0.268	0.117	6.256	0.635	1.216
*ABELL_4038	0.028	369	0.525	0.009	0.286	0.118	2.878	0.263	3.540
*ABELL_S0295	0.300	529	14.464	0.487	0.257	0.059	7.072	0.896	1.200
ABELL_S0520	0.295	573	10.757	0.330	0.140	0.076	8.269	0.732	1.167
ABELL_S0579	0.152	449	2.119	0.078	0.213	0.092	4.789	0.352	1.146
ABELL_S0592	0.222	598	13.233	0.313	0.312	0.080	8.581	0.651	1.363
*ABELL_S0780	0.236	551	8.395	0.117	0.310	0.122	7.021	0.628	1.065
ABELL_S0821	0.237	511	8.184	0.261	0.302	0.072	6.386	0.506	1.108
ABELL_S1063	0.347	663	41.905	0.765	0.359	0.070	11.302	0.722	1.219
*ABELL_S1101	0.058	345	0.726	0.013	0.199	0.089	2.698	0.286	2.076
Abell_222	0.211	404	2.287	0.092	0.216	0.070	4.137	0.274	1.032
Abell_223	0.207	473	1.981	0.089	0.247	0.100	5.470	0.500	1.152
*BLOX_J1023.6+0411.1	0.291	589	14.162	0.213	0.285	0.096	8.052	0.966	1.289
BLOX_J1056.9-0337.3	0.823	401	11.420	0.607	0.096	0.107	7.494	1.083	1.444
*Bullet_Cluster	0.296	708	46.462	0.252	0.208	0.066	12.364	1.145	1.326
*CIZA_J0107.7+5408	0.107	634	6.191	0.092	0.184	0.136	6.642	1.385	1.257
CIZA_J0616.3-2156	0.171	557	4.678	0.105	0.313	0.086	7.236	0.511	1.178
CIZA_J1804.4+1002	0.152	545	8.034	0.225	0.092	0.075	7.097	0.592	1.225
CIZA_J1938.3+5409	0.260	539	13.629	0.546	0.356	0.091	7.202	0.728	1.124
*CIZA_J2242.8+5301	0.192	595	6.747	0.088	0.183	0.120	7.813	1.165	1.048
ClG_1137.5+6625	0.782	334	7.728	0.495	0.228	0.122	5.174	0.629	1.088
*ClG_2153.8+3746	0.292	608	19.077	0.256	0.240	0.103	8.940	1.321	1.148
Cl_0016+16	0.541	557	28.163	0.619	0.198	0.063	9.727	0.745	0.964
G113.82+44.35	0.226	495	3.891	0.189	0.004	0.053	6.017	0.680	1.037
G139.59+24.18	0.270	539	12.273	0.440	0.378	0.086	7.189	0.635	1.169
*GALEX_J094712.4+762313	0.354	550	12.772	0.291	0.286	0.196	8.581	0.841	1.088
GMBCG_J179.81192+49.79669	0.383	569	13.915	0.702	0.267	0.141	10.276	1.691	1.111
*GMBCG_J215.94948+24.07846	0.543	462	9.624	0.185	0.327	0.029	6.887	0.360	1.000
*Hercules_A	0.155	419	2.531	0.047	0.181	0.097	3.653	1.309	1.224
*Hydra_A	0.055	431	1.566	0.006	0.289	0.046	3.951	0.219	1.219
*IC_1365	0.049	429	0.781	0.034	0.509	0.083	3.966	0.438	2.480
*LCDCS_0829	0.451	718	41.656	0.503	0.213	0.073	13.426	2.267	1.160
MACS0140.0-0555	0.454	476	10.985	0.610	0.256	0.103	7.139	0.822	1.149
MACS_J0011.7-1523	0.378	451	8.839	0.285	0.271	0.066	5.892	0.399	1.132
MACS_J0025.4-1222	0.584	470	14.205	0.557	0.256	0.060	7.817	0.597	1.134

ACCEPT2.0 Name	redshift	r_{2500} (kpc)	L_X (10^{44} erg s^{-1})	e_L_X	Z ($Z_{\odot}$)	Z_err	kT (keV)	kT_err	χ^2/d.o.f
MACS_J0242.6-2132	0.314	459	7.085	0.436	0.151	0.115	5.751	0.774	1.156
MACS_J0308.9+2645	0.324	603	18.580	0.518	0.159	0.085	9.656	1.047	1.285
MACS_J0358.8-2955	0.425	548	21.346	0.564	0.143	0.052	8.747	0.487	1.130
*MACS_J0417.5-1154	0.440	624	40.079	0.680	0.211	0.093	10.945	0.936	1.108
MACS_J0429.6-0253	0.399	491	8.315	0.393	0.302	0.132	7.000	0.900	1.159
MACS_J0451.9+0006	0.430	443	8.608	0.533	0.411	0.206	5.844	0.829	1.101
MACS_J0455.2+0657	0.425	478	9.878	0.634	0.571	0.226	6.845	0.998	1.135
MACS_J0553.4-3342	0.407	649	24.118	0.382	0.192	0.055	10.463	0.680	1.119
*MACS_J0717+3745	0.546	647	51.818	0.734	0.181	0.048	12.868	1.576	1.136
MACS_J0744.9+3927	0.698	442	21.465	0.924	0.179	0.067	7.805	0.634	1.114
MACS_J0911.2+1746	0.505	460	8.253	0.497	0.133	0.102	6.808	0.894	1.124
MACS_J0949.8+1708	0.383	576	16.267	0.681	0.184	0.151	10.311	1.712	1.258
MACS_J1108.9+0906	0.449	472	8.786	0.414	0.193	0.106	6.863	0.744	1.128
MACS_J1115.8+0129	0.352	589	13.674	0.388	0.189	0.068	9.180	0.730	1.253
MACS_J1206.2-0847	0.440	606	31.633	0.913	0.225	0.109	11.369	1.423	1.235
MACS_J1311.0-0311	0.494	428	6.435	0.280	0.228	0.071	6.031	0.482	1.128
MACS_J1354.6+7715	0.397	467	7.024	0.378	0.314	0.119	6.384	0.815	1.103
MACS_J1427.6-2521	0.318	410	2.865	0.132	0.443	0.114	4.689	0.340	1.186
*MACS_J1532.8+3021	0.345	522	10.388	0.177	0.239	0.065	7.129	0.720	1.141
MACS_J1621.3+3810	0.465	482	7.763	0.291	0.199	0.066	7.226	0.580	1.167
MACS_J1720.2+3536	0.391	530	10.872	0.331	0.367	0.080	7.870	0.653	1.279
MACS_J1829.0+6913	0.203	402	1.151	0.060	0.335	0.109	4.057	0.305	1.234
*MACS_J1931.8-2635	0.352	540	14.152	0.168	0.374	0.147	7.793	0.786	1.326
MACS_J2046.0-3430	0.423	428	6.100	0.314	0.212	0.086	5.606	0.447	1.136
MACS_J2129-0741	0.589	479	19.708	1.086	0.454	0.126	8.117	0.943	1.130
MACS_J2135-0102	0.325	557	7.826	0.360	0.580	0.154	8.365	1.066	1.246
*MACS_J2140.2-2339	0.313	468	5.860	0.162	0.306	0.144	5.638	0.740	1.070
MACS_J2214-1359	0.483	530	18.292	0.705	0.194	0.093	8.833	0.989	1.120
MACS_J2229.8-2756	0.324	464	5.967	0.279	0.397	0.108	5.882	0.562	1.233
MACS_J2245.0+2637	0.304	499	6.835	0.368	0.330	0.146	6.710	0.933	1.224
MCXC_J0027.8+2616	0.367	477	4.615	0.294	0.039	0.082	6.438	0.978	1.086
MCXC_J0035.4-2015	0.364	509	16.792	0.554	0.338	0.090	7.187	0.645	1.146
MCXC_J0142.0+2131	0.280	526	8.543	0.258	0.118	0.090	7.218	0.649	1.265
MCXC_J0152.5-2853	0.341	457	6.018	0.186	0.058	0.081	5.815	0.584	1.125
MCXC_J0220.9-3829	0.229	414	3.225	0.187	0.546	0.140	4.346	0.368	1.230
MCXC_J0301.6+0155	0.170	432	2.341	0.110	0.233	0.090	4.450	0.333	1.190
MCXC_J0303.7-7752	0.274	630	11.840	0.338	0.318	0.085	9.344	0.891	1.143
MCXC_J0331.1-2100	0.188	495	3.827	0.153	0.204	0.092	5.859	0.528	1.380

ACCEPT2.0 Name	redshift	r_{2500} (kpc)	L_X (10^{44} erg s^{-1})	e_L_X	Z ($Z_\odot$)	Z_err	kT (keV)	kT_err	χ^2/d.o.f
*MCXC_J0352.9+1941	0.109	364	1.362	0.055	0.263	0.124	3.085	0.533	1.111
*MCXC_J0425.8-0833	0.040	379	0.514	0.022	0.256	0.073	3.088	0.125	3.255
*MCXC_J0437.1+0043	0.285	518	7.580	0.205	0.265	0.041	6.101	0.632	1.251
MCXC_J0439.0+0520	0.208	451	2.670	0.145	0.251	0.107	5.024	0.480	1.220
MCXC_J0439.0+0715	0.230	513	8.038	0.252	0.293	0.083	6.528	0.534	1.160
MCXC_J0454.1-0300	0.550	576	28.925	0.536	0.206	0.082	10.644	0.768	1.309
MCXC_J0510.7-0801	0.220	552	13.101	0.330	0.280	0.060	7.152	0.434	1.082
MCXC_J0520.7-1328	0.340	515	9.131	0.284	0.345	0.111	7.335	0.692	1.265
*MCXC_J0528.2-2942	0.158	434	2.245	0.119	0.564	0.197	4.607	0.499	1.327
MCXC_J0532.9-3701	0.275	594	11.333	0.329	0.136	0.080	8.644	0.843	1.134
MCXC_J0547.0-3904	0.210	457	1.398	0.086	0.046	0.106	5.186	0.699	1.352
MCXC_J0819.6+6336	0.119	384	1.025	0.060	0.170	0.088	3.498	0.321	1.238
MCXC_J1000.5+4409	0.154	367	1.437	0.095	0.183	0.095	3.278	0.268	1.243
MCXC_J1010.5-1239	0.301	494	6.139	0.127	0.222	0.062	6.484	0.395	1.108
MCXC_J1215.4-3900	0.119	494	2.315	0.055	0.429	0.110	5.505	0.361	1.167
MCXC_J1234.2+0947	0.229	421	2.439	0.154	0.134	0.112	4.552	0.485	1.255
MCXC_J1514.9-1523	0.223	616	9.372	0.151	0.141	0.048	8.899	0.481	1.105
*MCXC_J1524.2-3154	0.103	444	1.900	0.026	0.362	0.129	4.426	0.719	1.326
*MCXC_J1558.3-1410	0.097	483	2.850	0.029	0.371	0.106	5.018	0.356	1.330
MCXC_J1623.5+2634	0.426	449	5.798	0.342	0.201	0.124	6.365	0.908	1.005
MCXC_J1731.6+2251	0.366	551	11.278	0.351	0.299	0.123	8.608	0.849	1.320
MCXC_J1750.2+3504	0.171	442	2.364	0.109	0.126	0.083	4.639	0.356	1.187
MCXC_J1852.1+5711	0.109	418	0.635	0.026	0.259	0.096	4.003	0.283	1.345
MCXC_J1853.9+6822	0.093	423	1.419	0.034	0.190	0.074	4.129	0.221	1.199
MCXC_J1947.3-7623	0.217	574	8.604	0.280	0.338	0.086	7.337	0.632	1.214
MCXC_J2003.5-2323	0.317	599	13.401	0.324	0.131	0.072	9.178	0.804	1.222
*MCXC_J2014.8-2430	0.161	560	6.499	0.154	0.447	0.125	6.629	0.996	1.190
MCXC_J2031.8-4037	0.342	494	12.201	0.659	0.128	0.117	6.735	0.918	1.116
MCXC_J2049.9-3216	0.325	528	8.338	0.348	0.262	0.109	7.423	0.952	1.259
MCXC_J2211.7-0349	0.270	655	11.029	0.383	0.221	0.121	9.815	1.315	1.394
MCXC_J2218.6-3853	0.138	499	4.789	0.134	0.200	0.075	5.604	0.330	1.240
MCXC_J2228.6+2036	0.412	550	16.485	0.569	0.352	0.116	8.249	0.824	1.176
MCXC_J2311.5+0338	0.300	598	12.544	0.486	0.334	0.103	9.518	1.005	1.333
*MCXC_J2344.2-0422	0.079	450	2.031	0.052	0.406	0.261	4.501	0.143	1.422
*MKW_03s	0.045	394	0.875	0.008	0.261	0.113	3.434	0.404	2.072
*MaxBCG_J016.70077+01.05926	0.254	419	2.961	0.098	0.267	0.111	4.059	0.412	1.028
NSCS_J000619+105206	0.167	466	2.636	0.102	0.350	0.092	5.184	0.399	1.073
NSCS_J121831+401236	0.320	475	6.320	0.271	0.210	0.116	6.090	0.651	1.216

ACCEPT2.0 Name	redshift	r_{2500}	L_X	e_L_X	Z	Z_err	kT	kT_err	χ^2/d.o.f
		(kpc)	(10^{44} erg s^{-1})		($Z_{\odot}$)		(keV)		
NSCS_J122648+215157	0.370	407	2.259	0.115	0.191	0.095	4.785	0.474	1.082
NSCS_J135021+094042	0.090	399	0.540	0.032	0.128	0.088	3.634	0.343	1.538
*NSCS_J145715+222009	0.258	452	5.650	0.115	0.296	0.101	5.120	0.434	1.135
*NSC_J084254+292723	0.194	505	2.174	0.070	0.519	0.181	5.023	0.901	1.052
NSC_J092017+303027	0.258	506	4.554	0.184	0.352	0.105	6.352	0.661	1.115
*NSC_J121733+033929	0.077	576	3.947	0.077	0.292	0.170	6.694	0.647	2.787
NSC_J174715+451155	0.157	447	2.128	0.093	0.182	0.084	4.729	0.378	1.142
OC02_J1701+6412	0.453	453	3.720	0.188	0.379	0.154	6.371	0.771	1.122
*PKS_0745-19	0.103	628	9.484	0.055	0.304	0.083	8.360	0.483	1.593
PLCKESZ_G167.65+17.64	0.174	517	7.219	0.165	0.229	0.080	6.176	0.412	1.140
PLCKESZ_G264.41+19.48	0.240	567	5.726	0.203	0.090	0.077	7.503	0.702	1.126
PLCKESZ_G286.58-31.25	0.210	536	5.678	0.194	0.301	0.091	6.484	0.540	1.060
PLCKESZ_G292.51+21.98	0.300	606	9.902	0.287	0.233	0.076	8.702	0.784	1.104
PLCKESZ_G304.84-41.42	0.410	559	13.102	0.470	0.150	0.096	9.797	1.232	1.170
PLCKESZ_G337.09-25.97	0.264	563	10.438	0.221	0.118	0.070	7.658	0.539	1.181
*RBS_0653	0.284	594	13.057	0.185	0.258	0.066	8.558	0.836	1.153
RDCS_J0542-4100	0.640	410	5.691	0.327	0.108	0.125	6.455	0.885	1.168
*SDSS-C4_3072	0.164	560	6.753	0.116	0.413	0.059	7.066	0.427	1.371
*SDSS_+137.3+11.0+0.18	0.180	475	3.869	0.112	0.248	0.072	5.605	0.799	1.140
SDSS_J1115+5319_CLUSTER	0.466	604	14.554	0.651	0.141	0.157	10.328	1.639	1.084
SPT-CLJ0014-4952	0.752	388	7.853	0.517	0.406	0.162	6.880	0.966	1.096
SPT-CLJ2135-5726	0.427	477	5.541	0.307	0.108	0.157	6.922	1.301	1.099
SPT-CLJ2148-6116	0.571	436	5.327	0.351	0.272	0.195	6.735	1.175	1.039
SPT-CLJ2233-5339	0.480	466	6.750	0.406	0.075	0.121	6.791	1.168	1.089
SPT-CLJ2259-6057	0.750	411	7.715	0.384	0.694	0.215	7.265	1.064	1.200
SPT-CL_J0232-4421	0.284	541	13.995	0.485	0.218	0.095	7.636	0.811	1.259
SPT-CL_J0509-5342	0.463	565	7.291	0.353	0.145	0.164	9.069	1.716	1.176
SPT-CL_J2023-5535	0.232	609	9.627	0.283	0.291	0.085	8.387	0.761	1.121
*SSGC_081	0.050	398	0.565	0.020	0.282	0.087	3.207	0.393	2.178
WARP_J1226.9+3332	0.890	539	22.466	1.035	0.193	0.189	13.126	1.968	1.117
WARP_J2302.8+0843	0.722	407	2.667	0.170	0.169	0.180	6.818	1.234	1.139
WEIN_051	0.022	545	0.580	0.015	0.282	0.055	5.348	0.263	2.898
WHL_J093820.9+520243	0.360	477	8.169	0.274	0.165	0.073	6.417	0.504	1.081
WHL_J102339.9+490838	0.144	533	5.034	0.168	0.156	0.083	6.513	0.589	1.099
WHL_J114224.8+583205	0.311	609	13.142	0.306	0.127	0.073	8.855	0.679	1.166
WHL_J125933.4+600409	0.330	501	6.024	0.223	0.112	0.068	6.894	0.515	1.062
WHL_J130558.9+263048	0.305	537	6.829	0.300	0.151	0.097	7.269	0.948	1.082
WHL_J131505.2+514902	0.291	583	11.224	0.229	0.025	0.048	8.765	0.771	1.149

ACCEPT2.0 Name	redshift	r_{2500} (kpc)	L_X (10^{44} erg s^{-1})	e_L_X	Z ($Z_\odot$)	Z_err	kT (keV)	kT_err	χ^2/d.o.f
WHL_J135949.5+623047	0.322	509	6.184	0.186	0.199	0.084	6.859	0.590	1.468
WHL_J142716.1+440730	0.498	601	11.975	0.486	0.236	0.142	10.403	1.424	1.328
*WHL_J150407.5-024816	0.215	620	16.069	0.219	0.238	0.070	8.482	0.751	1.463
WHL_J224319.8-093530	0.432	488	21.842	0.811	0.267	0.085	7.179	0.672	1.214
ZwCl_0008.8+5215	0.104	456	1.052	0.043	0.164	0.087	4.711	0.300	1.264
*ZwCl_0040.8+2404	0.083	437	1.129	0.038	0.291	0.102	3.826	0.623	1.280
*ZwCl_0735.7+7421	0.216	516	5.843	0.050	0.331	0.103	6.447	0.632	1.236
ZwCl_0823.2+0425	0.225	427	2.383	0.148	0.510	0.168	4.660	0.514	1.271
*ZwCl_0857.9+2107	0.230	414	2.994	0.110	0.356	0.160	4.517	0.176	0.993
*ZwCl_0949.6+5207	0.214	479	3.243	0.069	0.291	0.096	5.346	0.581	1.088
*ZwCl_1006.1+1201	0.221	488	4.111	0.105	0.305	0.027	5.860	0.459	1.133
*ZwCl_1742.1+3306	0.076	437	1.507	0.024	0.374	0.179	4.076	0.352	1.653

5 Data reduction pipeline for the SOAR Adaptive-optics Multi-Object Spectrograph (SAMOS)

The SAMOS instrument is a multi-object spectrograph which uses a Digital Micromirror Device (DMD) (Smee et al., 2018) to focus light towards either an imaging or spectroscopy channel. The DMD allows for multiple slit configurations in a single observing run. Multi-object capabilities of the *Goodman High Throughput Spectrograph* require slit masks to be made in advance, and are installed in the afternoon leading up to the observation. SAMOS has the unique feature of being able to create on-the-fly slit patterns, which will be saved in the FITS headers. The instrument is not set to be commissioned until at least 2021, so the current version of the SAMOS data reduction pipeline (SRP) uses multi-object data from the SOAR Goodman Spectrograph. This SRP will provide the foundation for SAMOS data reduction upon its commissioning. The test data used for the SRP was taken by *SOAR Goodman* on March 19, 2014. Eventually, the pipeline will be used to reduce multi-object spectroscopy data taken with the SOAR Adaptive-Module Optical Spectrograph (SAMOS).

There are two main parts to the SRP: basic image reduction and spectroscopic reduction. For optical spectroscopy, we use detectors called charge-coupled devices (CCDs) to detect and convert light to a digital signal. When sensors on the CCD are hit by incoming photons, they save the information and it gets read out to a two-dimensional pixel array after the exposure. The exposure is saved as a FITS (Flexible Image Transport System) file, which is able to store both the image data and calibration information in a header.

There are a couple important systematics at play during exposure and readout, an obvious one being that CCDs are not perfect photon detectors. This imperfection means that pixels can vary in sensitivity across the array. We correct for this variation by normalizing, or flattening, the data. Additionally, CCDs are not completely cleared of their information after readout, which means that each exposure starts with a certain amount of signal. We call this "pre-charge" is called the readout bias. Sometimes a region of the CCD called the "overscan" is used to correct for this readout noise. A cartoon layout of a CCD is shown in figure 5.1.

When dispersed photons[1] hit the detector, they are mapped to the 2-D array, the mapping of light intensity, location along the spectroscopic slit (1 dimension), and wavelength (orthogonal dimension to slit location) is not perfectly aligned with the pixels. We usually correct for this distortion by fitting the continuum (track of illuminated pixels) of a standard star as a function of pixel location (Marsh, 1989;

---

[1] Like a rainbow.

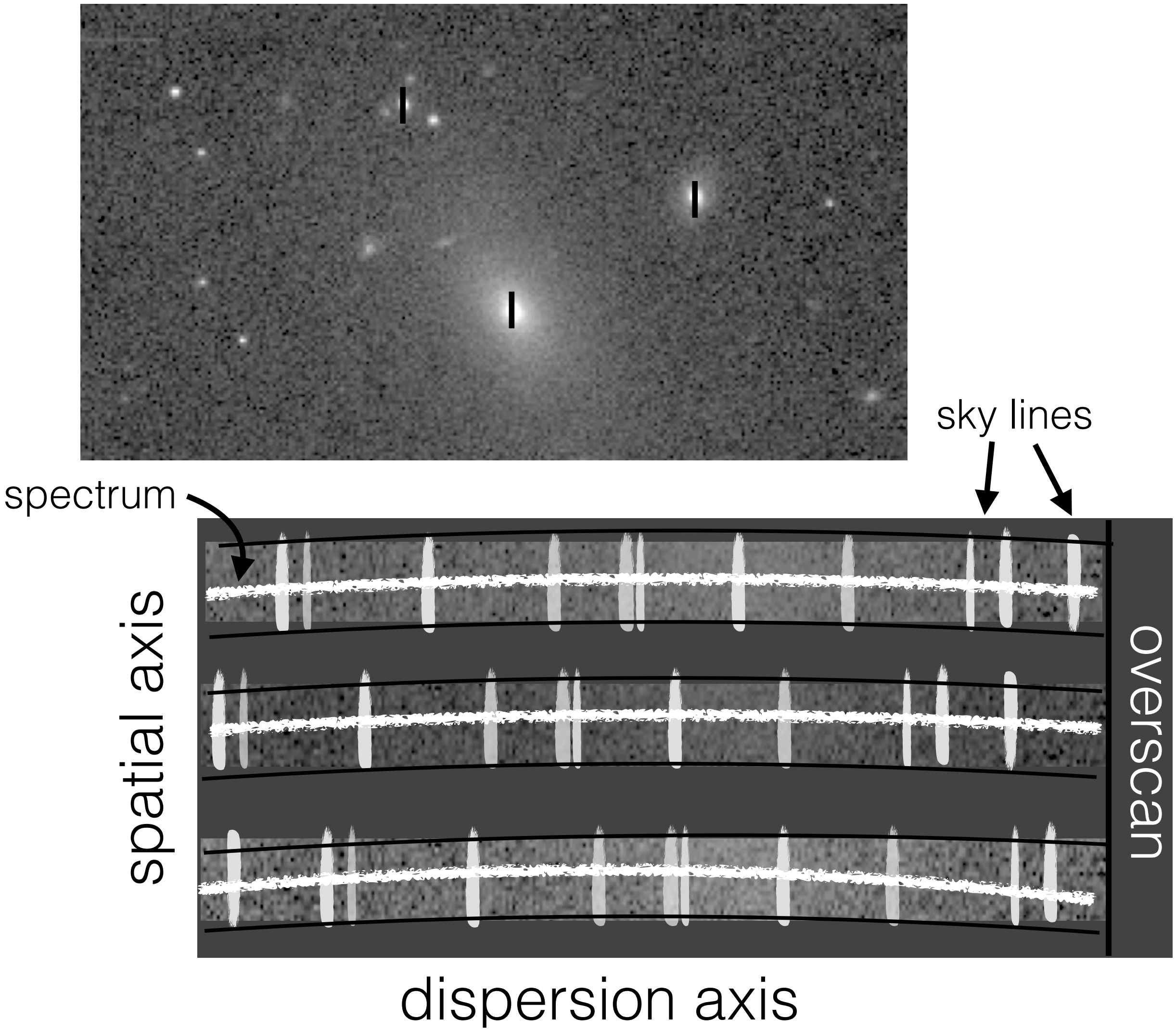

Figure 5.1 Simplified depiction of multi-object spectra. Sky light is also dispersed and appears as emission lines on either side of the spectrum. The lines are the same in each spectrum, but shift depending on slit position.

Horne, 1986). This spectrum trace, shapes measured at different slit positions, can be used to rectify the corresponding science images. Once the correction is applied to the 2-D spectrum, we collapse it to one dimension for wavelength calibration. Wavelength calibration involves converting pixel coordinates of the 1-D spectrum to wavelength coordinates based on characteristics of the spectrum grating.

Because each instrument comes with its own systematics, image reduction is rarely a cookie-cutting exercise, and spectral tracing and wavelength calibration are particularly difficult and tedious. Thus far, the Image Reduction and Analysis Facility (IRAF) (Tody, 1986, 1993)) has been the only reduction package with enough robustness and versatility to make it the go-to spectroscopic data reduction source for nearly 30 years. However, the command language (CL) in which IRAF is written has been unable to keep up with more versatile languages such as Python. IRAF's imminent demise is a source of worry, and there have only been a few efforts made to start the transition to a new generic reduction package (Lucas et al., 2018; Price-Whelan et al., 2018). The goal of the SRP is to have a complete spectral reduction package for SAMOS data which is completely independent of IRAF.

5.1 Pipeline Organization

The SAMOS reduction pipeline is meant to be run within a *Jupyter* notebook, as it allows for the user to track the reduction progress. Begin each new session with the execution of the `SAMOSNight` class. This class stores the data and information for a particular night (defined by some observation ID), which is updated with each step of the data reduction. The current capabilities of the SAMOS pipeline are summarized in table 5.1, and each step is further described in the sections below. Each section is prefaced by the code used to execute the step. The code represented in this chapter is from the tutorial `jupyter_NBtutorial/SAMOS_tutorial`.

Major updates for this pipeline will occur when we obtain test data from the SAMOS instrument. It should therefore be noted that some parts of the pipeline in its current state employ more generic data reduction methods, with the plan that more sophisticated methods can be chosen and applied once the actual parameters of the operational system are better known. Until then, we have adapted some working assumptions about the performance of the spectrograph which may differ from its actual performance. For instance, the pipeline assumes that the spectrum will not perfectly co-align with the rows and columns of the detector, the data have an overscan region which can be used for bias calibrations, and that other calibrations such as arc lamp exposures can be taken in the afternoon or during the night. The methods used for SAMOS data anaysis are heavily influenced by the Goodman Spectroscopic Pipeline (Torres-Robledo & Briceño, 2019) and the Astropy image reduction package `ccdproc` (Craig et al., 2017).

The working directory for SRP contains the following required files and directories:

Table 5.1 Current status of the SAMOS reduction pipeline. Each row describes a step in the data reduction process, its current completion status, and the planned updates for accomodating SAMOS data. Each step's current status is in reference to its processing of the Goodman test data.

Reduction Step	Step Description	Current Status	Planned Updates
`SAMOSNight(...)`	initialize pipeline and organize raw data	complete	This will eventually include the ability to make SQL queries for SAMOS data stored on a separate server
`ImageProcessor(...)`	image trim, overscan, flat correction	complete	add bias level correction using bias frames
`SlitBuckets(...)`	trace and crop individual slits	complete	slit tracing method will need to read SAMOS slit mask patterns from the FITS headers
`WaveCalBuckets(...)`	fits wavelength solution using comparison lamp data	complete	linelists for first-guess solutions will refer to those obtained from calibration lamps observed with SAMOS
Spectral Extraction	extract source spectrum from slit	in progress	method will outline and crop out main spectral source
Sky Subtraction/Flux Calibration	subtract sky contribution from spectrum	in progress	

- `UNCOMP_GDMN_DATA/`: directory containing Goodman observations.
- `SAMOS_DRP/`: directory containing main pipeline modules.
- `comp_refs/`: directory containing linelists and wavelength solutions for comparison lamps in every spectroscopic configuration.
- `slit_refs`: text file containing manually selected slit edges used as a first-guess when cropping slit data.
- `SAMOSenv.yml`: independent environment file which contains the packages necessary to run the pipeline.

5.2 Step 0: Pipeline Initialization

```
from SAMOS_DRP.SAMOS_NIGHT import SAMOSNight

SAMOS_setup = SAMOSNight(obsid='',
                         raw_data_dir='',
                         proc_dir='',
                         LOG_FILENAME='',
                         ignore_flats=False,
                         ignore_bias=True)
```

Listing 5.1 The above listing is the first step of the SAMOS reduction pipeline. This step initializes the data from a night of observations and by gathering header information and sorting the image files.

The SAMOS pipeline is initialized via when the user executes the code shown in listing 5.2, where obsid is the observation ID corresponding to the night on which the data were observed, raw_data_dir is the directory containing the raw observation data, proc_dir is the directory for storage of pipeline results, LOG_FILENAME is the name of the .log file (if a file of the same name exists it is overwritten), ignore_flats gives the option to apply a flat field correction, and ignore_bias tells the pipeline whether to include bias correction from a series of zero exposures in the absence of the overscan region.

First, the pipeline makes a directory for the data products and checks the files in raw_data_dir. Data are stored as *FITS* (Flexible Image Transport System) (Wells et al., 1981) files, which store digital information in the form of multi-dimensional arrays. *FITS* is the "standard" archival data format for astronomers because it is able to store (and transfer) astronomical data that is completely self-contained. A typical *FITS* file has a primary header and data unit (*HDU*) extension, which is split into two arrays. The first array contains the top-level meta data for the exposure and is called the primary header. The primary header stores the information about an image in the form of keywords (observation date, target coordinates, exposure time, etc.) The second array usually contains the main data, but may be empty in a new *FITS* file. They may also contain multiple other extensions, where each extension shares the same primary header information, but the local header contains information specific to that extension's data (more information on *FITS* files can be found in Pence et al. (2010)).

The pipeline sorts the observations depending on exposure type (e.g. BIAS,FLAT,OBJ) by reading the *FITS* headers. Once the data is organized, the user can view the main information by executing SAMOS_setup.data_buckets, and check that the data has been sorted properly. Each subsequent reduction step inherits the attributes of the previous step. Whenever something is done to the data, a new *FITS* file is created. To keep track of what procedures were already performed, the intermediate products have the same base file names as their raw data, but with a new letter based on the intermediate step (e.g. trimmed+bias-corrected ∼ to_fname.FITS).

The code reads the FITS headers and creates arrays which separate the data into flats, comparison lamps, and science data. Information for a night of observations is organized into a `pandas.DataFrame` called a 'night_bucket'. This bucket object is further divided into the following main data reduction buckets:

- Bias frames: not currently implemented because bias in the Goodman test images is accounted for via the overscan region, but these frames also can be used to verify the gain setting and can verify that the 2-d bias is "quiet".
- Flats: quartz flats to characterize nonuniformity in CCD pixel sensitivity.
- Comparison lamps: Arc lamp exposures for wavelength calibration.
- Science/Comparison pairs: Object exposures and the corresponding comparison lamps.

5.3 Step 1: CCD Image Processing

```
from SAMOS_DRP.ImageProcessor import ImageProcessor

SAMOS_ccd_proc = ImageProcessor(SAMOS_setup)
SAMOS_ccd_proc()
```

Listing 5.2 Before spectral analysis, run the above code to remove noise due systematics of the CCD.

The first step in reducing CCD data is to account for systematic effects during data acquisition and readout. CCDs are made of pixels which are sensitive to specific photon energies. Electrons in the pixel become excited by incoming light, and that charge is read out by the CCD. Every observation contains a bias level due to a combination of the camera noise from the readout process and electric "pre-charge" on a

CCD chip by the electronics. Bias-subtraction and flat correction is executed with the command shown in listing

The pipeline parses the `FITS` data array into regions of bias and target data by reading the `FITS` headers `BIASSEC` and `DATASEC` respectively. The latter section trims the field mask to the correct size.

The `BIASSEC` header gives the region of overscan, which is a series of detector pixels that are shielded from incoming light. An array of this overscan region is made by grabbing the rows and columns from the data array. The function then takes the median (or mean) of the overscan regions along the rows (axis=1), and subtracts these values from each data value in their respective data rows.

$$\begin{pmatrix} cropped & and \\ bias & subtracted \\ data & matrix \end{pmatrix} = \begin{pmatrix} d_{11} & d_{12} & d_{13} & ... & d_{1m} \\ d_{21} & d_{22} & ... & ... & d_{2m} \\ ... & ... & ... & ... & ... \\ d_{n1} & ... & ... & ... & d_{nm} \end{pmatrix} - \begin{pmatrix} [b_1] & [b_2] & [b_3] & [...] & [b_n] \end{pmatrix} \otimes \begin{pmatrix} 1 \\ 1 \\ ... \\ ... \\ 1 \end{pmatrix} \tag{5.1}$$

Flat field images are used to characterize the variation in pixel sensitivity across the detector. During this step, each flat is scaled by its median so that the average pixel correction is 1. This normalization allows the statistics of the image to be maintained without having to pass along the details of the flat. The data are then median-combined to create the master flat. Finally, the pipeline divides the master flat from the science images. Examples of output of the pipeline through the first few steps are shown in figure 5.2.

5.4 Step 2: Slit tracing and extraction

```python
from SAMOS_DRP.SlitBuckets import SlitBuckets

SAMOS_slits = SlitBuckets(SAMOS_ccd_proc)
SAMOS_slits()
```

Listing 5.3 This step crops each of the slits based on edges found by tracing the master flat. This method should work no matter how the instrument performs, but we anticipate the instrument will produce very reliable maps of DMD position to instrument (x,y) position without any variation, so this step might not even be necessary in practice.

SAMOS is designed with a large Digital Micromirror Device (DMD). The mirrors can be selected to direct light to a spectrograph arm or an imaging arm, with the slit configurations stored in the `FITS` headers for each exposure and accessible to the pipeline upon instantiation. The current version of this pipeline uses data acquired from *Goodman* using multi-slit masks made in advance of the observation. The most exciting

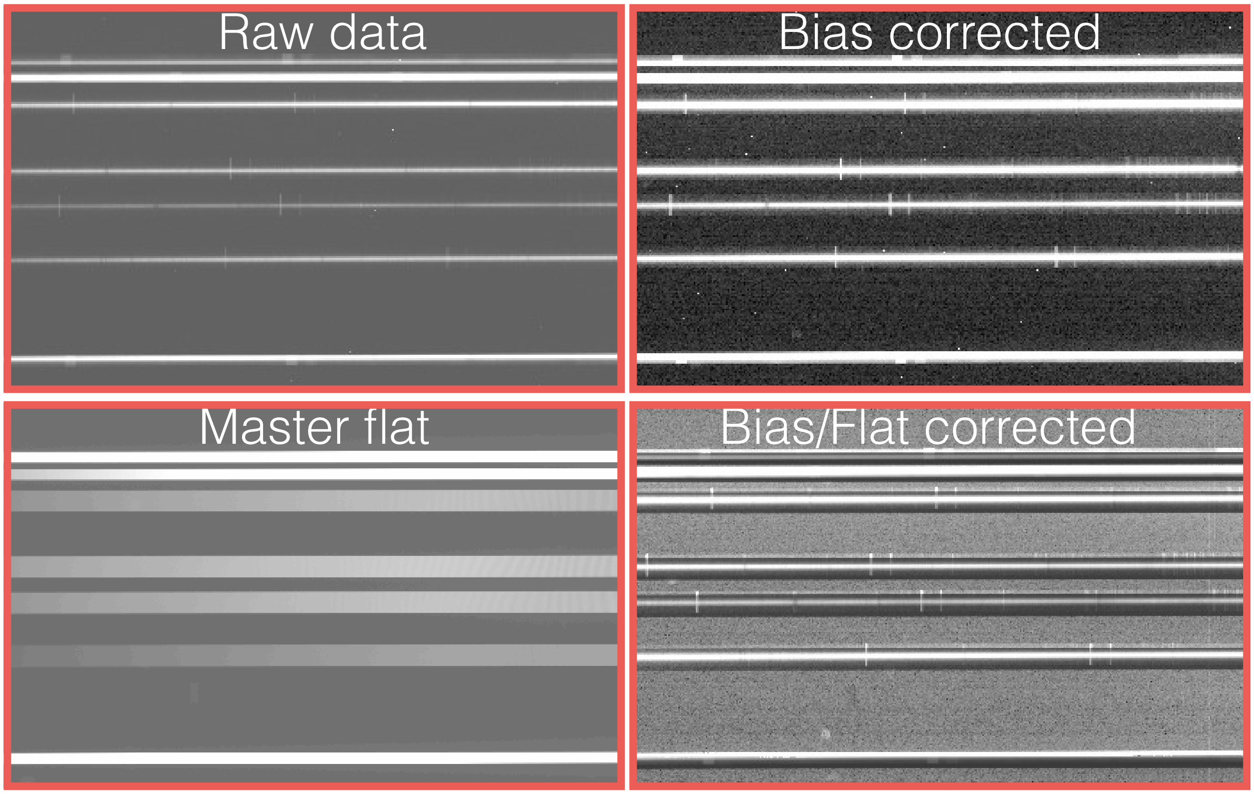

Figure 5.2 Data output after initial pipeline steps for CCD reduction. The raw data is in the upper left. (make better image and caption)

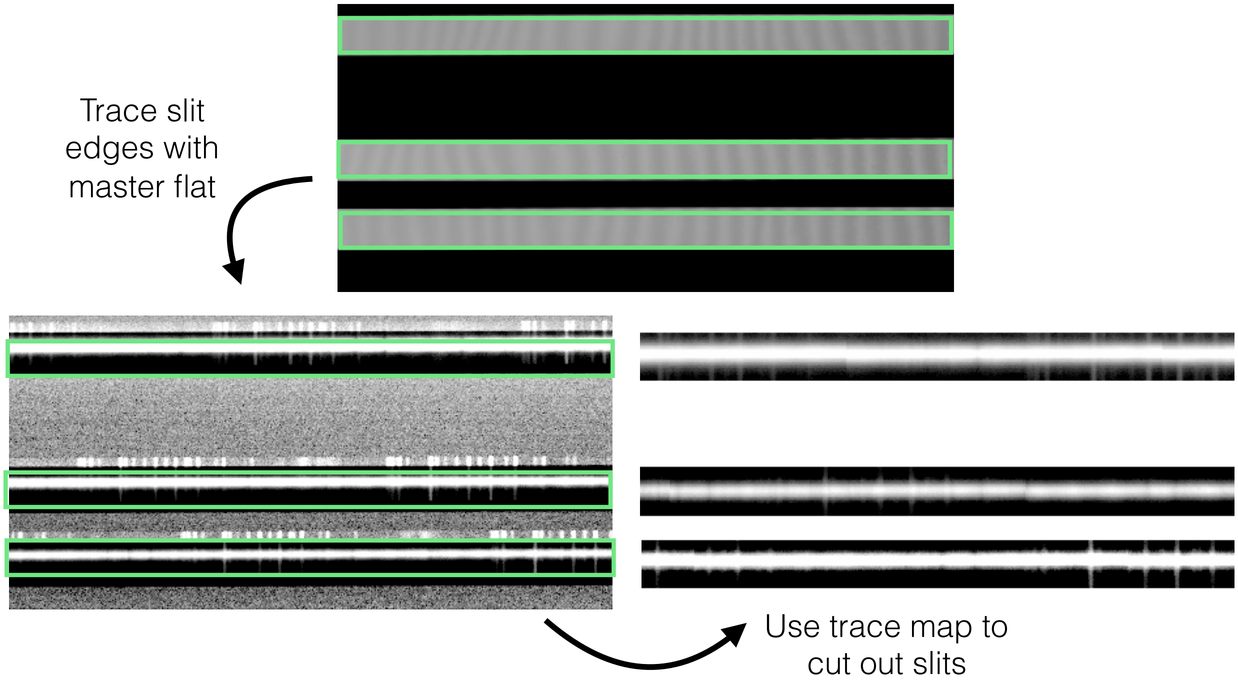

Figure 5.3 Simplified version of slit tracing and extraction. The master flat (*top*) is used to find the slit edges, then a map of the pixel coordinates is applied to the science exposures (*lower left*) exposures. Each slit is saved as a new FITS image which is ready to be wavelength calibrated (*lower right*).

feature of SAMOS will be its ability to create slit patterns in real time and save them the `FITS` header for easy retrieval by the pipeline. Therefore, the slit location procedure is somewhat brute force as it will replaced for analysis of SAMOS data.

The method for identifying and excising individual slits from the images uses a manually made text file of pixel locations. The mask reference file `slit_refs` contains the y-pixel values for the top middle edge of each slit, obtained by inspection from the master flat file[2]. These reference pixels provide a first guess for the pipeline to map out the slit edges by calculating peaks in the difference of pixel intensity. The mask template is used to crop and pair the individual slits for the science and calibration lamp exposures. The cropped images are stored in new directory corresponding to each slit number. The output of this procedure is shown in figure 5.3.

5.4.1 Note on spectral extraction and tracing

As mentioned above, the development version of the pipeline does not deal with spectral extraction as robustly as it will in the future. Once each slit is cut out and saved as its own FITS file, instead of fitting

---

[2] The master flat provides the greatest contrast between the illuminated and non-illuminated sections of the detector. The SAMOS instrument team is developing a calibration from DMD to detector that will be verified during engineering testing at SOAR. We hope it goes well and turns out to be robust. Otherwise, the code described here can implement it as a first-guess.

the spectrum to a function based on the (minor) tilt with respect to the spatial axis, the pipeline takes sections of the slit and aligns them for a quick look at the pipeline progress. The crop-and-move alignment is adequate for testing purposes, as the spectra from *Goodman* are relatively well-behaved with respect to more extreme spatial distortions. A one-dimensional spectrum is “extracted” by taking the middle few rows of a spectrum and using their median to collapse them to a single row. This spectral extraction is a very crude method and only for the purposes of testing. In the future, the SRP will fit a function to characterize the layout of the spectrum over pixel coordinates. More information about the spatial distortion of spectra can be found in Marsh (1989) and Horne (1986).

5.5 Step 3: Wavelength calibration

```
from SAMOS_DRP.DoWavecal import WaveCalBuckets

SAMOS_wavecal = WaveCalBuckets(SAMOS_slits)
SAMOS_wavecal()
```

Listing 5.4 Wavelength calibration is the final step of the pipeline. This step uses pairs of calibration lamp and science exposures to emission lines from the

Each science exposure is paired with a calibration lamp. Calibration lamps, or arc lamps, are comprised of gas with emission lines which have been measured in a laboratory setting. Calibration lamp exposures are taken during the observing night so that each science spectrum is calibrated to the correct grating/filter setting. Each slit in the mask is paired with its own set of arc lamp exposures. Therefore, we must choose an arc lamp that features emission lines that are also present in the science spectrum.

The angular dispersion of a grating is the change in angle of diffraction per change in wavelength (Å/arcsec). The simple diagram in figure 5.4 shows how a spectrum is produced. The main source of light passes through a slit and is dispersed by a diffraction grating, after which the spectrum is projected onto the CCD. The angular dispersion is related to linear dispersion by the plate scale (arcsec/pixel). Therefore, the solution requires us to compare the linear pixel distance between emission lines in the uncorrected arc lamp exposure to change in wavelength $\Delta\lambda$. It should be noted that the wavelength calibration for the SAMOS pipeline is not original code and it performs the fit using procedures from the GSP (Torres-Robledo & Briceño, 2019). The SAMOS pipeline will be updated to work with real SAMOS data in the future, with the GSP code as a solid foundation. The GSP simplifies the wavelength calibration process with a library of reference lamps with wavelength solutions for multiple grating/filter configurations which have already been calibrated. The use of a pre-fitted calibration spectrum means that the lines only need to be identified once, and then applied to future spectra.

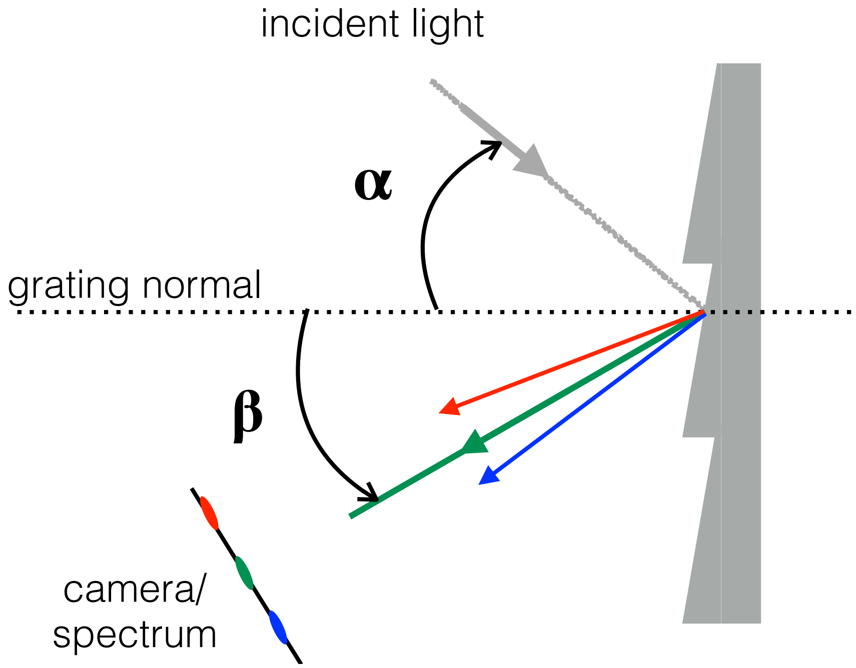

Figure 5.4 Simplified depiction of how source light is dispersed by a diffraction grating and becomes a spectrum.

For a given arc lamp, the pipeline steps along the dispersion axis and collects pixel locations for lines which meet a certain count threshold. We are fitting to a model that matches a linear pixel distance from a central point to a change in wavelength. However, the mapping between pixels and wavelength is not necessarily linear, and the linear approximation can break down if the spectrum is distorted. Finding the coefficients for the non-linear model is made simpler with a low order first-guess solution from the reference arc exposure. The pre-fitted reference lamp contains a list of emission lines with their pixel and angstrom values, along with its best fit solution is stored as the coefficients of a polynomial model[3]. With the approximate wavelength solution, the pipeline interpolates over the locations of the known lines to estimate wavelengths of the unknown features in the spectrum. Once we have a pixel-to-angstrom map, we can convert the dispersion axis in the science exposures from pixels to angstroms. An example of the final wavelength calibrated spectrum is provided in figure 5.5.

5.6 Remaining steps

While the pipeline is able to produce a wavelength calibrated spectrum for the test data, there is still much to be done before SAMOS is commissioned in 2021, and development of the pipeline is ongoing. The remaining

---

[3] The current pipeline version is only able to handle a Chebyshev1D model from astropy.models, but will be expanded in the future.

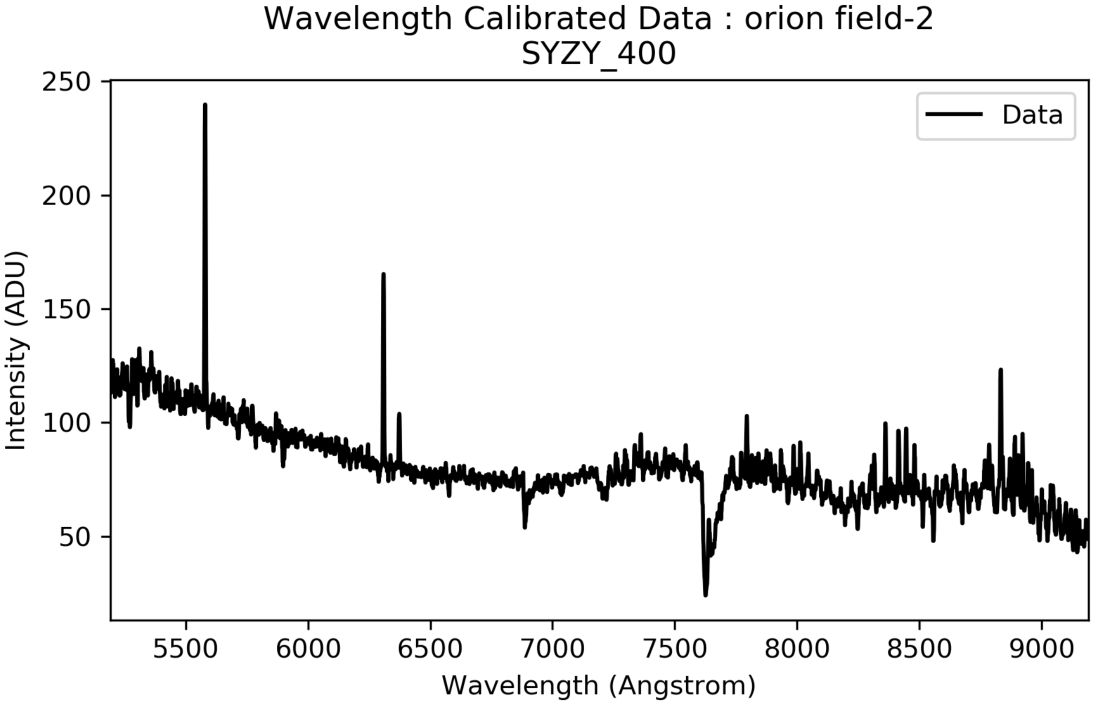

Figure 5.5 Final wavelength calibrated spectrum for extracted slit. Spectrum does not include background subtraction or flux calibration.

high priority reduction steps are described below.

- Flux calibration: The flux of an object is captured by the CCD in photon counts. Because CCDs have different sensitivities across their pixels, the pipeline will need to fit produce a fit to the sensitivity function and scale the photon counts to units of magnitude. Flux calibration will use the continuum emission for a standard star exposure.

- Background subtraction: Spectra contain emission from the sky within the line of sight of an object. This background emission needs to be subtracted from the science spectra. One technique for sky subtraction is nod-and-shuffle, wherein the source is shuffled between the lower edge of a slit and the upper edge. By having spectrum cover different regions of the slit, the sky emission at the opposite end can be characterized to a higher degree of accuracy.

- Tracing/Spectral extraction: As mentioned previously, spectra can be distorted with respect to the spatial axis. Currently, the SRP uses a crude method of spectral extraction which will be updated to include a routine that traces the distortion, and then extracts a spectrum based on that trace.

In addition to the remaining data reduction procedures, the SRP will include a suite of settings such that user will be able to have more control over what data is reduced and how. Right now, the user only has the options to name the directory of the data output, and whether to include flat or bias correction. A future version will include options to choose specific types of exposures, places to pause and restart the pipeline, and other features that allow the user to customize their data reduction. Before $SAMOS$ is taken to $SOAR$, we plan to test the pipeline using simulated spectroscopic data from $SAMOS$. The test data from *Goodman* will therefore be replaced with simulated data from $SAMOS$, which should make the transition from testing to science even easier.

$SAMOS$ will be an exciting addition to the $SOAR$. As a multi-object spectrograph, it will allow an observer to take spectra of multiple targets within a single exposure, which is particularly useful for observations of galaxy clusters. $SAMOS$ will be able to maximize the its multi-object capabilities, as it will be able to create a number of slit mask patterns throughout the night. This key aspect makes $SAMOS$ a highly anticipated instrument, and it has received a no-cost extension and access to reserve funds to aid in completion by Summer, 2021. We have been able to build a strong foundation for the $SAMOS$ pipeline using methods from the *Goodman* pipeline (Torres-Robledo & Briceño, 2019) and data reduction packages provided by Price-Whelan et al. (2018), and we are actively making progress towards completion.

6 Conclusion

In this dissertation, we used X-ray observations of galaxy clusters from the Archive of Chandra Cluster Entropy Profile Tables (ACCEPT2.0) to show their effectiveness as tools for studying properties of the intracluster medium (ICM). In chapter 2, we showed that ACCEPT2.0 global properties measured in the aperture [0.3-1]R_{2500} are able to adequately remove bias due to core emission by showing that the scatter in the $L_X - T$ relation is reduced when fit with core-excised quantities. Our $L_X - T$ results were also shown to be consistent with previous works, and therefore confirms our confidence in the quality of our data.

Sticking with the theme of the $L_X - T$ relation, chapter 3 used the core-excised luminosities and temperatures to test recent challenges by Migkas et al. (2020) to cosmology. We showed that our data support the generally accepted assumption of spatially isotropic expansion of the Universe by fitting the $L_X - T$ relation to subsamples of ACCEPT2.0 clusters towards different regions of the sky. We suspect that differences between ours and the results of Migkas et al. (2020) is likely due to systematic differences in the data, rather than a different cosmological model. Our conclusions are supported by the fact that no other tests of expansion have suggested the large anisotropies reported by Migkas et al. (2020).

Chapter 4 discusses the dependence of cluster metallicity with factors such as cluster core status, luminosity, and redshift. We showed that CCs and NCCs have different radial metallicities in their cores (CCs more peaked, NCCs with flatter profiles), but the core metallicity does not affect the global core-excised abundance of a cluster. Our core-excised global metallicity estimates between CCs and NCCs were shown to be nearly identical. The similarity between CCs and NCCs outside of $0.3R_{2500}$ is in agreement with recent observations and theoretical models which suggest that thermodynamics affecting the distribution of metals in the ICM is mostly constrained to the cluster core, where the gas is more influence by the active galactice nucleus (AGN) than the cluster gravitational potential.

Finally, in chapter 5, we introduced a data reduction pipeline for the SOAR Adaptive-optics Multi-Object Spectrograph (SAMOS). While the SAMOS instrument will not be commissioned until 2021, we show that the pipeline has a strong foundation based on the *Goodman* Spectroscopic Pipeline (GSP, (Torres-Robledo & Briceño, 2019)) and data reduction methods provided by Price-Whelan et al. (2018). SAMOS will be advantageous for optical spectroscopic observations of galaxy clusters because of it‘s ability to make new slit masks in real-time.

6.1 Future work

The matter content of the Universe is an essential part of our cosmological model. As the most massive and recently formed structures in the Universe, galaxy clusters hold key information as to how small clumps of dark matter in the early Universe eventually grow into the structures we see today, and the time scales over which these structures evolve. Our understanding of galaxy clusters and their relation to this cosmic growth and evolution is driven by collaboration and the sharing of data. As a publicly available catalog with nearly ~ 400 citations, the original ACCEPT project (Cavagnolo et al., 2009) has already helped to improve our understanding of the entropy evolution of a cluster, and the relationship between AGN and the gas in the ICM. With over twice the number of clusters and an expanded suite of X-ray observable properties, we anticipate that we will be able to learn even more about clusters with ACCEPT2.0.

We have shown how aspects of large-scale structure formation and evolution can manifest in the X-ray observables of clusters through the use of ACCEPT2.0, and their agreement with recent observations and theoretical models within the redshift range of our sample. We will also be able to compare X-ray properties from ACCEPT2.0 to optical properties of clusters, including spectroscopic observations of clusters with $SAMOS$. Once public, we hope others will be able to use ACCEPT2.0 to provide even better constraints for our cosmological model.

APPENDICES

Appendix A Bolometric and K-correction procedure

The code below shows the procedure used for making corrections to bolometric and rest-frame fluxes and luminosities. The code reads in a .CSV file with the names, redshifts, temperatures, and metallicities of the clusters. Then it simulates observed fluxes for each cluster, along with the bolometric and rest-frame luminosities. The main procedure is described in chapter 2.3. Below shows the *XSPEC* code used to simulate the observed fluxes and luminosities used to compute the correction factors.

```
# set cosmology to H0=70 q0=-0.55 Omega_Lambda=0.7
cosmo 70 -0.55 0.7

# set energy grid to cover a large range
energies 0.05 100.0 10000 log

set outfile [open outfile w+]

set f [open nocore_lumcorr_input] #read in cluster data from file
set lines [split [read $f] ``\n'']
close $f

puts ``$lines''

# make simulated spectra
foreach row $lines {

  set line [split $row ``,'']
  set name [lindex $line 0]
  puts ``name is $name''
  set z [lindex $line 1]
  puts ``redshift is $z''
  set T [lindex $line 2]
```

```
set Zsol [lindex $line 3]

puts ‘‘kT, Zsol, z is $T, $Zsol, $z’’

# set mekal model params kT, nH, Zsolar, redshift, Switch,
   Normalization
model mekal
$T #set temperature
1.0
$Zsol
$z
1
1.e-4

# store the first number in the string from tclout
# into variables fluxout,lum05_70,lum_bol
flux 0.5 7.0
tclout flux
set fluxout [string range $xspec_tclout 0 [string first ‘‘ ’’
   $xspec_tclout]]
lum 0.5 7.0 $z
tclout lum ;
set lum05_70 [string range $xspec_tclout 0 [string first ‘‘ ’’
   $xspec_tclout]]
lum 0.1 100.0 $z
tclout lum
set lum_bol [string range $xspec_tclout 0 [string first ‘‘ ’’
   $xspec_tclout]]

# save kT, Zsol, z, fluxout, lum05_70, lumbol to file
# Luminosities are in units of 1e44 erg/s
```

```
  puts $outfile ‘‘$name,$T,$Zsol,$z,$fluxout,$lum05_70,$lum_bol’’  ;
  # writes line to file
}
close $outfile
```

Listing A.1 *XSPEC* script used to apply bolometric and K-corrections to ACCEPT2.0 data.

The simulated fluxes are read in from the *XSPEC* results and used to compute an observed luminosity with $L \propto F((1+z)d)^2$, where F is the flux and d is the co-moving or Hubble distance of the cluster (section 1.2.1). Then we create the correction factor for each cluster as the ratio of the corrected-to-observed luminosity (and correction type) in the simulated clusters. These correction factors were multiplied by the observed luminosities in the real data. Below shows the general code used to compute the corrected luminosity for each cluster. This version has been simplified to show the main parts.

```
import numpy as np
import cosmocalc as cosmo
import pandas as pd

H0 = 70
WM = 0.3

SIMdata = pd.read_csv(sim_file)
A2data = pd.read_csv(ACCEPT2.0_data)

cosmo = cosmocalc(A2data['z'],H0,WM,1-WM)


DL = cosmo['DL_cm']


sim_flx = SIMdata.loc['fluxout'] #simulated flux
sim_restlum = SIMdata['rest_lum']
sim_bollum = SIMdata['bol_lum']

sim_obsLum = (sim_flx*4*np.pi*DL**2)/1e44

uncorr_lum = A2data['Lx'] #uncorrected luminosity and error from ACCEPT2.0
uncorr_lumerr = A2data['Lxe']


r_corr = sim_restlum/(obsLum) #correction factors from simulated data
b_corr = sim_bollum/(obsLum)

newLx_rest, newLx_restErr = uncorr_lum*r_corr, uncorr_lumerr*r_corr #multiply by
     observed luminosities
newLx_bol, newLx_bolErr = uncorr_lum*b_corr, uncorr_lumerr*b_corr
```

Appendix B ACCEPT2.0 Radial Metallicity Profiles

Radial metallicity profiles for 154 ACCEPT2.0 clusters. (For a description, see chapter 2.)

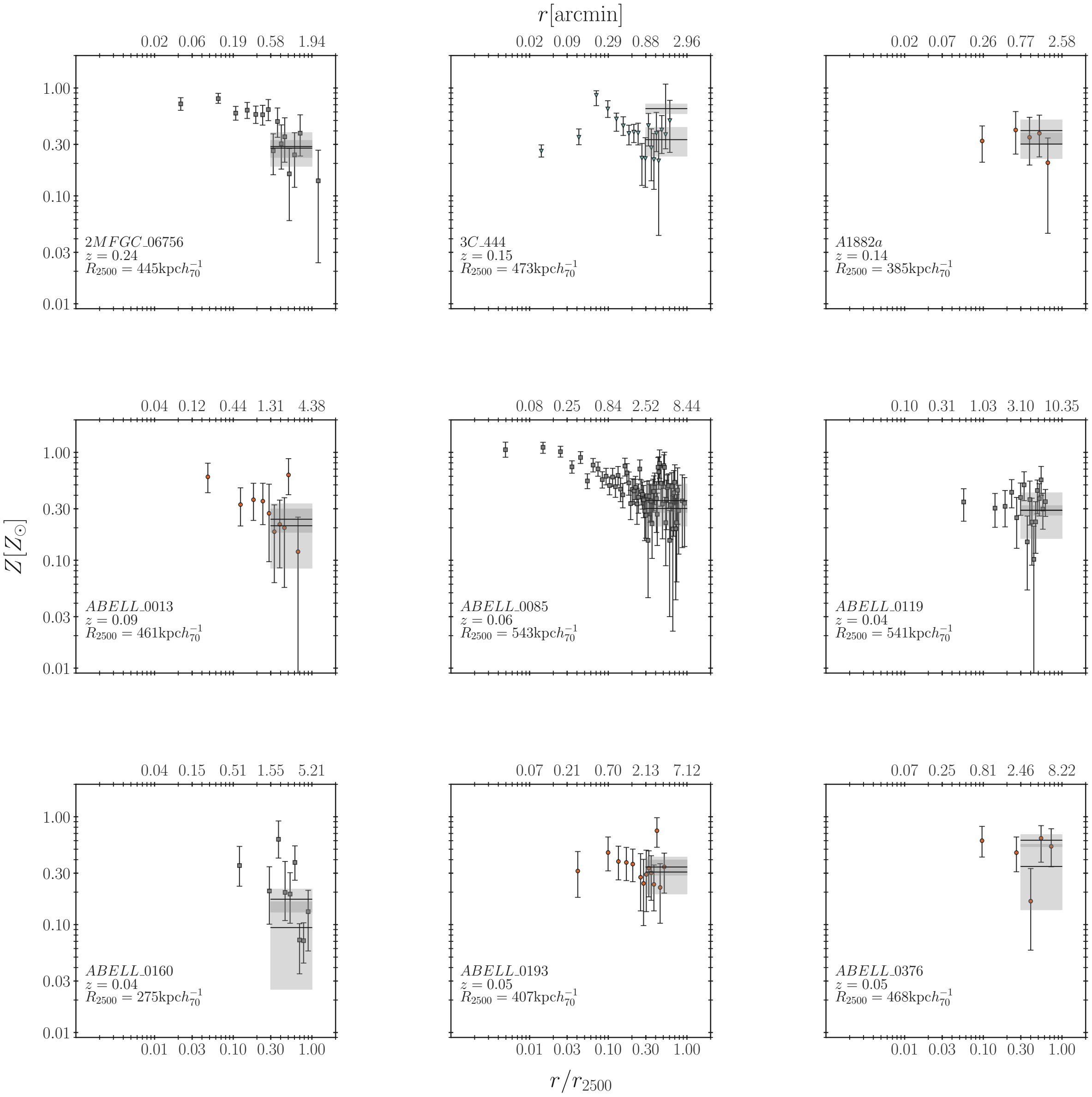
r[arcmin]
0.02 0.06 0.19 0.58 1.94
0.02 0.09 0.29 0.88 2.96
0.02 0.07 0.26 0.77 2.58
0.04 0.12 0.44 1.31 4.38
0.08 0.25 0.84 2.52 8.44
0.10 0.31 1.03 3.10 10.35
0.04 0.15 0.51 1.55 5.21
0.07 0.21 0.70 2.13 7.12
0.07 0.25 0.81 2.46 8.22
$Z[Z_\odot]$
1.00
0.30
0.10
0.03
0.01
$2MFGC\_06756$
$z = 0.24$
$R_{2500} = 445\mathrm{kpc}h_{70}^{-1}$
$3C\_444$
$z = 0.15$
$R_{2500} = 473\mathrm{kpc}h_{70}^{-1}$
$A1882a$
$z = 0.14$
$R_{2500} = 385\mathrm{kpc}h_{70}^{-1}$
$ABELL\_0013$
$z = 0.09$
$R_{2500} = 461\mathrm{kpc}h_{70}^{-1}$
$ABELL\_0085$
$z = 0.06$
$R_{2500} = 543\mathrm{kpc}h_{70}^{-1}$
$ABELL\_0119$
$z = 0.04$
$R_{2500} = 541\mathrm{kpc}h_{70}^{-1}$
$ABELL\_0160$
$z = 0.04$
$R_{2500} = 275\mathrm{kpc}h_{70}^{-1}$
$ABELL\_0193$
$z = 0.05$
$R_{2500} = 407\mathrm{kpc}h_{70}^{-1}$
$ABELL\_0376$
$z = 0.05$
$R_{2500} = 468\mathrm{kpc}h_{70}^{-1}$
0.01 0.03 0.10 0.30 1.00
r/r_{2500}

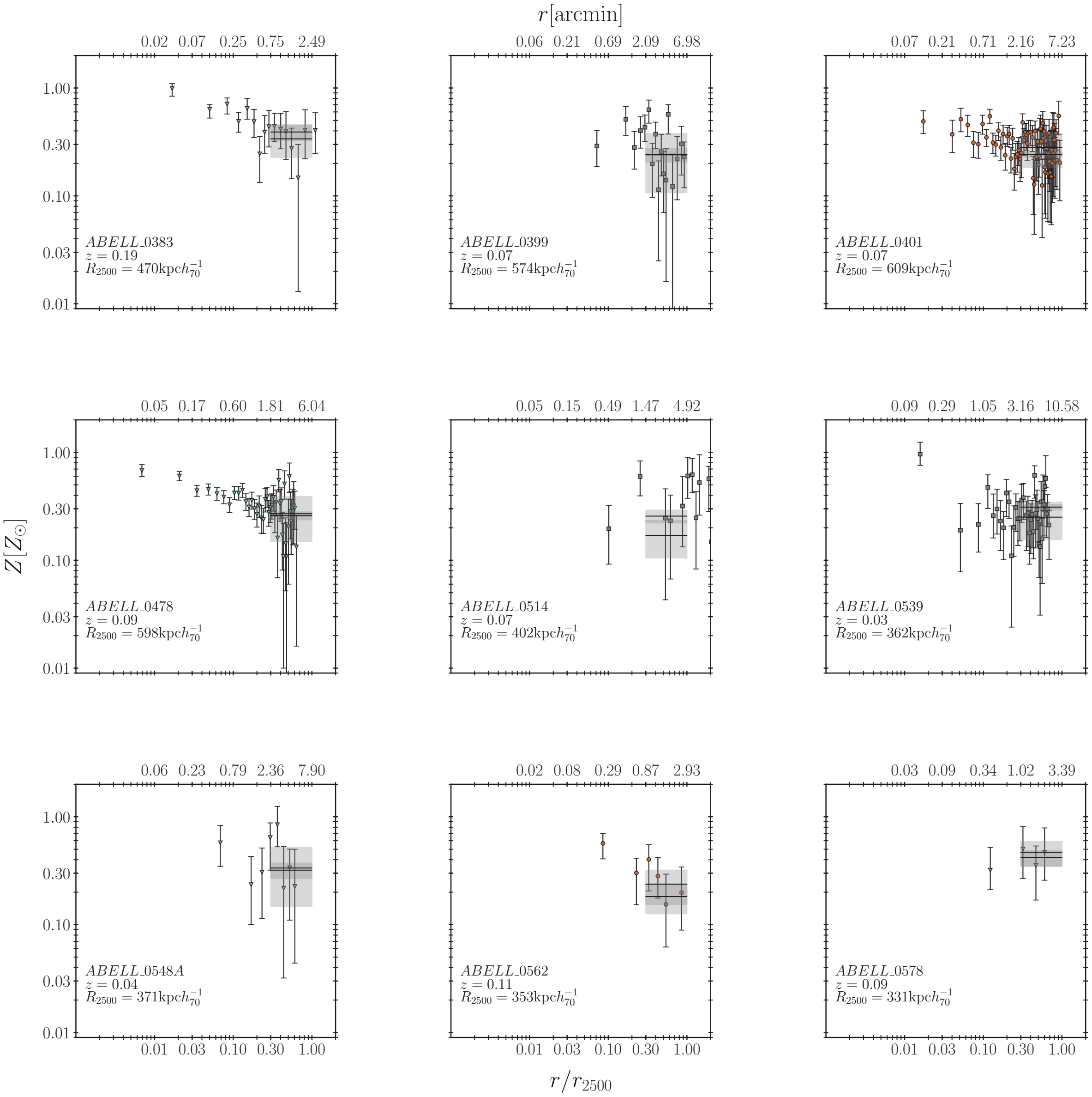
r[arcmin]
0.02 0.07 0.25 0.75 2.49
0.06 0.21 0.69 2.09 6.98
0.07 0.21 0.71 2.16 7.23
$ABELL\_0383$
$z = 0.19$
$R_{2500} = 470 \mathrm{kpc} h_{70}^{-1}$
$ABELL\_0399$
$z = 0.07$
$R_{2500} = 574 \mathrm{kpc} h_{70}^{-1}$
$ABELL\_0401$
$z = 0.07$
$R_{2500} = 609 \mathrm{kpc} h_{70}^{-1}$
0.05 0.17 0.60 1.81 6.04
0.05 0.15 0.49 1.47 4.92
0.09 0.29 1.05 3.16 10.58
$Z[Z_\odot]$
$ABELL\_0478$
$z = 0.09$
$R_{2500} = 598 \mathrm{kpc} h_{70}^{-1}$
$ABELL\_0514$
$z = 0.07$
$R_{2500} = 402 \mathrm{kpc} h_{70}^{-1}$
$ABELL\_0539$
$z = 0.03$
$R_{2500} = 362 \mathrm{kpc} h_{70}^{-1}$
0.06 0.23 0.79 2.36 7.90
0.02 0.08 0.29 0.87 2.93
0.03 0.09 0.34 1.02 3.39
$ABELL\_0548A$
$z = 0.04$
$R_{2500} = 371 \mathrm{kpc} h_{70}^{-1}$
$ABELL\_0562$
$z = 0.11$
$R_{2500} = 353 \mathrm{kpc} h_{70}^{-1}$
$ABELL\_0578$
$z = 0.09$
$R_{2500} = 331 \mathrm{kpc} h_{70}^{-1}$
1.00
0.30
0.10
0.03
0.01
0.01 0.03 0.10 0.30 1.00
r/r_{2500}

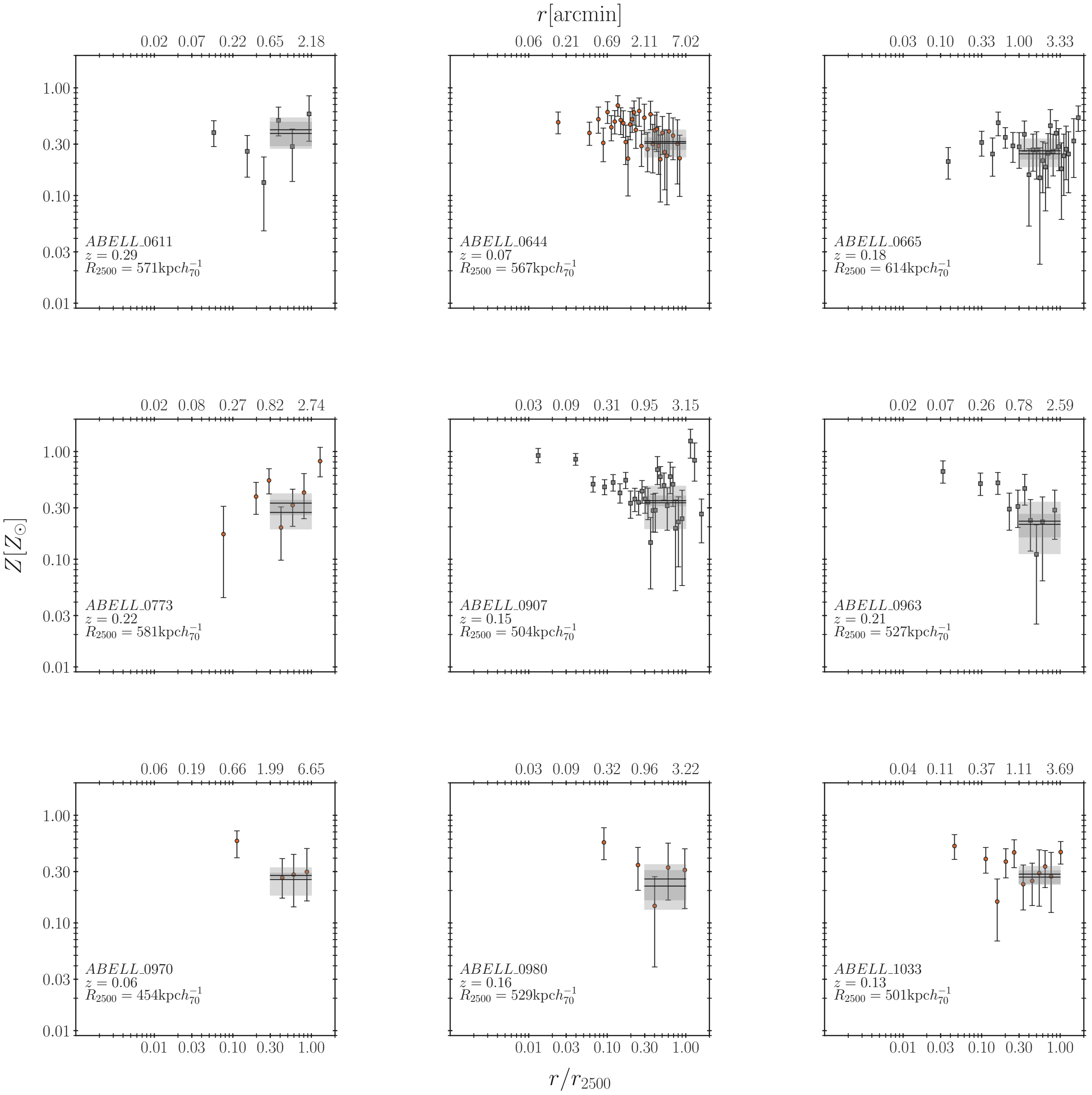
r[arcmin]
0.02 0.07 0.22 0.65 2.18
0.06 0.21 0.69 2.11 7.02
0.03 0.10 0.33 1.00 3.33
0.02 0.08 0.27 0.82 2.74
0.03 0.09 0.31 0.95 3.15
0.02 0.07 0.26 0.78 2.59
0.06 0.19 0.66 1.99 6.65
0.03 0.09 0.32 0.96 3.22
0.04 0.11 0.37 1.11 3.69
1.00
0.30
0.10
0.03
0.01
$Z[Z_\odot]$
ABELL_0611
$z = 0.29$
$R_{2500} = 571\mathrm{kpc}h_{70}^{-1}$
ABELL_0644
$z = 0.07$
$R_{2500} = 567\mathrm{kpc}h_{70}^{-1}$
ABELL_0665
$z = 0.18$
$R_{2500} = 614\mathrm{kpc}h_{70}^{-1}$
ABELL_0773
$z = 0.22$
$R_{2500} = 581\mathrm{kpc}h_{70}^{-1}$
ABELL_0907
$z = 0.15$
$R_{2500} = 504\mathrm{kpc}h_{70}^{-1}$
ABELL_0963
$z = 0.21$
$R_{2500} = 527\mathrm{kpc}h_{70}^{-1}$
ABELL_0970
$z = 0.06$
$R_{2500} = 454\mathrm{kpc}h_{70}^{-1}$
ABELL_0980
$z = 0.16$
$R_{2500} = 529\mathrm{kpc}h_{70}^{-1}$
ABELL_1033
$z = 0.13$
$R_{2500} = 501\mathrm{kpc}h_{70}^{-1}$
0.01 0.03 0.10 0.30 1.00
r/r_{2500}

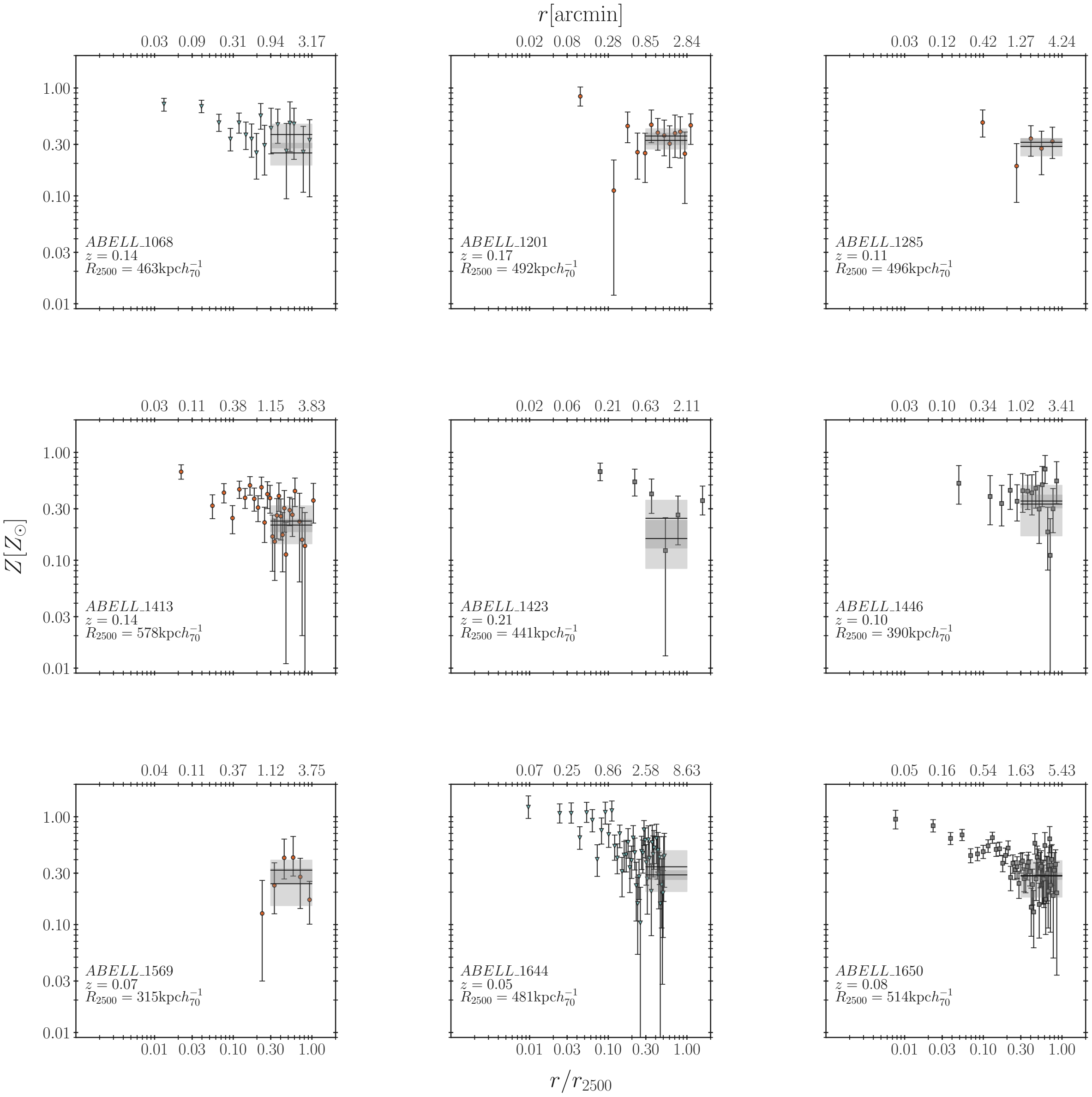
r[arcmin]
Z[Z⊙]
r/r2500
0.03 0.09 0.31 0.94 3.17
ABELL_1068
z = 0.14
R2500 = 463kpch70^-1
0.02 0.08 0.28 0.85 2.84
ABELL_1201
z = 0.17
R2500 = 492kpch70^-1
0.03 0.12 0.42 1.27 4.24
ABELL_1285
z = 0.11
R2500 = 496kpch70^-1
0.03 0.11 0.38 1.15 3.83
ABELL_1413
z = 0.14
R2500 = 578kpch70^-1
0.02 0.06 0.21 0.63 2.11
ABELL_1423
z = 0.21
R2500 = 441kpch70^-1
0.03 0.10 0.34 1.02 3.41
ABELL_1446
z = 0.10
R2500 = 390kpch70^-1
0.04 0.11 0.37 1.12 3.75
ABELL_1569
z = 0.07
R2500 = 315kpch70^-1
0.07 0.25 0.86 2.58 8.63
ABELL_1644
z = 0.05
R2500 = 481kpch70^-1
0.05 0.16 0.54 1.63 5.43
ABELL_1650
z = 0.08
R2500 = 514kpch70^-1
1.00
0.30
0.10
0.03
0.01
0.01 0.03 0.10 0.30 1.00

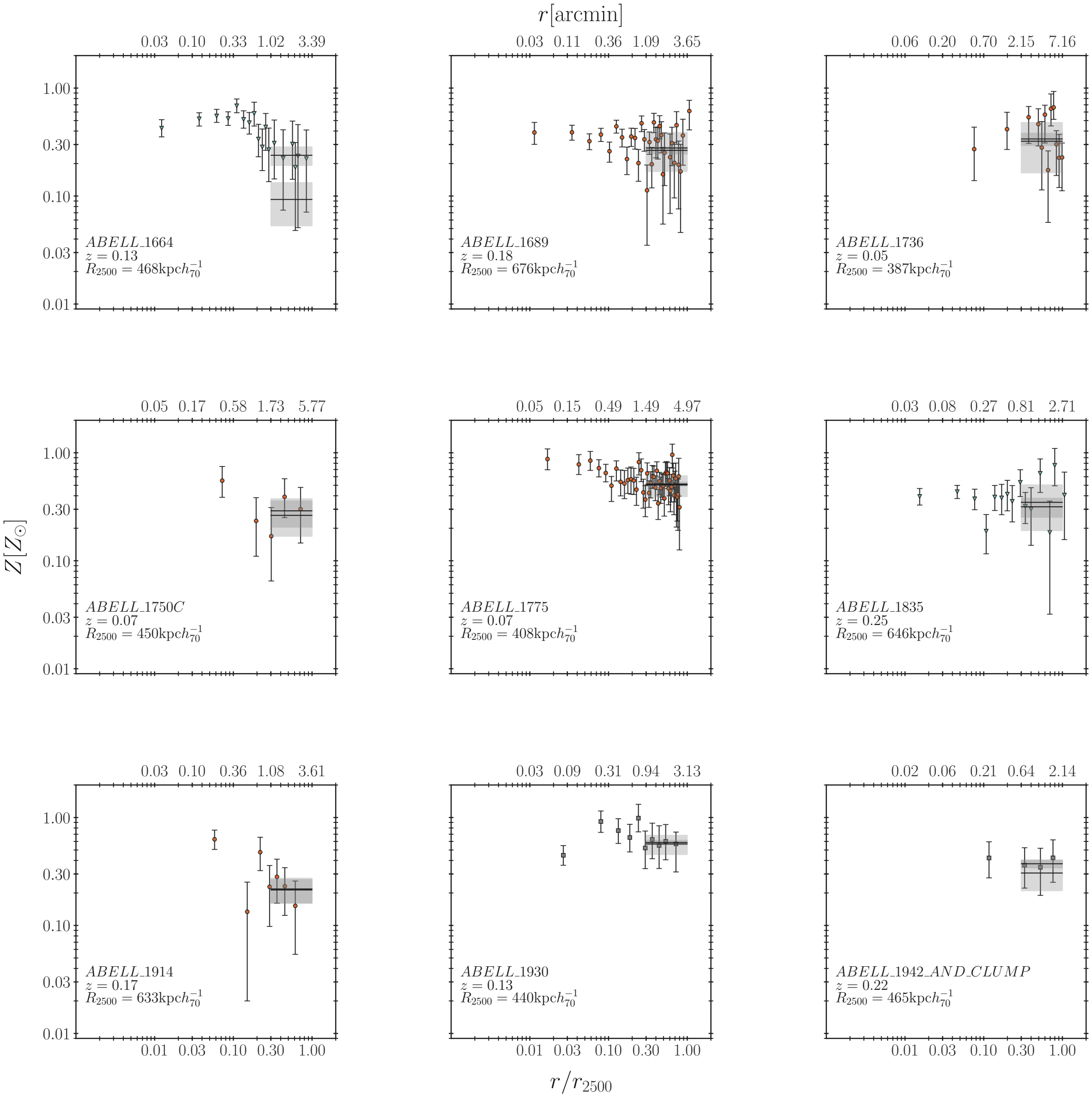

r[arcmin]
$Z[Z_\odot]$
r/r_{2500}
0.03 0.10 0.33 1.02 3.39
$ABELL\_1664$
$z = 0.13$
$R_{2500} = 468\text{kpc}h_{70}^{-1}$
0.03 0.11 0.36 1.09 3.65
$ABELL\_1689$
$z = 0.18$
$R_{2500} = 676\text{kpc}h_{70}^{-1}$
0.06 0.20 0.70 2.15 7.16
$ABELL\_1736$
$z = 0.05$
$R_{2500} = 387\text{kpc}h_{70}^{-1}$
0.05 0.17 0.58 1.73 5.77
$ABELL\_1750C$
$z = 0.07$
$R_{2500} = 450\text{kpc}h_{70}^{-1}$
0.05 0.15 0.49 1.49 4.97
$ABELL\_1775$
$z = 0.07$
$R_{2500} = 408\text{kpc}h_{70}^{-1}$
0.03 0.08 0.27 0.81 2.71
$ABELL\_1835$
$z = 0.25$
$R_{2500} = 646\text{kpc}h_{70}^{-1}$
0.03 0.10 0.36 1.08 3.61
$ABELL\_1914$
$z = 0.17$
$R_{2500} = 633\text{kpc}h_{70}^{-1}$
0.03 0.09 0.31 0.94 3.13
$ABELL\_1930$
$z = 0.13$
$R_{2500} = 440\text{kpc}h_{70}^{-1}$
0.02 0.06 0.21 0.64 2.14
$ABELL\_1942\_AND\_CLUMP$
$z = 0.22$
$R_{2500} = 465\text{kpc}h_{70}^{-1}$
1.00
0.30
0.10
0.03
0.01
0.01 0.03 0.10 0.30 1.00

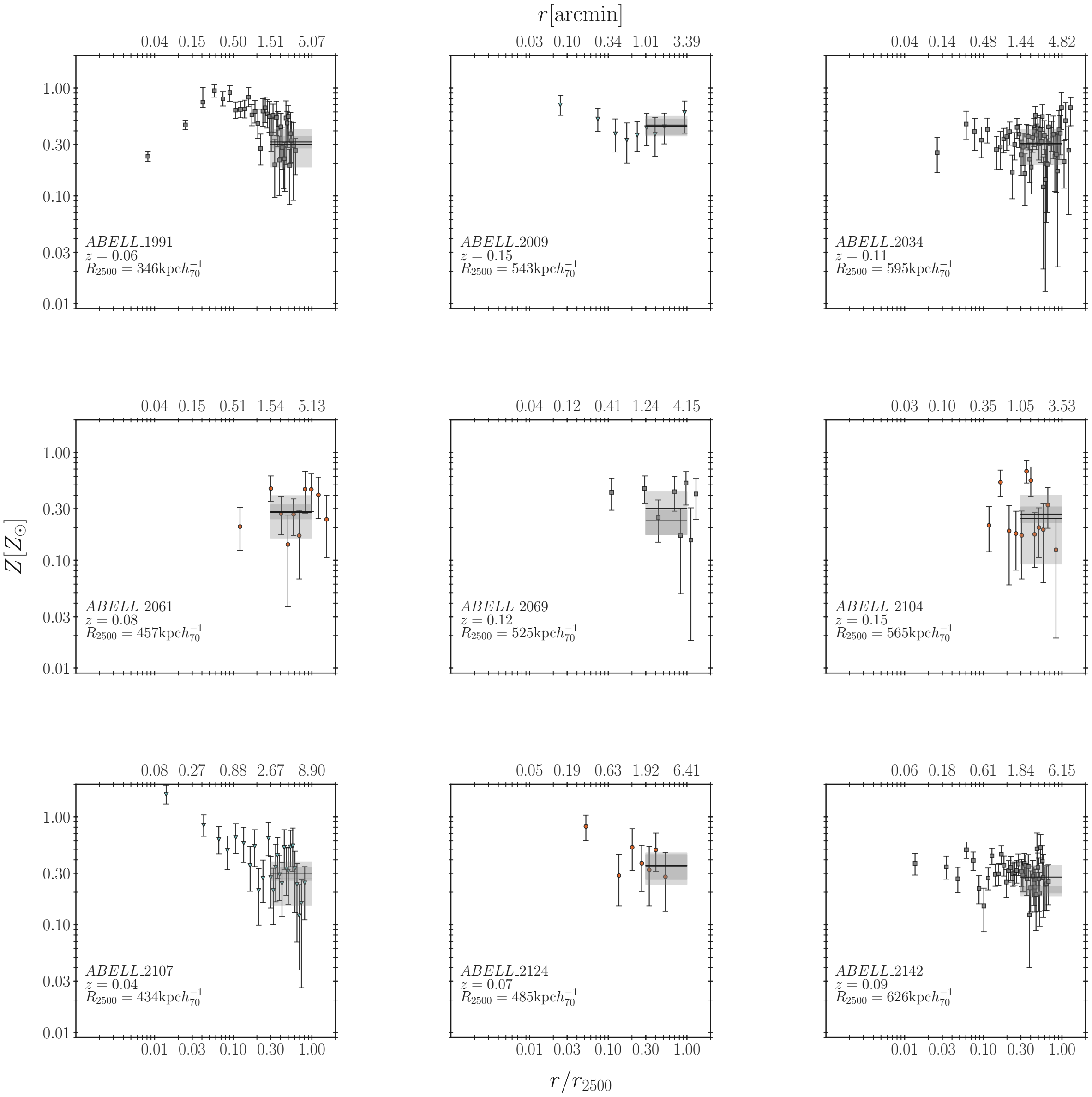
r[arcmin]
0.04 0.15 0.50 1.51 5.07
0.03 0.10 0.34 1.01 3.39
0.04 0.14 0.48 1.44 4.82
0.04 0.15 0.51 1.54 5.13
0.04 0.12 0.41 1.24 4.15
0.03 0.10 0.35 1.05 3.53
0.08 0.27 0.88 2.67 8.90
0.05 0.19 0.63 1.92 6.41
0.06 0.18 0.61 1.84 6.15
1.00
0.30
0.10
0.03
0.01
Z[Z⊙]
ABELL_1991
z = 0.06
R2500 = 346kpch70−1
ABELL_2009
z = 0.15
R2500 = 543kpch70−1
ABELL_2034
z = 0.11
R2500 = 595kpch70−1
ABELL_2061
z = 0.08
R2500 = 457kpch70−1
ABELL_2069
z = 0.12
R2500 = 525kpch70−1
ABELL_2104
z = 0.15
R2500 = 565kpch70−1
ABELL_2107
z = 0.04
R2500 = 434kpch70−1
ABELL_2124
z = 0.07
R2500 = 485kpch70−1
ABELL_2142
z = 0.09
R2500 = 626kpch70−1
0.01 0.03 0.10 0.30 1.00
r/r2500

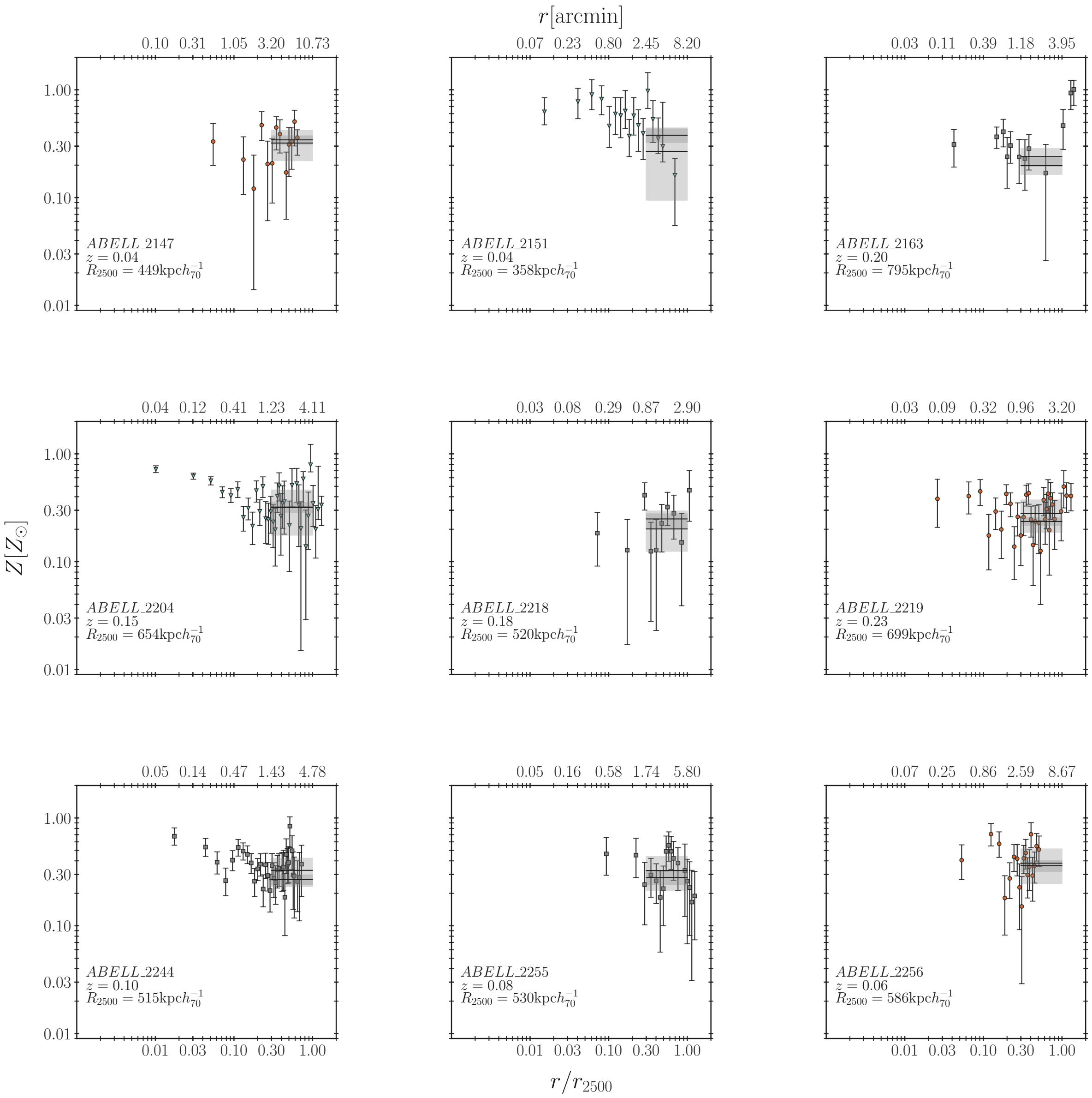
r[arcmin]
0.10 0.31 1.05 3.20 10.73
0.07 0.23 0.80 2.45 8.20
0.03 0.11 0.39 1.18 3.95
ABELL_2147
z = 0.04
R_2500 = 449kpch_70^-1
ABELL_2151
z = 0.04
R_2500 = 358kpch_70^-1
ABELL_2163
z = 0.20
R_2500 = 795kpch_70^-1
0.04 0.12 0.41 1.23 4.11
0.03 0.08 0.29 0.87 2.90
0.03 0.09 0.32 0.96 3.20
ABELL_2204
z = 0.15
R_2500 = 654kpch_70^-1
ABELL_2218
z = 0.18
R_2500 = 520kpch_70^-1
ABELL_2219
z = 0.23
R_2500 = 699kpch_70^-1
0.05 0.14 0.47 1.43 4.78
0.05 0.16 0.58 1.74 5.80
0.07 0.25 0.86 2.59 8.67
ABELL_2244
z = 0.10
R_2500 = 515kpch_70^-1
ABELL_2255
z = 0.08
R_2500 = 530kpch_70^-1
ABELL_2256
z = 0.06
R_2500 = 586kpch_70^-1
Z[Z_⊙]
1.00
0.30
0.10
0.03
0.01
0.01 0.03 0.10 0.30 1.00
r/r_2500

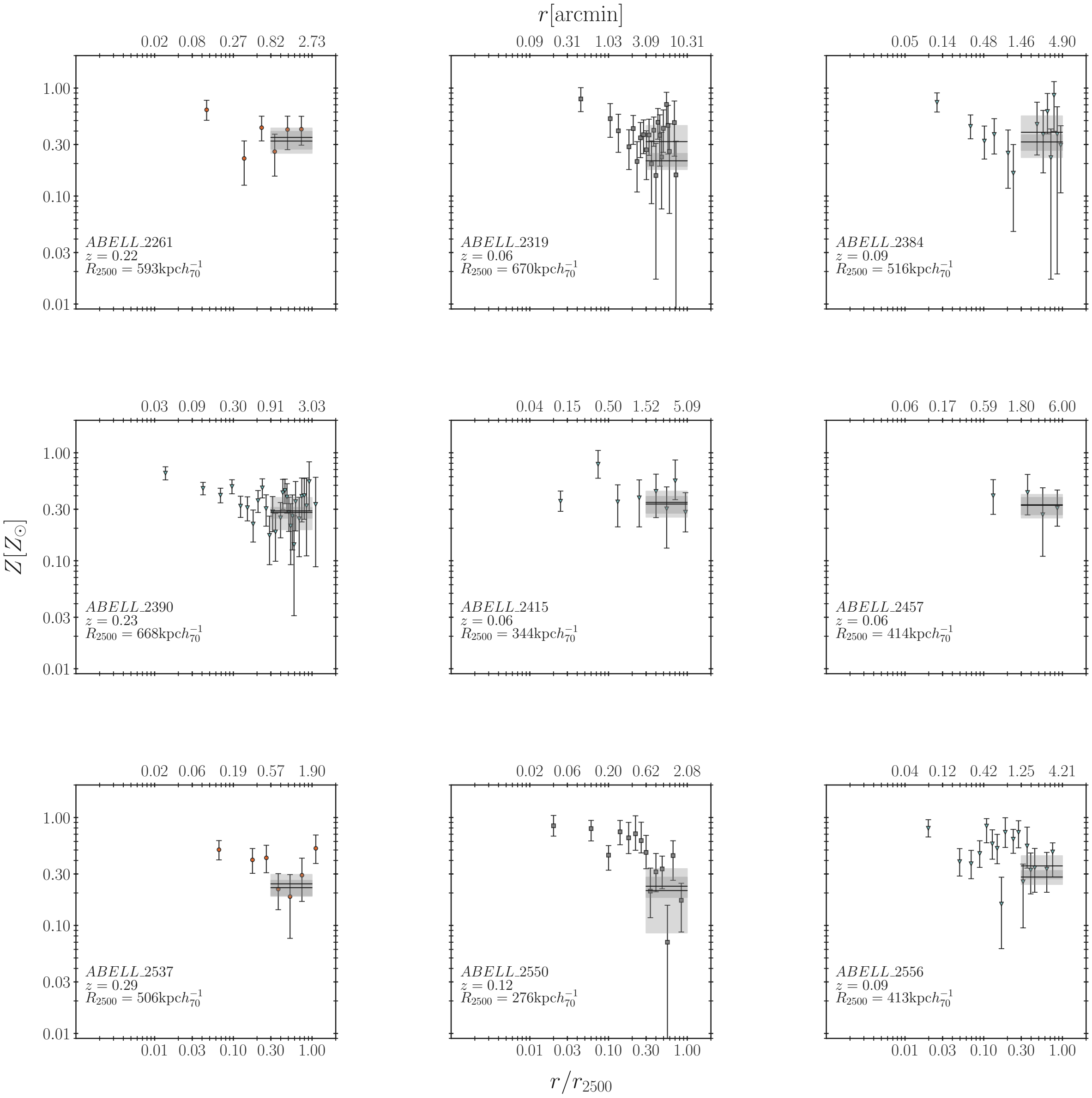

r[arcmin]
Z[Z⊙]
r/r2500
0.02 0.08 0.27 0.82 2.73
ABELL_2261
z = 0.22
R2500 = 593kpch70^-1
0.09 0.31 1.03 3.09 10.31
ABELL_2319
z = 0.06
R2500 = 670kpch70^-1
0.05 0.14 0.48 1.46 4.90
ABELL_2384
z = 0.09
R2500 = 516kpch70^-1
0.03 0.09 0.30 0.91 3.03
ABELL_2390
z = 0.23
R2500 = 668kpch70^-1
0.04 0.15 0.50 1.52 5.09
ABELL_2415
z = 0.06
R2500 = 344kpch70^-1
0.06 0.17 0.59 1.80 6.00
ABELL_2457
z = 0.06
R2500 = 414kpch70^-1
0.02 0.06 0.19 0.57 1.90
ABELL_2537
z = 0.29
R2500 = 506kpch70^-1
0.02 0.06 0.20 0.62 2.08
ABELL_2550
z = 0.12
R2500 = 276kpch70^-1
0.04 0.12 0.42 1.25 4.21
ABELL_2556
z = 0.09
R2500 = 413kpch70^-1
1.00
0.30
0.10
0.03
0.01
0.01 0.03 0.10 0.30 1.00

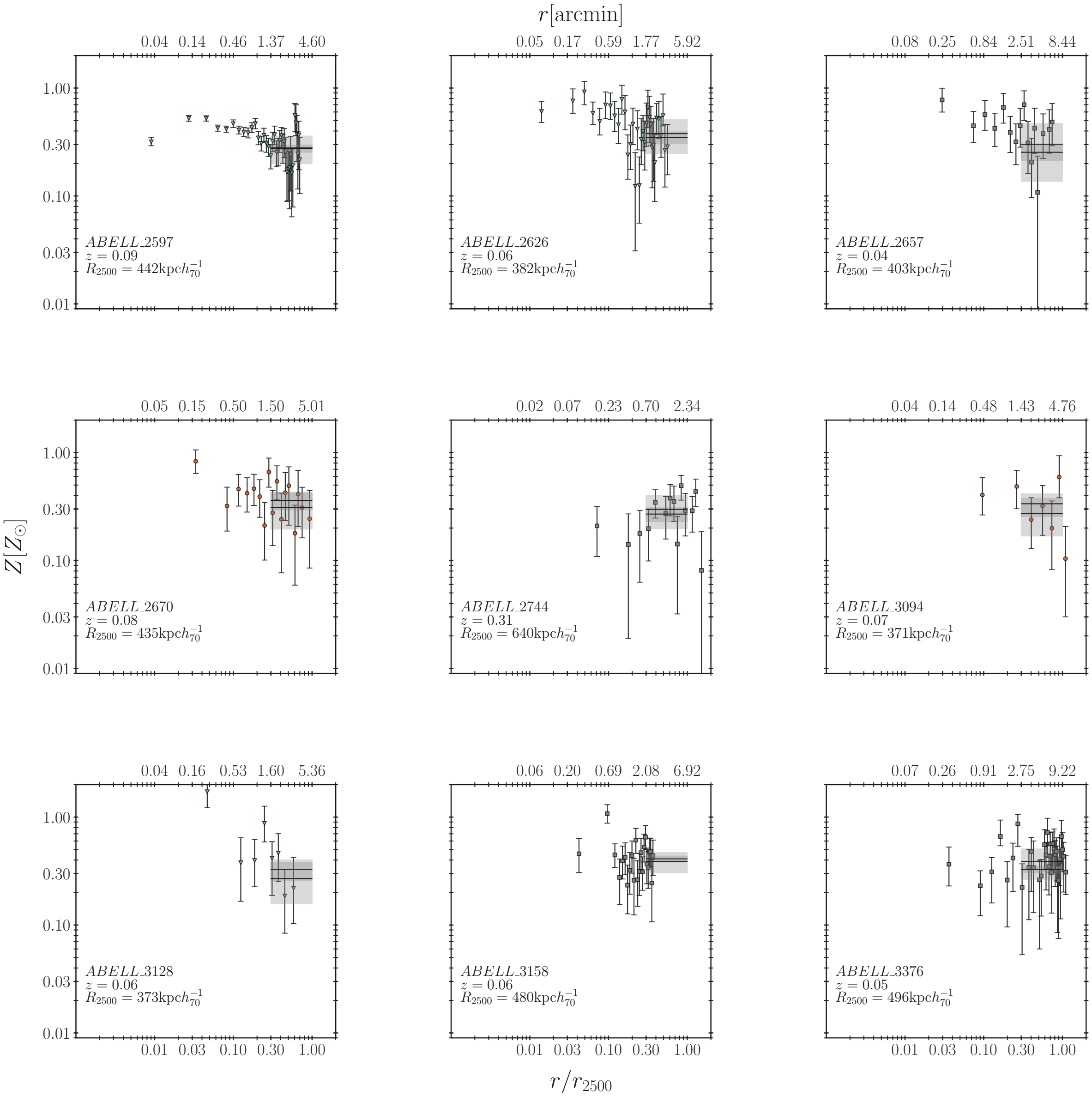r[arcmin]
0.04 0.14 0.46 1.37 4.60
0.05 0.17 0.59 1.77 5.92
0.08 0.25 0.84 2.51 8.44
1.00
0.30
0.10
0.03
0.01
$ABELL\_2597$
$z = 0.09$
$R_{2500} = 442\mathrm{kpc}h_{70}^{-1}$
$ABELL\_2626$
$z = 0.06$
$R_{2500} = 382\mathrm{kpc}h_{70}^{-1}$
$ABELL\_2657$
$z = 0.04$
$R_{2500} = 403\mathrm{kpc}h_{70}^{-1}$
0.05 0.15 0.50 1.50 5.01
0.02 0.07 0.23 0.70 2.34
0.04 0.14 0.48 1.43 4.76
$Z[Z_\odot]$
$ABELL\_2670$
$z = 0.08$
$R_{2500} = 435\mathrm{kpc}h_{70}^{-1}$
$ABELL\_2744$
$z = 0.31$
$R_{2500} = 640\mathrm{kpc}h_{70}^{-1}$
$ABELL\_3094$
$z = 0.07$
$R_{2500} = 371\mathrm{kpc}h_{70}^{-1}$
0.04 0.16 0.53 1.60 5.36
0.06 0.20 0.69 2.08 6.92
0.07 0.26 0.91 2.75 9.22
$ABELL\_3128$
$z = 0.06$
$R_{2500} = 373\mathrm{kpc}h_{70}^{-1}$
$ABELL\_3158$
$z = 0.06$
$R_{2500} = 480\mathrm{kpc}h_{70}^{-1}$
$ABELL\_3376$
$z = 0.05$
$R_{2500} = 496\mathrm{kpc}h_{70}^{-1}$
0.01 0.03 0.10 0.30 1.00
r/r_{2500}

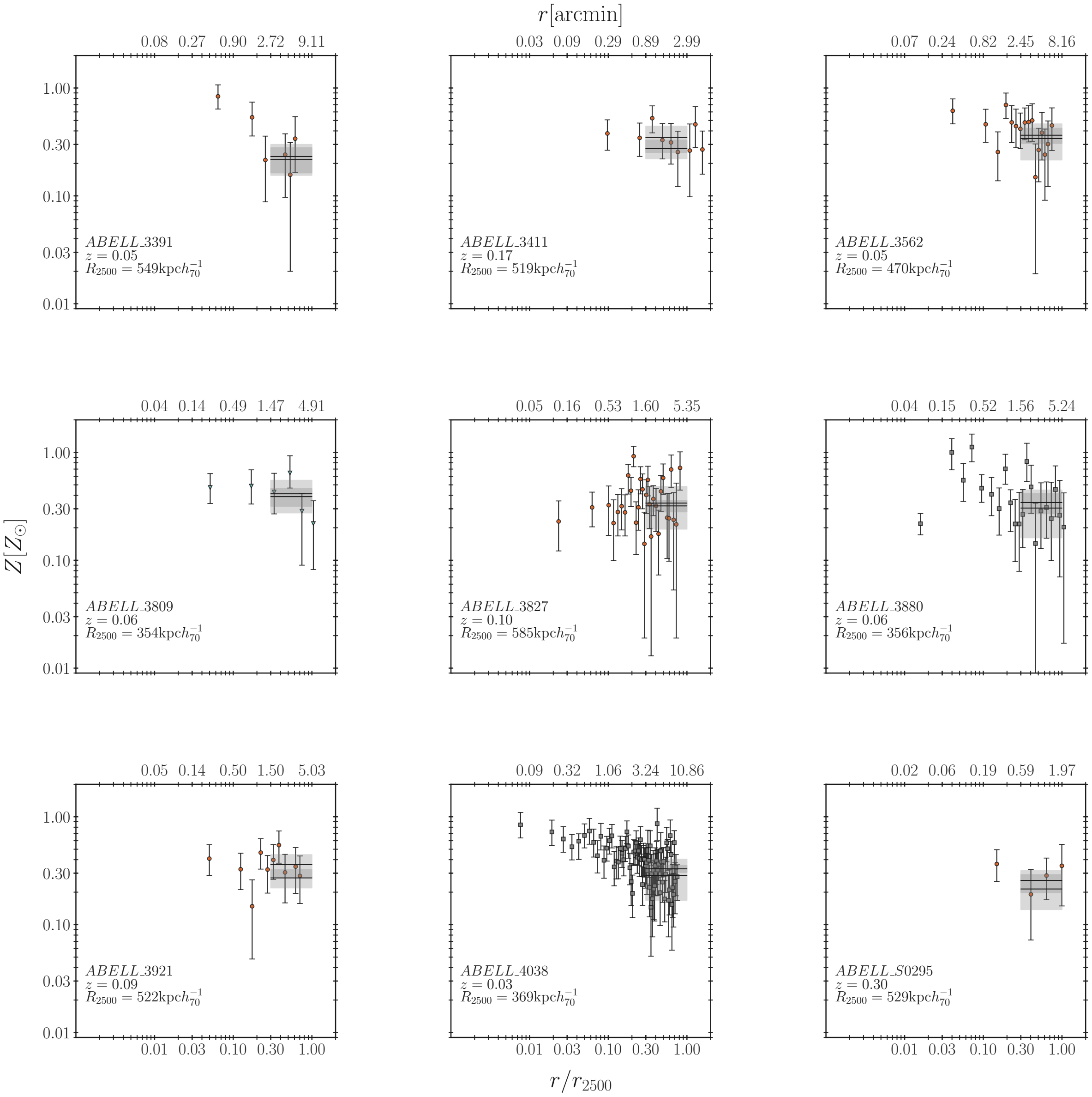
r[arcmin]
0.08 0.27 0.90 2.72 9.11
0.03 0.09 0.29 0.89 2.99
0.07 0.24 0.82 2.45 8.16
0.04 0.14 0.49 1.47 4.91
0.05 0.16 0.53 1.60 5.35
0.04 0.15 0.52 1.56 5.24
0.05 0.14 0.50 1.50 5.03
0.09 0.32 1.06 3.24 10.86
0.02 0.06 0.19 0.59 1.97
$Z[Z_\odot]$
1.00
0.30
0.10
0.03
0.01
$ABELL\_3391$
$z = 0.05$
$R_{2500} = 549\mathrm{kpc}h_{70}^{-1}$
$ABELL\_3411$
$z = 0.17$
$R_{2500} = 519\mathrm{kpc}h_{70}^{-1}$
$ABELL\_3562$
$z = 0.05$
$R_{2500} = 470\mathrm{kpc}h_{70}^{-1}$
$ABELL\_3809$
$z = 0.06$
$R_{2500} = 354\mathrm{kpc}h_{70}^{-1}$
$ABELL\_3827$
$z = 0.10$
$R_{2500} = 585\mathrm{kpc}h_{70}^{-1}$
$ABELL\_3880$
$z = 0.06$
$R_{2500} = 356\mathrm{kpc}h_{70}^{-1}$
$ABELL\_3921$
$z = 0.09$
$R_{2500} = 522\mathrm{kpc}h_{70}^{-1}$
$ABELL\_4038$
$z = 0.03$
$R_{2500} = 369\mathrm{kpc}h_{70}^{-1}$
$ABELL\_S0295$
$z = 0.30$
$R_{2500} = 529\mathrm{kpc}h_{70}^{-1}$
0.01 0.03 0.10 0.30 1.00
r/r_{2500}

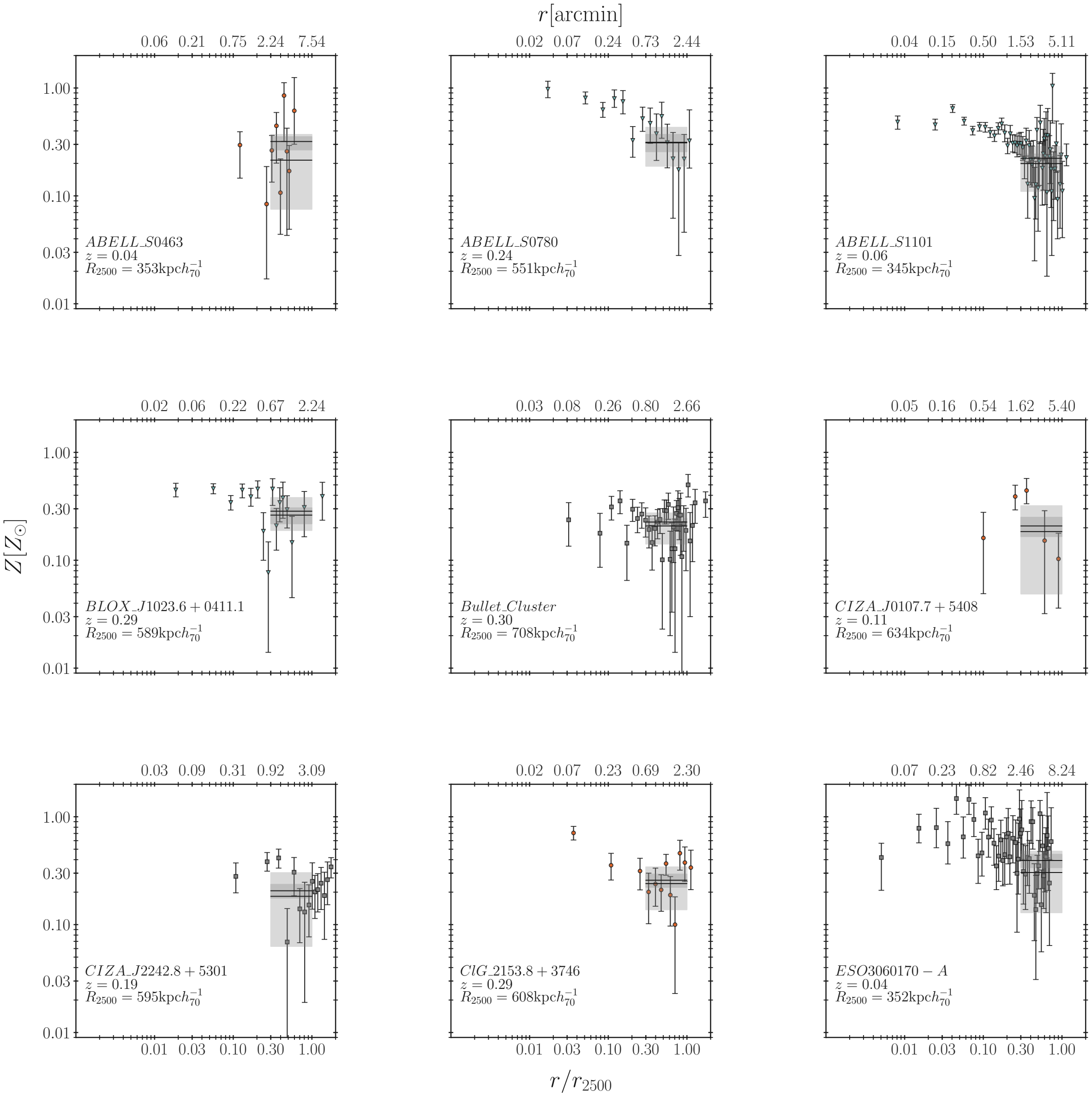
r[arcmin]
0.06 0.21 0.75 2.24 7.54
0.02 0.07 0.24 0.73 2.44
0.04 0.15 0.50 1.53 5.11
$ABELL\_S0463$
$z = 0.04$
$R_{2500} = 353\mathrm{kpc}h_{70}^{-1}$
$ABELL\_S0780$
$z = 0.24$
$R_{2500} = 551\mathrm{kpc}h_{70}^{-1}$
$ABELL\_S1101$
$z = 0.06$
$R_{2500} = 345\mathrm{kpc}h_{70}^{-1}$
0.02 0.06 0.22 0.67 2.24
0.03 0.08 0.26 0.80 2.66
0.05 0.16 0.54 1.62 5.40
$BLOX\_J1023.6 + 0411.1$
$z = 0.29$
$R_{2500} = 589\mathrm{kpc}h_{70}^{-1}$
$Bullet\_Cluster$
$z = 0.30$
$R_{2500} = 708\mathrm{kpc}h_{70}^{-1}$
$CIZA\_J0107.7 + 5408$
$z = 0.11$
$R_{2500} = 634\mathrm{kpc}h_{70}^{-1}$
0.03 0.09 0.31 0.92 3.09
0.02 0.07 0.23 0.69 2.30
0.07 0.23 0.82 2.46 8.24
$CIZA\_J2242.8 + 5301$
$z = 0.19$
$R_{2500} = 595\mathrm{kpc}h_{70}^{-1}$
$ClG\_2153.8 + 3746$
$z = 0.29$
$R_{2500} = 608\mathrm{kpc}h_{70}^{-1}$
$ESO3060170 - A$
$z = 0.04$
$R_{2500} = 352\mathrm{kpc}h_{70}^{-1}$
$Z[Z_\odot]$
1.00
0.30
0.10
0.03
0.01
0.01 0.03 0.10 0.30 1.00
r/r_{2500}

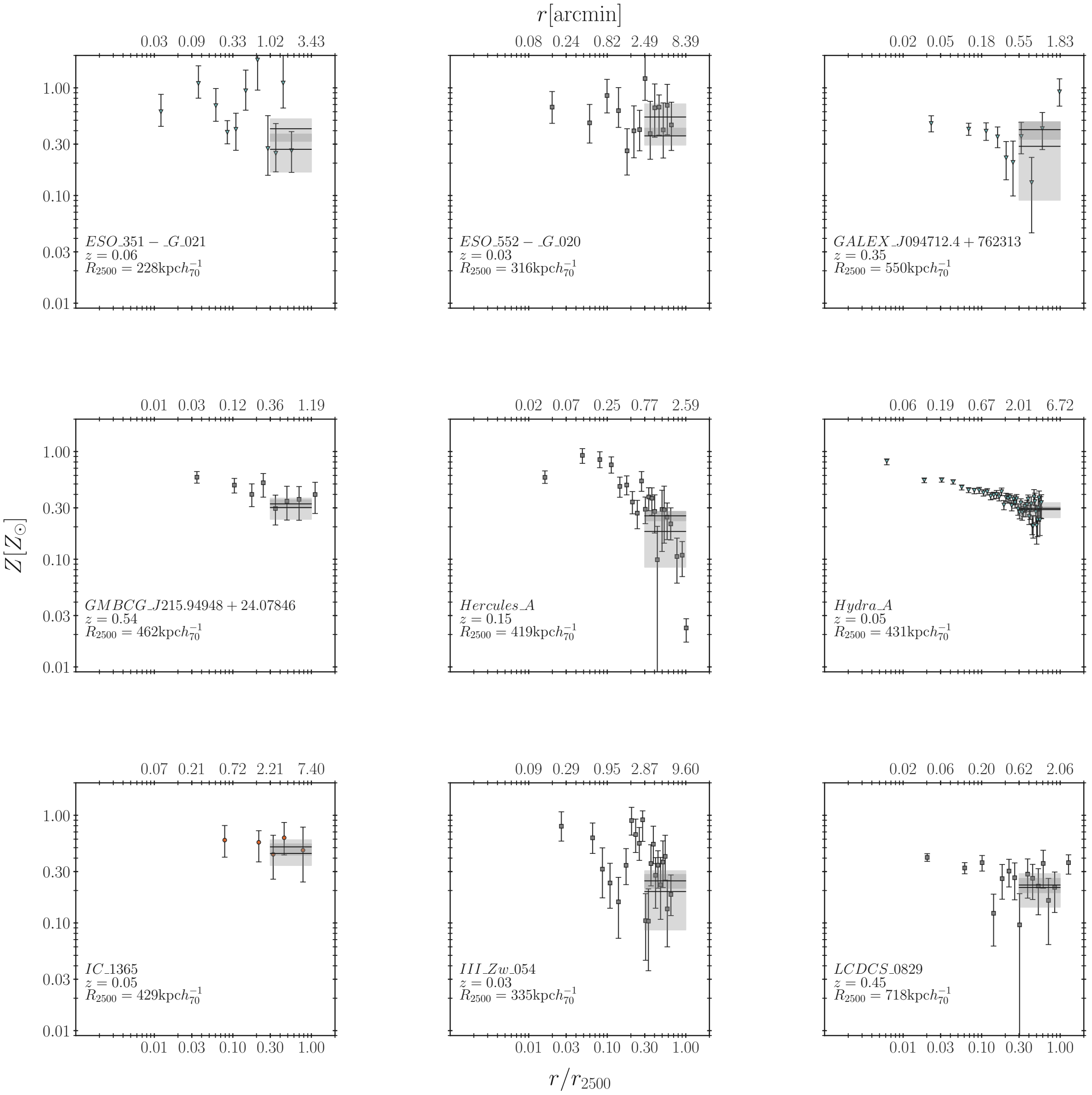
r[arcmin]
Z[Z⊙]
r/r2500
0.03 0.09 0.33 1.02 3.43
ESO_351 − _G_021
z = 0.06
R2500 = 228kpch70^-1
0.08 0.24 0.82 2.49 8.39
ESO_552 − _G_020
z = 0.03
R2500 = 316kpch70^-1
0.02 0.05 0.18 0.55 1.83
GALEX_J094712.4 + 762313
z = 0.35
R2500 = 550kpch70^-1
0.01 0.03 0.12 0.36 1.19
GMBCG_J215.94948 + 24.07846
z = 0.54
R2500 = 462kpch70^-1
0.02 0.07 0.25 0.77 2.59
Hercules_A
z = 0.15
R2500 = 419kpch70^-1
0.06 0.19 0.67 2.01 6.72
Hydra_A
z = 0.05
R2500 = 431kpch70^-1
0.07 0.21 0.72 2.21 7.40
IC_1365
z = 0.05
R2500 = 429kpch70^-1
0.09 0.29 0.95 2.87 9.60
III_Zw_054
z = 0.03
R2500 = 335kpch70^-1
0.02 0.06 0.20 0.62 2.06
LCDCS_0829
z = 0.45
R2500 = 718kpch70^-1
1.00 0.30 0.10 0.03 0.01
0.01 0.03 0.10 0.30 1.00

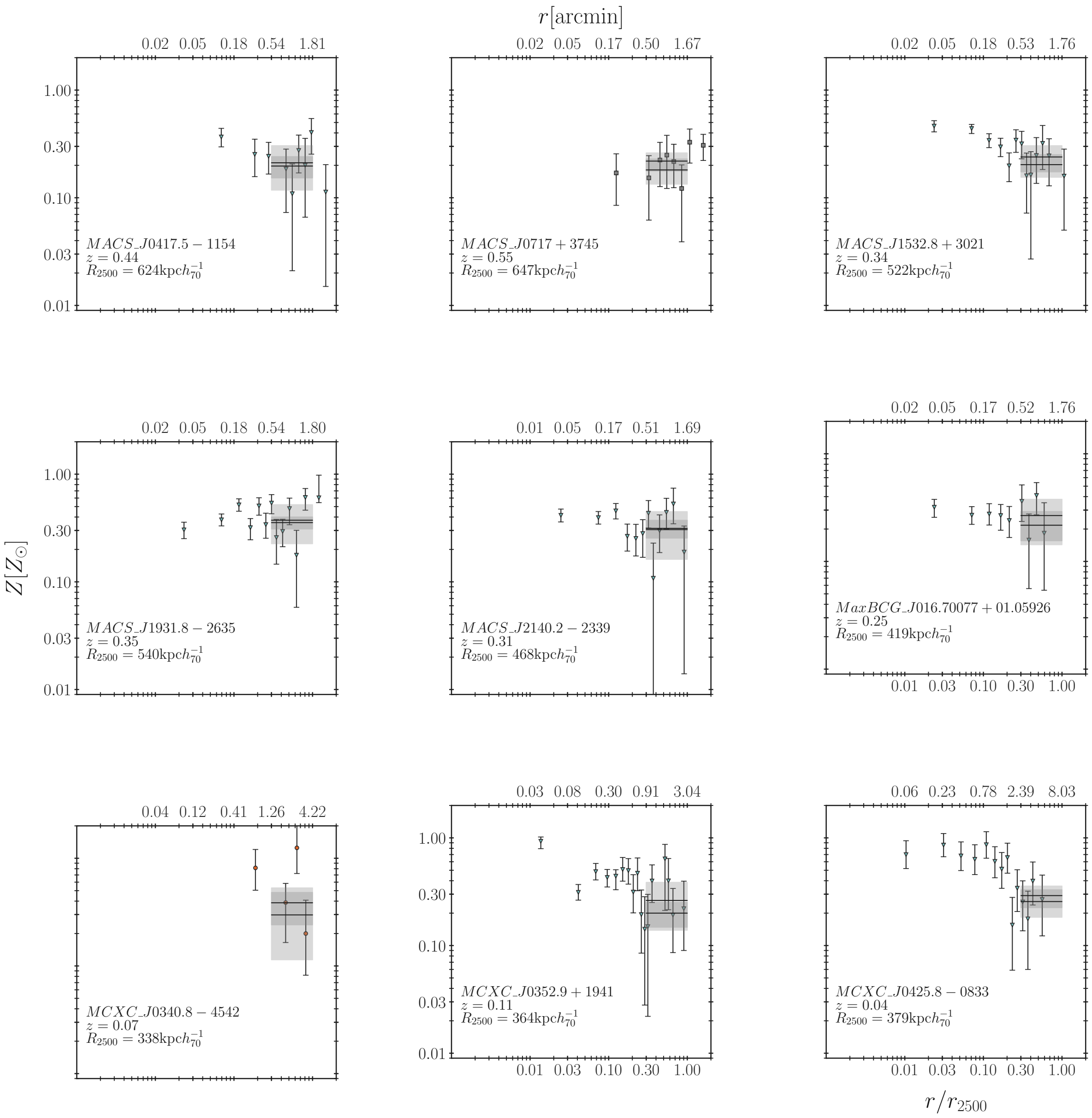

r[arcmin]
Z[Z_⊙]
r/r_2500
1.00
0.30
0.10
0.03
0.01
0.01 0.03 0.10 0.30 1.00
0.02 0.05 0.18 0.54 1.81
MACS_J0417.5 − 1154
z = 0.44
R_2500 = 624kpch_70^−1
0.02 0.05 0.17 0.50 1.67
MACS_J0717 + 3745
z = 0.55
R_2500 = 647kpch_70^−1
0.02 0.05 0.18 0.53 1.76
MACS_J1532.8 + 3021
z = 0.34
R_2500 = 522kpch_70^−1
0.02 0.05 0.18 0.54 1.80
MACS_J1931.8 − 2635
z = 0.35
R_2500 = 540kpch_70^−1
0.01 0.05 0.17 0.51 1.69
MACS_J2140.2 − 2339
z = 0.31
R_2500 = 468kpch_70^−1
0.02 0.05 0.17 0.52 1.76
MaxBCG_J016.70077 + 01.05926
z = 0.25
R_2500 = 419kpch_70^−1
0.04 0.12 0.41 1.26 4.22
MCXC_J0340.8 − 4542
z = 0.07
R_2500 = 338kpch_70^−1
0.03 0.08 0.30 0.91 3.04
MCXC_J0352.9 + 1941
z = 0.11
R_2500 = 364kpch_70^−1
0.06 0.23 0.78 2.39 8.03
MCXC_J0425.8 − 0833
z = 0.04
R_2500 = 379kpch_70^−1

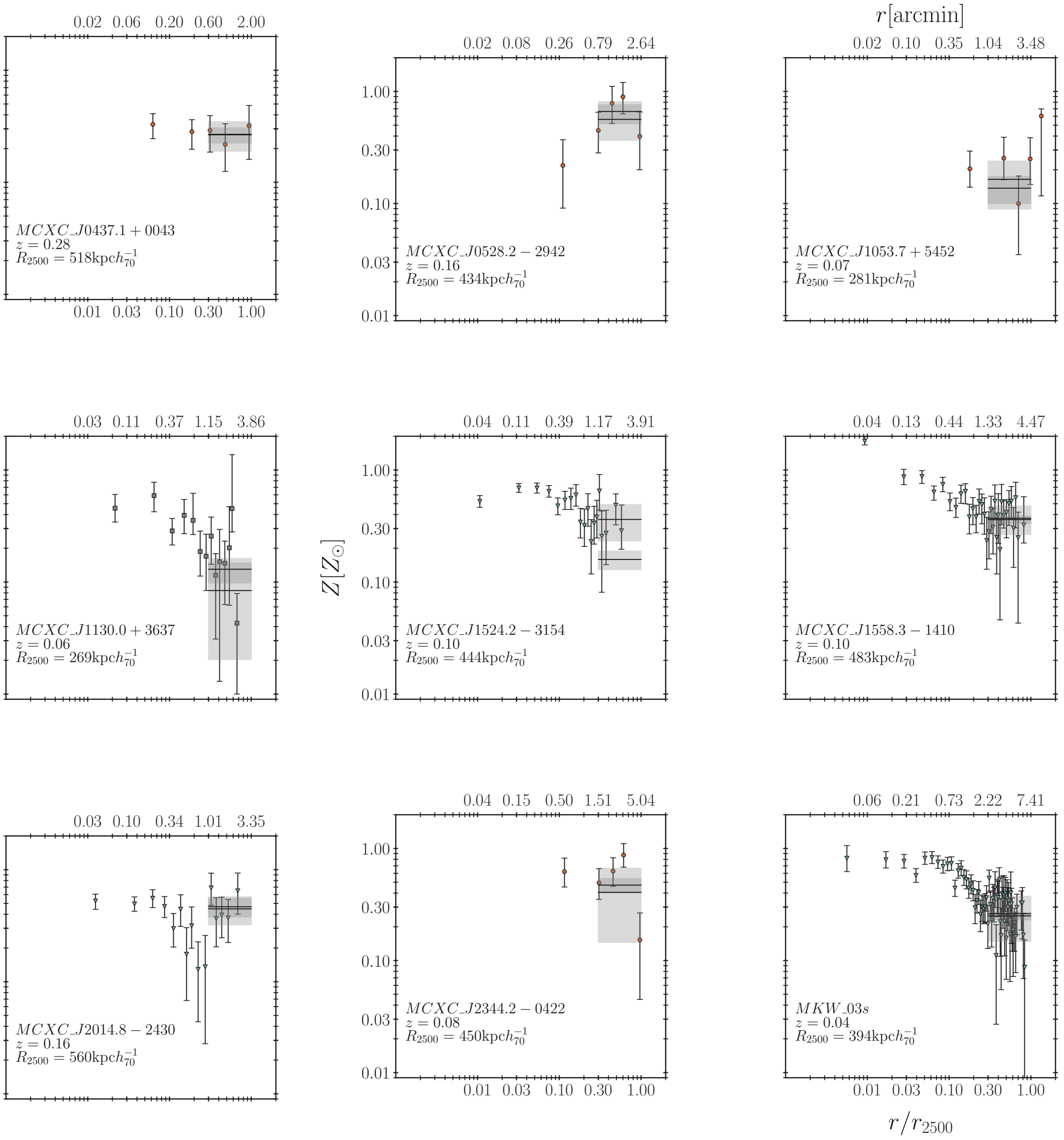
r[arcmin]
Z[Z⊙]
r/r2500
0.02 0.06 0.20 0.60 2.00
0.01 0.03 0.10 0.30 1.00
MCXC_J0437.1+0043
z = 0.28
R2500 = 518kpch70^-1
0.02 0.08 0.26 0.79 2.64
1.00 0.30 0.10 0.03 0.01
MCXC_J0528.2−2942
z = 0.16
R2500 = 434kpch70^-1
0.02 0.10 0.35 1.04 3.48
MCXC_J1053.7+5452
z = 0.07
R2500 = 281kpch70^-1
0.03 0.11 0.37 1.15 3.86
MCXC_J1130.0+3637
z = 0.06
R2500 = 269kpch70^-1
0.04 0.11 0.39 1.17 3.91
MCXC_J1524.2−3154
z = 0.10
R2500 = 444kpch70^-1
0.04 0.13 0.44 1.33 4.47
MCXC_J1558.3−1410
z = 0.10
R2500 = 483kpch70^-1
0.03 0.10 0.34 1.01 3.35
MCXC_J2014.8−2430
z = 0.16
R2500 = 560kpch70^-1
0.04 0.15 0.50 1.51 5.04
MCXC_J2344.2−0422
z = 0.08
R2500 = 450kpch70^-1
0.06 0.21 0.73 2.22 7.41
MKW_03s
z = 0.04
R2500 = 394kpch70^-1

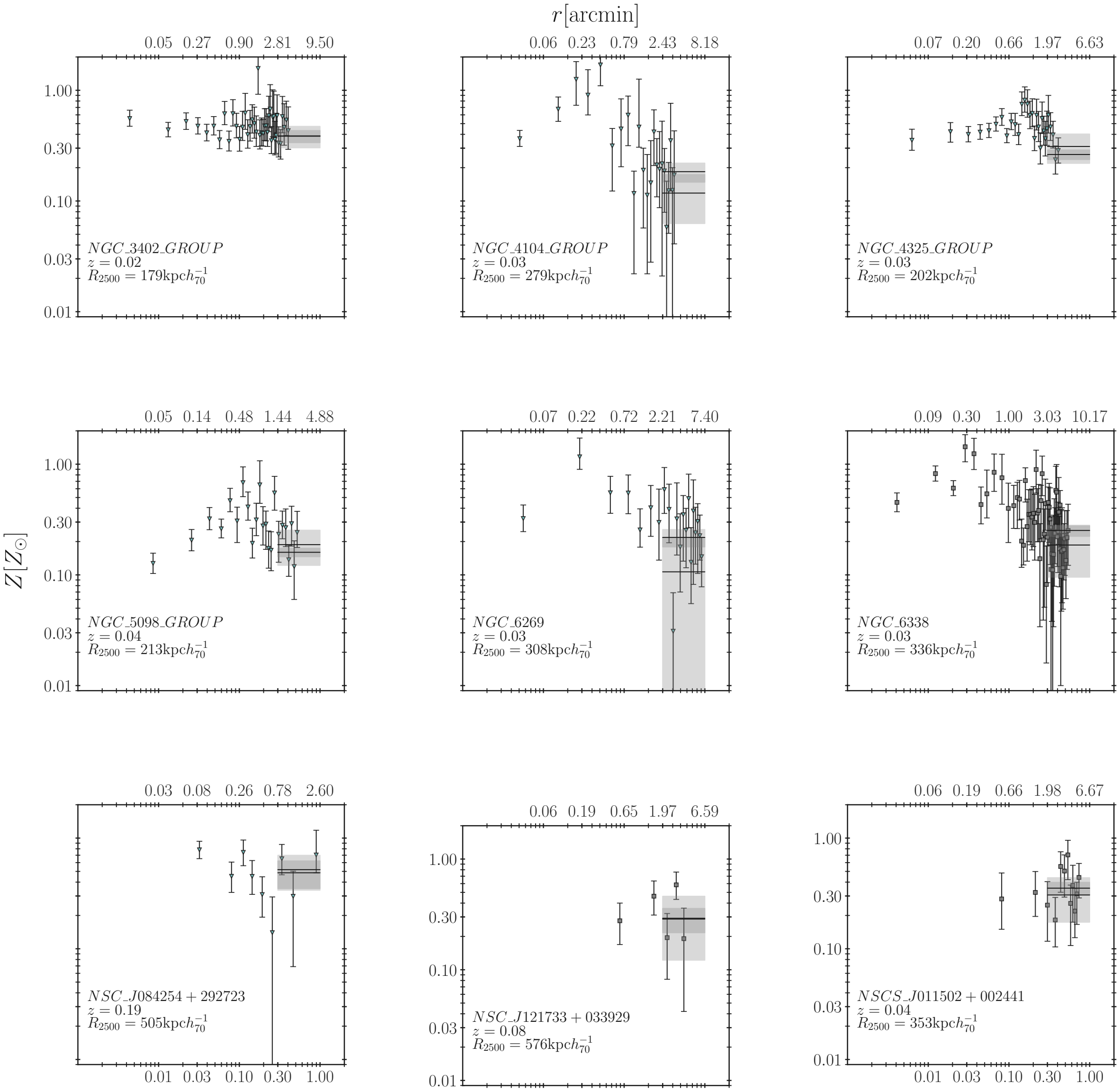
r[arcmin]
$Z[Z_\odot]$
0.05 0.27 0.90 2.81 9.50
NGC_3402_GROUP
$z = 0.02$
$R_{2500} = 179\mathrm{kpc}h_{70}^{-1}$
0.06 0.23 0.79 2.43 8.18
NGC_4104_GROUP
$z = 0.03$
$R_{2500} = 279\mathrm{kpc}h_{70}^{-1}$
0.07 0.20 0.66 1.97 6.63
NGC_4325_GROUP
$z = 0.03$
$R_{2500} = 202\mathrm{kpc}h_{70}^{-1}$
0.05 0.14 0.48 1.44 4.88
NGC_5098_GROUP
$z = 0.04$
$R_{2500} = 213\mathrm{kpc}h_{70}^{-1}$
0.07 0.22 0.72 2.21 7.40
NGC_6269
$z = 0.03$
$R_{2500} = 308\mathrm{kpc}h_{70}^{-1}$
0.09 0.30 1.00 3.03 10.17
NGC_6338
$z = 0.03$
$R_{2500} = 336\mathrm{kpc}h_{70}^{-1}$
0.03 0.08 0.26 0.78 2.60
$NSC\_J084254 + 292723$
$z = 0.19$
$R_{2500} = 505\mathrm{kpc}h_{70}^{-1}$
0.06 0.19 0.65 1.97 6.59
$NSC\_J121733 + 033929$
$z = 0.08$
$R_{2500} = 576\mathrm{kpc}h_{70}^{-1}$
0.06 0.19 0.66 1.98 6.67
$NSCS\_J011502 + 002441$
$z = 0.04$
$R_{2500} = 353\mathrm{kpc}h_{70}^{-1}$
1.00
0.30
0.10
0.03
0.01
0.01 0.03 0.10 0.30 1.00

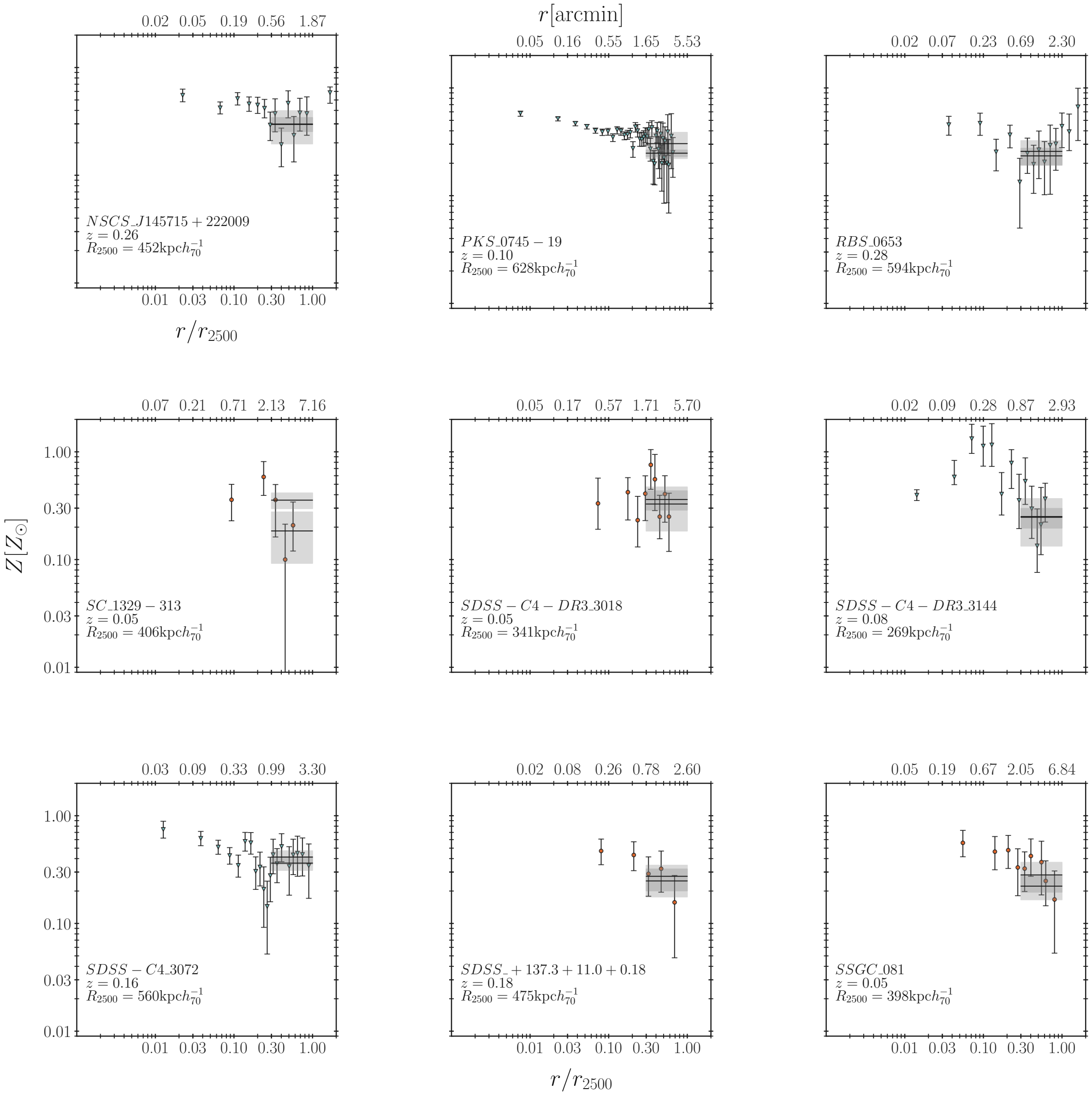
r[arcmin]
Z[Z_⊙]
r/r_2500
0.01 0.03 0.10 0.30 1.00
0.01 0.03 0.10 0.30 1.00
NSCS_J145715 + 222009
z = 0.26
R_2500 = 452kpch_70^-1
0.02 0.05 0.19 0.56 1.87
PKS_0745 − 19
z = 0.10
R_2500 = 628kpch_70^-1
0.05 0.16 0.55 1.65 5.53
RBS_0653
z = 0.28
R_2500 = 594kpch_70^-1
0.02 0.07 0.23 0.69 2.30
SC_1329 − 313
z = 0.05
R_2500 = 406kpch_70^-1
0.07 0.21 0.71 2.13 7.16
SDSS − C4 − DR3_3018
z = 0.05
R_2500 = 341kpch_70^-1
0.05 0.17 0.57 1.71 5.70
SDSS − C4 − DR3_3144
z = 0.08
R_2500 = 269kpch_70^-1
0.02 0.09 0.28 0.87 2.93
SDSS − C4_3072
z = 0.16
R_2500 = 560kpch_70^-1
0.03 0.09 0.33 0.99 3.30
SDSS_ + 137.3 + 11.0 + 0.18
z = 0.18
R_2500 = 475kpch_70^-1
0.02 0.08 0.26 0.78 2.60
SSGC_081
z = 0.05
R_2500 = 398kpch_70^-1
0.05 0.19 0.67 2.05 6.84

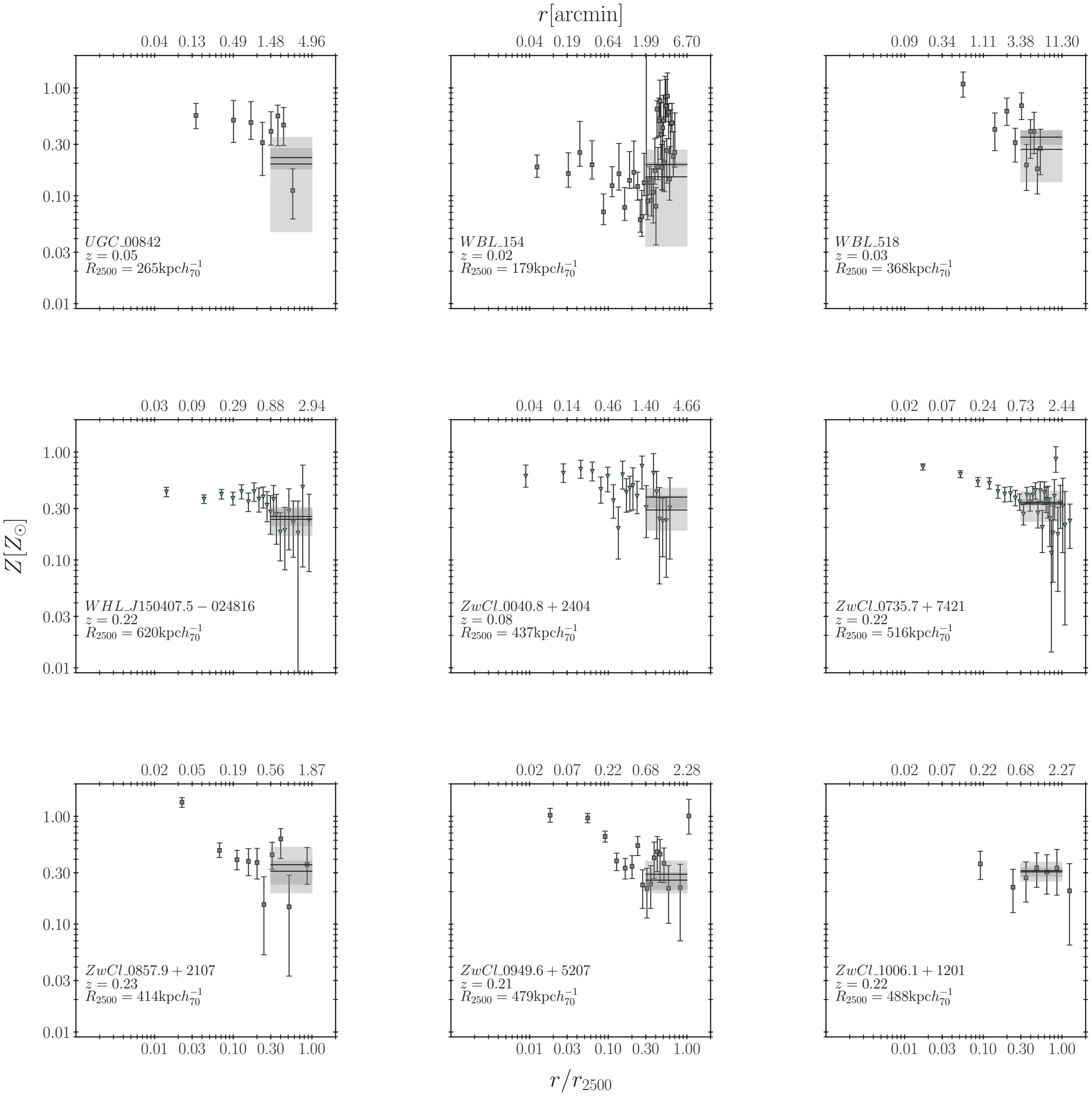
r[arcmin]
0.04 0.13 0.49 1.48 4.96
0.04 0.19 0.64 1.99 6.70
0.09 0.34 1.11 3.38 11.30
1.00
0.30
0.10
0.03
0.01
UGC_00842
z = 0.05
R2500 = 265kpch70^-1
WBL_154
z = 0.02
R2500 = 179kpch70^-1
WBL_518
z = 0.03
R2500 = 368kpch70^-1
0.03 0.09 0.29 0.88 2.94
0.04 0.14 0.46 1.40 4.66
0.02 0.07 0.24 0.73 2.44
Z[Z⊙]
WHL_J150407.5 − 024816
z = 0.22
R2500 = 620kpch70^-1
ZwCl_0040.8 + 2404
z = 0.08
R2500 = 437kpch70^-1
ZwCl_0735.7 + 7421
z = 0.22
R2500 = 516kpch70^-1
0.02 0.05 0.19 0.56 1.87
0.02 0.07 0.22 0.68 2.28
0.02 0.07 0.22 0.68 2.27
ZwCl_0857.9 + 2107
z = 0.23
R2500 = 414kpch70^-1
ZwCl_0949.6 + 5207
z = 0.21
R2500 = 479kpch70^-1
ZwCl_1006.1 + 1201
z = 0.22
R2500 = 488kpch70^-1
0.01 0.03 0.10 0.30 1.00
r/r2500

Appendix C ACCEPT2.0 Radial Temperature Profiles

Radial temperature profiles for 154 ACCEPT2.0 clusters. (For a description, see chapter 2.)

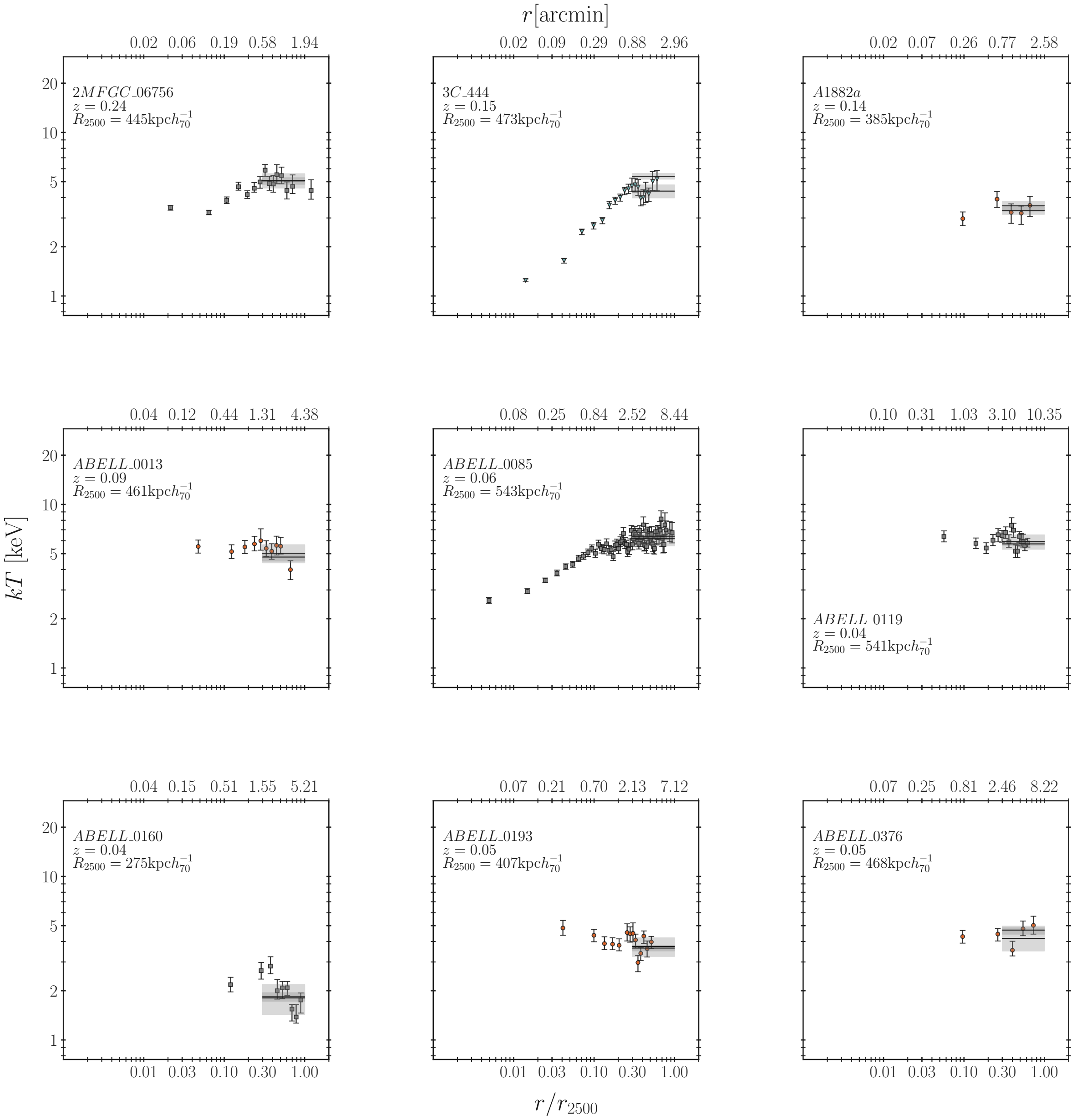
r[arcmin]
kT [keV]
r/r_{2500}
20
10
5
2
1
0.01 0.03 0.10 0.30 1.00
0.02 0.06 0.19 0.58 1.94
$2MFGC\_06756$
$z = 0.24$
$R_{2500} = 445\text{kpc}h_{70}^{-1}$
0.02 0.09 0.29 0.88 2.96
$3C\_444$
$z = 0.15$
$R_{2500} = 473\text{kpc}h_{70}^{-1}$
0.02 0.07 0.26 0.77 2.58
$A1882a$
$z = 0.14$
$R_{2500} = 385\text{kpc}h_{70}^{-1}$
0.04 0.12 0.44 1.31 4.38
$ABELL\_0013$
$z = 0.09$
$R_{2500} = 461\text{kpc}h_{70}^{-1}$
0.08 0.25 0.84 2.52 8.44
$ABELL\_0085$
$z = 0.06$
$R_{2500} = 543\text{kpc}h_{70}^{-1}$
0.10 0.31 1.03 3.10 10.35
$ABELL\_0119$
$z = 0.04$
$R_{2500} = 541\text{kpc}h_{70}^{-1}$
0.04 0.15 0.51 1.55 5.21
$ABELL\_0160$
$z = 0.04$
$R_{2500} = 275\text{kpc}h_{70}^{-1}$
0.07 0.21 0.70 2.13 7.12
$ABELL\_0193$
$z = 0.05$
$R_{2500} = 407\text{kpc}h_{70}^{-1}$
0.07 0.25 0.81 2.46 8.22
$ABELL\_0376$
$z = 0.05$
$R_{2500} = 468\text{kpc}h_{70}^{-1}$

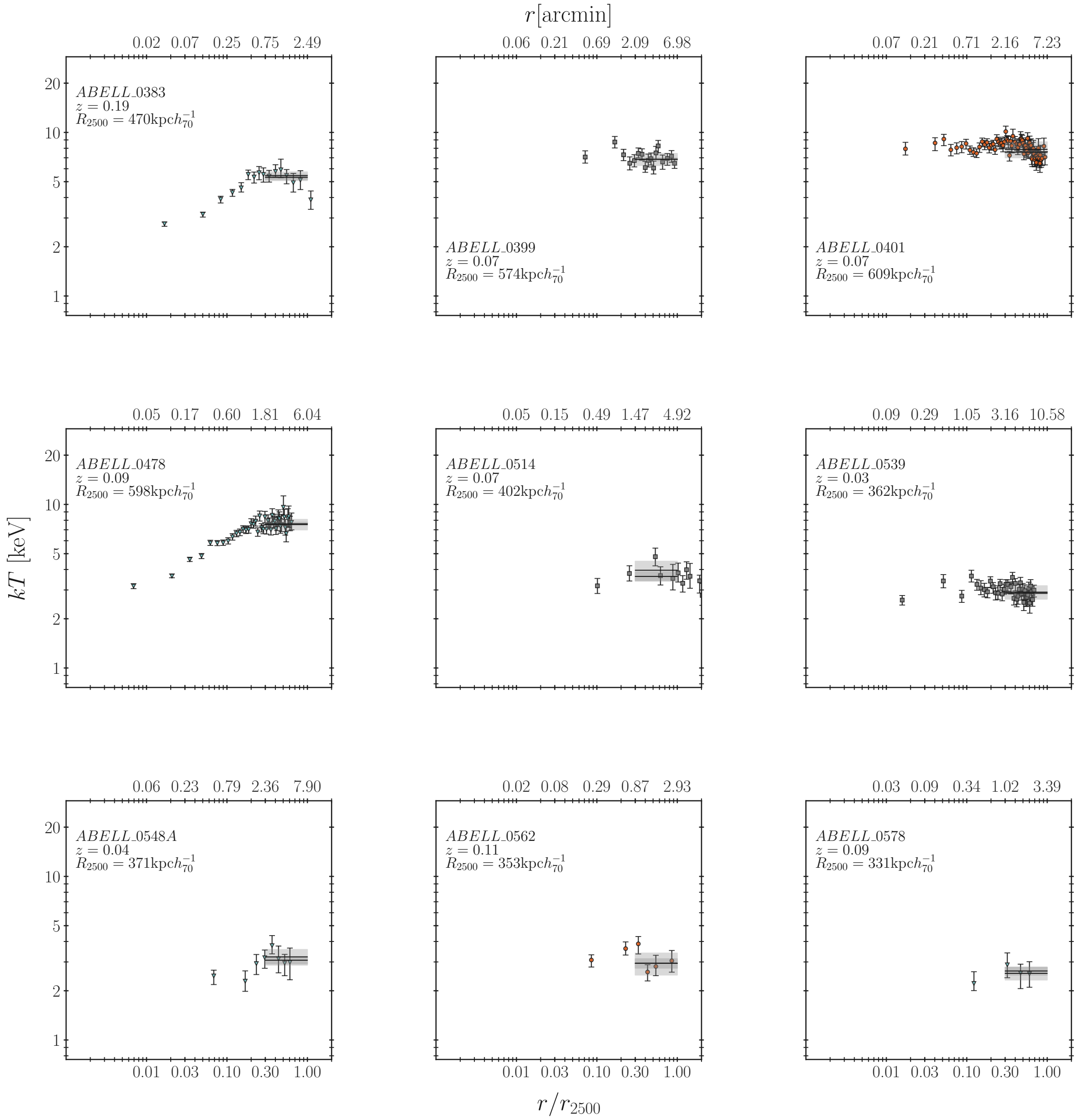r[arcmin]
0.02 0.07 0.25 0.75 2.49
ABELL_0383
z = 0.19
R2500 = 470kpch70^-1
0.06 0.21 0.69 2.09 6.98
ABELL_0399
z = 0.07
R2500 = 574kpch70^-1
0.07 0.21 0.71 2.16 7.23
ABELL_0401
z = 0.07
R2500 = 609kpch70^-1
0.05 0.17 0.60 1.81 6.04
ABELL_0478
z = 0.09
R2500 = 598kpch70^-1
0.05 0.15 0.49 1.47 4.92
ABELL_0514
z = 0.07
R2500 = 402kpch70^-1
0.09 0.29 1.05 3.16 10.58
ABELL_0539
z = 0.03
R2500 = 362kpch70^-1
0.06 0.23 0.79 2.36 7.90
ABELL_0548A
z = 0.04
R2500 = 371kpch70^-1
0.02 0.08 0.29 0.87 2.93
ABELL_0562
z = 0.11
R2500 = 353kpch70^-1
0.03 0.09 0.34 1.02 3.39
ABELL_0578
z = 0.09
R2500 = 331kpch70^-1
kT [keV]
20
10
5
2
1
0.01 0.03 0.10 0.30 1.00
r/r2500

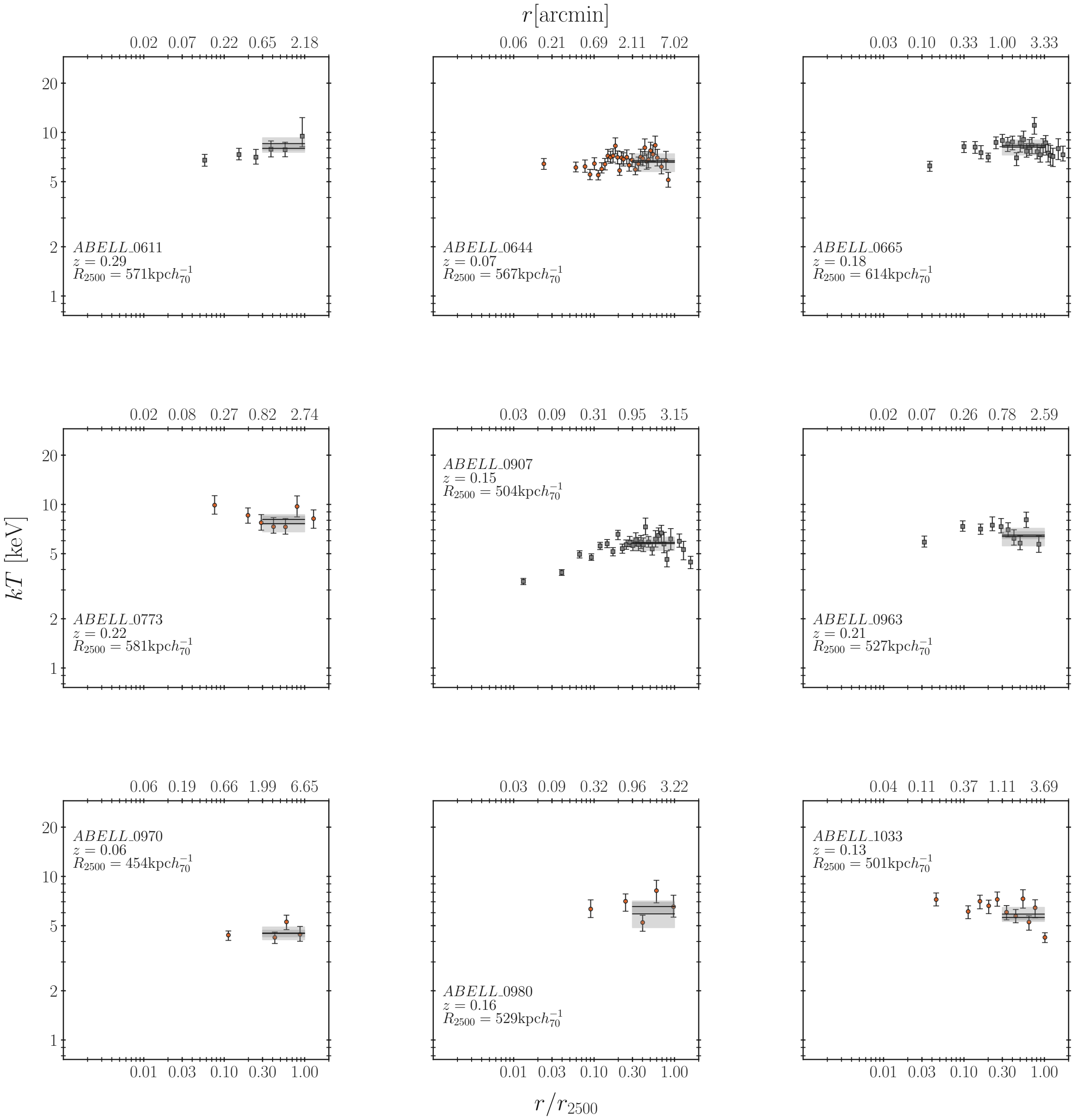
r[arcmin]
kT [keV]
r/r_2500
ABELL_0611
z = 0.29
R_2500 = 571kpch_70^-1
0.02 0.07 0.22 0.65 2.18
ABELL_0644
z = 0.07
R_2500 = 567kpch_70^-1
0.06 0.21 0.69 2.11 7.02
ABELL_0665
z = 0.18
R_2500 = 614kpch_70^-1
0.03 0.10 0.33 1.00 3.33
ABELL_0773
z = 0.22
R_2500 = 581kpch_70^-1
0.02 0.08 0.27 0.82 2.74
ABELL_0907
z = 0.15
R_2500 = 504kpch_70^-1
0.03 0.09 0.31 0.95 3.15
ABELL_0963
z = 0.21
R_2500 = 527kpch_70^-1
0.02 0.07 0.26 0.78 2.59
ABELL_0970
z = 0.06
R_2500 = 454kpch_70^-1
0.06 0.19 0.66 1.99 6.65
ABELL_0980
z = 0.16
R_2500 = 529kpch_70^-1
0.03 0.09 0.32 0.96 3.22
ABELL_1033
z = 0.13
R_2500 = 501kpch_70^-1
0.04 0.11 0.37 1.11 3.69
1 2 5 10 20
0.01 0.03 0.10 0.30 1.00

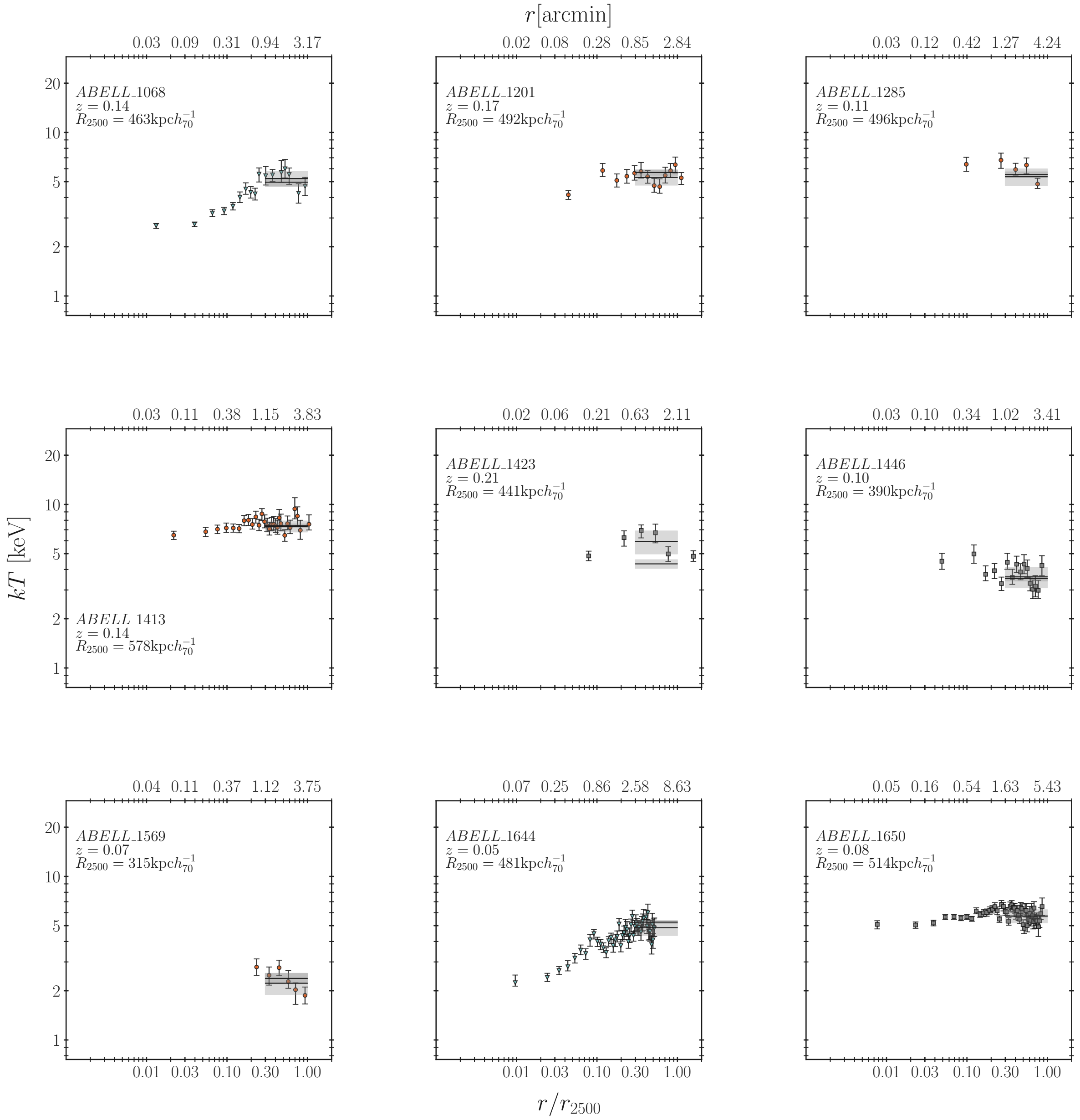
r[arcmin]
kT [keV]
r/r2500
ABELL_1068
z = 0.14
R2500 = 463kpch70^-1
0.03 0.09 0.31 0.94 3.17
ABELL_1201
z = 0.17
R2500 = 492kpch70^-1
0.02 0.08 0.28 0.85 2.84
ABELL_1285
z = 0.11
R2500 = 496kpch70^-1
0.03 0.12 0.42 1.27 4.24
ABELL_1413
z = 0.14
R2500 = 578kpch70^-1
0.03 0.11 0.38 1.15 3.83
ABELL_1423
z = 0.21
R2500 = 441kpch70^-1
0.02 0.06 0.21 0.63 2.11
ABELL_1446
z = 0.10
R2500 = 390kpch70^-1
0.03 0.10 0.34 1.02 3.41
ABELL_1569
z = 0.07
R2500 = 315kpch70^-1
0.04 0.11 0.37 1.12 3.75
ABELL_1644
z = 0.05
R2500 = 481kpch70^-1
0.07 0.25 0.86 2.58 8.63
ABELL_1650
z = 0.08
R2500 = 514kpch70^-1
0.05 0.16 0.54 1.63 5.43
20
10
5
2
1
0.01 0.03 0.10 0.30 1.00

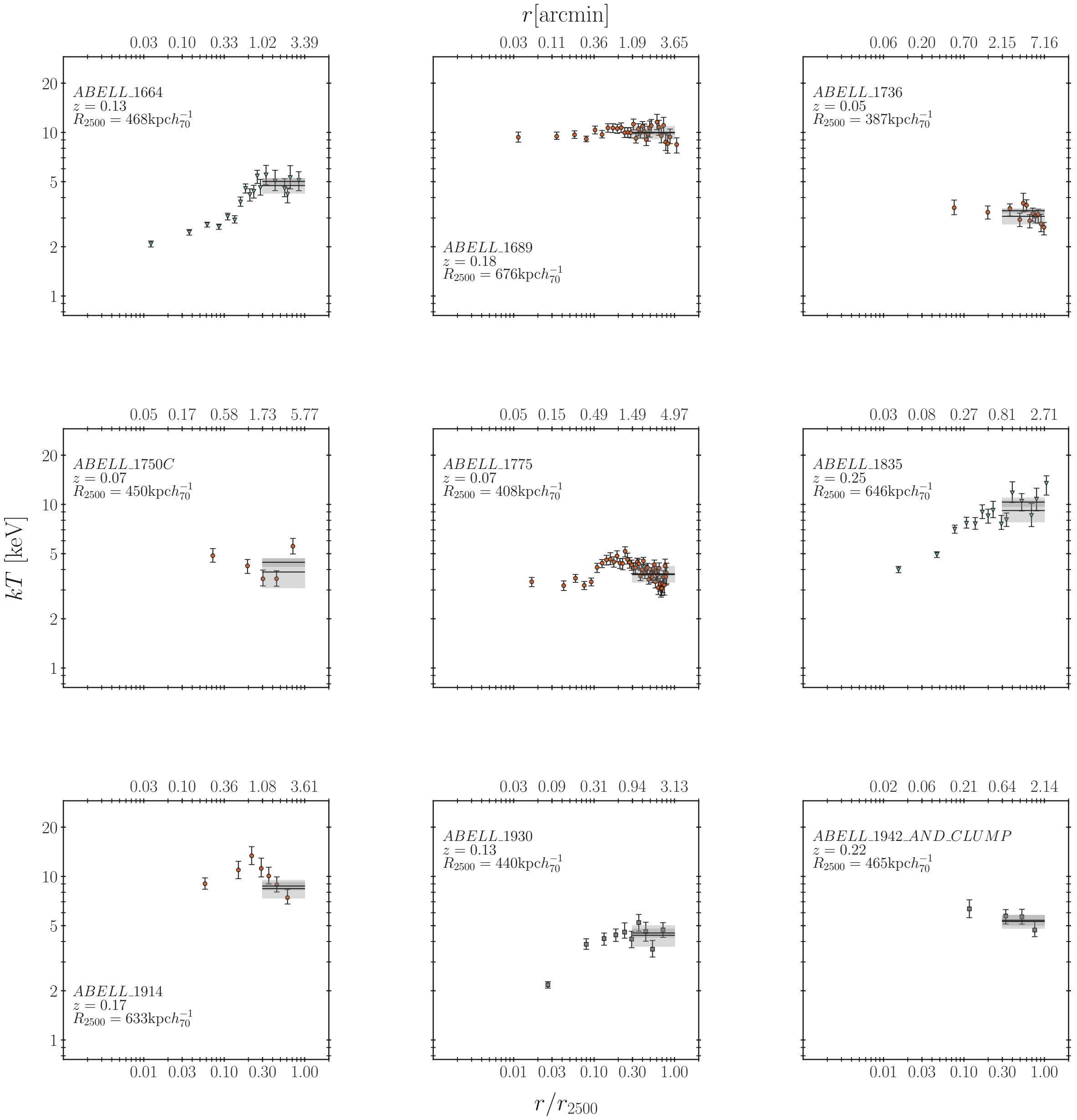

r[arcmin]
kT [keV]
r/r2500
0.03 0.10 0.33 1.02 3.39
ABELL_1664
z = 0.13
R2500 = 468kpch70^-1
0.03 0.11 0.36 1.09 3.65
ABELL_1689
z = 0.18
R2500 = 676kpch70^-1
0.06 0.20 0.70 2.15 7.16
ABELL_1736
z = 0.05
R2500 = 387kpch70^-1
0.05 0.17 0.58 1.73 5.77
ABELL_1750C
z = 0.07
R2500 = 450kpch70^-1
0.05 0.15 0.49 1.49 4.97
ABELL_1775
z = 0.07
R2500 = 408kpch70^-1
0.03 0.08 0.27 0.81 2.71
ABELL_1835
z = 0.25
R2500 = 646kpch70^-1
0.03 0.10 0.36 1.08 3.61
ABELL_1914
z = 0.17
R2500 = 633kpch70^-1
0.03 0.09 0.31 0.94 3.13
ABELL_1930
z = 0.13
R2500 = 440kpch70^-1
0.02 0.06 0.21 0.64 2.14
ABELL_1942_AND_CLUMP
z = 0.22
R2500 = 465kpch70^-1
20
10
5
2
1
0.01 0.03 0.10 0.30 1.00

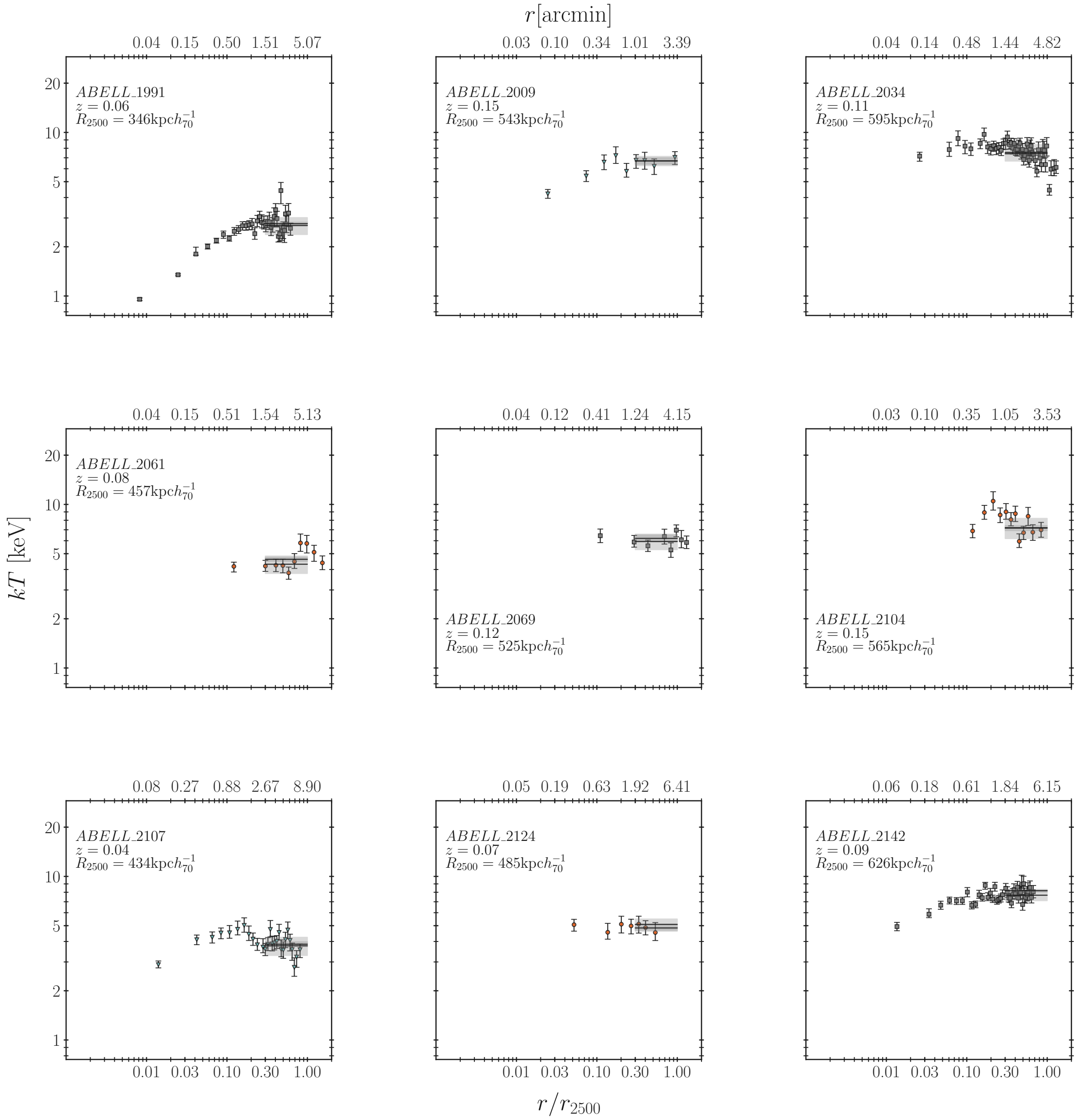
r[arcmin]
0.04 0.15 0.50 1.51 5.07
$ABELL\_1991$
$z = 0.06$
$R_{2500} = 346\mathrm{kpc}h_{70}^{-1}$
0.03 0.10 0.34 1.01 3.39
$ABELL\_2009$
$z = 0.15$
$R_{2500} = 543\mathrm{kpc}h_{70}^{-1}$
0.04 0.14 0.48 1.44 4.82
$ABELL\_2034$
$z = 0.11$
$R_{2500} = 595\mathrm{kpc}h_{70}^{-1}$
0.04 0.15 0.51 1.54 5.13
$ABELL\_2061$
$z = 0.08$
$R_{2500} = 457\mathrm{kpc}h_{70}^{-1}$
0.04 0.12 0.41 1.24 4.15
$ABELL\_2069$
$z = 0.12$
$R_{2500} = 525\mathrm{kpc}h_{70}^{-1}$
0.03 0.10 0.35 1.05 3.53
$ABELL\_2104$
$z = 0.15$
$R_{2500} = 565\mathrm{kpc}h_{70}^{-1}$
0.08 0.27 0.88 2.67 8.90
$ABELL\_2107$
$z = 0.04$
$R_{2500} = 434\mathrm{kpc}h_{70}^{-1}$
0.05 0.19 0.63 1.92 6.41
$ABELL\_2124$
$z = 0.07$
$R_{2500} = 485\mathrm{kpc}h_{70}^{-1}$
0.06 0.18 0.61 1.84 6.15
$ABELL\_2142$
$z = 0.09$
$R_{2500} = 626\mathrm{kpc}h_{70}^{-1}$
kT [keV]
20
10
5
2
1
0.01 0.03 0.10 0.30 1.00
r/r_{2500}

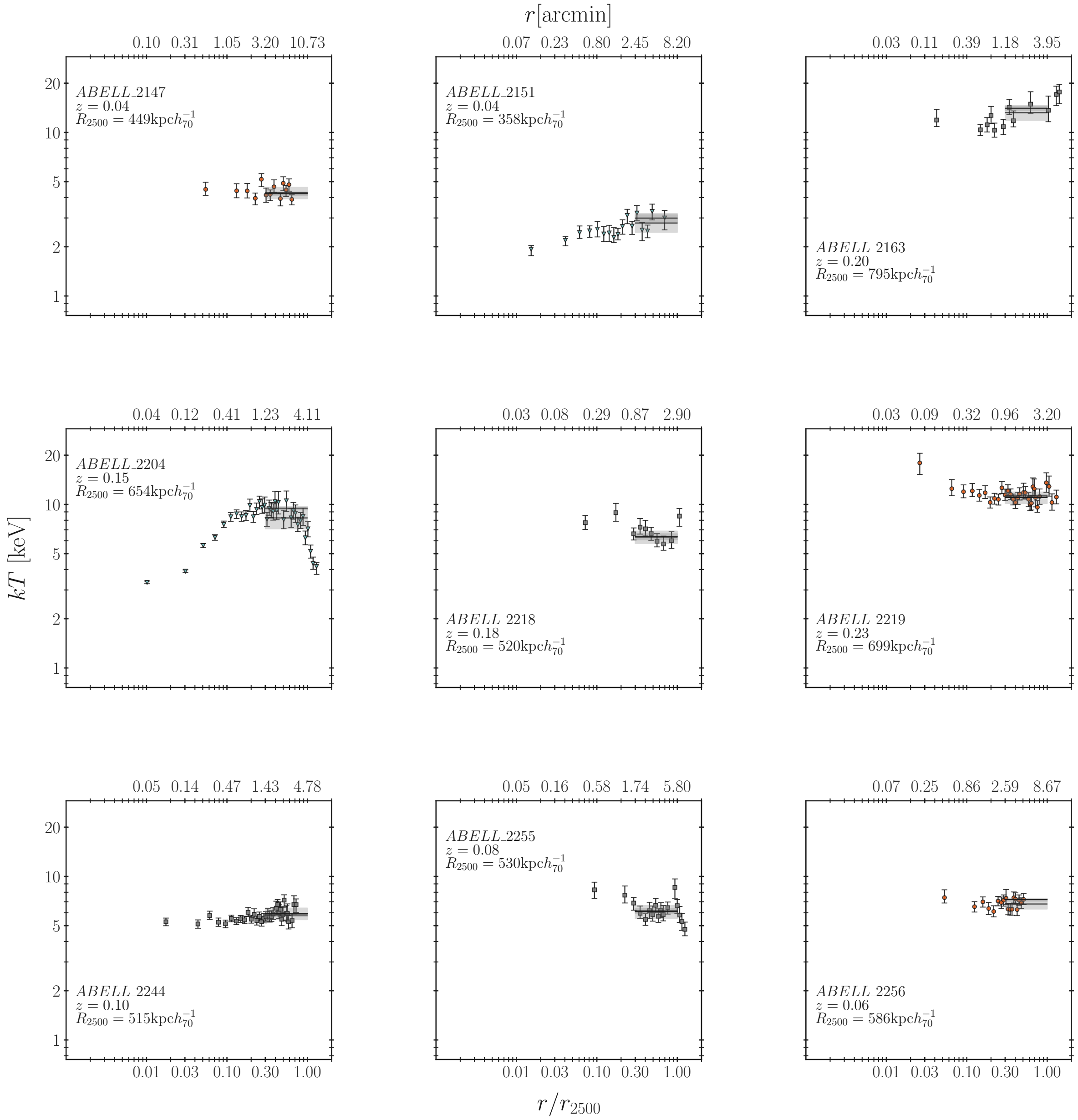
r[arcmin]
0.10 0.31 1.05 3.20 10.73
$ABELL\_2147$
$z = 0.04$
$R_{2500} = 449 \mathrm{kpc} h_{70}^{-1}$
0.07 0.23 0.80 2.45 8.20
$ABELL\_2151$
$z = 0.04$
$R_{2500} = 358 \mathrm{kpc} h_{70}^{-1}$
0.03 0.11 0.39 1.18 3.95
$ABELL\_2163$
$z = 0.20$
$R_{2500} = 795 \mathrm{kpc} h_{70}^{-1}$
0.04 0.12 0.41 1.23 4.11
$ABELL\_2204$
$z = 0.15$
$R_{2500} = 654 \mathrm{kpc} h_{70}^{-1}$
0.03 0.08 0.29 0.87 2.90
$ABELL\_2218$
$z = 0.18$
$R_{2500} = 520 \mathrm{kpc} h_{70}^{-1}$
0.03 0.09 0.32 0.96 3.20
$ABELL\_2219$
$z = 0.23$
$R_{2500} = 699 \mathrm{kpc} h_{70}^{-1}$
0.05 0.14 0.47 1.43 4.78
$ABELL\_2244$
$z = 0.10$
$R_{2500} = 515 \mathrm{kpc} h_{70}^{-1}$
0.05 0.16 0.58 1.74 5.80
$ABELL\_2255$
$z = 0.08$
$R_{2500} = 530 \mathrm{kpc} h_{70}^{-1}$
0.07 0.25 0.86 2.59 8.67
$ABELL\_2256$
$z = 0.06$
$R_{2500} = 586 \mathrm{kpc} h_{70}^{-1}$
kT [keV]
20
10
5
2
1
0.01 0.03 0.10 0.30 1.00
r/r_{2500}

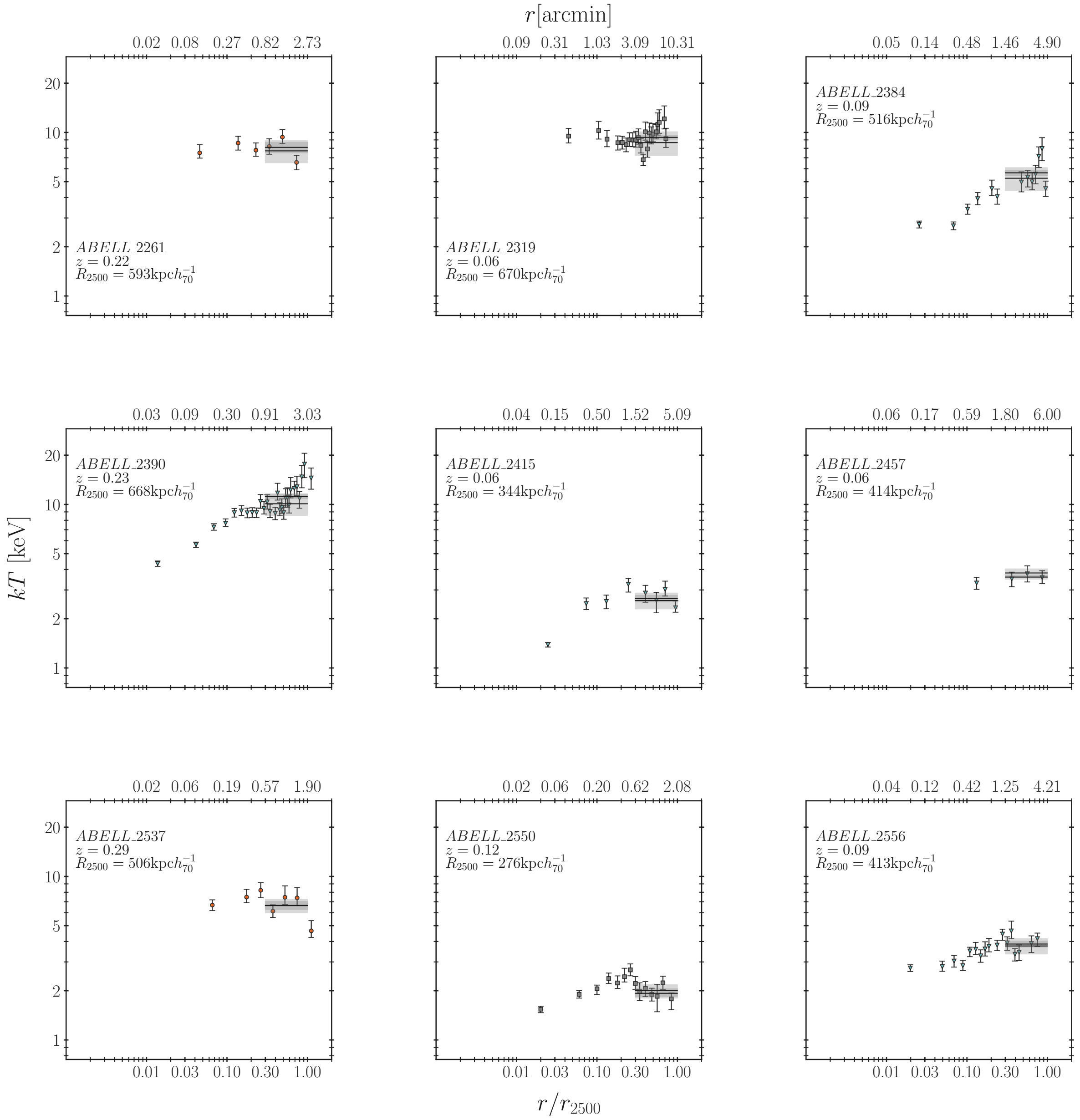
r[arcmin]
0.02 0.08 0.27 0.82 2.73
0.09 0.31 1.03 3.09 10.31
0.05 0.14 0.48 1.46 4.90
ABELL_2261
z = 0.22
R2500 = 593kpch70^-1
ABELL_2319
z = 0.06
R2500 = 670kpch70^-1
ABELL_2384
z = 0.09
R2500 = 516kpch70^-1
0.03 0.09 0.30 0.91 3.03
0.04 0.15 0.50 1.52 5.09
0.06 0.17 0.59 1.80 6.00
ABELL_2390
z = 0.23
R2500 = 668kpch70^-1
ABELL_2415
z = 0.06
R2500 = 344kpch70^-1
ABELL_2457
z = 0.06
R2500 = 414kpch70^-1
0.02 0.06 0.19 0.57 1.90
0.02 0.06 0.20 0.62 2.08
0.04 0.12 0.42 1.25 4.21
ABELL_2537
z = 0.29
R2500 = 506kpch70^-1
ABELL_2550
z = 0.12
R2500 = 276kpch70^-1
ABELL_2556
z = 0.09
R2500 = 413kpch70^-1
kT [keV]
20
10
5
2
1
0.01 0.03 0.10 0.30 1.00
r/r2500

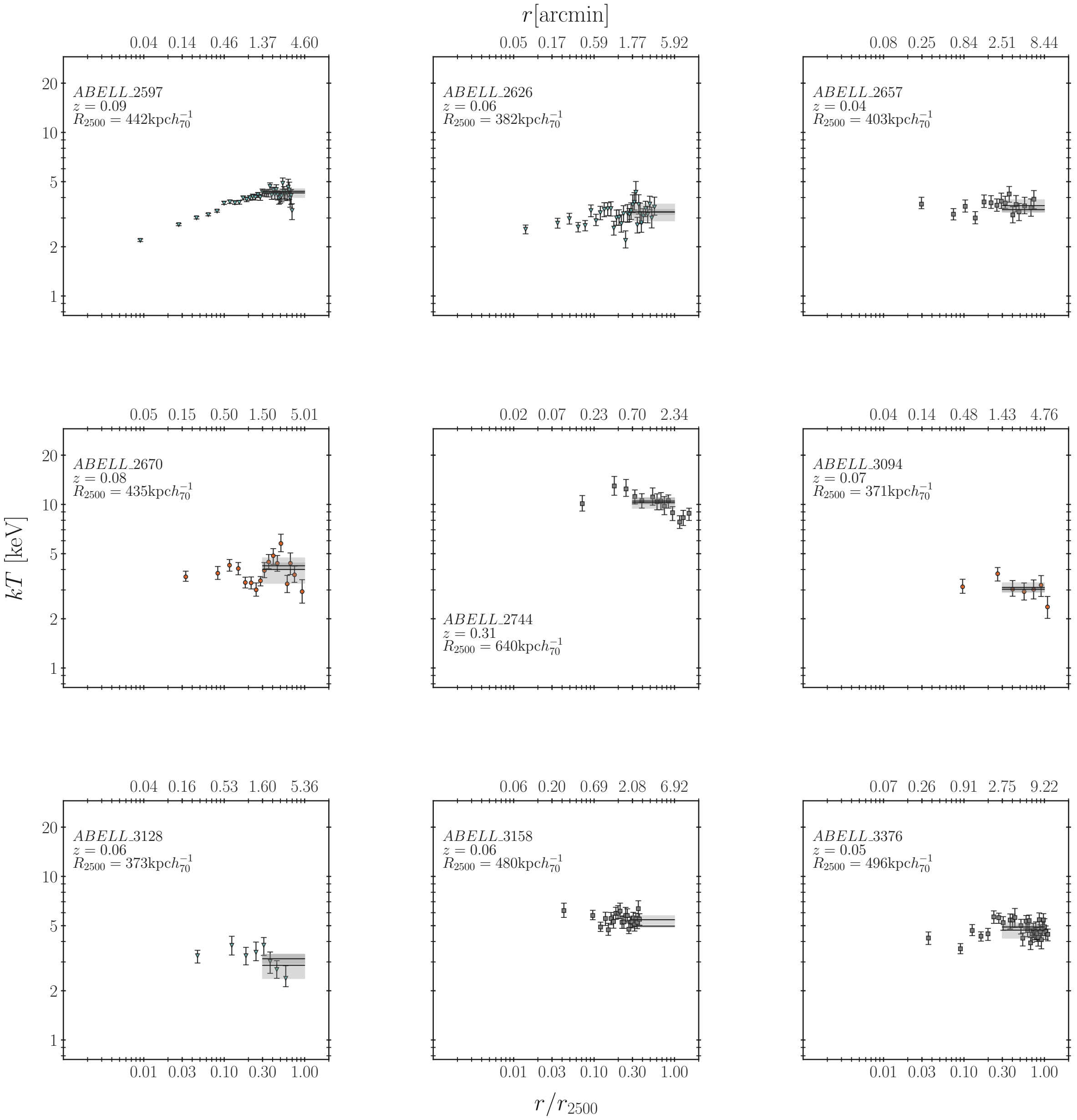
r[arcmin]
0.04 0.14 0.46 1.37 4.60
ABELL_2597
z = 0.09
R2500 = 442kpch70^-1
0.05 0.17 0.59 1.77 5.92
ABELL_2626
z = 0.06
R2500 = 382kpch70^-1
0.08 0.25 0.84 2.51 8.44
ABELL_2657
z = 0.04
R2500 = 403kpch70^-1
0.05 0.15 0.50 1.50 5.01
ABELL_2670
z = 0.08
R2500 = 435kpch70^-1
0.02 0.07 0.23 0.70 2.34
ABELL_2744
z = 0.31
R2500 = 640kpch70^-1
0.04 0.14 0.48 1.43 4.76
ABELL_3094
z = 0.07
R2500 = 371kpch70^-1
0.04 0.16 0.53 1.60 5.36
ABELL_3128
z = 0.06
R2500 = 373kpch70^-1
0.06 0.20 0.69 2.08 6.92
ABELL_3158
z = 0.06
R2500 = 480kpch70^-1
0.07 0.26 0.91 2.75 9.22
ABELL_3376
z = 0.05
R2500 = 496kpch70^-1
kT [keV]
20
10
5
2
1
0.01 0.03 0.10 0.30 1.00
r/r2500

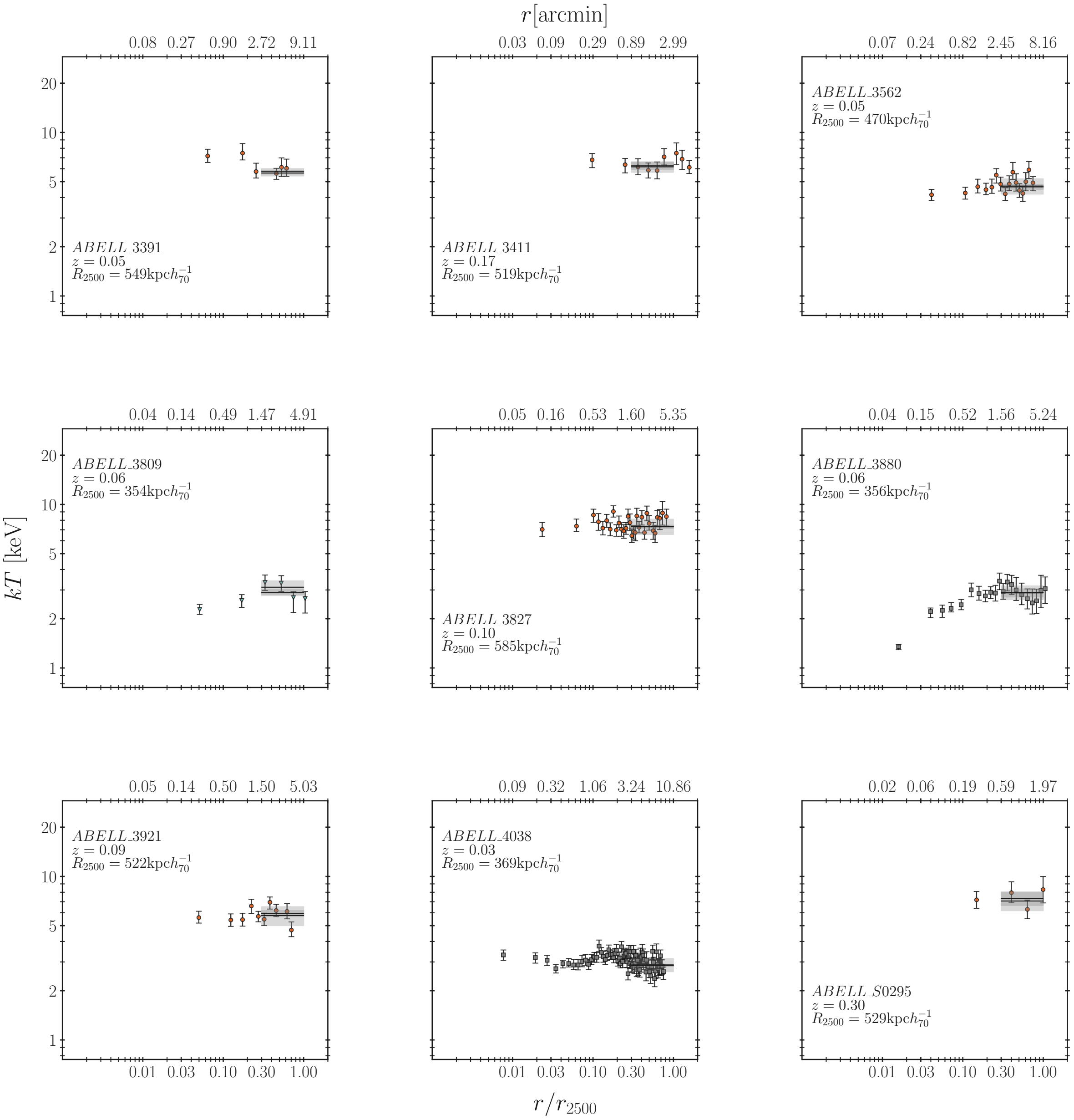
r[arcmin]
kT [keV]
r/r_2500
0.08 0.27 0.90 2.72 9.11
ABELL_3391
z = 0.05
R_2500 = 549kpch_70^-1
0.03 0.09 0.29 0.89 2.99
ABELL_3411
z = 0.17
R_2500 = 519kpch_70^-1
0.07 0.24 0.82 2.45 8.16
ABELL_3562
z = 0.05
R_2500 = 470kpch_70^-1
0.04 0.14 0.49 1.47 4.91
ABELL_3809
z = 0.06
R_2500 = 354kpch_70^-1
0.05 0.16 0.53 1.60 5.35
ABELL_3827
z = 0.10
R_2500 = 585kpch_70^-1
0.04 0.15 0.52 1.56 5.24
ABELL_3880
z = 0.06
R_2500 = 356kpch_70^-1
0.05 0.14 0.50 1.50 5.03
ABELL_3921
z = 0.09
R_2500 = 522kpch_70^-1
0.09 0.32 1.06 3.24 10.86
ABELL_4038
z = 0.03
R_2500 = 369kpch_70^-1
0.02 0.06 0.19 0.59 1.97
ABELL_S0295
z = 0.30
R_2500 = 529kpch_70^-1
20
10
5
2
1
0.01 0.03 0.10 0.30 1.00

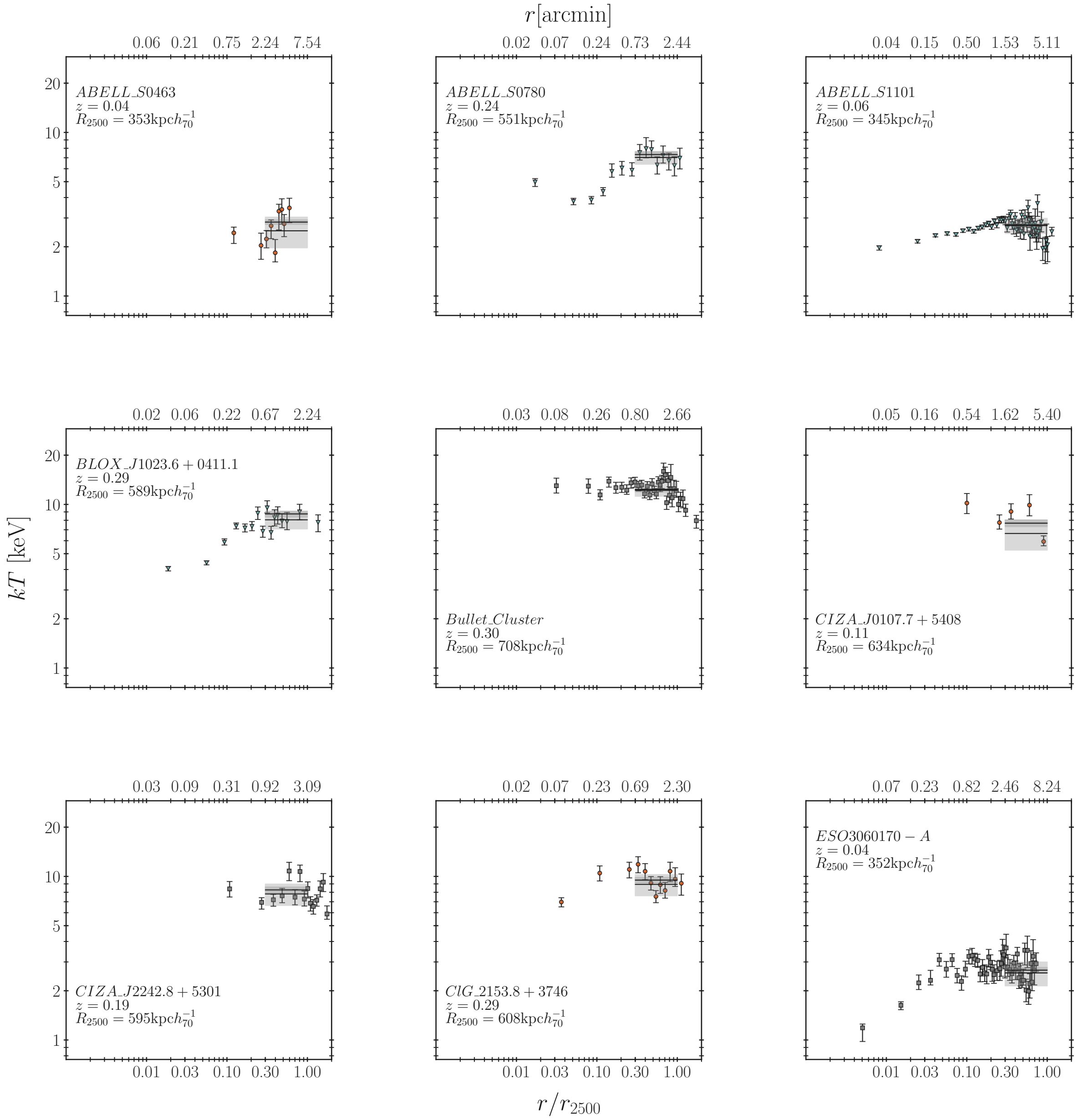
r[arcmin]
0.06 0.21 0.75 2.24 7.54
ABELL_S0463
z = 0.04
R2500 = 353kpch70^-1
0.02 0.07 0.24 0.73 2.44
ABELL_S0780
z = 0.24
R2500 = 551kpch70^-1
0.04 0.15 0.50 1.53 5.11
ABELL_S1101
z = 0.06
R2500 = 345kpch70^-1
0.02 0.06 0.22 0.67 2.24
BLOX_J1023.6 + 0411.1
z = 0.29
R2500 = 589kpch70^-1
0.03 0.08 0.26 0.80 2.66
Bullet_Cluster
z = 0.30
R2500 = 708kpch70^-1
0.05 0.16 0.54 1.62 5.40
CIZA_J0107.7 + 5408
z = 0.11
R2500 = 634kpch70^-1
0.03 0.09 0.31 0.92 3.09
CIZA_J2242.8 + 5301
z = 0.19
R2500 = 595kpch70^-1
0.02 0.07 0.23 0.69 2.30
ClG_2153.8 + 3746
z = 0.29
R2500 = 608kpch70^-1
0.07 0.23 0.82 2.46 8.24
ESO3060170 − A
z = 0.04
R2500 = 352kpch70^-1
kT [keV]
1 2 5 10 20
0.01 0.03 0.10 0.30 1.00
r/r2500

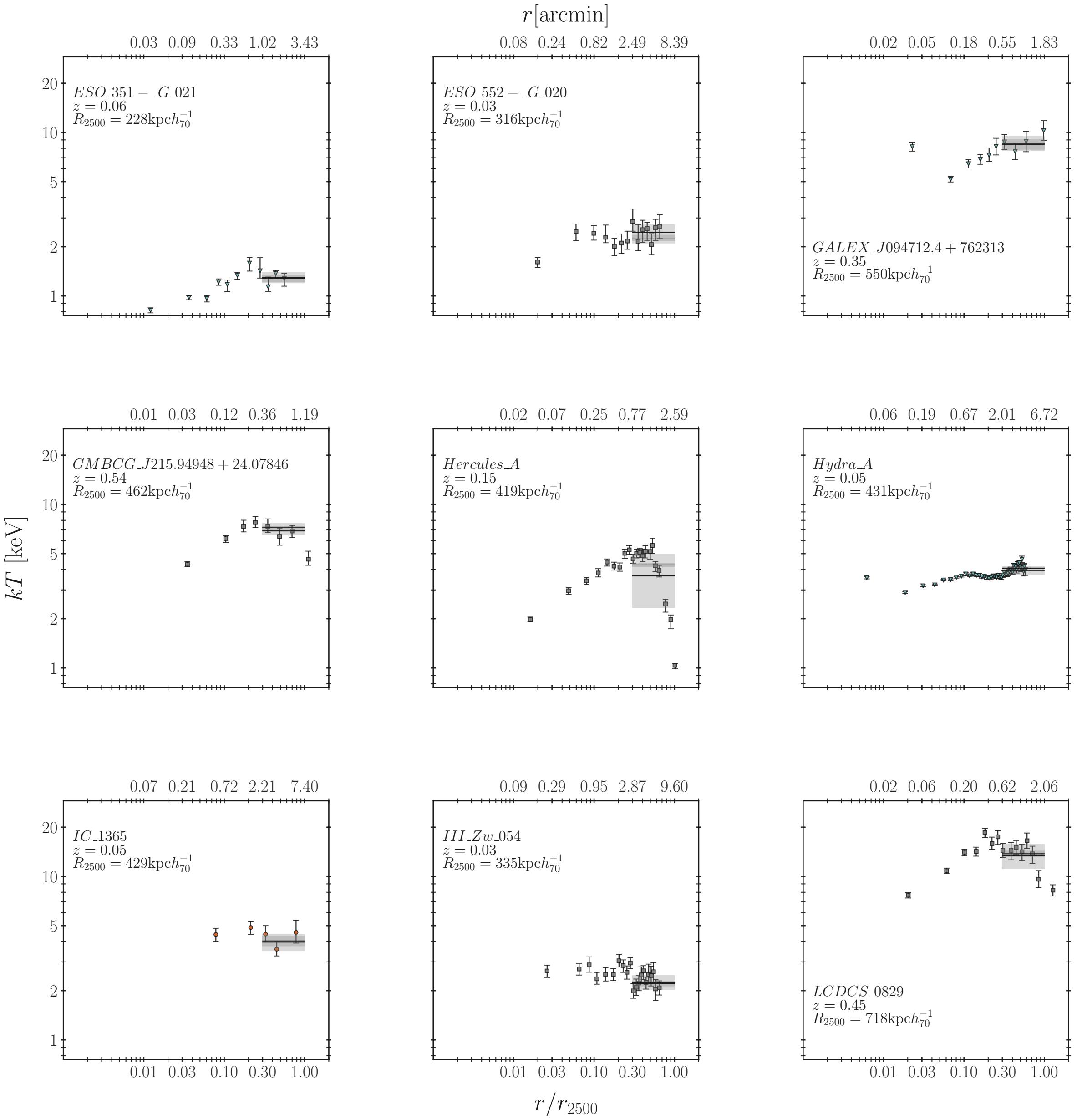

r[arcmin]
kT [keV]
r/r_{2500}
ESO_351 − _G_021
$z = 0.06$
$R_{2500} = 228\mathrm{kpc}h_{70}^{-1}$
ESO_552 − _G_020
$z = 0.03$
$R_{2500} = 316\mathrm{kpc}h_{70}^{-1}$
GALEX_J094712.4 + 762313
$z = 0.35$
$R_{2500} = 550\mathrm{kpc}h_{70}^{-1}$
GMBCG_J215.94948 + 24.07846
$z = 0.54$
$R_{2500} = 462\mathrm{kpc}h_{70}^{-1}$
Hercules_A
$z = 0.15$
$R_{2500} = 419\mathrm{kpc}h_{70}^{-1}$
Hydra_A
$z = 0.05$
$R_{2500} = 431\mathrm{kpc}h_{70}^{-1}$
IC_1365
$z = 0.05$
$R_{2500} = 429\mathrm{kpc}h_{70}^{-1}$
III_Zw_054
$z = 0.03$
$R_{2500} = 335\mathrm{kpc}h_{70}^{-1}$
LCDCS_0829
$z = 0.45$
$R_{2500} = 718\mathrm{kpc}h_{70}^{-1}$
0.03 0.09 0.33 1.02 3.43
0.08 0.24 0.82 2.49 8.39
0.02 0.05 0.18 0.55 1.83
0.01 0.03 0.12 0.36 1.19
0.02 0.07 0.25 0.77 2.59
0.06 0.19 0.67 2.01 6.72
0.07 0.21 0.72 2.21 7.40
0.09 0.29 0.95 2.87 9.60
0.02 0.06 0.20 0.62 2.06
20
10
5
2
1
0.01 0.03 0.10 0.30 1.00

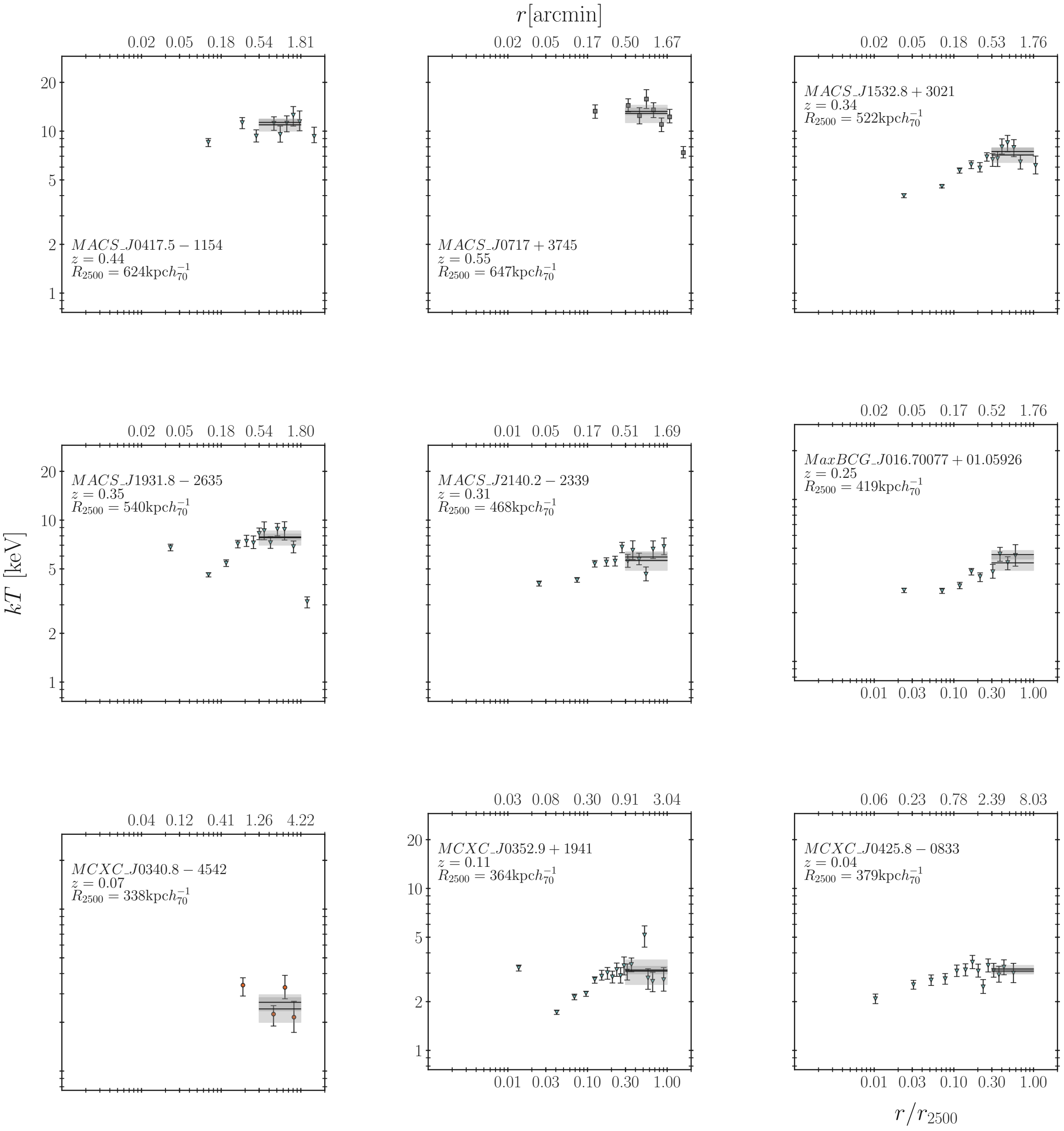
r[arcmin]
kT [keV]
r/r_2500
MACS_J0417.5 − 1154
z = 0.44
R_2500 = 624kpch_70^−1
0.02 0.05 0.18 0.54 1.81
MACS_J0717 + 3745
z = 0.55
R_2500 = 647kpch_70^−1
0.02 0.05 0.17 0.50 1.67
MACS_J1532.8 + 3021
z = 0.34
R_2500 = 522kpch_70^−1
0.02 0.05 0.18 0.53 1.76
MACS_J1931.8 − 2635
z = 0.35
R_2500 = 540kpch_70^−1
0.02 0.05 0.18 0.54 1.80
MACS_J2140.2 − 2339
z = 0.31
R_2500 = 468kpch_70^−1
0.01 0.05 0.17 0.51 1.69
MaxBCG_J016.70077 + 01.05926
z = 0.25
R_2500 = 419kpch_70^−1
0.02 0.05 0.17 0.52 1.76
MCXC_J0340.8 − 4542
z = 0.07
R_2500 = 338kpch_70^−1
0.04 0.12 0.41 1.26 4.22
MCXC_J0352.9 + 1941
z = 0.11
R_2500 = 364kpch_70^−1
0.03 0.08 0.30 0.91 3.04
MCXC_J0425.8 − 0833
z = 0.04
R_2500 = 379kpch_70^−1
0.06 0.23 0.78 2.39 8.03
20
10
5
2
1
0.01 0.03 0.10 0.30 1.00

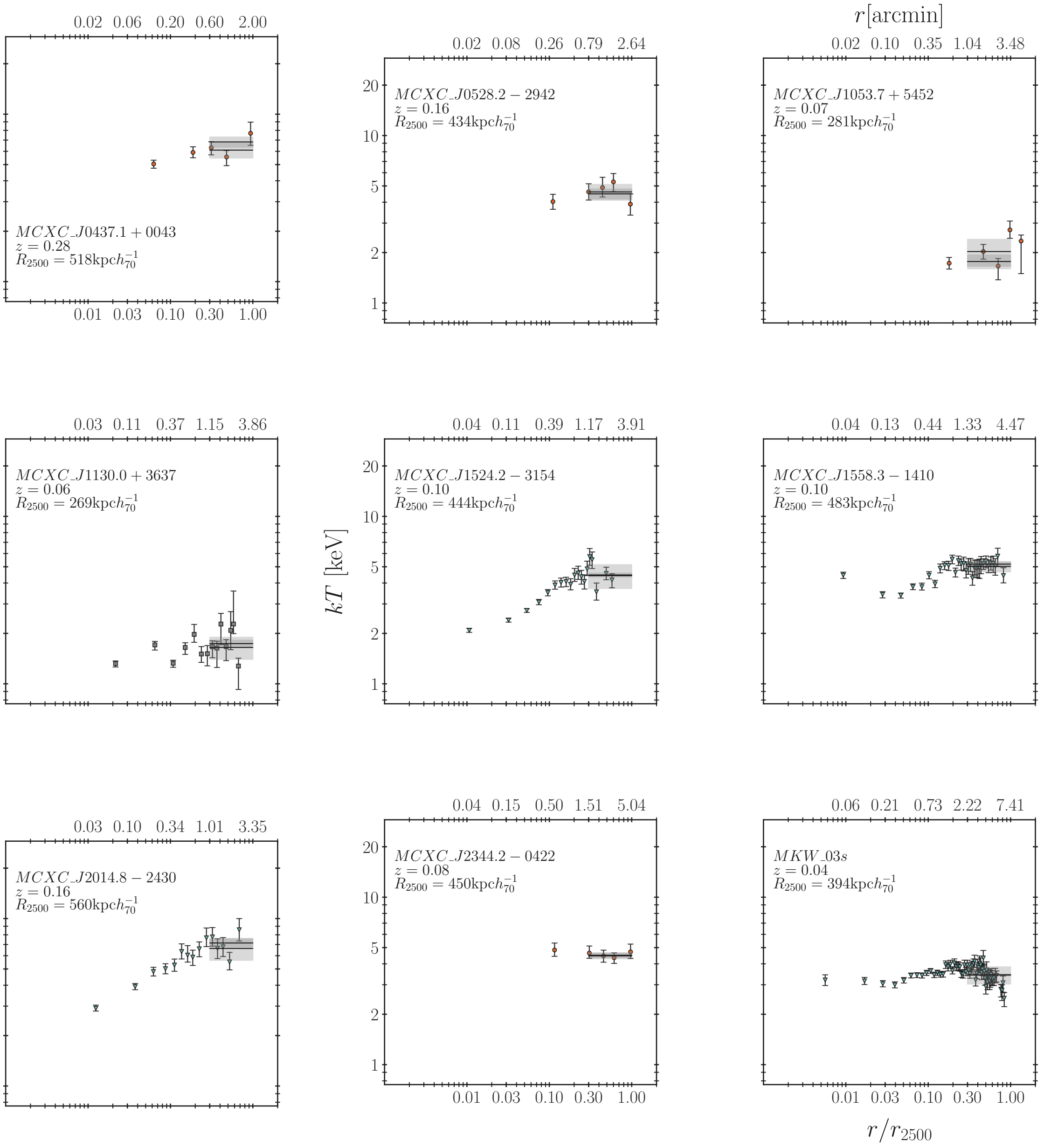

r[arcmin]
0.02 0.06 0.20 0.60 2.00
$MCXC\_J0437.1+0043$
$z = 0.28$
$R_{2500} = 518\mathrm{kpc}h_{70}^{-1}$
0.01 0.03 0.10 0.30 1.00
0.02 0.08 0.26 0.79 2.64
$MCXC\_J0528.2-2942$
$z = 0.16$
$R_{2500} = 434\mathrm{kpc}h_{70}^{-1}$
0.02 0.10 0.35 1.04 3.48
$MCXC\_J1053.7+5452$
$z = 0.07$
$R_{2500} = 281\mathrm{kpc}h_{70}^{-1}$
0.03 0.11 0.37 1.15 3.86
$MCXC\_J1130.0+3637$
$z = 0.06$
$R_{2500} = 269\mathrm{kpc}h_{70}^{-1}$
0.04 0.11 0.39 1.17 3.91
$MCXC\_J1524.2-3154$
$z = 0.10$
$R_{2500} = 444\mathrm{kpc}h_{70}^{-1}$
0.04 0.13 0.44 1.33 4.47
$MCXC\_J1558.3-1410$
$z = 0.10$
$R_{2500} = 483\mathrm{kpc}h_{70}^{-1}$
kT [keV]
20
10
5
2
1
0.03 0.10 0.34 1.01 3.35
$MCXC\_J2014.8-2430$
$z = 0.16$
$R_{2500} = 560\mathrm{kpc}h_{70}^{-1}$
0.04 0.15 0.50 1.51 5.04
$MCXC\_J2344.2-0422$
$z = 0.08$
$R_{2500} = 450\mathrm{kpc}h_{70}^{-1}$
0.01 0.03 0.10 0.30 1.00
0.06 0.21 0.73 2.22 7.41
MKW_03s
$z = 0.04$
$R_{2500} = 394\mathrm{kpc}h_{70}^{-1}$
0.01 0.03 0.10 0.30 1.00
r/r_{2500}

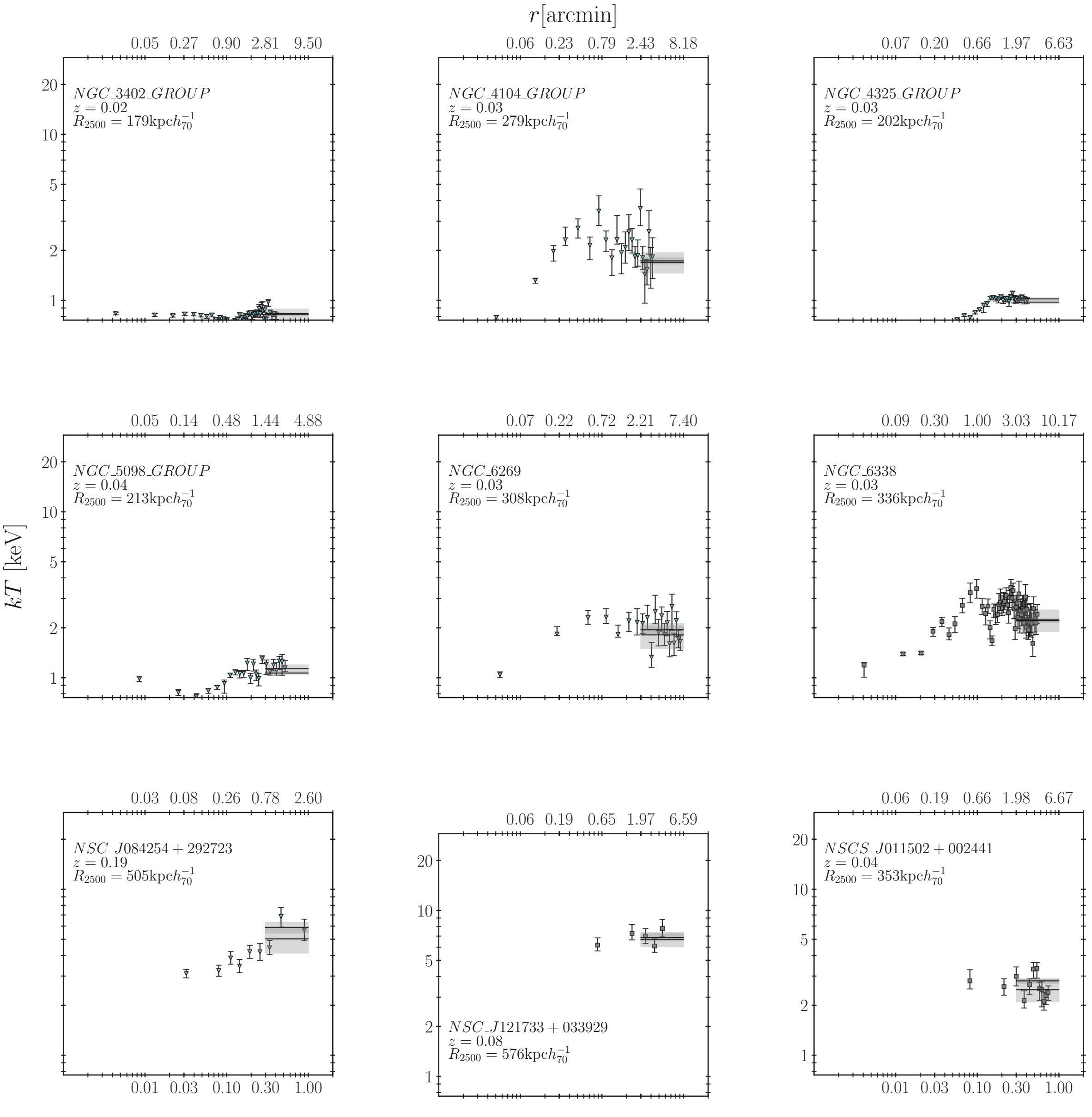
r[arcmin]
kT [keV]
0.05 0.27 0.90 2.81 9.50
NGC_3402_GROUP
$z = 0.02$
$R_{2500} = 179\mathrm{kpc}h_{70}^{-1}$
0.06 0.23 0.79 2.43 8.18
NGC_4104_GROUP
$z = 0.03$
$R_{2500} = 279\mathrm{kpc}h_{70}^{-1}$
0.07 0.20 0.66 1.97 6.63
NGC_4325_GROUP
$z = 0.03$
$R_{2500} = 202\mathrm{kpc}h_{70}^{-1}$
0.05 0.14 0.48 1.44 4.88
NGC_5098_GROUP
$z = 0.04$
$R_{2500} = 213\mathrm{kpc}h_{70}^{-1}$
0.07 0.22 0.72 2.21 7.40
NGC_6269
$z = 0.03$
$R_{2500} = 308\mathrm{kpc}h_{70}^{-1}$
0.09 0.30 1.00 3.03 10.17
NGC_6338
$z = 0.03$
$R_{2500} = 336\mathrm{kpc}h_{70}^{-1}$
0.03 0.08 0.26 0.78 2.60
$NSC\_J084254 + 292723$
$z = 0.19$
$R_{2500} = 505\mathrm{kpc}h_{70}^{-1}$
0.01 0.03 0.10 0.30 1.00
0.06 0.19 0.65 1.97 6.59
$NSC\_J121733 + 033929$
$z = 0.08$
$R_{2500} = 576\mathrm{kpc}h_{70}^{-1}$
0.06 0.19 0.66 1.98 6.67
$NSCS\_J011502 + 002441$
$z = 0.04$
$R_{2500} = 353\mathrm{kpc}h_{70}^{-1}$
0.01 0.03 0.10 0.30 1.00
20
10
5
2
1

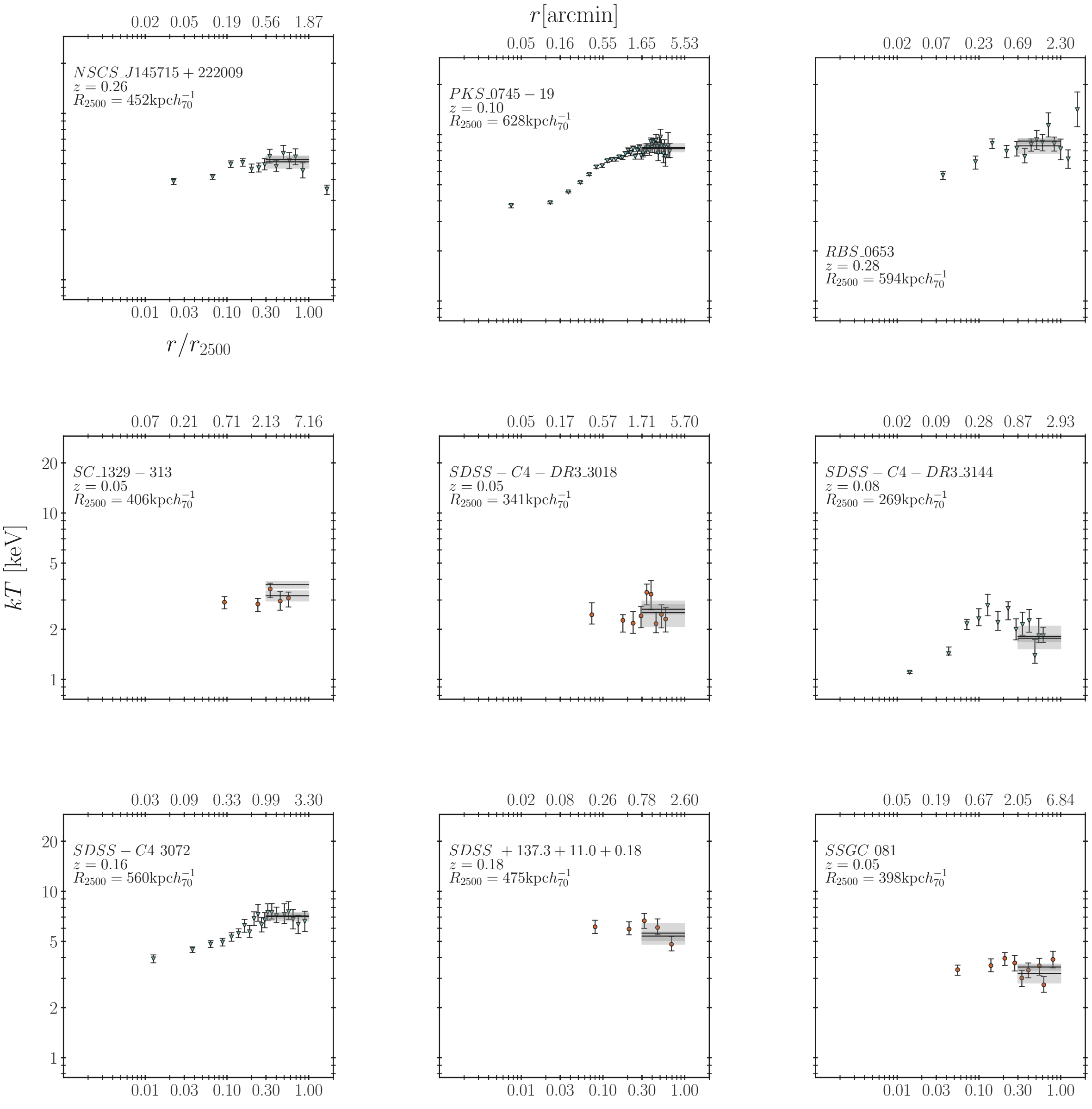
r[arcmin]
kT [keV]
r/r2500
NSCS_J145715 + 222009
z = 0.26
R2500 = 452kpch70^-1
0.02 0.05 0.19 0.56 1.87
PKS_0745 − 19
z = 0.10
R2500 = 628kpch70^-1
0.05 0.16 0.55 1.65 5.53
RBS_0653
z = 0.28
R2500 = 594kpch70^-1
0.02 0.07 0.23 0.69 2.30
SC_1329 − 313
z = 0.05
R2500 = 406kpch70^-1
0.07 0.21 0.71 2.13 7.16
SDSS − C4 − DR3_3018
z = 0.05
R2500 = 341kpch70^-1
0.05 0.17 0.57 1.71 5.70
SDSS − C4 − DR3_3144
z = 0.08
R2500 = 269kpch70^-1
0.02 0.09 0.28 0.87 2.93
SDSS − C4_3072
z = 0.16
R2500 = 560kpch70^-1
0.03 0.09 0.33 0.99 3.30
SDSS_ + 137.3 + 11.0 + 0.18
z = 0.18
R2500 = 475kpch70^-1
0.02 0.08 0.26 0.78 2.60
SSGC_081
z = 0.05
R2500 = 398kpch70^-1
0.05 0.19 0.67 2.05 6.84
1 2 5 10 20
0.01 0.03 0.10 0.30 1.00

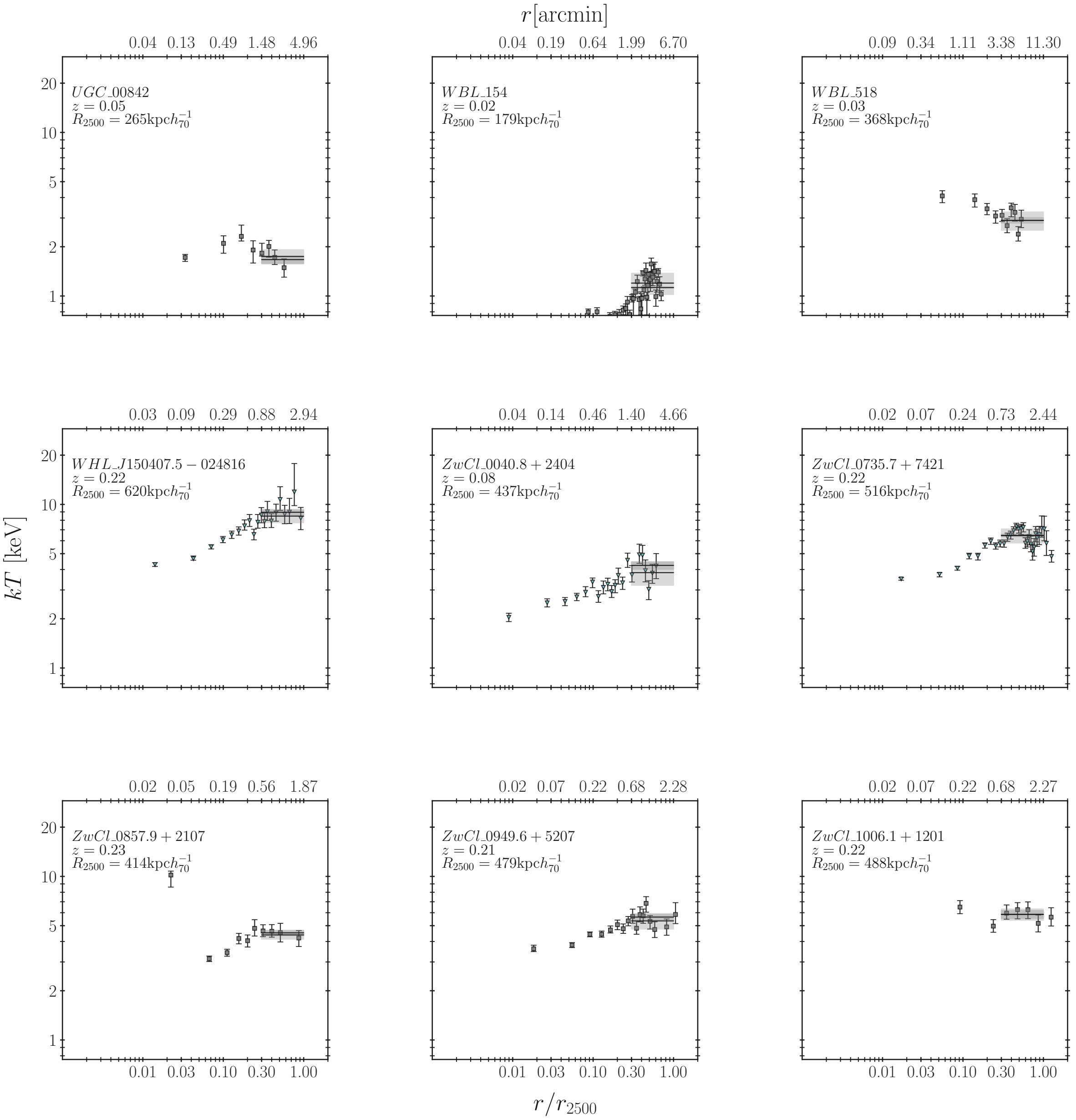
r[arcmin]
0.04 0.13 0.49 1.48 4.96
0.04 0.19 0.64 1.99 6.70
0.09 0.34 1.11 3.38 11.30
UGC_00842
$z = 0.05$
$R_{2500} = 265\mathrm{kpc}h_{70}^{-1}$
WBL_154
$z = 0.02$
$R_{2500} = 179\mathrm{kpc}h_{70}^{-1}$
WBL_518
$z = 0.03$
$R_{2500} = 368\mathrm{kpc}h_{70}^{-1}$
0.03 0.09 0.29 0.88 2.94
0.04 0.14 0.46 1.40 4.66
0.02 0.07 0.24 0.73 2.44
$WHL\_J150407.5-024816$
$z = 0.22$
$R_{2500} = 620\mathrm{kpc}h_{70}^{-1}$
$ZwCl\_0040.8+2404$
$z = 0.08$
$R_{2500} = 437\mathrm{kpc}h_{70}^{-1}$
$ZwCl\_0735.7+7421$
$z = 0.22$
$R_{2500} = 516\mathrm{kpc}h_{70}^{-1}$
0.02 0.05 0.19 0.56 1.87
0.02 0.07 0.22 0.68 2.28
0.02 0.07 0.22 0.68 2.27
$ZwCl\_0857.9+2107$
$z = 0.23$
$R_{2500} = 414\mathrm{kpc}h_{70}^{-1}$
$ZwCl\_0949.6+5207$
$z = 0.21$
$R_{2500} = 479\mathrm{kpc}h_{70}^{-1}$
$ZwCl\_1006.1+1201$
$z = 0.22$
$R_{2500} = 488\mathrm{kpc}h_{70}^{-1}$
kT [keV]
20
10
5
2
1
0.01 0.03 0.10 0.30 1.00
r/r_{2500}

BIBLIOGRAPHY

BIBLIOGRAPHY

Abell, G. O. 1958, The Astrophysical Journal Supplement Series, 3, 211

Ahn, C. P., Alexandroff, R., Allende Prieto, C., et al. 2012, The Astrophysical Journal Supplement Series, 203, 21

Alam, S., Albareti, F. D., Allende Prieto, C., et al. 2015, ApJS, 219, 12. `https://arxiv.org/abs/1501.00963`

Anders, E., & Grevesse, N. 1989, Geochimica et Cosmochimica Acta, 53, 197

Anderson, M. E., Bregman, J. N., Butler, S. C., & Mullis, C. R. 2009, The Astrophysical Journal, 698, 317, doi: `10.1088/0004-637x/698/1/317`

Andrade-Santos, F., Jones, C., Forman, W. R., et al. 2017, The Astrophysical Journal, 843, 76

Arnaud, K. A. 1996, in Astronomical Society of the Pacific Conference Series, Vol. 101, Astronomical Data Analysis Software and Systems V, ed. G. H. Jacoby & J. Barnes, 17

Arnaud, M., Aghanim, N., & Neumann, D. M. 2002, Astronomy & Astrophysics, 389, 1

Arnaud, M., & Evrard, A. E. 1999, Monthly Notices of the Royal Astronomical Society, 305, 631

Baldi, A., Ettori, S., Molendi, S., et al. 2012, Astronomy & Astrophysics, 537, A142, doi: `10.1051/0004-6361/201117836`

Balestra, I., Tozzi, P., Ettori, S., et al. 2007, Astronomy & Astrophysics, 462, 429, doi: `10.1051/0004-6361:20065568`

Balestra, I., Tozzi, P., Ettori, S., et al. 2006, Astronomy & Astrophysics, 462, 429, doi: `10.1051/0004-6361:20065568`

Bennett, C. L., Hill, R. S., Hinshaw, G., et al. 2011, The Astrophysical Journal Supplement Series, 192, 17

Biffi, V., Planelles, S., Borgani, S., et al. 2017, Monthly Notices of the Royal Astronomical Society, 468, 531, doi: `10.1093/mnras/stx444`

Bleem, L. E., Stalder, B., de Haan, T., et al. 2015, The Astrophysical Journal Supplement Series, 216, 27. `https://arxiv.org/abs/1409.0850`

Böhringer, H., & Werner, N. 2009, The Astronomy and Astrophysics Review, 18, 127

Borgani, S., Fabjan, D., Tornatore, L., et al. 2008, Space Science Reviews, 134, 379, doi: `10.1007/s11214-008-9322-7`

Bower, R. G. 1997, Monthly Notices of the Royal Astronomical Society, 288, 355

Bower, R. G., Benson, A. J., Malbon, R., et al. 2006, Monthly Notices of the Royal Astronomical Society, 370, 645

Bradt, H., Mayer, W., Naranan, S., Rappaport, S., & Spada, G. 1967, The Astrophysical Journal, 150, L199

Branduardi-Raymont, G., Fabricant, D., Feigelson, E., et al. 1981, The Astrophysical Journal, 248, 55

Branduardi-Raymont, G., Mason, K. O., Murdin, P. G., & Martin, C. 1985, Monthly Notices of the Royal Astronomical Society, 216, 1043

Briel, U. G., Henry, J. P., & Boehringer, H. 1992, Astronomy & Astrophysics, 259, L31

Buote, D. A. 2000, Monthly Notices of the Royal Astronomical Society, 311, 176, doi: `10.1046/j.1365-8711.2000.03046.x`

Caminha, G. B., Grillo, C., Rosati, P., et al. 2017, Astronomy & Astrophysics, 600, A90. `https://arxiv.org/abs/1607.03462`

Cavagnolo, K. W., Donahue, M., Voit, G. M., & Sun, M. 2009, The Astrophysical Journal Supplement Series, 182, 12, doi: `10.1088/0067-0049/182/1/12`

Cavaliere, A., Menci, N., & Tozzi, P. 1997, The Astrophysical Journal, 484, L21, doi: `10.1086/310767`

Colgate, S. A. 1979, The Astrophysical Journal, 232, 404

Craig, M., Crawford, S., Seifert, M., et al. 2017, astropy/ccdproc: v1.3.0.post1, v1.3.0.post1, Zenodo, doi: `10.5281/zenodo.1069648`. `https://doi.org/10.5281/zenodo.1069648`

De Grandi, S., Ettori, S., Longhetti, M., & Molendi, S. 2004, Astronomy & Astrophysics, 419, 7, doi: `10.1051/0004-6361:20034228`

De Grandi, S., & Molendi, S. 2001, The Astrophysical Journal, 551, 153, doi: `10.1086/320098`

Dickey, J. M., & Lockman, F. J. 1990, Annual Review of Astronomy and Astrophysics, 28, 215

Donahue, M., Horner, D. J., Cavagnolo, K. W., & Voit, G. M. 2006, The Astrophysical Journal, 643, 730

Donahue, M., Scharf, C. A., Mack, J., et al. 2002, The Astrophysical Journal, 569, 689, doi: `10.1086/339401`

Eckert, D., Molendi, S., & Paltani, S. 2011, Astronomy & Astrophysics, 526, A79, doi: `10.1051/0004-6361/201015856`

Ettori, S. 2005, Monthly Notices of the Royal Astronomical Society, 362, 110, doi: `10.1111/j.1365-2966.2005.09284.x`

Ettori, S., Baldi, A., Balestra, I., et al. 2015, Astronomy & Astrophysics, 578, A46, doi: `10.1051/0004-6361/201425470`

Ettori, S., Tozzi, P., Borgani, S., & Rosati, P. 2004, Astronomy & Astrophysics, 417, 13

Fabian, A. C. 1994, Annual Review of Astronomy and Astrophysics, 32, 277, doi: `10.1146/annurev.aa.32.090194.001425`

Fabian, A. C., Arnaud, K. A., Bautz, M. W., & Tawara, Y. 1994, The Astrophysical Journal, 436, L63, doi: `10.1086/187633`

Forman, W., Kellogg, E., Gursky, H., Tananbaum, H., & Giacconi, R. 1972, The Astrophysical Journal, 178, 309, doi: `10.1086/151791`

Freeman, P., Doe, S., & Siemiginowska, A. 2001, Astronomical Data Analysis

Fruscione, A., McDowell, J. C., Allen, G. E., et al. 2006, in Society of Photo-Optical Instrumentation Engineers (SPIE) Conference Series, Vol. 6270, Society of Photo-Optical Instrumentation Engineers (SPIE) Conference Series, 62701V

Fukazawa, Y., Ohashi, T., Fabian, A. C., et al. 1994, Publications of the Astronomical Society of Japan, 46, L55

Gursky, H., Kellogg, E., Murray, S., et al. 1971, The Astrophysical Journal, 167, L81

Hogan, M. T., McNamara, B. R., Pulido, F. A., et al. 2017, The Astrophysical Journal, 851, 66

Horne, K. 1986, Publications of the Astronomical Society of the Pacific, 98, 609

Hubble, E. 1936, The Astrophysical Journal, 84, 517

Jones, C., & Forman, W. 1984, The Astrophysical Journal, 276, 38

—. 1999, The Astrophysical Journal, 511, 65

Kaastra, J. S., Mewe, R., & Nieuwenhuijzen, H. 1996, in UV and X-ray Spectroscopy of Astrophysical and Laboratory Plasmas, 411–414

Kaiser, N. 1986, Monthly Notices of the Royal Astronomical Society, 222, 323

Kinney, A. L., Calzetti, D., Bohlin, R. C., et al. 1996, The Astrophysical Journal, 467, 38

Leccardi, A., & Molendi, S. 2008, Astronomy & Astrophysics, 487, 461, doi: `10.1051/0004-6361:200810113`

Leccardi, A., Rossetti, M., & Molendi, S. 2010, Astronomy & Astrophysics, 510, A82, doi: `10.1051/0004-6361/200913094`

Liedahl, D. A., Osterheld, A. L., & Goldstein, W. H. 1995, The Astrophysical Journal, 438, L115, doi: `10.1086/187729`

Lucas, R. A., Desjardins, T. D., & STScI ACS (Advanced CameraSurveys) Team. 2018, in American Astronomical Society Meeting Abstracts, Vol. 232, American Astronomical Society Meeting Abstracts #232, 119.03

Mantz, A. B., Allen, S. W., Morris, R. G., et al. 2017, Monthly Notices of the Royal Astronomical Society, 472, 2877, doi: `10.1093/mnras/stx2200`

Markevitch, M. 1998, The Astrophysical Journal, 504, 27, doi: `10.1086/306080`

Marsh, T. R. 1989, Publications of the Astronomical Society of the Pacific, 101, 1032

Maughan, B. J., Giles, P. A., Randall, S. W., Jones, C., & Forman, W. R. 2012, Monthly Notices of the Royal Astronomical Society, 421, 1583, doi: `10.1111/j.1365-2966.2012.20419.x`

Maughan, B. J., Giles, P. A., Randall, S. W., Jones, C., & Forman, W. R. 2012, Monthly Notices of the Royal Astronomical Society, 421, 1583

Maughan, B. J., Jones, C., Forman, W., & Van Speybroeck, L. 2008, The Astrophysical Journal Supplement Series, 174, 117, doi: `10.1086/521225`

McDonald, M., Stalder, B., Bayliss, M., et al. 2016, The Astronomical Journal, 817, 86. `https://arxiv.org/abs/1508.06283`

McDonald, M., Bulbul, E., Haan, T. d., et al. 2016, The Astrophysical Journal, 826, 124, doi: `10.3847/0004-637x/826/2/124`

McNamara, B., & Nulsen, P. 2007, Annual Review of Astronomy and Astrophysics, 45, 117

Meekins, J. F., Fritz, G., Chubb, T. A., Friedman, H., & Henry, Richard, C. 1971, Nature, 231, 107

Mernier, F., de Plaa, J., Kaastra, J. S., et al. 2017, Astronomy & Astrophysics, 603, A80, doi: `10.1051/0004-6361/201630075`

Mernier, F., Biffi, V., Yamaguchi, H., et al. 2018, Space Science Reviews, 214, doi: `10.1007/s11214-018-0565-7`

Migkas, K., Schellenberger, G., Reiprich, T. H., et al. 2020, Astronomy & Astrophysics, 636, A15, doi: `10.1051/0004-6361/201936602`

Mitchell, R. J., & Culhane, J. L. 1977, Monthly Notices of the Royal Astronomical Society, 178, 75P, doi: `10.1093/mnras/178.1.75p`

Mitchell, R. J., Culhane, J. L., Davison, P. J. N., & Ives, J. C. 1976, Monthly Notices of the Royal Astronomical Society, 175, 29P, doi: `10.1093/mnras/175.1.29p`

Mittal, R., Hicks, A., Reiprich, T. H., & Jaritz, V. 2011, The Astrophysical Journal, 532, A133, doi: `10.1051/0004-6361/200913714`

Mushotzky, R., Loewenstein, M., Arnaud, K. A., et al. 1996, The Astrophysical Journal, 466, 686, doi: `10.1086/177541`

Mushotzky, R. F., & Loewenstein, M. 1997, The Astrophysical Journal, 481, L63, doi: `10.1086/310651`

Neumann, D. M. 2005, Astronomy & Astrophysics, 439, 465, doi: `10.1051/0004-6361:20053015`

Neumann, D. M., & Arnaud, M. 1999, Astronomy & Astrophysics, 348, 711. `https://arxiv.org/abs/astro-ph/9901092`

Panagoulia, E. K., Fabian, A. C., & Sanders, J. S. 2013, Monthly Notices of the Royal Astronomical Society, 438, 2341

Pearce, F. R., Thomas, P. A., Couchman, H. M. P., & Edge, A. C. 2000, Monthly Notices of the Royal Astronomical Society, 317, 1029

Pence, W. D., Chiappetti, L., Page, C. G., Shaw, R. A., & Stobie, E. 2010, A&A, 524, A42, doi: `10.1051/0004-6361/201015362`

Peterson, J., & Fabian, A. 2006, Physics Reports, 427, 1

Piffaretti, R., Arnaud, M., Pratt, G. W., Pointecouteau, E., & Melin, J. B. 2011, A&A, 534, A109. `https://arxiv.org/abs/1007.1916`

Ponman, T. J., Cannon, D. B., & Navarro, J. F. 1999, Nature, 397, 135

Ponman, T. J., Sanderson, A. J. R., & Finoguenov, A. 2003, Monthly Notices of the Royal Astronomical Society, 343, 331

Pratt, G. W., Böhringer, H., Croston, J. H., et al. 2006, Astronomy & Astrophysics, 461, 71

Pratt, G. W., Croston, J. H., Arnaud, M., & Böhringer, H. 2009, Astronomy & Astrophysics, 498, 361. `https://arxiv.org/abs/0809.3784`

Price-Whelan, A. M., Sipőcz, B. M., Günther, H. M., et al. 2018, The Astronomical Journal, 156, 123

Rasia, E., Borgani, S., Murante, G., et al. 2015, The Astrophysical Journal Supplement Series, 813, L17, doi: `10.1088/2041-8205/813/1/L17`

Reichert, A., Böhringer, H., Fassbender, R., & Mühlegger, M. 2011, Astronomy & Astrophysics, 535, A4, doi: `10.1051/0004-6361/201116861`

Renzini, A. 1997, The Astrophysical Journal, 488, 35, doi: `10.1086/304696`

Rykoff, E. S., Rozo, E., Hollowood, D., et al. 2016, ApJS, 224, 1, doi: `10.3847/0067-0049/224/1/1`

Sarazin, C. L. 1986, Reviews of Modern Physics, 58, 1

Serlemitsos, P. J., Smith, B. W., Boldt, E. A., Holt, S. S., & Swank, J. H. 1977, The Astrophysical Journal, 211, L63, doi: `10.1086/182342`

Sifón, C., Menanteau, F., Hasselfield, M., et al. 2013, ApJ, 772, 25. `https://arxiv.org/abs/1201.0991`

Smee, S. A., Barkhouser, R., Hope, S., et al. 2018, Ground-based and Airborne Instrumentation for Astronomy VII

Stark, A. A., Gammie, C. F., Wilson, R. W., et al. 1992, The Astrophysical Journal Supplement Series, 79, 77

Sun, M. 2012, New Journal of Physics, 14, 045004, doi: `10.1088/1367-2630/14/4/045004`

Tanaka, Y., Inoue, H., & Holt, S. S. 1994, Publications of the Astronomical Society of Japan, 46, L37

Tody, D. 1986, Instrumentation in Astronomy VI

Tody, D. 1993, in Astronomical Society of the Pacific Conference Series, Vol. 52, Astronomical Data Analysis Software and Systems II, ed. R. J. Hanisch, R. J. V. Brissenden, & J. Barnes, 173

Torres-Robledo, S., & Briceño, C. 2019, Astronomical Society of the Pacific Conference Series, Vol. 523, A Real-Time Data Reduction Pipeline for the Goodman Spectrograph, ed. P. J. Teuben, M. W. Pound, B. A. Thomas, & E. M. Warner, 203

Valdarnini, R. 2003, Monthly Notices of the Royal Astronomical Society, 339, 1117

Vikhlinin, A., Kravtsov, A., Forman, W., et al. 2006, The Astrophysical Journal, 640, 691

Vikhlinin, A., Markevitch, M., Murray, S. S., et al. 2005, The Astrophysical Journal, 628, 655

Vogelsberger, M., Marinacci, F., Torrey, P., et al. 2017, Monthly Notices of the Royal Astronomical Society, 474, 2073

Voit, G. M. 2005, Reviews of Modern Physics, 77, 207

Voit, G. M. 2005, Reviews of Modern Physics, 77, 207, doi: `10.1103/RevModPhys.77.207`

Webb, T. M. A., O'Donnell, D., Yee, H. K. C., et al. 2013, AJ, 146, 84. `https://arxiv.org/abs/1304.3335`

Wells, D. C., Greisen, E. W., & Harten, R. H. 1981, A&AS, 44, 363

Wen, Z. L., & Han, J. L. 2015, ApJ, 807, 178. `https://arxiv.org/abs/1506.04503`

Wen, Z. L., Han, J. L., & Liu, F. S. 2012, ApJS, 199, 34. `https://arxiv.org/abs/1202.6424`

Werner, N., Durret, F., Ohashi, T., Schindler, S., & Wiersma, R. P. C. 2008, Space Science Reviews, 134, 337, doi: `10.1007/s11214-008-9320-9`

Wirtz, C. 1918, Astronomische Nachrichten, 206, 109

Zwicky, F. 1933, Helvetica Physica Acta, 6, 110

Zwicky, F. 1937, The Astrophysical Journal, 86, 217